

---

Doctoral Dissertations

Student Theses and Dissertations


---

Summer 2018

## Multi-scale investigation of microstructure, fiber-matrix bond, and mechanical properties of ultra-high performance concrete

Zemei Wu

Follow this and additional works at: [https://scholarsmine.mst.edu/doctoral\\_dissertations](https://scholarsmine.mst.edu/doctoral_dissertations)

 Part of the [Civil Engineering Commons](#), and the [Materials Science and Engineering Commons](#)

Department: Civil, Architectural and Environmental Engineering

---

### Recommended Citation

Wu, Zemei, "Multi-scale investigation of microstructure, fiber-matrix bond, and mechanical properties of ultra-high performance concrete" (2018). *Doctoral Dissertations*. 2712.

[https://scholarsmine.mst.edu/doctoral\\_dissertations/2712](https://scholarsmine.mst.edu/doctoral_dissertations/2712)

This thesis is brought to you by Scholars' Mine, a service of the Missouri S&T Library and Learning Resources. This work is protected by U. S. Copyright Law. Unauthorized use including reproduction for redistribution requires the permission of the copyright holder. For more information, please contact [scholarsmine@mst.edu](mailto:scholarsmine@mst.edu).

MULTI-SCALE INVESTIGATION OF MICROSTRUCTURE, FIBER-MATRIX  
BOND, AND MECHANICAL PROPERTIES OF ULTRA-HIGH PERFORMANCE  
CONCRETE

by

ZEMEI WU

A DISSERTATION

Presented to the Faculty of the Graduate School of the

MISSOURI UNIVERSITY OF SCIENCE AND TECHNOLOGY

In Partial Fulfillment of the Requirements for the Degree

DOCTOR OF PHILOSOPHY

in

CIVIL ENGINEERING

2018

Approved by:

Dr. Kamal H. Khayat, Advisor  
Dr. Dimitri Feys  
Dr. Hongyan Ma  
Dr. Jeffrey Smith  
Dr. Caijun Shi

© 2018

Zemei Wu

All Rights Reserved

## ABSTRACT

The main objective of this study is to provide new insights into enhancing fiber-matrix bond and mechanical properties of ultra-high performance concrete (UHPC). Three main strategies were investigated: 1) use of supplementary cementitious materials; 2) use of nano-particles; and 3) use of deformed fibers. A multi-scale investigation involving the evaluation of non-fibrous UHPC mortar phase (matrix), fiber-matrix interface phase, and then UHPC composite material was undertaken to determine microstructural characteristics, fiber bond to matrix, and key mechanical properties of the UHPC matrix and UHPC. Test results indicate that the incorporation of 10%-20% silica fume effectively improved the fiber-matrix bond and mechanical properties due to increased C-S-H content and decreased porosity. The flexural and tensile strengths of UHPC were found to increase by approximately 15%-30% and 35%-70%, respectively. Optimal nano-CaCO<sub>3</sub> and nano-SiO<sub>2</sub> contents were found to be 3.2% and 1.0%, respectively, by mass of binder. High nano-particle content decreased the fiber-matrix bond and mechanical properties of matrix and UHPC due to the increased porosity and introduction of weak zone at fiber-matrix interface. The use of deformed fibers enhanced bond given additional mechanical interlocking and enhanced friction. Compared to straight fibers, the corrugated and hooked fibers improved the bond strengths by approximately three and seven times, respectively. Such values were three and four times greater for pullout energy. The flexural strengths of UHPC made with 2% corrugated and hooked fibers were enhanced by approximately 10%-30% and 15%-50%, respectively. The tensile/flexural strengths of UHPC can be predicted based on the composite theory given fiber-matrix bond strength, strength of matrix, and fiber characteristics.

## ACKNOWLEDGMENTS

I would like to express my sincere appreciation and deepest gratitude to Dr. Kamal H. Khayat for offering me great opportunities, precious and continuous guidance, support, and encouragement, and wonderful environment to effectively study and do my research at Missouri University of Science and Technology (Missouri S&T).

Warm thanks to Dr. Dimitri Feys, Dr. Hongyan Ma, Dr. Jeffrey Smith, and Dr. Caijun Shi for their precious time and effort to review my dissertation and offer insightful and valuable comments. I would like to acknowledge the great support provided by my dear friends and colleagues at Missouri S&T, including Dr. Weina Meng, Mr. Jason Cox, Dr. Jia Yu, Dr. Iman Mehdipour, Dr. Mahdi Valipour, Ms. Kavya Vallurupalli, Mr. Le Teng, Dr. Seyedhamed Sadati, Mr. Brian Swift, and Mr. Gary Abbott. The cooperation and support from Ms. Abigayle Sherman and Ms. Gayle Spitzmiller at the Center for Infrastructure Engineering Studies (CIES) are also greatly acknowledged.

Gratitude is extended to those people from weekly badminton group, with whom I shared a lot of beautiful times and memories.

I would like to acknowledge the financial supports from RE-CAST University Transportation Center at Missouri S&T under grant No. DTRT13-G-UTC45, as well as the National Science Foundation of China under project Nos. U1305243 and 51378196.

Finally, I would like to thank my beloved family members, who have always been there to support and encourage me. My deepest appreciation to my parents for their unconditional love. Special and sincere gratitude to my beloved husband, Saiyin, for his love along this long journey chasing my dreams and completing my Ph.D.

## TABLE OF CONTENTS

|   | Page |
|---|------|
| ABSTRACT.....   | iii  |
| ACKNOWLEDGMENTS .....   | iv   |
| LIST OF ILLUSTRATIONS .....   | xii  |
| LIST OF TABLES.....   | xvi  |
| <b>SECTION</b>  |      |
| 1. INTRODUCTION.....  | 1    |
| 1.1. BACKGROUND .....   | 1    |
| 1.2. RESEARCH OBJECTIVES AND SIGNIFICANCE.....                              | 3    |
| 1.3. SCOPE.....   | 5    |
| 1.4. DISSERTATION ORGANIZATION .....  | 6    |
| 2. LITERATURE REVIEW.....   | 9    |
| 2.1. UHPC.....  | 9    |
| 2.2. FUNDAMENTAL PRINCIPLES FOR PRODUCTION OF UHPC .....                    | 10   |
| 2.2.1. Reduction in Porosity.....   | 10   |
| 2.2.2. Improvement in Microstructure.....                                   | 11   |
| 2.2.3. Enhancement in Homogeneity.....                                      | 11   |
| 2.2.4. Increase in Strength and Toughness.....                              | 14   |
| 2.3. CHARACTERISTICS OF FIBER-MATRIX INTERFACE AND BOND<br>PROPERTIES ..... | 15   |
| 2.3.1. Formation of Interface.....  | 16   |
| 2.3.2. Characteristics of Fiber-Matrix Interface.....                       | 16   |
| 2.3.3. Fiber-Matrix Bond Properties.....                                    | 17   |
| 2.4. MECHANICAL PROPERTIES OF UHPC .....                                    | 19   |

|   |    |
|---|----|
|   | vi |
| 2.4.1. Compressive Strength Behavior.....                   | 19 |
| 2.4.2. Tensile Strength Behavior.....                       | 21 |
| 2.4.3. Flexural Strength Behavior.....                      | 22 |
| 2.4.4. Impact Properties.....                               | 23 |
| 2.5. FIBER STRENGTHENING AND REINFORCING MECHANISMS .....   | 25 |
| 2.5.1. Theory of Composite.....                             | 25 |
| 2.5.2. Fiber Space Theory.....                              | 27 |
| 2.6. CONCLUDING REMARKS AND RESEARCH NEED .....             | 29 |
| 2.6.1. Concluding Remarks.....                              | 29 |
| 2.6.2. Research Need.....                                   | 30 |
| 3. RAW MATERIALS, MIXTURE DESIGN, AND TESTING METHODS ..... | 32 |
| 3.1. CHARACTERISTICS OF RAW MATERIALS.....                  | 32 |
| 3.1.1. Cementitious Materials.....                          | 32 |
| 3.1.2. Sand.....  | 33 |
| 3.1.3. Steel Fiber.....                                     | 33 |
| 3.1.4. Superplasticizer.....                                | 33 |
| 3.2. MIXTURE PROPORTIONING.....                             | 34 |
| 3.2.1. UHPC Matrix without Steel Fiber.....                 | 34 |
| 3.2.1.1. Silica fume series.....                            | 34 |
| 3.2.1.2. Nano-CaCO <sub>3</sub> series.....                 | 34 |
| 3.2.1.3. Nano-SiO <sub>2</sub> series.....                  | 35 |
| 3.2.2. UHPC Reinforced with Steel Fiber.....                | 35 |
| 3.2.2.1. Silica fume series.....                            | 35 |
| 3.2.2.2. Nano-CaCO <sub>3</sub> series.....                 | 36 |

|  |    |
|--|----|
| 3.2.2.3. Nano-SiO <sub>2</sub> series.....   | 37 |
| 3.2.2.4. UHPC with optimized composition.....  | 37 |
| 3.3. UHPC MIXTURE PREPARATION AND CURING .....   | 37 |
| 3.4. TESTING METHODS .....   | 38 |
| 3.4.1. Flowability.....  | 38 |
| 3.4.2. Calorimetry Analysis.....   | 38 |
| 3.4.3. Fiber Pullout Test. ....  | 38 |
| 3.4.4. Compressive and Three-Point Flexural Strengths Tests. ....                                    | 40 |
| 3.4.5. Four-Point Flexural Properties Test. ....   | 41 |
| 3.4.6. Tensile Properties Test. ....   | 41 |
| 3.4.7. Drop-Weight Impact Flexural Properties Test. ....   | 42 |
| 3.4.8. Thermal Gravimetric Analysis. ....  | 43 |
| 3.4.9. Pore Structure Observation. ....  | 43 |
| 3.4.10. 3D Micro-Tomography. ....  | 43 |
| 3.4.11. Scanning Electron Microscopy (SEM) Observation.....  | 44 |
| 3.4.12. X-Ray Diffraction (XRD) Analysis. ....   | 44 |
| 3.4.13. Micro-Hardness Measurement. ....   | 45 |
| 4. INFLUENCE OF SILICA FUME CONTENT ON STENGTH AND<br>DEVELOPMENT MICROSTRUCTURE OF UHPC MATRIX..... | 46 |
| 4.1. BACKGROUND .....  | 46 |
| 4.2. EFFECT OF SILICA FUME CONTENT ON HEAT OF HYDRATION OF<br>UHPC MATRIX.....                       | 48 |
| 4.3. EFFECT OF SILICA FUME CONTENT ON COMPRESSIVE AND<br>FLEXURAL STRENGTHS OF UHPC MATRIX .....     | 49 |
| 4.4. TG/DTG ANALYSES.....  | 50 |



|  |    |
|--|----|
| 4.5. PORE STRUCTURE CHARACTERISTICS .....  | 53 |
| 4.6. DISCUSSION.....   | 58 |
| 4.7. SUMMARY .....   | 59 |
| 5. FIBER PULLOUT, TENSILE, AND FLEXURAL PROPERTIES OF UHPC<br>MADE WITH DIFFERENT SILICA FUME CONTENTS.....                        | 60 |
| 5.1. BACKGROUND .....  | 60 |
| 5.2. FIBER PULLOUT BEHAVIOR .....  | 62 |
| 5.3. FLEXURAL PROPERTIES OF UHPC MATRIX AND UHPC .....   | 63 |
| 5.4. TENSILE PROPERTIES OF UHPC MATRIX AND UHPC.....   | 66 |
| 5.5. FLEXURAL AND TENSILE STRENGTHS RELATIONSHIP.....  | 67 |
| 5.6. PREDICTION OF TENSILE STRENGTH BASED ON FIBER-MATRIX<br>BOND STRENGTH.....  | 68 |
| 5.7. SUMMARY .....   | 70 |
| 6. MULTI-SCALE INVESTIGATION OF MICROSTRUCTURE, FIBER BOND,<br>AND MECHANICAL PROPERTIES OF UHPC WITH NANO-CaCO <sub>3</sub> ..... | 72 |
| 6.1. BACKGROUND .....  | 72 |
| 6.2. EFFECT OF NANO-CaCO <sub>3</sub> ON INTERFACIAL FIBER-MATRIX BOND<br>AND MECHANICAL PROPERTIES OF UHPC MATRIX.....            | 74 |
| 6.2.1. Fiber Pullout-Slip Curves.....  | 74 |
| 6.2.2. Experimental and Predicted Bond Strengths.....  | 74 |
| 6.2.3. Experimental and Predicted Pullout Energies.....  | 79 |
| 6.3. EFFECT OF NANO-CaCO <sub>3</sub> ON MICROSTRUCTURE OF UHPC<br>MATRIX .....  | 81 |
| 6.3.1. MIP Results.....  | 81 |
| 6.3.2. TG/DTG Analysis.....  | 85 |
| 6.3.3. CH Content.....   | 87 |
| 6.3.4. BSEM Image Analysis.....  | 88 |

|   |     |
|---|-----|
|   | ix  |
| 6.3.5. Optical Microscopy Analysis. ....  | 89  |
| 6.3.6. Micro-Hardness Characteristics. ....   | 92  |
| 6.4. EFFECT OF NANO-CaCO <sub>3</sub> ON MECHANICAL PROPERTIES OF UHPC. ....                                    | 93  |
| 6.4.1. Compressive Strength. ....   | 93  |
| 6.4.2. Flexural Behavior. ....  | 94  |
| 6.5. DISCUSSION.....  | 96  |
| 6.6. SUMMARY.....   | 97  |
| 7. UNDERSTANDING MECHANISM UNDERLYING STRENGTH<br>ENHANCEMENT OF UHPC MODIFIED WITH NANO-SiO <sub>2</sub> ..... | 99  |
| 7.1. BACKGROUND.....  | 99  |
| 7.2. EFFECT OF NANO-SiO <sub>2</sub> ON FIBER-MATRIX BOND PROPERTIES OF<br>UHPC MATRIX.....                     | 100 |
| 7.3. MECHANICAL PROPERTIES OF UHPC WITH 2% STEEL FIBERS.....  | 104 |
| 7.4. EFFECT OF NANO-SiO <sub>2</sub> ON MICROSTRUCTURE OF UHPC.....   | 105 |
| 7.4.1. MIP Results. ....  | 105 |
| 7.4.2. 3D Micro-Tomography. ....  | 107 |
| 7.4.3. BSEM Observation of UHPC Matrix with and without Nano-SiO <sub>2</sub> . ....                            | 109 |
| 7.4.4. BSEM Observation of Fiber-Matrix Interface. ....   | 110 |
| 7.4.5. Element Mapping of Fiber-Matrix Interface. ....  | 112 |
| 7.4.6. Micro-Hardness of Matrix around Fiber. ....  | 117 |
| 7.5. SUMMARY.....   | 118 |
| 8. HOW DOES FIBER SHAPE AFFECT FIBER PULLOUT BEHAVIOR AND<br>MECHANICAL PROPERTIES OF UHPC?.....                | 120 |
| 8.1. BACKGROUND.....  | 120 |
| 8.2. EFFECT OF STEEL FIBER SHAPE ON INTERFACIAL BOND<br>PROPERTIES BETWEEN FIBER AND UHPC MATRIX.....           | 122 |

|  |     |
|--|-----|
|  | x   |
| 8.2.1. Pullout Load-Slip Relationship.....   | 122 |
| 8.2.2. Bond Strength to Embedded Fibers.....   | 125 |
| 8.2.3. Pullout Energy.....   | 127 |
| 8.3. MICROSTRUCTURAL EXAMINATION.....  | 128 |
| 8.3.1. MIP Measurement.....  | 128 |
| 8.3.2. Optical Microscopy Observation.....   | 129 |
| 8.3.3. XRD Analysis.....   | 130 |
| 8.3.4. Calcium Hydroxide Content.....  | 132 |
| 8.4. EFFECT OF STEEL FIBER SHAPE ON MECHANICAL PROPERTIES<br>OF UHPC WITH 2% STEEL FIBERS.....               | 133 |
| 8.4.1. Compressive Strength.....   | 133 |
| 8.4.2. Flexural Behavior.....  | 134 |
| 8.4.3. Bond Strength vs. Flexural Strength of UHPC.....  | 135 |
| 8.5. PREDICTION OF FLEXURAL STRENGTH OF UHPC BASED ON<br>COMPOSITE THEORY.....                               | 136 |
| 8.6. SUMMARY.....  | 139 |
| 9. COMPARISON OF STATIC AND IMPACT FLEXURAL PROPERTIES OF<br>OPTIMIZED UHPC WITH SCMS AND NANOPARTICLES..... | 141 |
| 9.1. BACKGROUND.....   | 141 |
| 9.2. STATIC AND IMPACT MECHANICAL PROPERTIES OF UHPC<br>MATRIX.....  | 144 |
| 9.2.1. Static Compressive and Flexural Strengths of UHPC Matrix.....   | 144 |
| 9.2.2. Impact Flexural Behavior of UHPC Matrix.....  | 146 |
| 9.3. BOND PROPERTIES BETWEEN EMBEDDED FIBERS AND UHPC<br>MATRIX.....   | 148 |
| 9.4. STATIC AND IMPACT MECHANICAL PROPERTIES OF UHPC.....  | 149 |

|   |     |
|---|-----|
|   | xi  |
| 9.4.1. Static Compressive and Flexural Strengths of UHPC.....                   | 149 |
| 9.4.2. Impact Flexural Properties of UHPC. ....                                 | 151 |
| 9.5. RADAR CHART ANALYSIS FOR FIBER-MATRIX BOND AND<br>FLEXURAL PROPERTIES..... | 154 |
| 9.6. SUMMARY .....  | 155 |
| 10. CONCLUSIONS AND FUTURE WORK.....  | 157 |
| 10.1. CONCLUSIONS .....   | 157 |
| 10.1.1. Silica Fume Series.....   | 157 |
| 10.1.1.1. UHPC matrix with fixed SP dosage. ....                                | 157 |
| 10.1.1.2. UHPC matrix and UHPC with fixed flowability.....                      | 158 |
| 10.1.2. Nano-CaCO <sub>3</sub> Series.....                                      | 158 |
| 10.1.3. Nano-SiO <sub>2</sub> Series.....                                       | 159 |
| 10.1.4. UHPC Reinforced with Different Fiber Geometries.....                    | 160 |
| 10.1.5. UHPC with Optimized Composition.....                                    | 161 |
| 10.2. FUTURE RESEARCH.....  | 162 |
| APPENDIX .....  | 164 |
| BIBLIOGRAPHY .....  | 172 |
| VITA .....  | 190 |

## LIST OF ILLUSTRATIONS

|  | Page |
|--|------|
| Figure 1.1. Scope of the research.....   | 5    |
| Figure 2.1. SEM observations of ITZ of UHPC under different curing regimes [32].....                                       | 12   |
| Figure 2.2. Energy-absorbing mechanisms through fiber-matrix interface [39] .....  | 15   |
| Figure 2.3. Schematic representation of ITZ between fiber and matrix [49] .....  | 16   |
| Figure 2.4. Fiber-reinforced concrete under tensile stress.....  | 25   |
| Figure 2.5. Crack restraining mechanism of fiber reinforcement in fiber-reinforced concrete (modified based on [90]) ..... | 28   |
| Figure 3.1. Morphology of nano-particles .....   | 32   |
| Figure 3.2. Illustration of dog-bone shaped specimen and pullout testing apparatus.....                                    | 40   |
| Figure 3.3. Illustration of tensile test .....   | 42   |
| Figure 3.4. Illustration of drop-weight impact system.....   | 42   |
| Figure 3.5. Micro-hardness testing for UHPC matrix with an embedded fiber.....   | 45   |
| Figure 4.1. Heat evolution rate of UHPC matrix with different silica fume contents .....                                   | 48   |
| Figure 4.2. Effect of silica fume content on compressive and flexural strengths of UHPC matrix .....                       | 50   |
| Figure 4.3. TG and DTG curves of matrix with different silica fume contents at 28 d.....                                   | 51   |
| Figure 4.4. TG and DTG curves of U15 and U20 samples at different curing ages.....   | 52   |
| Figure 4.5. Content of CH in UHPC matrix from TG analysis .....  | 53   |
| Figure 4.6. Pore structure of UHPC matrix with different silica fume contents at 1 d.....                                  | 54   |
| Figure 4.7. Pore structure of UHPC matrix with different silica fume contents at 28 d.....                                 | 55   |
| Figure 4.8. Pore structure of U20 mixture at different ages .....  | 56   |
| Figure 4.9. Pore volume distribution of UHPC matrix.....   | 57   |

|  |    |
|--|----|
| Figure 5.1. Fiber pullout behavior in non-fibrous UHPC matrix with different silica fume contents .....                      | 63 |
| Figure 5.2. Flexural behavior of UHPC matrix with different silica fume contents .....                                       | 64 |
| Figure 5.3. Flexural load-displacement relationship of UHPC made with 2% steel fibers at different silica fume contents..... | 65 |
| Figure 5.4. Flexural strength of UHPC made with 2% steel fibers at different silica fume contents .....                      | 65 |
| Figure 5.5. Tensile load-extension relationship of UHPC made with 2% steel fibers at different silica fume contents .....    | 66 |
| Figure 5.6. Tensile strengths of UHPC matrix and UHPC with different silica fume contents .....                              | 66 |
| Figure 5.7. Flexural-to-tensile strength ratios of UHPC matrix and UHPC.....   | 68 |
| Figure 5.8. Predicted and experimental tensile strengths of UHPC with 2% steel fibers .....                                  | 70 |
| Figure 6.1. Fiber pullout load-slip curves of UHPC matrix with different nano-CaCO <sub>3</sub> contents.....                | 75 |
| Figure 6.2. Effect of nano-CaCO <sub>3</sub> on fiber-matrix bond strength and compressive strength of UHPC matrix .....     | 76 |
| Figure 6.3. Predicted fiber-matrix bond strength with variation of nano-CaCO <sub>3</sub> content and curing age .....       | 79 |
| Figure 6.4. Effect of nano-CaCO <sub>3</sub> content on fiber-matrix pullout energy .....                                    | 80 |
| Figure 6.5. Predicted pullout energy with variation of nano-CaCO <sub>3</sub> content and curing age.....                    | 81 |
| Figure 6.6. Effect of nano-CaCO <sub>3</sub> content on porosity and pore size distribution of UHPC matrix at 28 d.....      | 82 |
| Figure 6.7. Effect of age on porosity and pore size distribution of NC series.....   | 83 |
| Figure 6.8. Effect of nano-CaCO <sub>3</sub> content and curing age on pore volume distribution of UHPC matrix.....          | 84 |
| Figure 6.9. TG and DTG curves of UHPC matrix with different nano-CaCO <sub>3</sub> contents at 28 d .....                    | 86 |
| Figure 6.10. TG and DTG curves of NS3.2 at different ages .....  | 87 |

|  |     |
|--|-----|
| Figure 6.11. Amount of CH formed in UHPC matrix with different nano-CaCO <sub>3</sub> contents with age.....                                 | 88  |
| Figure 6.12. BSEM images for UHPC matrix with an embedded fiber .....  | 90  |
| Figure 6.13. Optical microscopy observation of UHPC matrix made with 6.4% nano-CaCO <sub>3</sub> .....                                       | 91  |
| Figure 6.14. Compressive strength of UHPC with different nano-CaCO <sub>3</sub> contents.....  | 94  |
| Figure 6.15. Flexural load-deflection curves of UHPC with different nano-CaCO <sub>3</sub> contents .....                                    | 95  |
| Figure 7.1. Pullout load-slip curves of embedded fibers in UHPC matrix with different nano-SiO <sub>2</sub> contents .....                   | 101 |
| Figure 7.2. Typical pullout load versus slip relationship [180] .....  | 102 |
| Figure 7.3. Effect of nano-SiO <sub>2</sub> content on bond strength of fiber-matrix interface and compressive strength of UHPC matrix ..... | 103 |
| Figure 7.4. Effect of nano-SiO <sub>2</sub> content on compressive and flexural strengths of UHPC .....                                      | 104 |
| Figure 7.5. Effect of nano-SiO <sub>2</sub> content and curing age on total porosity of UHPC matrix .....                                    | 105 |
| Figure 7.6. Pore volume distribution of UHPC matrix made with different nano-SiO <sub>2</sub> contents and at various ages .....             | 107 |
| Figure 7.7. 3D micro-tomography of the reference sample (NS0) with an embedded fiber at 28 d after fiber pullout testing .....               | 108 |
| Figure 7.8. BSEM observation of UHPC matrix with and without nano-particles .....  | 110 |
| Figure 7.9. BSEM images of UHPC made with 0 and 1% nano-SiO <sub>2</sub> with an embedded fiber.....   | 111 |
| Figure 7.10. Surface plot of UHPC sample with an embedded fiber .....  | 112 |
| Figure 7.11. Element mappings of fiber-matrix interface in the reference mixture NS0 .....   | 113 |
| Figure 7.12. Element mappings of fiber-matrix interface in the NS1.0 mixture .....   | 114 |
| Figure 7.13. Morphology and element atomic number distribution along the scanning line in the NS0 mixture.....                               | 115 |

|   |     |
|---|-----|
| Figure 7.14. Morphology and element atomic number distribution along the scanning line in the NS1.0 mixture.....      | 116 |
| Figure 8.1. Pullout load-slip curves of the U15 and U20 matrix embedded with different fiber geometries.....          | 123 |
| Figure 8.2. Effect of fiber shape on bond strength between fiber and U15 and U20 matrix .....                         | 126 |
| Figure 8.3. Effect of fiber shape on pullout energy between fiber and matrix for the U15 and U20 matrix.....          | 127 |
| Figure 8.4. MIP results of the U15 and U20 matrix at 1 and 28 d .....   | 128 |
| Figure 8.5. Optical microscopy observation of fiber before and after pullout from matrix .....                        | 130 |
| Figure 8.6. XRD patterns of U20 mixture at different ages.....  | 131 |
| Figure 8.7. CH content in the U15 and U20 matrix at different ages .....  | 132 |
| Figure 8.8. Relationship between bond strength of straight fiber and CH content.....                                  | 132 |
| Figure 8.9. Compressive strength development of UHPC made with 2% straight, corrugated, and hooked steel fibers ..... | 134 |
| Figure 8.10. Flexural load-deflection curves of UHPC made with 2% straight, corrugated and hooked steel fibers .....  | 135 |
| Figure 8.11. Bond strength vs. flexural strength of UHPC with 2% steel fibers of different shapes .....               | 136 |
| Figure 9.1. Static compressive and flexural strengths of UHPC matrix at 7 and 28 d ....                               | 145 |
| Figure 9.2. Static flexural strengths of investigated UHPC matrix at 28 d .....                                       | 145 |
| Figure 9.3. Impact flexural load-deflection curves of UHPC matrix at 28 d.....  | 146 |
| Figure 9.4. Fiber-matrix bond properties at 7 and 28 d .....  | 149 |
| Figure 9.5. Static compressive and flexural strengths of UHPC at 7 and 28 d.....                                      | 150 |
| Figure 9.6. Static flexural load-deflection curves of UHPC at 7 d.....  | 151 |
| Figure 9.7. Impact flexural load-deflection curves of UHPC at 7 d.....  | 152 |
| Figure 9.8. Radar chart analysis.....   | 154 |



## LIST OF TABLES

|   | Page |
|---|------|
| Table 2.1. Mechanical properties and durability of CC, HPC, and UHPC [14].....  | 9    |
| Table 2.2. Micro-mechanical properties of constituents in UHPC [36] .....   | 13   |
| Table 3.1. Geometries of three selected fibers.....   | 33   |
| Table 3.2. Mixture proportioning of UHPC matrix with different silica fume contents .....                                     | 34   |
| Table 3.3. Mixture proportioning of UHPC matrix with different nano-CaCO <sub>3</sub> and nano-SiO <sub>2</sub> contents..... | 35   |
| Table 3.4. Mixture proportioning of UHPC with different silica fume contents.....   | 36   |
| Table 3.5. Mixture proportioning of UHPC with different NC and NS contents .....  | 36   |
| Table 3.6. Mixture proportioning of UHPC with optimized composition of different SCMs and/or nano-particles .....             | 37   |
| Table 6.1. Parameter estimates for fiber-matrix bond strength through statistical analysis.....                               | 78   |
| Table 6.2. Parameter estimates for pullout energy through statistical analysis .....  | 80   |
| Table 6.3. Variation of micro-harness in UHPC matrix with and without nano-CaCO <sub>3</sub> at different ages .....          | 93   |
| Table 7.1. Void distribution in UHPC matrix with and without nano-SiO <sub>2</sub> observed from 3D micro-tomography .....    | 109  |
| Table 7.2. Micro-harness of UHPC matrix within 240 μm from the fiber edge.....  | 118  |
| Table 8.1. Semi-quantitative analysis of hydration products in the U20 mixture at different ages.....                         | 131  |
| Table 8.2. Predicted and experimental values of flexural strength of UHPC.....  | 138  |
| Table 9.1. Summary of static and dynamic flexural properties of UHPC matrix at 28 d.....                                      | 147  |
| Table 9.2. Summary of static and dynamic flexural strengths of UHPC at 7 d.....   | 153  |

## 1. INTRODUCTION

### 1.1. BACKGROUND

Plain concrete is typical a brittle material exhibiting a relatively low tensile strength, which is on the order of 8% to 15% of its compressive strength [1]. After reaching the first cracking strength, a sudden drop in load carrying capacity is obtained. The use of reinforcing steel and/or steel fibers is needed to resist tensile stress and reduce cracking in concrete. Fiber-reinforced composite materials have attracted considerable interest in recent years due to wide applications, such as repair, retrofitting of structural elements, and construction of high strength and lightweight elements. ACI Committee 544 defines fiber reinforced concrete (FRC) as a composite material made of cement, fine and/or coarse aggregates, and discontinuous discrete fibers [2]. Fibers include steel fibers, glass fibers, synthetic fibers and natural fibers, each of which can lead to varying properties to the concrete. The randomly oriented discrete fibers can efficiently control the propagation of cracks because of stress transfer from the matrix to steel fiber. This can eventually improve the tensile, bending, and shear properties of the composite materials.

There has been an increasing interest in the development and use of FRC with high strength and toughness. Several studies have been conducted on the design and performance of FRC. ACI 544 [2] offers extensive information about the testing and design of FRC and its benefits of structure uses related to the durability and mechanical properties. The majority of FRC can exhibit single-cracking and tensile strain softening behaviors [3, 4].

The amount of fibers added into a concrete mixture is expressed as a percentage of the total volume of the composite, including concrete and fibers, which is termed as volume fraction. Typically, FRC can contain fiber volume of 0.1% to 3%, depending on mixture proportion and fiber type, geometry, and shape [5]. Greater volume of fiber can hinder workability, lead to non-uniform orientation of fibers and increased material cost. With recent development of self-consolidating concrete, greater volume of steel fibers, ranging from 0.5% to 1%, can be employed [6]. In addition to FRC, specialty concrete containing greater contents of fibers has been developed. For example, Haynes [7] reported a forming method with placing steel fibers in the mold then infiltrating the slurry into the network. Similar approach was developed to prepare slurry infiltrated fiber concrete (SIFCON). Lankard [8] comprehensively studied this method and investigated the performance of SIFCON. SIFCON can obtain high compressive and flexural strengths of 238 and 38.5 MPa, respectively, as well as good ductility. Haekman et al. [9] developed slurry infiltrated mat concrete (SIMCON) using 4%-6% steel fiber-mats.

Li and Leung [10-13] proposed engineered cementitious composites (ECC) based on micromechanics using short metallic and/or nonmetallic fibers that can exhibit strain-hardening behavior. Such composite material can develop a typical tensile strain capacity greater than 3% and a multiple-cracking behavior with a maximum crack width less than 100  $\mu\text{m}$  [11-13]. The ECC can develop a typical compressive strength of 40 - 80 MPa. Richard and Cheyrezy [14,15] used fine and active components to develop reactive powder concrete (RPC), which is the early form of what is known today as ultra-high performance concrete (UHPC). RPC has 800-1200  $\text{kg/m}^3$  of binder, a very low water-to-binder ratio (w/b) of 0.2, a very fine siliceous sand with a nominal maximum size of 0.4

$\mu\text{m}$ , superplasticizer, and steel fibers. ACI 239 defines UHPC as a new composite material that possesses a minimum specified compressive strength of 150 MPa with specified durability, tensile ductility, and toughness requirements in the presence of fibers [16]. Because of its extremely dense microstructure, high mechanical properties, and superior durability, UHPC has great potential applications in infrastructures, including pavements, bridges, repair and rehabilitation members, offshore structures, and protective shelters [17].

However, several challenges are faced before its wide use, including: 1) extremely high material cost associated with high binder content and steel fiber volume; 2) relatively low tensile/flexural strength compared to compressive strength due to mismatch in physical and mechanical properties between the non-fibrous matrix and the fibers; 3) high energy consumption associated with special curing regimen, such as 48 h of 90 °C curing, in order to achieve high compressive strength over 150 MPa. Some successful efforts have been recently made to reduce the material cost of UHPC without sacrificing mechanical properties of UHPC, including using river and masonry sand and supplementary cementitious materials [18,19]. As a type of inherently heterogeneous composite materials, its macro-properties have a close relationship with its microstructure, and/or bond to fiber. Limited work has been conducted on the effect of phase between the UHPC matrix and embedded fibers on the performance of UHPC.

## **1.2. RESEARCH OBJECTIVES AND SIGNIFICANCE**

The primary objective of this research is to provide new insights into enhancing the fiber-matrix bond and mechanical properties of UHPC through optimization of

microstructure, which finally targets at multi-optimization of performance for UHPC. Microstructure-bond-property relationship to link the characteristic of the bond at interfacial transition zone (ITZ) to the development of mechanical properties can be established. The specific objectives of work proposed in this thesis can be described as follows:

(1) To elucidate the effect of different factors on fiber-matrix interfacial bond properties, fresh and hardened properties of the UHPC matrix. Such factors include different types and contents of SCMs (silica fume, fly ash, and slag) as well as nanoparticles.

(2) To examine the silica fume content on fiber-bond behavior and key mechanical properties of non-fibrous UHPC matrix and UHPC with adequate rheology properties and uniform fiber orientation.

(3) To explore the features of microstructure development of the UHPC matrix and fiber-matrix interface using advanced techniques, including thermal-gravimetry analysis (TG), micro-hardness testing, scanning electron microscopy (SEM), X-ray diffraction (XRD), 3D micro-tomography, and mercury intrusion porosimetry (MIP).

(4) To evaluate fiber-matrix bond and mechanical properties of UHPC reinforced with different geometries. The composite mechanics theory can be employed to link the flexural/tensile strength of UHPC to fiber-matrix bond strength, mechanical properties of the matrix, and fiber parameters. This can give an important implication on predicting and enhancing the flexural/tensile strength of a complex UHPC structure with knowing the fundamental parameters of employed materials.

(5) To correlate relationship between microstructure, fiber-matrix bond properties, and static and impact mechanical properties of UHPC with relevant mixture composition.

The highlights of this proposed research would shed some light on how to optimize and/or predict the fiber-matrix bond properties and eventually mechanical properties of UHPC in the future research.

### 1.3. SCOPE

Figure 1.1 summarizes the scope of the proposed research that involved. The proposed work was carried out in four tasks as follows.

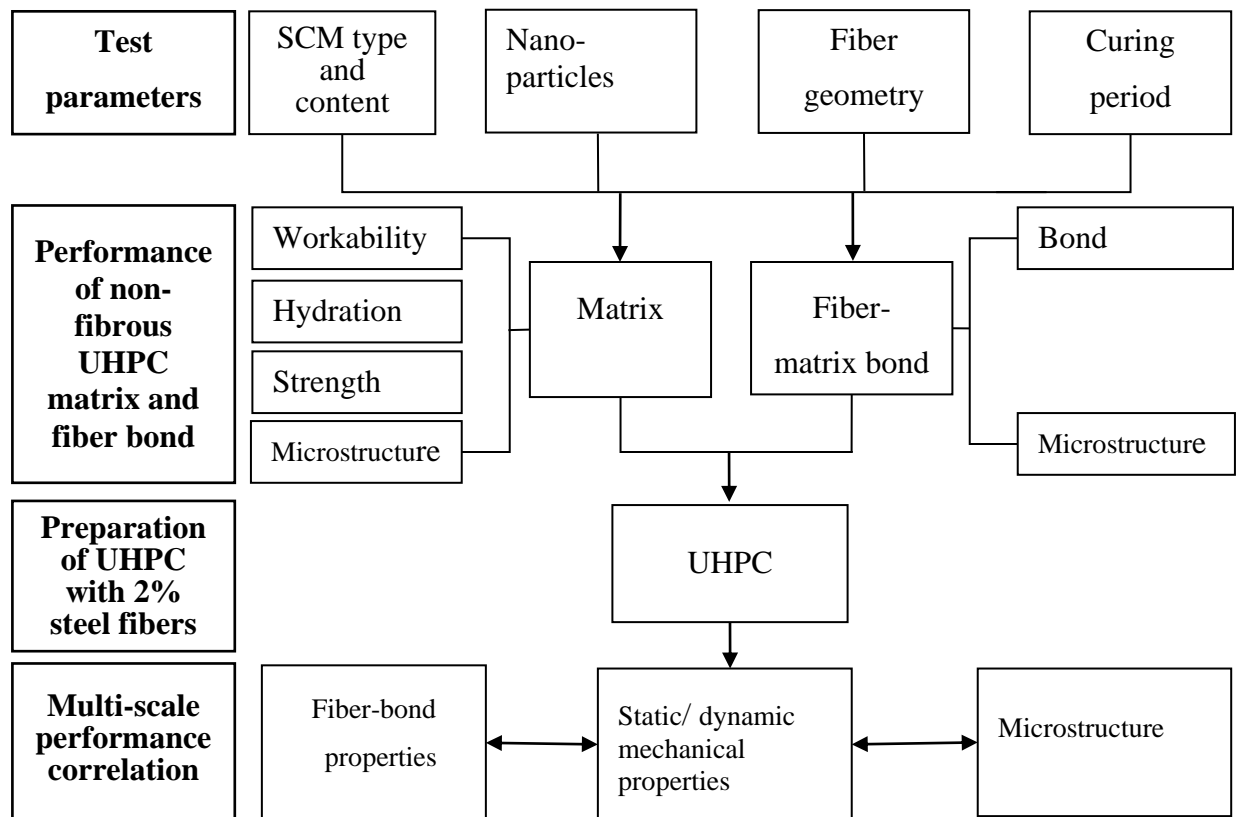


Figure 1.1. Scope of the research

Task 1: Influences of factors affecting fresh and hardened properties of UHPC matrix and bond properties of fiber-matrix interface;

Task 2: Investigation of microstructure of the UHPC matrix and fiber-matrix interface;

Task 3: Evaluation of fiber-matrix bond properties and mechanical properties of UHPC with different fiber geometries;

Task 4: Relationship between microstructure, fiber-matrix bond properties, and static and impact mechanical properties of UHPC.

#### **1.4. DISSERTATION ORGANIZATION**

The dissertation consists of 10 sections in the following sequence. Section 1 highlights the background, objectives, and scope of the research, and describes the organization of the dissertation.

Section 2 reviews the current state-of-the-art on the relevant topics, including fundamental principles for production of UHPC, characteristics of fiber-matrix interface and bond properties, mechanical properties of UHPC, fiber strengthening and reinforcing mechanisms. The concluding remarks and research need are then put forward. Part of the literature review has been published *Construction and Building Materials*.

Section 3 describes the constituent materials, mixture design, preparation and curing of specimens, and testing methods.

Section 4 investigates the effect of different silica fume contents on hydration kinetics, mechanical properties and microstructure of non-fibrous UHPC matrix at a fixed superplasticizer content. Advanced material characterization techniques, such as mercury

intrusion porosimetry (MIP) and thermal gravimetric (TG) are employed to investigate the microstructure development of the UHPC matrix. Focus is placed to secure high density and mechanical properties of UHPC matrix with optimized silica fume content. The findings from this section have been published in *Cement and Concrete Composites*.

Section 5 presents the fiber pullout, tensile, and flexural properties of UHPC matrix and UHPC made with 2% steel fibers with different silica fume contents at a fixed mini-slump flow of 280 mm. A simple and effective double-sided pullout test is proposed to examine the fiber-matrix bond properties. Flexural-to-tensile strength ratio of UHPC is determined and the tensile strength of UHPC made with different silica fume contents is evaluated using the composite theory based on fiber-matrix bond strength.

Section 6 presents a multi-scale investigation of microstructure, fiber-matrix bond, and mechanical properties of UHPC made with nano-CaCO<sub>3</sub>. The effect of nano-CaCO<sub>3</sub> on fiber-matrix bond and mechanical properties of UHPC is investigated. A statistical model is employed to fit the fiber-matrix bond properties with change in CaCO<sub>3</sub> content and curing time. Focus is placed to link the fiber-matrix bond to microstructure, and compressive and flexural strengths of UHPC with different nano-CaCO<sub>3</sub> contents. The results presented in this section have been published in *Cement and Concrete Composites*.

Section 7 explores the mechanism underlying strength enhancement of UHPC enhanced with nano-SiO<sub>2</sub>. The effect of nano-SiO<sub>2</sub> on fiber-matrix bond and mechanical properties of UHPC are investigated. Advanced material characterizations, including MIP, 3D micro-tomography, and BSEM were used to evaluate the microstructure of the matrix and the fiber-matrix interface. Micro-hardness around the embedded fiber was evaluated



as well. The results found from this section have been published in *Cement and Concrete Research* and *Cement and Concrete Composites*.

Section 8 aims at evaluating the efficiency of fiber strengthening and reinforcing mechanisms of UHPC made with different fiber geometries. The influence of straight, hooked, and corrugated fibers on fiber-matrix bond and mechanical properties of UHPC is studied. The composite theory is employed to predict the flexural strength of UHPC based on the experimental parameters, such as fiber length and volume, strength of UHPC matrix, fiber characteristics, and flexural-to-tensile strength ratio as determined from Section 5. The results have been submitted to *Cement and Concrete Composites*.

Section 9 discusses the static and impact flexural properties of optimized UHPC mixtures with various types of SCMs and nano-particles. Drop weight impact three-point bending testing is conducted to investigate the impact flexural behavior of the specimens, while the static flexural behavior is evaluated using the same-size specimens. Emphasis is placed on comparing the static and impact behavior of UHPC mixtures. The results have been submitted to *Construction and Building Materials*.

Section 10 summarizes the outcomes and findings of this dissertation and proposes perspectives for future research.

## 2. LITERATURE REVIEW

### 2.1. UHPC

ACI 239 defines UHPC as a new composite material that possesses a minimum specified compressive strength of 150 MPa with specified durability, tensile ductility, and toughness requirements in the presence of fibers [16]. On the other hand, ASTM C1856 addresses the UHPC specimens with a specified compressive strength of at least 120 MPa, with nominal maximum size aggregate of less than 5 mm, and a flow between 200 and 250, for the purpose of determining the performance [20]. Typical mechanical properties and durability of characteristics of conventional concrete (CC), high performance concrete (HPC), and UHPC are summarized in Table 2.1.

Table 2.1. Mechanical properties and durability of CC, HPC, and UHPC [14]

| Performance                                 | UHPC          | HPC      | CC          |
|---|---------------|----------|-------------|
| Compressive strength (MPa)                  | $\geq 150$    | 60-100   | 20-60       |
| Flexural strength (MPa)                     | 25-60         | 6-10     | 3-5         |
| Tensile strength (MPa)                      | 5-15          | $\leq 5$ | $\leq 3$    |
| Elastic modulus (GPa)                       | 40-60         | 30-40    | 20-30       |
| Fracture energy (J/m <sup>2</sup> )         | 20,000-40,000 | 120-500  | 30-100      |
| Chloride-ion diffusion (mm)                 | 1             | 8        | 23          |
| Carbonation depth after 3 years (mm)        | 1.5           | 4        | 7           |
| Salt-scaling resistance (g/m <sup>2</sup> ) | 20-50         | 150      | $\leq 1500$ |

Compared to CC and HPC, UHPC can develop: 1) very high mechanical properties, rendering it as an exceptional candidate for prefabricated structure members

with reduced dead-weight load and occupied space; 2) superior durability and extended service life and reduced maintenance cost given the nearly impermeable material to carbon dioxide, chlorides, and sulphates. It is important to note that hardened UHPC can have considerable amount of unhydrated cement particles that can further hydrate providing self-healing potential to cracked structures.

## **2.2. FUNDAMENTAL PRINCIPLES FOR PRODUCTION OF UHPC**

The fundamental principles for the production of UHPC involve four aspects, including the reduction in porosity, improvement in microstructure, enhancement in homogeneity, and increase in strength and toughness [21,22]. The following section briefly describes these aspects.

**2.2.1. Reduction in Porosity.** Pore characteristics, including porosity, pore size distribution, shape, and position of pores, have marked effect on mechanical and transport properties of hardened cement-based materials. It is widely accepted that the reduction of compressive strength can increase the total porosity, which is closely related to the water-to-cement ratio (w/c) [23,24]. Generally, the lower the w/c is, the lower the porosity is, and the higher the compressive strength is [25]. The porosity and pore size distribution of a hardened concrete can be effectively improved by the use of superplasticizer (SP), incorporation of SCMs, and proper curing [26,27]. SP can disperse cement particles due to high electrostatic repulsion and steric hindrance when a polycarboxylate type SP is used. This can increase the potential of hydration of the cement particles and result in finer porosity. The use of SP can also liberate some of the water that entrapped among agglomerated cement particles, thus enhancing the

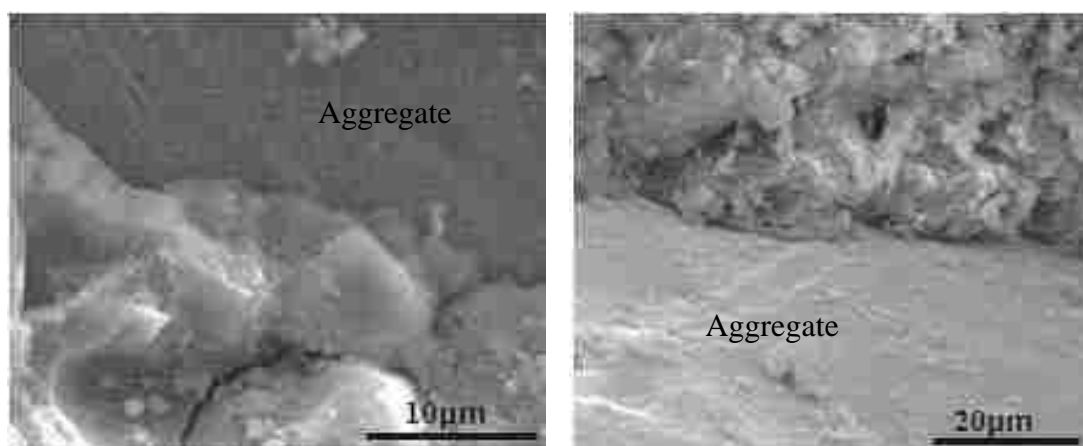
rheological properties of the material [28]. The use of SCMs has a marked effect on reducing the capillary pores through the filler and pozzolanic effect. Proper moist and heat curing are also essential to reduce porosity. Heat curing can accelerate cement hydration at early ages because of exerted energy from high temperature, thus reducing porosity. However, heat curing can be detrimental to strength development at long-term, including when applied to HPC and UHPC [29,30]. These strategies of reducing porosity lay the theoretical foundation for the design of UHPC.

**2.2.2. Improvement in Microstructure.** Compared to CC, UHPC can exhibit much denser and uniform microstructure due to: (1) close packing of the system associated with high amount of fine particles and absence of coarse aggregate; (2) acceleration of hydration and pozzolanic reaction related to elevated temperature curing; (3) reduction in relatively weak zones at interfacial transition zone (ITZ) associated with the use of small-size aggregates. The low w/b of UHPC can result in low porosity with null small pores from 30 to 100 nm [31]. This can restrict the space available for the growth of large calcium hydroxide (CH) crystals and reduce the CH content.

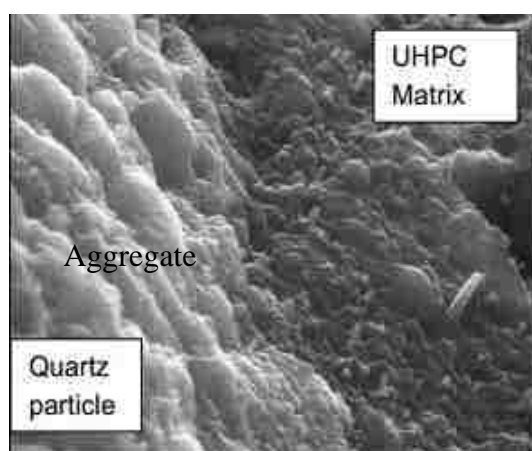
Scanning electronic microscopy (SEM) observations of ITZ in a conventional mortar and in UHPC under different curing regimes are shown in Figure 2.1 [32]. Because of the low w/b and highly pozzolanic reaction stemming from high content of silica fume, the ITZ in UHPC was greatly improved [33]. Such ITZ in UHPC appears to be as dense as the matrix, especially under autoclave curing, as indicated in Figure 2.1 (c).

**2.2.3. Enhancement in Homogeneity.** Aggregate, acting as a skeleton in mortar and concrete, can exhibit greater hardness than that of the cement paste. Its large

volume used in concrete reduces binder content and results in cost saving. However, shear and tensile stresses can easily occur between the aggregate and paste matrix given the mismatch in thermal and mechanical properties. The coefficient of thermal expansion of aggregate is  $5.6 - 6.7 \times 10^{-6}/^{\circ}\text{C}$ , while  $10 - 20 \times 10^{-6}/^{\circ}\text{C}$  for cement paste, depending on hydration time and w/b [34]. This can eventually lead to initiation and propagation of cracks in the ITZ, which can also propagate in the bulk cement paste. The larger the aggregate size is, the greater the crack size is, and the more the defect zone is [35].



(a) ITZ in UHPC after standard curing (b) ITZ in UHPC after 48 h steam curing



(c) ITZ in UHPC after autoclave curing

Figure 2.1. SEM observations of ITZ of UHPC under different curing regimes [32]

Therefore, the homogeneity of UHPC is significantly improved with the absence of coarse aggregate [15]. As observed from Figure 2.1 (a-c), ITZ in UHPC seems as dense as the matrix, indicating the homogeneity of its microstructure.

UHPC with optimization of micro-mechanical properties is also critical because of different constituents in UHPC have various indentation modulus that related to Young's modulus and hardness levels, as summarized in Table 2.2 [36, 37].

Table 2.2. Micro-mechanical properties of constituents in UHPC [36]

| Constituents       | Reference values  |   |
|--------------------|---|---|
|                    | Indentation modulus (GPa)                                     | Hardness (GPa)                          |
| Quartz powder      | 23.5  | 58.5 ± 19.4                             |
| Quartz sand        | 73 ± 1.6  | 10 ± 0.3                                |
| Cement clinker     | 125–145 ± 25, 126.8 ± 8.1                                     | 8–10.8 ± 3, 6.7 ± 1.2                   |
| Steel fiber        | 201.9 ± 20.3  | 11.99 ± 1.97                            |
| Micro porosity     | 9.1 ± 2.3   | 0.16 ± 0.07                             |
| Low density C-S-H  | 19.1 ± 5.0, 21.7 ± 2.2, 20.2 ± 2.0,<br>18.8 ± 4.0, 23.7 ± 0.8 | 0.80 ± 0.20, 0.66 ± 0.3,<br>0.47 ± 0.17 |
| High density C-S-H | 34.2 ± 5.0, 32.3 ± 3.0  | 1.36 ± 0.35, 1.29±0.1                   |

The UHPC is composed of C-S-H, CH, residual cement clinkers, fine aggregates, steel fibers, and pores. In term of stress transfer at the ITZ from the matrix to fiber, the quality of ITZ plays a dominated role in strength and toughness of UHPC. Although fiber used in UHPC is small, usually with diameter of 0.2 mm and length of 6-40 mm, porous zones exist due to the wall and bleeding effect. Given the multiple components of UHPC, including different SCM types and different curing regimes, differences in micro-

mechanical properties can exist. This can affect stress transferring efficiencies from the matrix to the fiber. Therefore, it is critical to develop UHPC with improved homogeneity in size and micro-mechanical properties. Limited work has been done to enhance the interface between the cement paste and embedded fibers in UHPC, which is affected by the various mechanisms elaborated here.

**2.2.4. Increase in Strength and Toughness.** Steel reinforcements in concrete is used to resist tensile loads and enhance toughness. Toughness is an indication of the energy absorption capacity of a material, which is the area under load-displacement curves [38]. Plain concrete on its own has relatively low tensile strength, strain capacity, and fracture toughness compared to performance of composite, regardless of level of compressive strength. The incorporation of reinforcement in concrete can effectively prevent and control the propagation of cracks. When loads are acted on a composite material, the fiber does not sustain the load at the very beginning. The load initially acts on the matrix, and then transferred to the fibers through the fiber-matrix interface.

Figure 2.2 illustrates the fiber energy-absorbing mechanism through the fiber-matrix interface [39]. Starting from the rightmost along the cracking path towards the left, matrix cracking, fiber-matrix debonding, fiber bridging, pull-out and/or fiber rupture sequentially occur.

Wu et al. [40] compared the flexural properties of UHPC made with 0-3% steel fibers measuring 13 mm length at a w/b of 0.18. A reference specimen with no fiber (A0) showed a sudden drop of load carrying capacity when achieving ultimate flexural strength [40]. The incorporation of steel fibers resulted additional load carrying capacity after reaching the first cracking load. After the peak load, the curves showed obvious

zigzag patterns, indicating an enhancement in toughness during fiber pullout. The higher volume of steel fiber led to greater flexural strength and toughness [40]. Greater volume of steel fibers up to 4%-6% was also employed in UHPC made with a low water-to-cement ratio of 0.15 [41]. However, high steel fiber content can lead to reduced flowability, non-uniform fiber dispersion, and high materials cost. The use of 2% steel fibers can secure high strength and toughens of UHPC. Long fibers enhanced the flexural strength and energy absorption capacity of UHPC, but exerted a limited effect on the first cracking properties [42].

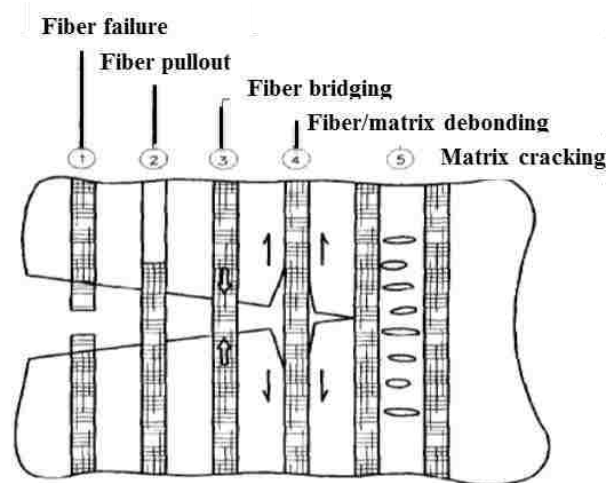


Figure 2.2. Energy-absorbing mechanisms through fiber-matrix interface [39]

### 2.3. CHARACTERISTICS OF FIBER-MATRIX INTERFACE AND BOND PROPERTIES

The characteristics of fiber-matrix interface and bond properties between the fiber and matrix are discussed with the consideration of different factors affecting such performance.



**2.3.1. Formation of Interface.** According to Maso [43], in the mixing process of cement-based materials, when solid particles are in contact with water, a water film with a thickness of several micro-meters can form around the fiber or aggregate surface. Dissolved ions from cement particles can penetrate into the water film and deposit and crystallize around the fiber or aggregate surface at different diffusion rates. For portland cement, the ion diffusion ability follows the order of  $\text{Na}^+ > \text{K}^+ > \text{SO}_4^{2-} > \text{Ca}^{2+} > \text{Si}^{4+}$  [44]. The first formed products would be ettringite and CH. Crystal CH has a preferential orientation with c-axis perpendicular toward the fiber or aggregate surface, which can leave some space near each other and makes the ITZ more porous than the matrix, as shown in Figure 2.3 [45]. Furthermore, the fiber and/or aggregate can block the upward movement of water and keep it underneath, eventually leading to the porous interface [46].

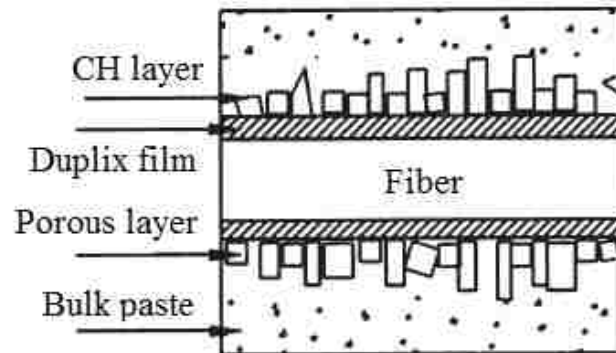


Figure 2.3. Schematic representation of ITZ between fiber and matrix [49]

**2.3.2. Characteristics of Fiber-Matrix Interface.** A fiber reinforced cement-based material is a multi-phase system made up of pores, matrix, aggregate, fiber, aggregate-matrix interface, and fiber-matrix interface. The existence of fiber-matrix and aggregate-matrix interfaces with a thickness of 50-100  $\mu\text{m}$  was confirmed by several

scholars [47-49]. Compared to the matrix, the interface exhibits the following characteristics:

(1) Higher w/c and greater porosity. The higher w/c of the matrix can result in higher w/c at the interface and thicker duplex film [50]. A relatively thicker duplex film can hinder the unhydrated particles to establish full contact with the fibers or aggregate. This can result in lower concentration of ions at the interface around aggregate and fiber and eventually a looser microstructure of the ITZ [51].

(2) Greater CH content. Due to the higher w/c at the interface compared to that of the matrix, ettringite and CH crystals can grow in unconstrained space. A layer of CH can precipitate initially with its c-axis preferentially oriented perpendicular to the surface of the fiber or aggregate. The CH content at the interface is 20%-40% greater than that in a matrix in conventional concrete [52].

(3) Lower micro-hardness. The porous zones can decrease the homogeneity of microstructure and contact area during micro-hardness testing and hence the decreased micro-hardness [53,54].

**2.3.3. Fiber-Matrix Bond Properties.** The fiber-matrix bond properties are related to the quality of the matrix, fiber, and fiber-matrix interface. Factors influencing such properties include matrix strength, fiber type, fiber geometry, fiber orientation, fiber surface modification. Matrix strength is the main factor affecting bond properties. The bond can be enhanced by the use of SCMs and high-temperature curing. Generally, the higher the matrix strength is, the better the bond properties would be. Abu-Lebdeh et al. [55] studied the fiber-matrix bond properties of eight very-high strength concrete (VHSC) mixture and two normal strength concrete mixtures using single fiber pullout

testing. It was observed that the bond strength of VHSC was increased by 92%-106%, while the total pullout energy was enhanced by 95%-187%, in comparison to the conventional concrete [55].

The influence of fiber type on bond properties mainly depends on the friction with matrix, mechanical anchorage, and chemical compatibility with matrix and/or mechanical parameters. Chan et al. [56] investigated the effect of steel, brass, and polyethylene fibers on bond properties of three matrices with w/c of 0.4, 0.27, and 0.27. The adhesion between the brass fiber and the matrix was found to be greater than that between the steel fiber and the matrix.

Geometric characteristics of fiber, including fiber shape, fiber length, surface area, aspect ratio, and roughness, also exert effect on bond properties. Generally, a good bond exists between deformed fiber and matrix because of mechanical anchorage associated with the deformed section [57]. This can significantly increase friction and adhesion between the fiber and the matrix. The bond strength of corrugated fiber in ordinary concrete was two to three times greater than that with straight fibers, and the pullout energy was five to six times higher [58]. In UHPC, the equivalent bond strengths of hooked and twisted fibers were about four to five times higher than that of straight fiber [59]. Park et al. [60] investigated the influence of incorporating 0%, 0.5%, 1%, and 1.5% micro-fibers ( $d_f = 0.2$  mm,  $l_f = 13$  mm) on bond properties of UHPC embedded with four types of macro-fibers ( $d_f \geq 0.3$  mm,  $l_f \geq 30$  mm). UHPC embedded with twist fibers demonstrated the highest equivalent bond strength of 24-34 MPa, while those with straight or hooked fibers was 5-12 MPa.

## 2.4. MECHANICAL PROPERTIES OF UHPC

Mechanical properties of UHPC, including compressive, tensile, and flexural strengths, as well as impact properties, are discussed in the following section. The effect of matrix strength, fiber type and content, curing regime and age, specimen size, fiber distribution, and loading rate, on mechanical properties are discussed.

**2.4.1. Compressive Strength Behavior.** The compressive strength of UHPC is governed by the fiber type, fiber content, fiber shape, curing regime, and curing age. The development of compressive properties of UHPC is closely correlated to the degree of hydration of cementitious materials. Habel et al. [61] reported that the 7-d compressive strength of UHPC designed with 0.16 w/b and 11% steel fibers that subjected to heat curing reached 140 MPa. Such value was 81% of the final strength of 175 MPa. Filho et al. [62] studied the compressive strength of UHPC made with a w/b of 0.17 containing a fiber content of 2%. UHPC is subjected to moist curing and its compressive strengths at curing age of 3, 7, 28, and 180 d were evaluated. The 3-d compressive strength and of elastic modulus were 74 MPa and 36 GPa, respectively, and increased to 161 MPa and 48 GPa at 28 d, respectively.

Zhang [63] investigated the effect of fiber content and curing regime on the compressive strength of “green reactive powder concrete” (GRPC). The results demonstrated that the compressive strength of GRPC improved with the increase of steel fiber content. The compressive strength of the mixture with 4% fibers, by volume, was 30-50 MPa greater than that of the matrix without any fiber. In addition, GRPC under 28-d of standard curing regime had the lowest strength (150 MPa), followed by that under 24-h steam curing (165-180 MPa), and then that under 8-h autoclave curing (over 200

MPa). Yang et al. [64,65] studied the effect of different curing temperatures on compressive strength of UHPC made with w/b of 0.15 and 2% steel fibers. It was observed that the compressive strength under 20 °C curing was 20% lower than that under 90 °C curing.

The fiber type is an important factor affecting compressive strength of UHPC. The mineral and/or synthetic fibers can have limited influence on compressive strength and elastic modulus of concrete [66]. However, steel fibers can improve compressive strength because of the intrinsic rigidity of the steel fibers. Generally, with the increase of steel fiber content up to 4%, the compressive strength of GRPC increased by 30 - 50 MPa compared to that without any fiber [63]. Hassan et al. [67] reported that the use of steel fibers had a relatively small effect on the pre-cracking of UHPC in compressive, but a significant influence on the post-cracking behavior. The reference UHPC specimens made without any fiber behaved elastically until the peak load and then showed a strain softening behavior. However, strain hardening behavior was observed for UHPC specimens. The use of hooked-end fibers in UHPC can result in the greatest compressive strength, followed by corrugated fibers, and then straight fibers [40]. Compared to the reference mixture made without any fiber, the incorporation of 2% hooked-end, corrugated, and straight fibers increased the compressive strengths by 49%, 44%, and 40%, respectively. When hybrid fibers (long and short fibers) were incorporated, the uniaxial compressive strength was shown to increase first and then decrease with the increase of the short fiber volume. At a total hybrid fibers volume of 2%, UHPC samples with 1.5% long fibers and 0.5% short fibers at a w/b of 0.18 obtained the greatest compressive strength, whereas those with 2% short fibers showed the lowest value [22].

**2.4.2. Tensile Strength Behavior.** Three types of testing methods, including direct tension, splitting tension, and flexural tests, can be used to determine tensile properties of concrete material using dog-bone shaped, cylinder, and prismatic specimens, respectively. Habel et al. [61] studied the tensile properties of UHPC and observed that the tensile strength after 7 d was 6 MPa, which was 60% of the final stable strength. Charron [68] studied the tensile behavior of notched-prism UHPC specimens using direct tensile test and found the maximal tensile strength at 28 d was 11 MPa. Kang et al. [69] studied the tensile fracture properties of UHPC with fiber volumes ranging from 0% to 5% and indicated that the tensile strength of UHPC linearly increased with the increase of fiber volume. Wille et al. [70] developed UHPC strain hardening behavior with 28 - d compressive strength of 200 MPa using 2.5% short and smooth steel fibers. The UHPC possessed a post-cracking strength of 14.2 MPa in tension and had a strain capacity of 0.24%. However, the authors reported that it is difficult to obtain strain capacity more than 0.5% and tensile post-cracking strength over 15 MPa using mono-fiber.

Park et al [71] investigated the effect of a combination of macro-fiber and micro-fiber on the tensile behavior of UHPC. The micro-fiber volume varied from 0 to 1.5%, while the macro-fiber volume was fixed at 1.0%. The type of macro-fiber played a significant role in determining the overall shape of tensile stress-strain curves. UHPC made with twisted macro-fibers showed the best tensile behavior, while those with long smooth macro-fibers exhibited the worst behavior.

**2.4.3. Flexural Strength Behavior.** The flexural properties are highly affected by the fiber type, fiber content, fiber blending, size effect, fiber distribution and orientation, loading rate, and placing methods. Huang et al. [72] showed that the use of 2% polyethylene fibers increased the flexural strength by 47% compared to the reference specimen. Birol et al. [73] proposed that the characteristic of the flexural load-deflection curve of UHPC was mainly affected by fiber type and fiber volume. Wu et al. [40] investigated the effect of different fiber volumes (0, 1%, 2%, and 3%) and shapes (straight, corrugated, and hooked-end) of steel fibers on flexural properties of UHPC. The results indicated that the incorporation of 2% straight, hooked-end, and corrugated fibers increased the 28-d flexural strength of UHPC subjected to standard curing by 46%, 81%, and 61%, respectively, compared to the specimens without any fiber.

Fiber blending can improve the flexural performance of UHPC due to combined functions from each type of fiber. For example, for UHPC made with short and long fibers, after the first-cracking of the matrix, the initiated micro-cracks were initially restrained by the short fibers. As the micro-cracks propagate further, the short fibers are pulled out from the matrix. The loads are mainly sustained by the long fibers. This means that more time and energy are needed to fracture the material compared to UHPC made with mono-fiber. Fiber blending in normal strength matrices produced favorable blending effect on the mechanical performance in comparison with FRC with mono-fiber [74,75]. Kim et al. [76] found that the flexural performance of UHPC made with hooked fiber was the greatest, followed by that made with twisted fibers, and then that with long smooth fibers. Hai et al. [77] showed that steel and polyvinyl alcohol fibers efficiently improved the flexural and compression ratio by 40%.

The method of casting of UHPC can affect fiber distribution and hence mechanical performance [78,79]. Kang et al. [80] investigated the effect of placing direction on the flexural strength of UHPC and found that UHPC placed parallel to the longitudinal direction of prismatic samples exhibited approximately 6% greater initial cracking strength and 60% greater ultimate flexural strength than UHPC placed transversely. Barnett [79] evaluated the flexural strength of UHPC by placing round panels in three different casting methods and found the panels cast from the center showed the highest flexural strength.

The specimen size also has a significant effect on flexural properties of UHPC because of the size effect, where larger specimens can have greater probabilities of weak zones. Nguyen et al [81] investigated the flexural behavior of three prismatic UHPC specimen sizes measuring  $50 \times 50 \times 150$ ,  $100 \times 100 \times 300$ , and  $150 \times 150 \times 450$  mm. Results showed that the equivalent flexural strength of UHPC decreased with the increase of specimen size.

**2.4.4. Impact Properties.** Given its high resistance to impact loads, UHPC can be used in structures requiring high resistance to explosion and penetration, such as protective shelter of military engineering application [82]. Two common methods to measure the dynamic behavior of concrete are drop weight and split Hopkinson pressure bar (SHPB) tests. The drop weight test has the ability to reproduce conditions under which real-life component would be subject to impact loading [83]. Habel et al. [84] studied the impact tensile performance of UHPC using the drop weight tests and found the strength increased with the increase of strain rate, showing strain hardening characteristics up to approximately  $d\varepsilon/dt = 2 \text{ s}^{-1}$ .



Because impact performance obtained through drop weight testing is greatly influenced by the configuration, such as drop weight and speed, specimen size, and support stiffness, some researchers used the SHPB testing instead. Rong et al. [85] stated that the dynamic compressive strength of UHPC was sensitive to the strain rate and increased with the increase of fiber volume. The non-fibrous UHPC matrix was found crushed, while the UHPC with 3% or 4% of steel fibers remained intact under the same loading rate. Zhang et al. [63] found the dynamic tensile strength of UHPC increased obviously with the increase of impact velocity, ranging from 4 to 14 m/s. The dynamic tensile strength of GRPC with 4% steel fibers reached 15 MPa, which was 50% greater than the static tensile strength.

Fiber hybridization can also improve the dynamic mechanical properties. For example, high modulus fiber plays a significant role in enhancing the tensile strength, while low modulus fibers contribute a lot in ductility [86]. Long steel fibers play a dominated role in improving the impact resistance capacity of UHPC [87]. At a total fiber volume of 2%, UHPC reinforced with 1.5% long fibers (13 mm) and 0.5% short fibers (6 mm) demonstrated the best static and dynamic compressive behaviors, which were 19% and 14%-24%, respectively, greater than those with 2% short fibers [88]. However, comparable dynamic compressive properties were observed between UHPC samples with 2% long fibers and those with 2% short fibers due to very fast loading rate and synergistic effect associated with fiber geometry, spacing, and quantity.

## 2.5. FIBER STRENGTHENING AND REINFORCING MECHANISMS

Two types of fiber strengthening and reinforcing theories can be used to investigate the mechanical properties of a given composite material, including the composite theory and the fiber space theory.

**2.5.1. Theory of Composite.** UHPC is a typical composite material, which consists of a matrix, fibers, and interface between the two. Based on this, the mechanical properties can be investigated using the theory of the composite material. This theory can be used to calculate tensile stress, elastic modulus of FRC. Figure 2.4 illustrates fiber-reinforced concrete under tensile stress. The properties of the composite material are the combined effect exerted from each component. The hypotheses for the composite theory are stated as follows:

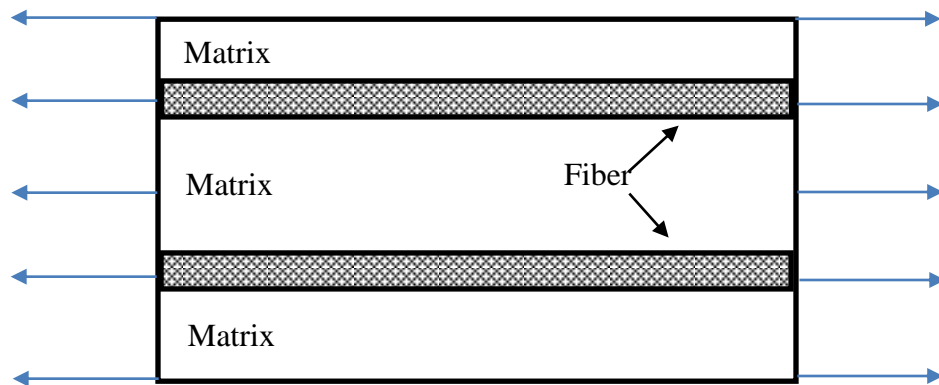


Figure 2.4. Fiber-reinforced concrete under tensile stress

(1) Fibers are continuously and homogeneously dispersed in the matrix. It is assumed that their orientation is parallel to the loading direction.

(2) Good bond exists between the fiber and matrix, suggesting the same strain between them with no slip.

(3) Both the fiber and matrix present elastic deformation and have the same lateral deformation.

According to the basic hypotheses, when external loads are applied to the fibers, the maximum tensile stress and the elastic modulus can be calculated according to Equations (2.1) and (2.2), respectively:

$$f_c = f_f V_f + f_m V_m = f_f V_f + f_m (1 - V_f) \quad (2.1)$$

$$E_c = E_f V_f + E_m V_m = E_f V_f + E_m (1 - V_f) \quad (2.2)$$

where  $f_c$  (MPa) and  $E_c$  (MPa) are the maximum tensile stress and elastic modulus of FRC (composite material), respectively;  $f_m$  (MPa),  $E_m$  (MPa), and  $V_m$  (unit-less) are the tensile stress, elastic modulus, and volume of the matrix, respectively;  $f_f$  (MPa),  $E_f$  (MPa), and  $V_f$  (unit-less) are the stress, elastic modulus, and volume of the fiber, respectively.

Equation (2.2) indicates that the deformation of the fiber equals to that of the matrix in the elastic range. Hence, when the orientation of the fiber is similar to the loading direction, the tensile stress (or the elastic modulus) of the concrete is equal to the sum of the matrix stress and fiber stress (or the elastic modulus of the matrix and steel fiber) multiplying their volume.

However, these hypotheses are ideal because fibers are randomly and disorderly oriented in composite material, such as fiber-reinforced material. Therefore, the concrete heterogeneity, the length and orientation of short fibers can affect the mechanical properties of FRC. The bond properties between the fiber and matrix need to be taken into account. Therefore, an improved model was proposed by Naaman [89], in which the

tensile stress of the composite material is assumed to be the superimposed stresses of the fiber and the matrix. The post-cracking tensile strength could be calculated using Equation (2.3):

$$f_c = f_m(1 - V_f) + \eta\tau V_f \frac{l}{d} \quad (2.3)$$

where  $f_c$  (MPa) is the average stress of the composite material;  $f_m$  (MPa) is the stress of the matrix;  $V_f$  (unit-less) is the fiber volume;  $l/d$  (unit-less) is the aspect ratio;  $\tau$  is the average interface shear stress (MPa), which can be determined by fiber pullout testing;  $\eta$  (unit-less) is the reduction factor,  $\eta = \eta_1\eta_2\eta_3$ ;  $\eta_1$ ,  $\eta_2$ , and  $\eta_3$  are the direction coefficient, the effective coefficient in the loading direction, and the reduction factor of the fiber, respectively. The stress after cracking of matrix is mainly sustained by the fiber, therefore, the stress could be as follows:

$$f_c = \eta\tau V_f \frac{l}{d} \quad (2.4)$$

**2.5.2. Fiber Space Theory.** The fiber space theory was proposed by Romualdi et al. [90,91], which is based on the linear elastic fracture mechanics. This theory can explain how the fiber restrains crack initiation and propagation. The theory assumes that the failure of concrete results from interior defects, such as micro-cracks and pores, which can produce crack tip stress concentration under external forces. With the increase of stress, the crack can extend further into large cracks, thus resulting in the destruction of concrete members. Romualdi assumed that continuous fibers are evenly distributed along the loading direction with a chessboard-shaped in the matrix [90,91]. The model shown in Figure 2.5 can be used to illustrate the increased strength and main cause for crack propagation in FRC. As shown in Figure 2.5(a), a crack with a radius of  $a$  is

surrounded by four fibers with a fiber spacing of  $S$ . Under tensile loads, regions of the cracks around the fiber can produce cohesive force distribution ( $\tau$ ), as shown in Figure 2.5(b). The cohesive force on the crack tip can yield reverse stress field, which can reduce the degree of stress and eventually constraint the development of cracks.

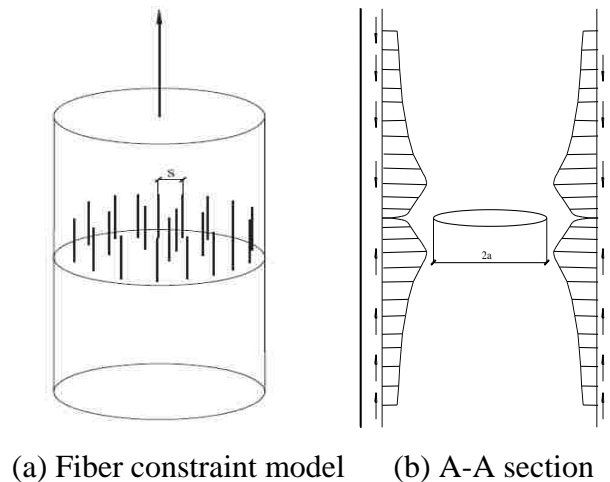


Figure 2.5. Crack restraining mechanism of fiber reinforcement in fiber-reinforced concrete (modified based on [90])

The fiber space can be determined based on the fiber geometry and volume used in the fiber-reinforced concrete. The tensile strength can be calculated according to an relative equation related to fiber space. Generally, the greater the fiber space is, the lower the tensile strength would be.

Although this theory is simple without the need of material properties, it is difficult to obtain the fiber spacing of composite material. Fiber spacing is a combined effect of multiple factors, including fiber shape, length, volume, orientation, mixing and vibrating processes, and dispersing technology. Therefore, the actual tensile strength can vary with the change of the factors.

## 2.6. CONCLUDING REMARKS AND RESEARCH NEED

Based on the results published in the literature, the following conclusions can be drawn:

**2.6.1. Concluding Remarks.** (1) Fiber-matrix bond properties play a dominated role in enhancing tensile/flexural strength and toughness of UHPC. The main factors affecting this behavior involve the matrix strength, use of SCMs, curing regime, fiber geometry, fiber distribution, and specimen size. The densification of the matrix is the most fundamental and practical approach to enhance the fiber-matrix bond properties. However, its efficiency to enhance fiber-matrix bond and mechanical properties of UHPC is lower than those improved with the use of deformed fibers.

(2) The compressive strength of UHPC is dependent on the curing regime and time, fiber content, fiber type and geometry, and mixture composition. UHPC with 3% or 4% steel fibers after 28 d standard room curing can develop a compressive strength over 150 MPa. UHPC subjected to 24-h steam curing and 8-h autoclave curing can obtain compressive strength of 165-180 MPa and over 200 MPa, respectively.

(3) The incorporation of mineral and synthetic fibers has limited influence on compressive strength of UHPC, whereas steel fibers can increase the compressive strength because of their intrinsic rigidity. The addition of micro-fibers can favorably affect the strain hardening and lead to multiple cracking behavior. The use of various sizes and types of fibers can enhance strength and strain capacity due to combined functions exerted from each type of fiber. The use of deformed fibers can significantly increase the flexural and tensile strengths of UHPC. However, the large amount of fibers prone to cause fiber agglomeration issues, and thus reversely affecting the mechanical

properties. Therefore, designing UHPC with appropriate steel fiber content and adequate rheology is essential to effective fiber orientation and improved mechanical properties.

(4) The dynamic response of UHPC are found to be sensitive to the applied strain rate. The incorporation of steel fibers can improve the dynamic properties. The UHPC matrix made without any steel fiber is found shattered after dynamic loading. On the other hand, UHPC made with steel fibers remains essentially intact under the same dynamic compressive loading. UHPC with hybrid steel fibers shows better impact performance than those with mono-fiber. At a total fiber volume of 2%, UHPC with 1.5% long fibers and 0.5% short fibers exhibits the best mechanical properties.

(5) The theory of composite and fiber space theory can be employed to understand fiber strengthening and reinforcing mechanisms. The former considers the mechanical properties of the composite material consist the addition of actions from each of its components: matrix, fiber, and fiber-matrix interface. The orientation of fiber distribution needs to be considered in UHPC composite because steel fibers are not ideally oriented to the loading direction. The fiber space theory assumes that the tensile strength of FRC is related mainly to fiber spacing. Fiber spacing is a combined effect of multiple factors, such as flowability, fiber length, volume, orientation, which changes with these factors and is difficult to determine in a real concrete.

**2.6.2. Research Need.** The literature review on the microstructure, fiber-bond properties, mechanical properties, and fiber strengthening and toughening mechanisms demonstrate perceived lack information and research need in the following topics:

(1) Different types and contents of SCM and nano-particles can remarkably affect the hardening process of cement-based materials. A perceived lack of information exists

about the effect of SCMs and nano-particles on strength development of UHPC matrix and fiber-matrix bond properties.

(2) The existence of ITZ is unavoidable, and the intrinsic nature of a composite material associated with different mixture compositions varies accordingly. There is a need to optimize the fiber-matrix bond and microstructure of UHPC that are closely related to macro-properties, such as flexural and tensile strengths and toughness.

(3) Among the existing research on mechanical properties of UHPC, factors such as fiber type, fiber volume, fiber shape, fiber orientation, fiber blending, and curing regime, have been systematically evaluated. However, most of the research involves quantitative comparison of various factors. There is a need to clarify the role of the fiber-matrix bond properties on mechanical properties of UHPC.

(4) Fiber strengthening and reinforcing mechanisms are well-documented for conventional concrete. Whether those theories could be applied to UHPC or need to be updated with taking the consideration of new parameters, such as fiber geometry coefficient, remains unknown.

Therefore, it is necessary to examine the mechanical properties of UHPC by taking into consideration of the microstructure of the UHPC matrix, fiber-matrix interface, and fiber-matrix bond characteristics. Of great interest is the degree of enhancement of tensile/flexural strength and toughness of UHPC through optimization from the nano- and micro-scales.



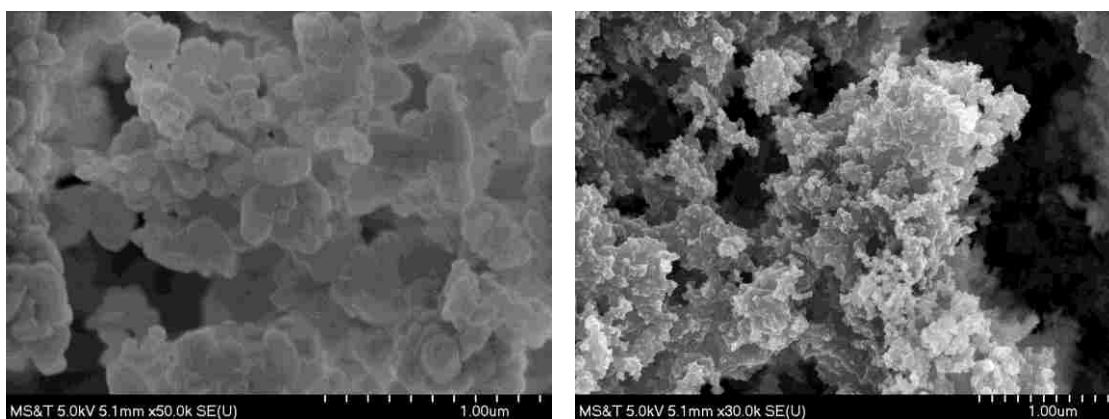
### 3. RAW MATERIALS, MIXTURE DESIGN, AND TESTING METHODS

#### 3.1. CHARACTERISTICS OF RAW MATERIALS

Characteristic of raw materials, such as cementitious materials, aggregate, steel fiber, and superplasticizer, are shown in the following part.

**3.1.1. Cementitious Materials.** Portland cement P.I. 425 (similar to ASTM C150 Type I cement) and Type III cement (Section 5) with surface areas of 336 and 465  $\text{m}^2/\text{kg}$ , respectively, were used. The P.I. 425 has 3-d and 28-d compressive strengths are 26 and 57.2 MPa, respectively.

Silica fume (SF) with a particle size in the range of 0.02-0.28  $\mu\text{m}$  was used. Its BET specific surface area was 18,500  $\text{m}^2/\text{kg}$ . Slag with density and specific surface area of 2,900  $\text{kg}/\text{m}^3$  and 410  $\text{m}^2/\text{kg}$ , respectively, was used. Fly ash (FA) with a specific surface area of 360  $\text{m}^2/\text{kg}$  was used. Nano- $\text{CaCO}_3$  (NC) and nano- $\text{SiO}_2$  (NS) were used, as shown in Figure 3.1. The nano- $\text{CaCO}_3$  has a size of about 15 to 105 nm with 97.8% calcite content. The nano- $\text{SiO}_2$  has a size of 5 to 35 nm with 99.8%  $\text{SiO}_2$  content.



(a) NC particles

(b) NS particles

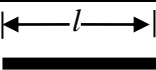
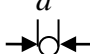
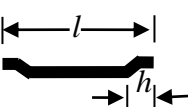

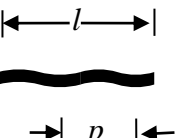
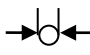
Figure 3.1. Morphology of nano-particles

**3.1.2. Sand.** Natural river sand with a fineness modulus of 3.0 was used.

Particles with size greater than 2.36 mm were removed by sieving.

**3.1.3. Steel Fiber.** As shown in Table 3.1, three types of brass-coated steel fibers, including straight, hooked, and corrugated fibers with diameters of 0.2 mm and lengths of 13 mm, were selected for investigation. The tensile strength is approximately 2,800 MPa.

Table 3.1. Geometries of three selected fibers

| Shape      | Geometry   | Section   | Details   |
|------------|--|---|---|
| Straight   |   |    | $l = 13 \text{ mm}, d = 0.2 \text{ mm}$                     |
| Hooked     |   |    | $l = 13 \text{ mm}, d = 0.2 \text{ mm}, h = 0.2 \text{ mm}$ |
| Corrugated |  |  | $l = 13 \text{ mm}, d = 0.2 \text{ mm}, p = 6 \text{ mm}$   |

**3.1.4. Superplasticizer.** A polycarboxylate-based superplasticizer (SP) with a solid content of 20% and water-reducing efficiency greater than 30% was used. To investigate the effect of different binder contents, such as silica fume, nano- $\text{CaCO}_3$ , and nano- $\text{SiO}_2$  contents, on heat of hydration and flowability of UHPC matrix (without fiber), the SP content was fixed at 2%. The steel fiber can decrease the flowability of UHPC mixture and hence reducing the tensile and flexural properties of UHPC through altering the distribution of fiber. For UHPC made with steel fiber, the SP was adjusted in order to achieve appropriate workability without any vibration consolidation. The mini-slump flow of UHPC mixtures was adjusted in the range of 240 to 280 mm.

### 3.2. MIXTURE PROPORTIONING

The mixture proportion in this research includes two phases. Initially, in order to investigate the effect of binder content on flowability, microstructure, and fiber-matrix pullout behavior, non-fibrous UHPC matrix (without fiber) was used.

**3.2.1. UHPC Matrix without Steel Fiber.** These mixtures include four series, such as silica fume, slag and fly ash, nano-CaCO<sub>3</sub>, and nano-SiO<sub>2</sub> series. The water-to-cementitious materials ratio (W/CM) was determined at 0.18.

**3.2.1.1. Silica fume series.** The mixture proportioning is shown in Table 3.2. In the silica fume series, 0, 5%, 10%, 15%, 20%, and 25% of silica fume by the mass of binder were used. They were designated as U0, U5, U10, U15, U20, and U25, respectively.

Table 3.2. Mixture proportioning of UHPC matrix with different silica fume contents

| Code | W/CM | Mass of ingredient (kg/m <sup>3</sup> ) |      |        |     |      |
|------|------|---|------|--------|-----|------|
|      |      | Water                                   | Sand | Cement | SF  | SP   |
| U0   | 0.18 | 177                                     | 1079 | 1079   | 0   | 21.6 |
| U5   | 0.18 | 177                                     | 1079 | 1025   | 54  | 21.6 |
| U10  | 0.18 | 177                                     | 1079 | 971    | 108 | 21.6 |
| U15  | 0.18 | 177                                     | 1079 | 917    | 162 | 21.6 |
| U20  | 0.18 | 177                                     | 1079 | 863    | 216 | 21.6 |
| U25  | 0.18 | 177                                     | 1079 | 809    | 270 | 21.6 |

**3.2.1.2. Nano-CaCO<sub>3</sub> series.** In the nano-CaCO<sub>3</sub> series, mixtures containing 0, 1.6%, 3.2%, 4.8%, and 6.4% nano-CaCO<sub>3</sub>, by the mass of cementitious material, were

used. They were designated as NC0 (U20), NC1.6, NC3.2, NC4.8, and NC6.4. Table 3.3 summarizes the mixture proportioning.

Table 3.3. Mixture proportioning of UHPC matrix with different nano-CaCO<sub>3</sub> and nano-SiO<sub>2</sub> contents

| Code  | W/CM | Mass of ingredient (kg/m <sup>3</sup> ) |      |        |     |      |      |
|-------|------|---|------|--------|-----|------|------|
|       |      | Water                                   | Sand | Cement | SF  | NC   | SP   |
| NC0   | 0.18 | 177                                     | 1079 | 863    | 216 | 0    | 21.6 |
| NC1.6 | 0.18 | 177                                     | 1079 | 846    | 216 | 17.3 | 21.6 |
| NC3.2 | 0.18 | 177                                     | 1079 | 829    | 216 | 34.5 | 21.6 |
| NC4.8 | 0.18 | 177                                     | 1079 | 811    | 216 | 51.8 | 21.6 |
| NC6.4 | 0.18 | 177                                     | 1079 | 794    | 216 | 69.1 | 21.6 |
| NS0.5 | 0.18 | 177                                     | 1079 | 858    | 216 | 5.4  | 21.6 |
| NS1.0 | 0.18 | 177                                     | 1079 | 852    | 216 | 10.8 | 21.6 |
| NS1.5 | 0.18 | 177                                     | 1079 | 847    | 216 | 16.2 | 21.6 |
| NS2.0 | 0.18 | 177                                     | 1079 | 842    | 216 | 21.6 | 21.6 |

**3.2.1.3. Nano-SiO<sub>2</sub> series.** In the nano-SiO<sub>2</sub> series, mixtures containing 0, 0.5%, 1.0%, 1.5%, and 2.0% nano-SiO<sub>2</sub>, by mass of cementitious material, were used. They were designated as NS0 (U20), NS0.5, NS1.0, NS1.5, and NS2.0.

**3.2.2. UHPC Reinforced with Steel Fiber.** Steel fibers with a volume of 2% were incorporated. The dosage of SP in the UHPC mixture made with 2% steel fibers was adjusted to obtain a mini-slump spread of 240-260 mm without any consolidation procedure.

**3.2.2.1. Silica fume series.** UHPC mixtures containing 0, 5%, 10%, 15%, 20%, and 25% silica fume, by mass of cementitious material, and 2% steel fibers were

prepared. They were designated as U0-2, U5-2, U10-2, U15-2, and U20-2. Table 3.4 summarizes the mixture proportioning.

Table 3.4. Mixture proportioning of UHPC with different silica fume contents

| Code  | W/CM | Mass of ingredient (kg/m <sup>3</sup> ) |      |        |     |             |
|-------|------|---|------|--------|-----|-------------|
|       |      | Water                                   | Sand | Cement | SF  | Steel fiber |
| U0-2  | 0.18 | 177                                     | 923  | 1079   | 0   | 156         |
| U5-2  | 0.18 | 177                                     | 923  | 1025   | 54  | 156         |
| U10-2 | 0.18 | 177                                     | 923  | 971    | 108 | 156         |
| U15-2 | 0.18 | 177                                     | 923  | 917    | 162 | 156         |
| U20-2 | 0.18 | 177                                     | 923  | 863    | 216 | 156         |
| U25-2 | 0.18 | 177                                     | 923  | 809    | 270 | 156         |

**3.2.2.2. Nano-CaCO<sub>3</sub> series.** The mixture proportioning of the UHPC made with different NC contents is summarized in Table 3.5.

Table 3.5. Mixture proportioning of UHPC with different NC and NS contents

| Item      | Code    | W/CM | Mass of ingredient (kg/m <sup>3</sup> ) |      |        |     |      |      |       |
|-----------|---------|------|---|------|--------|-----|------|------|-------|
|           |         |      | Water                                   | Sand | Cement | SF  | NC   | NS   | Fiber |
| Ref.      | NC0-2   | 0.18 | 177                                     | 923  | 863    | 216 | 0    | 0    | 156   |
| NC series | NC1.6-2 | 0.18 | 177                                     | 923  | 846    | 216 | 17.3 | 0    | 156   |
|           | NC3.2-2 | 0.18 | 177                                     | 923  | 829    | 216 | 34.5 | 0    | 156   |
|           | NC4.8-2 | 0.18 | 177                                     | 923  | 811    | 216 | 51.8 | 0    | 156   |
|           | NC6.4-2 | 0.18 | 177                                     | 923  | 794    | 216 | 69.1 | 0    | 156   |
| NS series | NS0.5-2 | 0.18 | 177                                     | 923  | 858    | 216 | 0    | 5.4  | 156   |
|           | NS1.0-2 | 0.18 | 177                                     | 923  | 852    | 216 | 0    | 10.8 | 156   |
|           | NS1.5-2 | 0.18 | 177                                     | 923  | 847    | 216 | 0    | 16.2 | 156   |
|           | NS2.0-2 | 0.18 | 177                                     | 923  | 842    | 216 | 0    | 21.6 | 156   |

**3.2.2.3. Nano-SiO<sub>2</sub> series.** The mixture proportioning of the UHPC made with different NS contents is also summarized in Table 3.5.

**3.2.2.4. UHPC with optimized composition.** Mixtures proportioned with slag, fly ash, or nano-particles with good mechanical properties and fiber-matrix bond are used to investigate the static and impact mechanical properties of UHPC (Table 3.6).

Table 3.6. Mixture proportioning of UHPC with optimized composition of different SCMs and/or nano-particles

| Code    | Water<br>(kg/m <sup>3</sup> ) | Sand<br>(kg/m <sup>3</sup> ) | Cement<br>(kg/m <sup>3</sup> ) | SF<br>(kg/m <sup>3</sup> ) | SL<br>(kg/m <sup>3</sup> ) | FA<br>(kg/m <sup>3</sup> ) | NC<br>(kg/m <sup>3</sup> ) | NS<br>(kg/m <sup>3</sup> ) | Steel fiber<br>(kg/m <sup>3</sup> ) |
|---------|-------------------------------|------------------------------|--------------------------------|----------------------------|----------------------------|----------------------------|----------------------------|----------------------------|-------------------------------------|
| U20-2   | 177                           | 923                          | 863.2                          | 215.8                      | 0                          | 0                          | 0                          | 0                          | 156                                 |
| SL20-2  | 177                           | 923                          | 647.4                          | 215.8                      | 215.8                      | 0                          | 0                          | 0                          | 156                                 |
| FA20-2  | 177                           | 923                          | 647.4                          | 215.8                      | 0                          | 215.8                      | 0                          | 0                          | 156                                 |
| UT-2    | 177                           | 923                          | 431.6                          | 215.8                      | 215.8                      | 215.8                      | 0                          | 0                          | 156                                 |
| NC3.2-2 | 177                           | 923                          | 828.7                          | 215.8                      | 0                          | 0                          | 34.5                       | 0                          | 156                                 |
| NS1.0-2 | 177                           | 923                          | 852.4                          | 215.8                      | 0                          | 0                          | 0                          | 10.8                       | 156                                 |

### 3.3. UHPC MIXTURE PREPARATION AND CURING

The mixing procedure was as follows: (1) dry cementitious materials and sand were mixed at a low speed for 3 min; (2) mixing water and SP were premixed and added at a low speed for 6 min then 1 min at a high speed; (3) fibers were introduced slowly if needed at a low speed and mixed for another 6 min; and (4) the material was obtained with good flowability. All the mixtures were cast into molds for the testing of flowability and mechanical properties. Specimens were then kept in a room at 20 °C and relative humidity (RH) greater than 95% for approximately 24 h. They were then demolded and cured in lime-saturated water at 20 °C until specified ages (1, 3, 7, 28, and 91 d).

### 3.4. TESTING METHODS

Testing methods including flowability, fiber-pullout test, microstructure characterization, and mechanical properties test are presented in the following section.

**3.4.1. Flowability.** The fresh mortar was filled into a mini cone placed on an automatic jump table [92]. The mini cone has an upper diameter of 70 mm, a lower diameter of 100 mm, and a height of 60 mm. After the mini cone was vertically lifted, two diameters perpendicular to each other of spread of mixture were then determined and mean value was reported.

The SP dosage in non-fibrous UHPC matrix was fixed at 2% in order to investigate the effect of cementitious materials content on heat of hydration. In the presence of steel fibers, the mini-slump flow of UHPC was adjusted to 240-280 mm by changing the SP dosage without consolidation procedure.

**3.4.2. Calorimetry Analysis.** A TAM air isothermal calorimeter was used to measure the heat of hydration of the binder mixtures at a constant temperature of 20 °C. This instrument has eight sample chambers fitted inside one thermostat to make eight measurements simultaneously. Based on the mixture proportion and sample preparation procedure as described above, corresponding cement pastes were prepared. Approximately 4 g paste of each mixture was weighed and placed into a sealed glass ampoule. Then they were placed into the isothermal calorimeter for measuring heat of hydration for 60 h.

**3.4.3. Fiber Pullout Test.** Dog-bone shape specimens were used to measure the pullout behavior of four embedded steel fibers within mortars, as shown in Figure 3.2.

The specimen was divided into two halves, namely a pullout half and a fixed half using a plastic clip at the center with four fibers perpendicularly installed to it. For the fiber holding and casting process, plastic clips with specified dimensions corresponding to the molds were manually cut first. The plastic clips were punched to get four holes with an evenly distributed space of 15 mm, as shown in Figure 3.2(a). Four fibers were prepared to go through the four holes. By using a self-made bamboo substrate with designed four vertical holes with a depth of 5 mm, the fibers length (5 mm in the pullout half) and orientation were ensured. After that, the fibers were fixed in the plastic clips by using super glue. Then the plastic clips were first put into two parallel slots located at the center of steel mold. In order to completely prevent adhesion of the two halves of the matrix, a plastic film was used to cover the whole casting zone in the mold through crossing the plastic clip. The matrix was then cast into the mold. According to the standard [93], the embedded length of fiber ( $l_{em}$ ) at the pullout section should meet the following requirements:

$$l_{em} \leq 0.4l_f \quad (3.1)$$

$$l_{em} > f_t d_{eq} / f_m \quad (3.2)$$

where  $l_{em}$  (mm) is the embedded fiber length at the pullout half;  $l_f$  (mm) is the total length of steel fiber;  $f_t$  (MPa) is the tensile strength of steel fiber;  $d_{eq}$  (mm) is the diameter of steel fiber; and  $f_m$  (MPa) is the compressive strength of UHPC matrix.

Through calculation, the fiber in length in the pullout section was set to 5 mm compared to 8 mm in the fixed section. An MTS testing machine with 20 kN load cell was used to carry out the pullout testing [93], as shown in Figure 3.2(b). The loading rate was 1 mm/min. Only the pullout strength and pullout energy of those samples with all



four fibers pulled out from the short embedment length section were used. For each matrix, five specimens were tested. The bond strength was calculated as follows:

$$\tau_{max} = \frac{P_{max}}{n\pi dl} \quad (3.3)$$

where  $\tau_{max}$  (MPa) is the bond strength of embedded fibers based on the maximum pullout load;  $P_{max}$  (N) is the maximum pullout load;  $d$  (mm) is the diameter of a single fiber;  $l$  (mm) is the embedment length of the fiber in pullout half (5 mm);  $n$  is the number of fibers embedded in a dog-bone specimen ( $n = 4$ ).

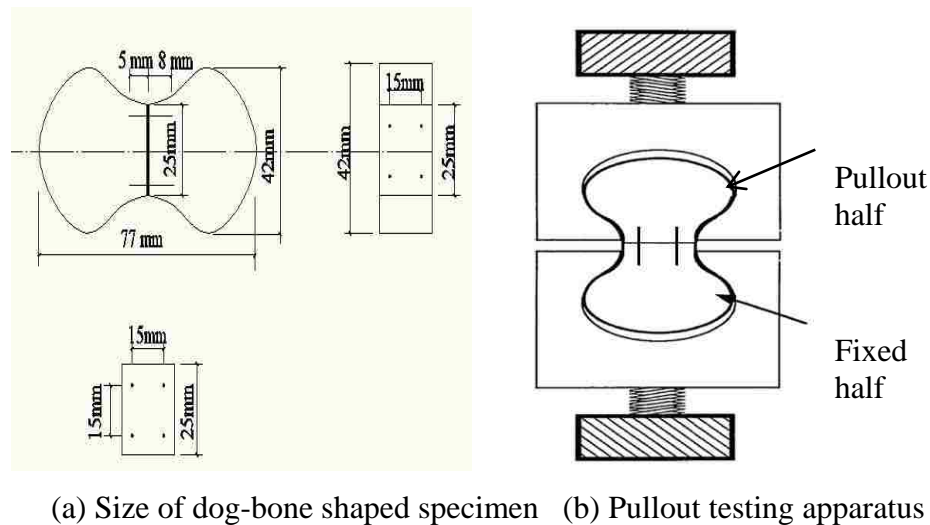


Figure 3.2. Illustration of dog-bone shaped specimen and pullout testing apparatus

**3.4.4. Compressive and Three-Point Flexural Strengths Tests.** Specimens measuring  $40 \times 40 \times 160$  mm were cast for the determination of compressive and flexural strengths. Three samples of each batch were tested. The bending and compressive strength tests of cement mortar were conducted [94]. The 3-point bending test was conducted using an MTS testing machine with a displacement rate of 1 mm/min at a span

of 100 mm. A 500 N preload was applied to allow accommodation of the loading apparatus. Deflections were measured using two linear variable differential transducer (LVDTs). The flexural test was continued until the mid-span deflection reached 10 mm. Then the six broken specimens were used to examine the compressive strength. The mean values of three flexural strengths and six compressive strengths were reported.

**3.4.5. Four-Point Flexural Properties Test.** The 28 d four-point flexural properties of UHPC mixtures were in accordance with ASTM C 1609 (Section 5). The used beam specimens were  $419 \times 76 \times 76$  mm in dimension and have a span of 305 mm. Three beams were tested for each mixture. The MTS load frame was used to apply loads at a controlled displacement rate of 1 mm/min. The deflection of the beam specimens and settlement of the two roller supports were recorded using LVDTs. The tests were continued until the mid-span deflection reached approximate 3 mm for UHPC mixtures.

The four-point flexural strength can be calculated using Equation (3.4).

$$F = PL/(bd^2) \quad (3.4)$$

where  $P$  (N) is the peak load;  $L$  (mm) is the span length;  $b$  (mm) is the beam width; and  $d$  (mm) is the beam depth.

**3.4.6. Tensile Properties Test.** Direct tensile tests were conducted using dog-bone specimens at a displacement rate of 0.5 mm/min, as shown in Figure 3.3. The specimens have a length of 526 mm and a thickness of 25 mm with a narrow neck of 175 mm in length. Two LVDTs were used to measure the deformation over a gage length of 160 mm, while the applied load was recorded by a load cell. Only those specimens with cracking occurred in the middle of gauges were used for the determination of final tensile strength.



Figure 3.3. Illustration of tensile test

**3.4.7. Drop-Weight Impact Flexural Properties Test.** A drop weight impact testing machine (Instron, CEAST9340) with a maximum load of 20 kN, as illustrated in Figure 3.4, was used to conduct the impact flexural properties.

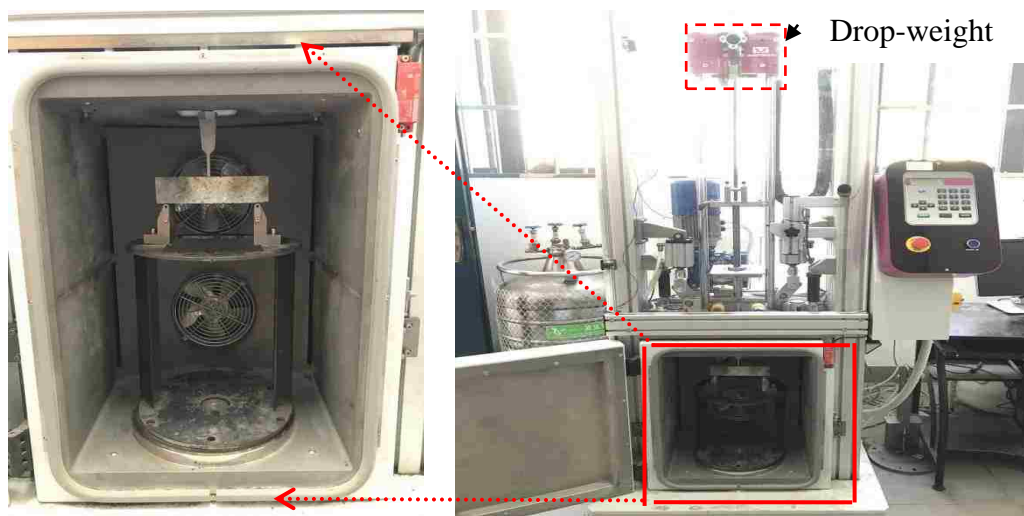


Figure 3.4. Illustration of drop-weight impact system

**3.4.8. Thermal Gravimetric Analysis.** Thermo-gravimetric (TG) and derivative thermo-gravimetric (DTG) analyses were used to quantitatively estimate the amount of  $\text{Ca(OH)}_2$  using a Netzsch STA 409PC equipment. Samples from the surface layer of UHPC specimens were firstly broken into 2.5-5.0 mm pieces by a hammer. Then the samples were put into a vacuum drying chamber to get a constant mass. After that, these dried samples were ground to powder and sieved on a square mesh sieve with diameter of 45  $\mu\text{m}$ . The tested samples, weighing up to 10 mg, were heated from 0 to 1200  $^{\circ}\text{C}$  under nitrogen gas flow at a constant heating rate of 10  $^{\circ}\text{C}$  per minute. The hydration products of  $\text{Ca(OH)}_2$  decomposed at around 430-550  $^{\circ}\text{C}$ . The proportion of CH content to residual mass was then calculated.

**3.4.9. Pore Structure Observation.** Mercury intrusion porosimetry (MIP) was used to test the pore structure of hardened concrete specimens. The mercury porosimeter (Auto Pore Master-60) is capable of generating 0-68,000 psi pressure and measuring 3 nm-380  $\mu\text{m}$  pore diameter. Samples for MIP test were broken into 3.5-5.0mm pieces and soaked in acetone to stop the further hydration of cement. Then they were dried at 60  $^{\circ}\text{C}$  in oven for 24 h before examination. The experiments were carried out under pressures of 40 and 60000 psi. Full-scan auto mode was selected with contact angle and surface tension of 140 $^{\circ}$  and 106.7 psi· $\mu\text{m}$ , respectively.

**3.4.10. 3D Micro-Tomography.** The three-dimensional (3D) internal structure, especially spatial distribution of air voids, of the UHPC matrix with an embedded fiber was evaluated using 3D micro-tomography. This testing was performed at the Technological Institute in Functional Safety Testing, Itt Fuse, at the Unisinos University in Brazil. The test was performed using a tomography with 160 kV cannon power and a

maximum resolution of 0.5  $\mu\text{m}$  [95]. The images of the internal microstructure were captured, and the void content was calculated based on the detected materials and void volumes.

**3.4.11. Scanning Electron Microscopy (SEM) Observation.** Scanning electron microscopy (SEM) was employed to study the microstructure of UHPC. Small samples with an embedded fiber at an approximate size of  $15 \times 15 \times 15$  mm were taken by cutting the dog-bone shaped specimens for the BSEM examination. This was done shortly after the pullout test. The broken samples were soaked in acetone to stop further hydration and then dried at 60 °C in a vacuum oven for 24 h. They were ground to obtain a relatively smooth surface, then mounted in epoxy resin and subjected to further grinding and polishing to ensure smooth surface quality. Silicon carbide (SiC) papers with grit sizes of 200, 400, 600, 800, and 1200 were sequentially selected for initial polishing. An ultra-fine diamond slurry with a size of 0.05  $\mu\text{m}$  was introduced for the final polishing. Ultrasonic bath cleaning was used to remove all dust and diamond particles. The samples were kept in an air-tight container until the time of testing.

The polished samples were coated with carbon and were examined using a Hitachi S4700-SEM with a back-scattered detector in high vacuum mode. All images were taken at a resolution of  $2560 \times 1920$  under a voltage of 15 kV. Elemental mapping was used to study the spatial distribution of the various elements, such as Si, Ca, Fe, Mg, O, C, and Al at the fiber-matrix interface.

**3.4.12. X-Ray Diffraction (XRD) Analysis.** UHPC matrix samples were taken from the dog-bone specimens after pullout testing for X-ray diffraction (XRD) analysis.

The samples were soaked in acetone to stop cement hydration, then dried at 60 °C for 24 h and ground into powder. CuK $\alpha$  X-ray diffraction was used to characterize the crystalline phases of the sample. The experiments were carried out at  $2\theta$  value from 5° to 65° with a scan rate of 2°/min.

**3.4.13. Micro-Hardness Measurement.** Micro-indentation is based on applying a static load for a known period of time and measuring the response in terms of the indentation size. In this study, a 498 mN load was applied to the same samples for BSEM testing for 10 s. Measurement was performed within a distance of 240  $\mu\text{m}$  from the edge of embedded fiber. Four replicate indentations with a constant distance of approximately 40  $\mu\text{m}$  to the previous indentation were performed, as shown in Figure 3.5(a).

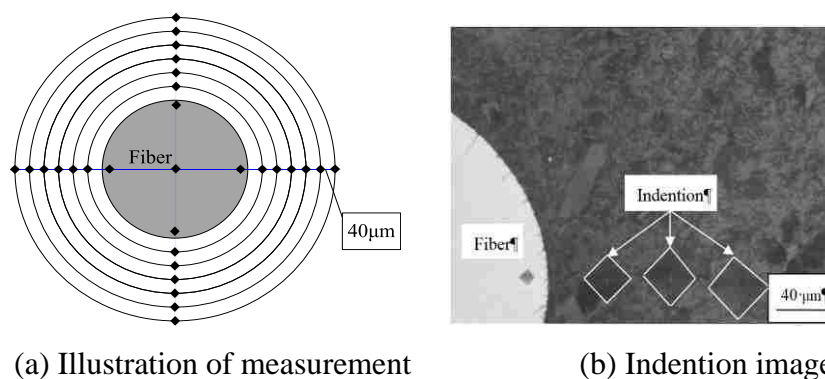


Figure 3.5. Micro-hardness testing for UHPC matrix with an embedded fiber

During the indentation process, areas with sand were avoided to ensure precise comparison of results from different matrices. A typical microscope image during testing is shown in Figure 3.5(b). Means of four values of micro-hardness or Vickers hardness (HV) situated along a given distance from fiber edge was determined and reported.

## 4. INFLUENCE OF SILICA FUME CONTENT ON STRENGTH AND DEVELOPMENT MICROSTRUCTURE OF UHPC MATRIX

### 4.1. BACKGROUND

The very low w/b and dense microstructure allow the compressive strength of UHPC matrix generally over 120 MPa and superior durability. However, the higher the compressive strength is, the more brittle the matrix becomes. Fiber has been proven as an essential part for UHPC [96,97]. With the incorporation of proper types of fibers, the initiation, propagation or coalescence of cracks can be efficiently controlled. Several types of fiber, such as carbon, steel, and polypropylene fibers have been used in UHPC. Steel fiber is the most commonly used one because of its superior tensile strength over 2000 MPa. The incorporation of such steel fiber ensures satisfactory mechanical properties, such as tensile, bending, and shear strengths of UHPC [59,98]. However, a bond failure associated with the fiber-matrix interface is the primary reason leading to the failure of the whole structure [99]. It was reported that there exist two different interfacial failure modes when steel fibers are pulled out from matrix [100]. One is adhesive failure often occurring at actual fiber-matrix interface, while the other one is adherent failure taking place in the matrix. Both failure modes would directly lead to underutilization of fiber or matrix without fully exerting their own mechanical capacity, and eventually result in cracking of composites. Therefore, improvement in the bond properties between fiber and matrix is of great significance.

The performance of fiber reinforced composites is governed by the quality of matrix, geometry, and type of fiber, and quality of interfacial transition zone (ITZ) between the fiber or aggregate and matrix [100,101]. Several strategies can be used to

improve the bond properties at the fiber-matrix interface, including: (1) densification of the cementitious matrix and ITZ [101]; (2) use of deformed fibers [40]; (3) surface treatment of fibers, such as plasma treatment for polyethylene fibers [100]. Because ITZ has a thickness varying between 10 and 100  $\mu\text{m}$ , and contains large preferentially calcium hydroxide (CH) crystals and high porosity [102,103], it is usually recognized as the weakest zone in concrete [104]. The basic strategy to improve the bond properties is densification of UHPC mixture and the ITZ as well. Many densification methods have been proposed, which include a reduction in w/b, prolongation of moist curing, heat curing, and incorporation of mineral admixtures [102,105]. Incorporation of silica fume is one of the most effective and economic methods because of its fine particle size and high pozzolanic activity [106]. These two characteristics of silica fume can lead to a remarkable reduction in porosity and permeability, as well as enhancement in strength and durability [106].

Extensive researches have been conducted on UHPC, but few of them are related to the microstructure development, the compressive and flexural strength, and the relationship between them. In this paper, the effect of silica fume content on heat of hydration, compressive and flexural strengths of non-fibrous UHPC matrix at a fixed SP dosage were investigated. Thermo-gravimetry (TG) analysis and mercury intrusion porosimetry (MIP) were used to characterize hydration products and pore structure of the matrix. Its goal is to provide important implications to improve the tensile and toughness properties of UHPC.



## 4.2. EFFECT OF SILICA FUME CONTENT ON HEAT OF HYDRATION OF UHPC MATRIX

Figure 4.1 shows the rate of heat evolution of non-fibrous UHPC matrix with and without silica fume.

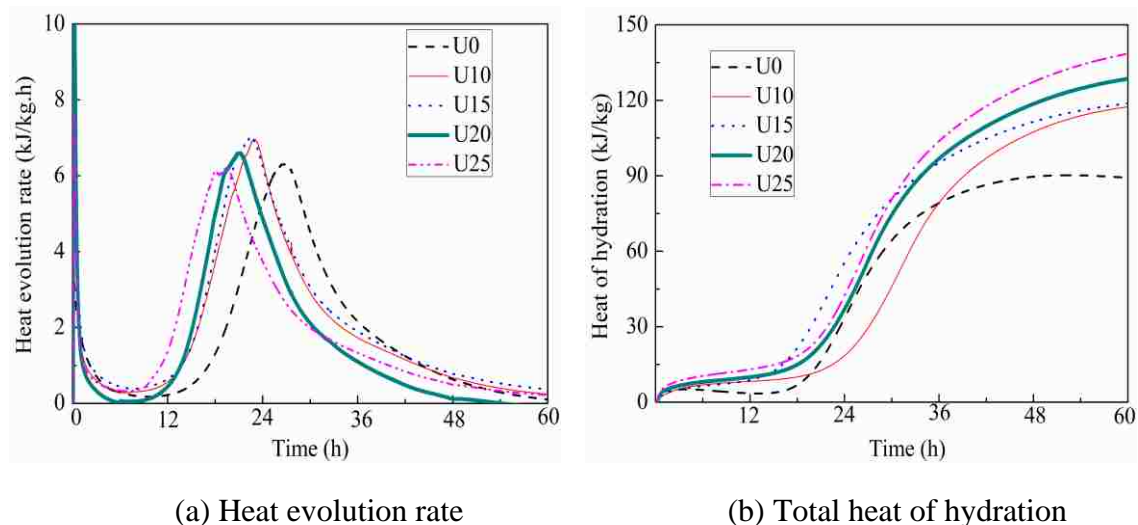


Figure 4.1. Heat evolution rate of UHPC matrix with different silica fume contents

As can be seen from Figure 4.1(a), compared to U0, the duration of the dormant period of UHPC matrix containing silica fume decreased from 12 to 9 h or less. As hydration proceeded, U25 samples first showed the accelerated hydration peak, followed by U20, U15, and U10. However, the accelerated hydration peak of U0 was delayed to 28 h. As illustrated in Figure 4.1(b), the heat of hydration of UHPC matrix incorporated with silica fume evolved quickly, and the heat generation was faster than that of the reference sample U0. This is because, on the first contact of cement with water,  $\text{Ca}^{2+}$  and  $\text{OH}^-$  ions are rapidly released from the surface of cement particles. When silica fume is

incorporated, the dissolution of  $\text{SiO}_4^{4-}$  ion can absorb  $\text{Ca}^{2+}$  and  $\text{OH}^-$  ions to form calcium silicate hydrate (C-S-H), which increases the rate of heat and amount of heat evolution [107].

#### **4.3. EFFECT OF SILICA FUME CONTENT ON COMPRESSIVE AND FLEXURAL STRENGTHS OF UHPC MATRIX**

The influence of silica fume content on compressive and flexural strengths of UHPC matrix are compared in Figure 4.2. The silica fume content had a significant effect on compressive and flexural strengths at early ages up to 7 d. After 7 d, the increase in compressive strength was only about 11%. For the flexural strength, it increased significantly from 1 to 3 d. However, it remained almost the same at 7 d. It should be noted that for U0, U20, and U25, the flexural strengths at 91 d slightly decreased when compared to that at 28 d. This may be due to the variation of testing.

A significant increase in strength was observed with the increase of silica fume replacement from 0 to 20%. However, when silica fume exceeded 20%, the strengths tended to decrease. The compressive and flexural strengths of U0 at 28 d were 89.8 and 19.1 MPa, respectively. When 10%, 15%, 20%, and 25% silica fume replacement were used, the compressive strength increased by approximately 18%, 16%, 28%, and 25%, respectively, as shown in Figure 4.2(a). The flexural strength increased by approximately 11%, 15%, 29%, and 18%, respectively. The addition of 15% to 20% silica fume decreased the porosity and improved the strength due to its filling effect in addition to the pozzolanic reaction [108]. However, a higher content of 25% silica fume increased plastic viscosity and yield stress, which could result in air entrapment [108]. Furthermore,

high silica fume content could significantly increase the risk of micro-cracking due to autogenous shrinkage, which can affect the mechanical properties [109,110].

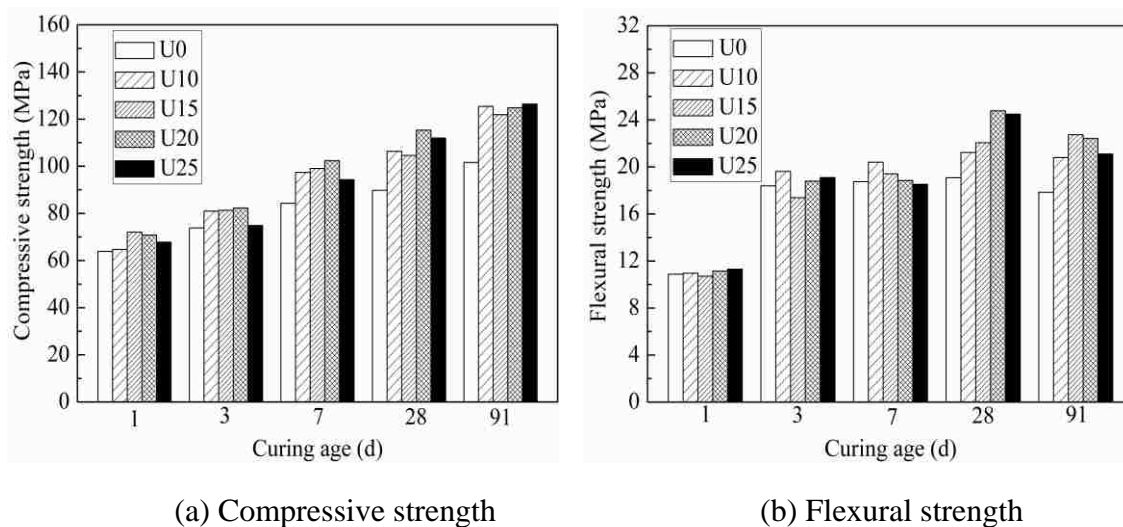


Figure 4.2. Effect of silica fume content on compressive and flexural strengths of UHPC matrix

#### 4.4. TG/DTG ANALYSES

The TG and DTG results of UHPC matrix with different silica fume contents at 28 d are shown in Figure 4.3. It is obvious that all the samples showed mass losses in the temperature ranges of 30-200, 370-470, and 600-730 °C. Mass loss between 30 and 200 °C can be attributed to the loss of combined water initially from C-S-H (80-90 °C) and then from ettringite (~130 °C) [111]. Mass loss in the range of 370-470 °C is due to the decomposition of CH [112]. From Figure 4.3(a), it can be found that UHPC matrix containing 15%-25% silica fume showed a larger mass loss in the range of 30-200°C, but a smaller mass loss from 370 to 470 °C, when compared to U0.

Additionally, the peak intensity of C-S-H was sharper than that of U0, as seen from Figure 4.3(b). These results indicated that pozzolanic reaction increased with the

increase of silica fume content. As the temperature increased from 600 to 730°C, the mass loss decreased further. This can be associated with the decomposition of calcium carbonate resulting from the carbonation of hydration products with CO<sub>2</sub> from air during sample preparation [113].

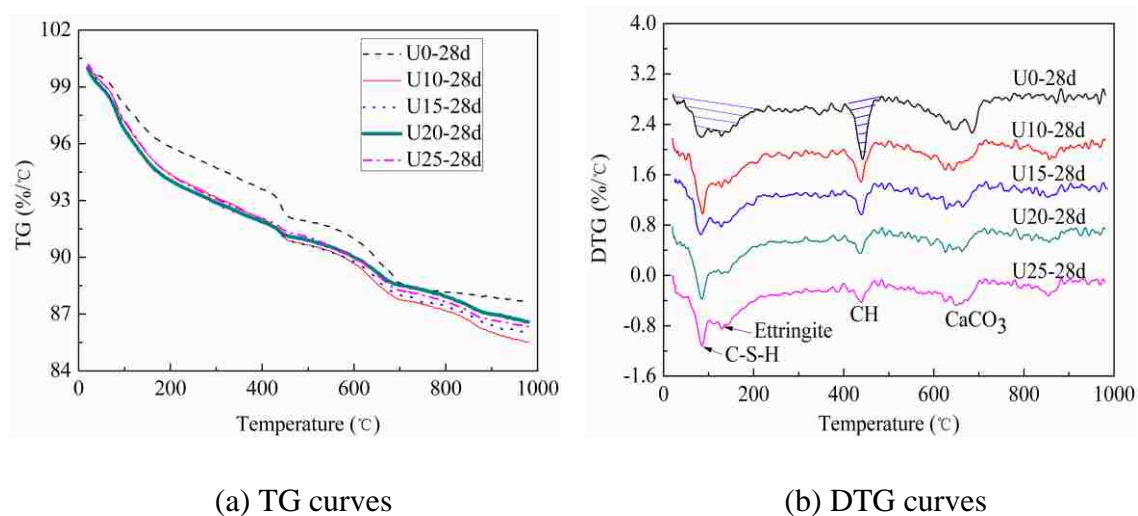


Figure 4.3. TG and DTG curves of matrix with different silica fume contents at 28 d

Figure 4.4 shows the effect of curing time on TG and DTG curves of UHPC matrices with 15% and 20% silica fume. With the increase of curing time, the mass loss between 30 and 200°C increased, as can be seen from Figure 4.4(b) and (d). Moreover, an obvious C-S-H peak at 80-90°C with high intensity first appeared at 7 d. This suggested that hydration products of C-S-H and/or ettringite phase in the U15 and U20 mixtures increased with curing time.

Besides, the mass loss in the range of 370-470°C decreased with curing age, which indicated reduced CH content. A relatively weak endothermic peak of CH for the

samples at 91 d was observed. Therefore, it is reasonable that CH was gradually consumed by pozzolanic reaction with silica fume to form C-S-H, which dominates the performance of UHPC matrix [114].

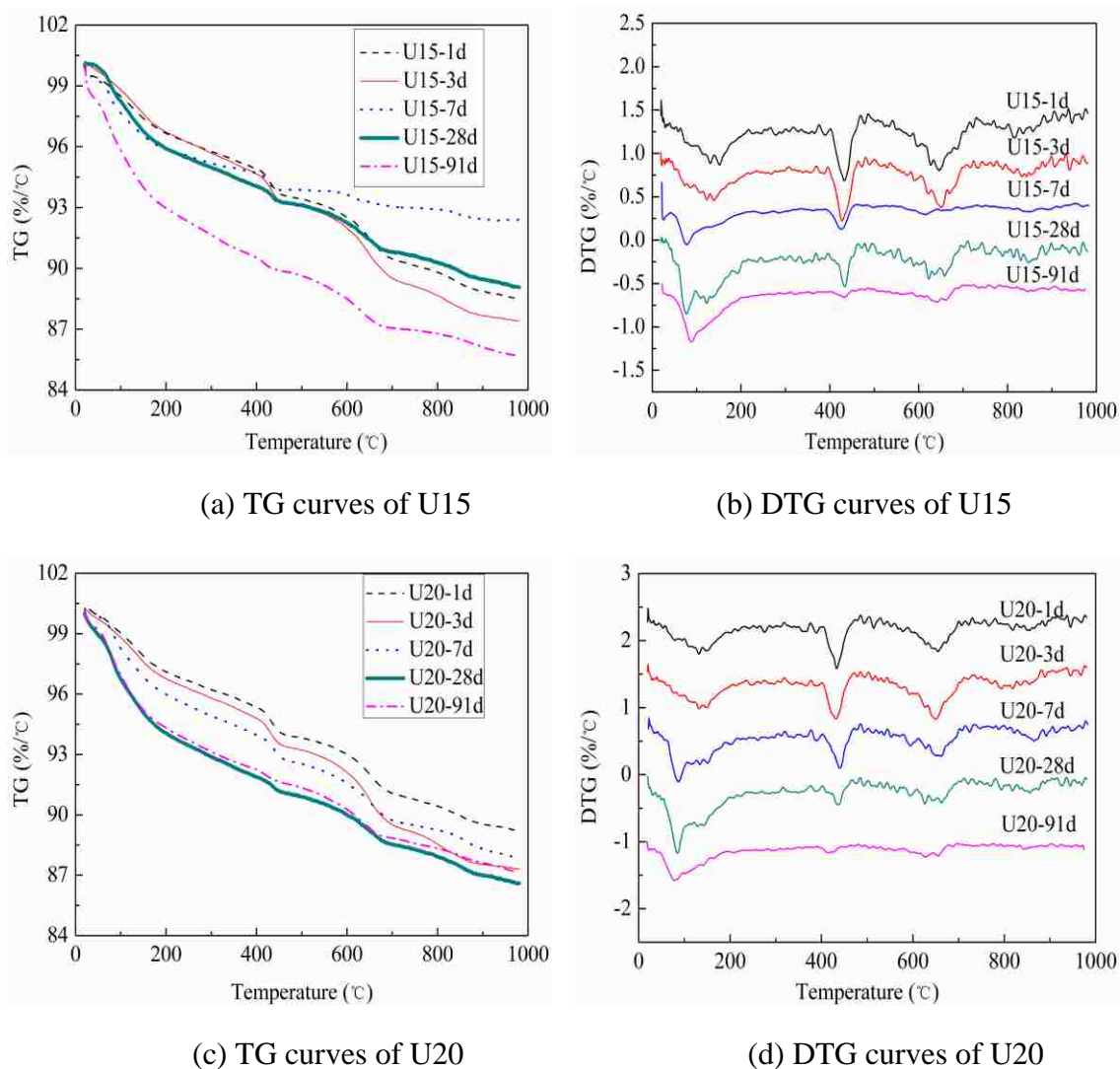


Figure 4.4. TG and DTG curves of U15 and U20 samples at different curing ages

The CH content of UHPC matrix at different ages is plotted in Figure 4.5. It can be seen that the CH content decreased with both the incorporation of silica fume and

prolongation of age. The reference batch U0 had a constant CH content of around 6% regardless of the age. However, it reduced gradually with the increase of silica fume content. U15, U20, and U25 had obvious lower CH contents compared with U0. It can be also seen from Figure 4.5 that no significant difference was observed for the samples at 1 and 3 d. However, the CH content of U15, U20, and U25 at 28 d was about 3% only, which was about 50% lower than that at 1 d. At 91 d, the CH contents of U15, U20, and U25 were reduced further to 2.3%. This indicated that silica fume could efficiently react with CH to form C-S-H due to the pozzolanic reaction, and thus improved the strengths of UHPC matrix.

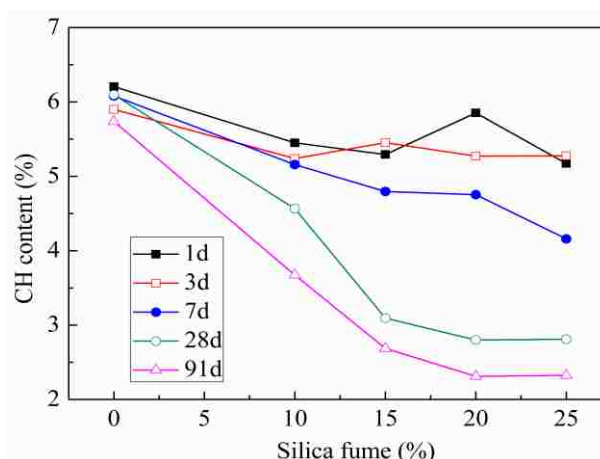
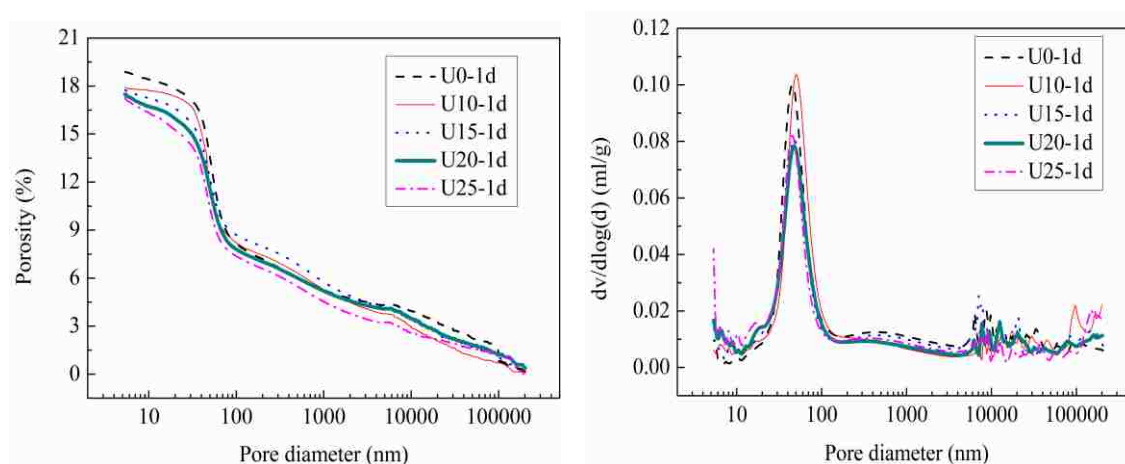


Figure 4.5. Content of CH in UHPC matrix from TG analysis

#### 4.5. PORE STRUCTURE CHARACTERISTICS

Figures 4.6 and 4.7 shows the effect of silica fume content on pore structure of UHPC matrix at 1 and 28 d, respectively, which cover the pore size range from around 5 to 200  $\mu\text{m}$ . It can be seen from Figure 4.6(a) and (b) that UHPC matrix incorporating silica fume at 1 d had slightly lower porosity and peak value at  $dv/d\log(d)$  curves

compared to U0. It is suggested that the most probable pore diameters, corresponding to the peak value in  $dv/d\log(d)$  curves, are strongly correlated with the permeability and ion diffusivity in cement-based materials [115]. When the curing age was prolonged to 28 d (Figure 4.7), it became apparent that a very low porosity of 6%-8% was observed for UHPC matrix with 15%-25% silica fume. This corresponds to a reduction of 67% in comparison to those of U0 and U10 mixtures.



(a) Cumulative porosity at 1 d

(b) Differential pore size distribution at 1 d

Figure 4.6. Pore structure of UHPC matrix with different silica fume contents at 1 d

It can also be noted that the U25 had a higher porosity than that of U20. This is consistent with the reduced flowability and strength. Besides, the most probable pore diameters decreased gradually with the increase of silica fume content, with the  $dv/d\log(d)$  curves shifted left to reflect pore refinement. Therefore, the incorporation of 15%-25% silica fume significantly densified the microstructure of UHPC matrix due to the combined filling and pozzolanic effect [116].

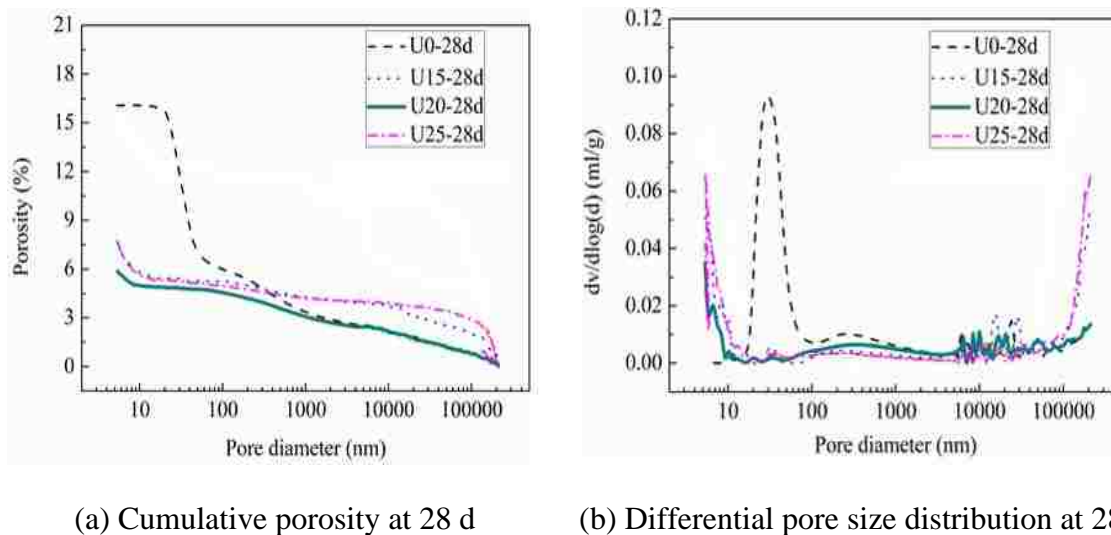


Figure 4.7. Pore structure of UHPC matrix with different silica fume contents at 28 d

Figure 4.8 shows the effects of the curing age on pore structure of the U20. As can be seen from Figure 4.8(a), the porosity at 1 d was 17.5%. However, at curing ages of 3, 7, and 28 d, the porosities were reduced to 11%, 9%, and 6%, respectively. At 91 d, the porosity was similar to that at 28 d. This is consistent with that strengths of UHPC matrix increased with curing time. The most probable pore diameters decreased from 20 to 7 nm, as shown in Figure 4.8(b), which corresponds to the pore refinement with the increase of curing age.

The measured pores can be divided into five size ranges, including gel micro-pores with appeared diameter < 10 nm, meso-pores of 10-50 nm, middle capillary pores of 50-100 nm, large capillary pores of 100 nm-5  $\mu\text{m}$  and macro-pore >5  $\mu\text{m}$  [117,118]. The change in pore size distribution of UHPC matrix with silica fume content and curing age are shown in Figure 4.9. As can be seen from Figure 4.9(a), the volume fraction of gel pores increased with the incorporation of silica fume although the difference was limited. It changed significantly with silica fume content at 28 d, as shown



in Figure 4.9(b). Compared with the U0, the proportion of gel micro-pores of the samples with silica fume increased from 0.02% to 25%, while the meso-pores reduced from 55% to 6%. It was reported that the nano-pores with diameter finer than 10 nm corresponds typically to gel pores in C-S-H with water held by hydrogen bond [119]. These pores mainly affect shrinkage and creep of the hardened cement-based materials. It can be also noted from Figure 4.9(b) that the total capillary pores (meso-pores, middle, and large capillary pores) of UHPC matrix with silica fume decreased considerably. Capillary pores larger than 50 nm can have great influence on mechanical properties and permeability of cement-based materials [117]. This is in good agreement with the results concerning significantly enhancement in the mechanical behavior of UHPC matrix made with silica fume.

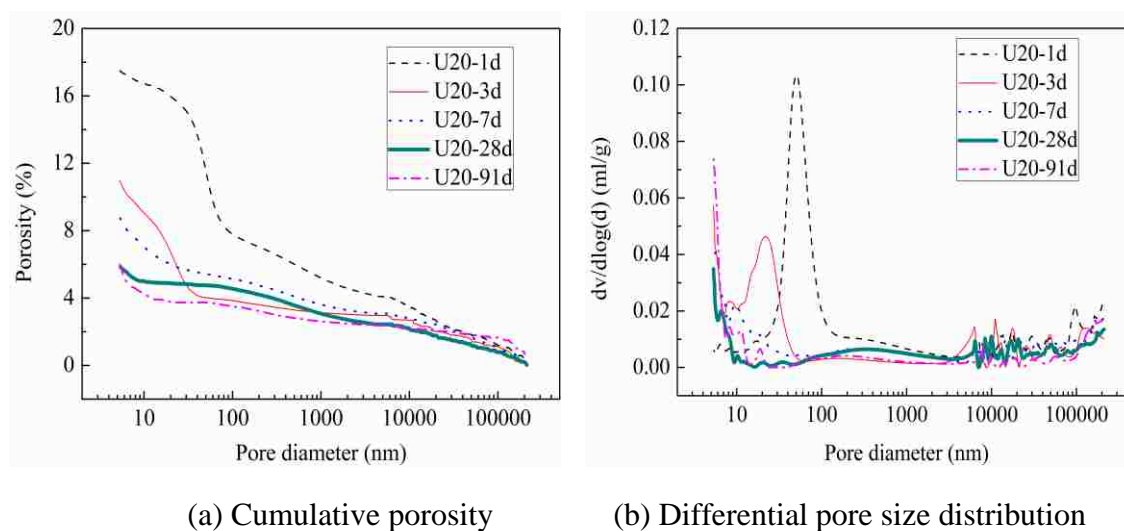
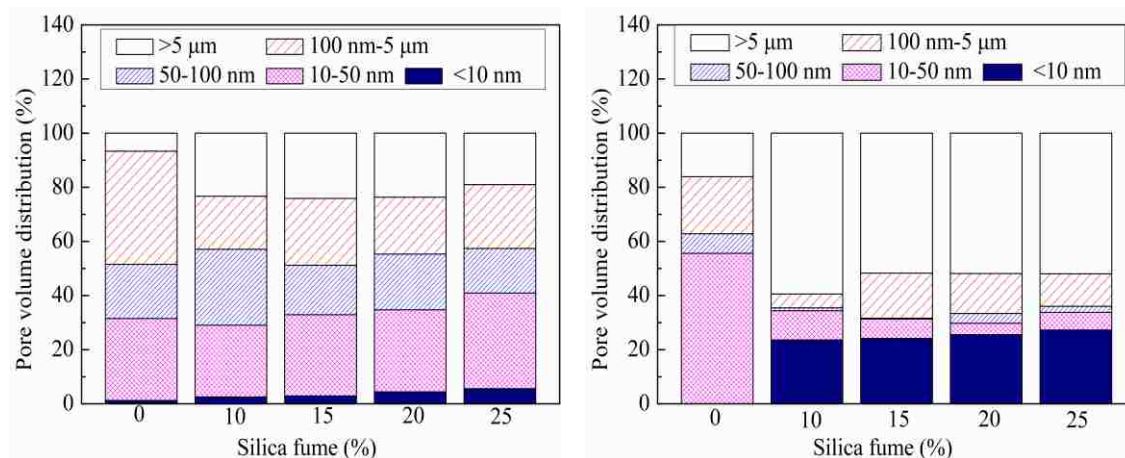
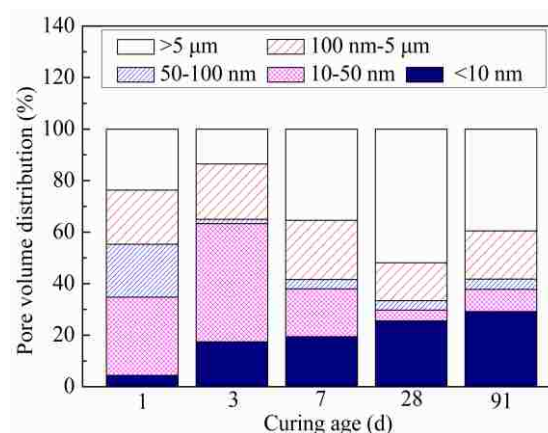


Figure 4.8. Pore structure of U20 mixture at different ages



(a) 1 d

(b) 28 d



(c) U20 at different curing ages

Figure 4.9. Pore volume distribution of UHPC matrix

The volume of macro-pores also increased. Such macro-pores include entrapped (1-3 mm) and entrained air bubbles (50-200 μm), which are often exhibited as discrete, individual bubbles with spherical shape in concrete [118]. The increased volume of macro-pores may be due to air entrapment associated with reduced workability of UHPC matrix with increased silica fume content [117]. The evolution of pore structure of the U20 mixture with increased curing age can be seen from Figure 4.9(c). It is interesting to note that the volume fraction of gel micro-pores of samples at 1 d was 4.7%. However,

such volume of gel micro-pores increased from 4.7% to 26%, while the total capillary pores decreased from 72% to 30% when curing age was prolonged from 1 to 91 d. In addition, the volume of meso-pores and middle capillary pores were reduced to very small portions.

#### 4.6. DISCUSSION

The results above show that the flowability, compressive and flexural strengths, and microstructure in UHPC matrix with different silica fume contents are closely related to each other. Because of highly fine particle size and high SiO<sub>2</sub> content of silica fume, the incorporation of silica fume can reduce the porosity, refine the pores, and increase the C-S-H content. The lower the porosity is, the higher the cement packing density in the bulk matrix and ITZ is [118]. Therefore, a greater content of the high strength cement hydration products, such as C-S-H, are necessary to ensure high compressive and flexural strengths.

Additionally, silica fume could significantly increase the autogenous shrinkage, especially in the UHPC matrix with low w/b and high cementitious materials content [120]. Generally, the higher the amount of silica fume is, the larger the autogenous shrinkage is. The autogenous shrinkage is controlled mainly by the size of the pores smaller than 10 nm [121]. It is obvious that the volume fraction of those pores increased with the increase of silica fume content, as described in Section 4.5. However, when the silica fume content exceeds a certain value, workability was reduced and the greater viscosity led to some entrapment of air bubbles [108]. This can reduce the quality of the matrix and interface, and thus reduce compressive and flexural strengths.

#### 4.7. SUMMARY

This paper investigated the effect of silica fume content on heat of hydration and compressive and flexural strengths of UHPC matrix made with constant SP content. TG analysis and MIP were used to characterize hydration products and pore structure of the matrix. Based on the results of this study, the following conclusions can be drawn:

(1) Due to the accelerated hydration of cement by silica fume, the compressive and flexural strengths of UHPC matrix containing 15%-25% silica fume were enhanced by 10-25 MPa after 28 d standard curing when compared to that of the reference sample.

(2) The CH content and porosity of samples with 15%-25% silica fume were only 3% and 5%-8% after 28 d of standard curing, respectively. However, when 25% silica fume was replaced, strengths began to decrease due to reduced flowability and slightly increased porosity.

## 5. FIBER PULLOUT, TENSILE, AND FLEXURAL PROPERTIES OF UHPC MADE WITH DIFFERENT SILICA FUME CONTENTS

### 5.1. BACKGROUND

Due to its very fine particle size and high surface area, silica fume acts as a stabilizing agent by reducing the mobility of water. The spherical silica fume particles provide “ball-bearing” effect when energy is applied to the fresh concrete, causing the mixture to flow easily in a well-dispersed system. Meanwhile, silica fume can consume Ca(OH) to form C-S-H gel, which benefits the mechanical properties of concrete. Previous research has indicated that the typical silica fume content in UHPC is approximately 25% to 30%, by mass of cementitious materials [122-125]. The silica fume content in a typical mixture proportion of commercial UHPC product that known as Ductal<sup>®</sup>, the most often used one in North America for both research and applications, is 25% [122]. Wille et al. [123] prepared UHPC with 28-d compressive strength over 200 MPa through cementitious matrix optimization without application of heat or pressure curing. In a study of the durability of UHPC, Teichmann and Schmidt used a UHPC mixture with 24% silica fume [124]. The researchers at the U.S. Army Corps reported a UHPC mixture proportion with silica fume of 28% [125]. Depending on the silica fume content as well as other mixture design characteristics, silica fume produce a double-edged sword effect on the performance and cost-effectiveness of UHPC. Low silica fume content can reduce concrete plastic viscosity with little or no change in yield stress and limited improvement in the microstructure and performance of UHPC [126]. High substitution can ensure sufficient pozzolanic reaction, but it also leads to high cost with a

plenty of silica fume working as inert and great increase in both the yield stress and plastic viscosity.

The interfacial bond properties of the fiber-matrix interface in UHPC have been extensively investigated using pullout testing [127-129]. The studied factors include matrix composition, fiber shape, fiber inclination angle, fiber embedment length, curing condition, and use of micro-fibers [55,98]. Generally, the pullout testing can be classified into single-sided and double-sided testing in terms of the methods of applying tensile force and/or fiber embedment [130]. The single-sided testing is relatively simple to be carried out. However, difficulty in gripping the free end of the fiber is inevitably encountered due to its very fine diameter [131]. To secure the reliability of the results, a large number of samples are required. Furthermore, the whole fiber is fully embedded in real composites, which is significantly different from that in the ideal test. The double-sided pullout testing was described by Chan et al [33]. Dog-bone samples with two separated halves from the sample center perpendicular to loading direction were used. In order to completely eliminate the adhesion of the two halves, one-half sample was cast first, then the other half 24 h later. However, this makes the casting process complicated and time-consuming. Therefore, to ensure proper interfacial stress transfer from the fiber to the matrix, so as to better evaluate the interfacial bond properties of fiber-matrix in UHPC, a simple and suitable method is needed.

In order to make highly flowable UHPC with satisfactory mechanical properties, the superplasticizer content was adjusted with considering adequate rheological properties. The main objective of this research is to evaluate the effect of silica fume content on fiber-bond behavior, flexural and tensile properties of non-fibrous UHPC

matrix and UHPC with 2% steel fibers at 28 d. The silica fume was determined at 0, 5%, 10%, 15%, 20%, and 25%, by mass of cementitious materials. The slump flow of the UHPC mixtures was fixed at  $280 \pm 5$  mm through changing the SP content. The flexural-to-tensile strength ratios of UHPC matrix and UHPC were determined and the tensile strength was predicted based on the fiber-matrix bond strength and material characteristics according to the composite theory. The tests performed aimed at covering the essential aspects of UHPC, in particular, workability and mechanical performance of the material with adequate silica fume content.

## 5.2. FIBER PULLOUT BEHAVIOR

Fiber pullout load-slip relationship of non-fibrous UHPC matrix with different silica fume contents is depicted in Figure 5.1. The bond of the interface between a steel fiber and the matrix is dominated by chemical adhesive bond, friction, and mechanical anchorage associated with the roughness of steel fiber. The fiber-matrix bond strength that calculated based on the peak value is illustrated in Figure 5.1(b). As the silica fume content was increased from 0 to 15%, the bond strength gradually increased and then kept a stable value at 20%. The bond strength of the U15-0 mixture was 4.77 MPa, which was 5.5 times greater than of the reference mixture. As the silica fume content increased further to 25%, the bond strength decreased to 1.88 MPa, which was even lower than that of the mixture with 5% silica fume. Therefore, adding adequate silica fume was beneficial to the fiber-matrix interfacial bond properties. However, adverse effect would occur with the greater content of silica fume. This agrees well with the previous results reported by the authors [132], in which the SP dosage was fixed at 2%. The difference

was that the decrease in fiber bond strength of UHPC mixture made with 25% silica fume in this research was much lower, which might due to various mixture composition, flowability, etc.

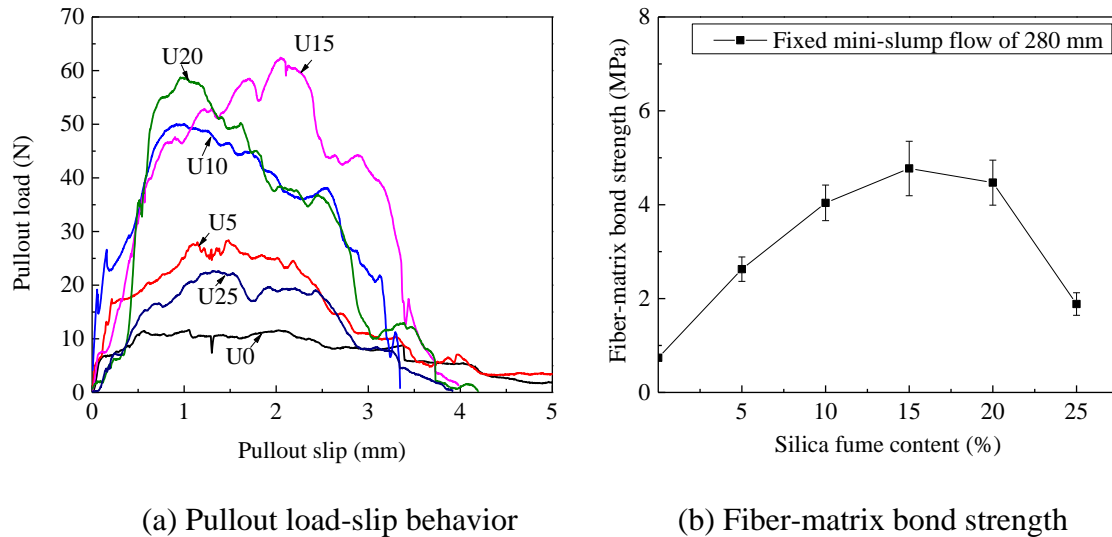


Figure 5.1. Fiber pullout behavior in non-fibrous UHPC matrix with different silica fume contents

### 5.3. FLEXURAL PROPERTIES OF UHPC MATRIX AND UHPC

The four-point flexural load-displacement relationship of UHPC matrix with different silica fume contents is shown in Figure 5.2. The UHPC matrix exhibited brittle failure after reaching the ultimate load at a displacement of approximately 0.05 mm. The flexural strength of the reference mixture was 4.7 MPa. The incorporation of 5%-25% silica fume enhanced the flexural strength by 10%-60%. The highest flexural strength of 7.5 MPa was achieved in UHPC matrix made with 15% silica fume. However, a higher silica fume content over 15% started to decrease the flexural strength by 26% when compared to the SF0 mixture.



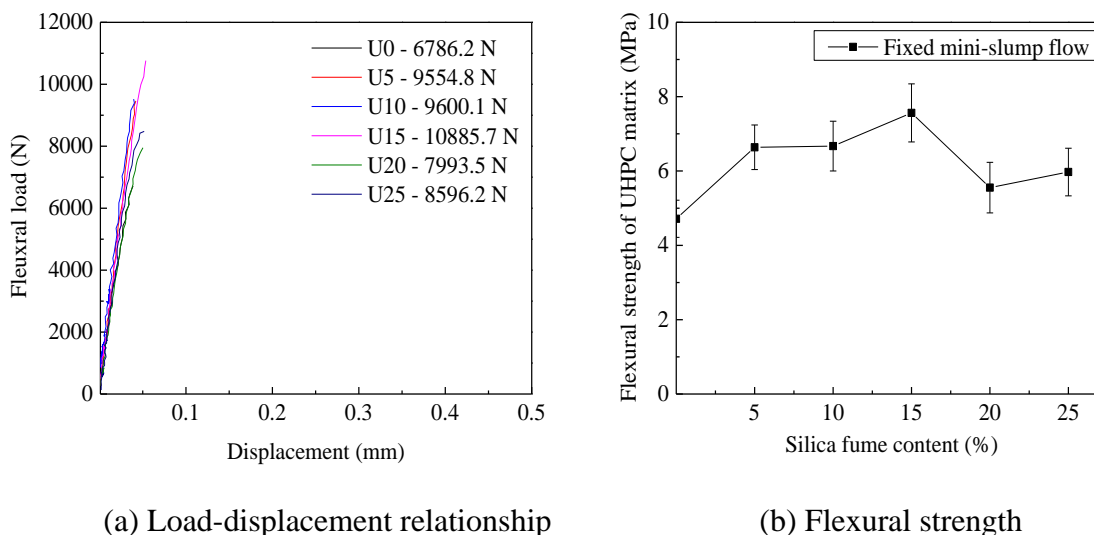


Figure 5.2. Flexural behavior of UHPC matrix with different silica fume contents

With the incorporation of steel fiber, ductile failure mode was observed because the steel fibers can bridge the cracking to further sustain load. Figure 5.3 illustrates the flexural load-displacement relationship of UHPC made with 2% steel fibers at different silica fume contents. All the five mixtures showed a linear load-displacement section within a displacement of 0.05 mm and then followed by a non-linear section to the peak load and finally a descending part with further loading. Obviously, the reference mixture SF0-2 showed an apparent smooth section in the descending curve. UHPC mixtures made with silica fume exhibited continuous zig-zag patterns, indicating enhancement in toughness because of improved bond properties at fiber-matrix interface correlated with silica fume.

The effect of silica fume content on flexural strength of UHPC made with 2% steel fibers is illustrated in Figure 5.4. The addition of 2% of steel fibers rendered the flexural strength of UHPC up to 13 – 17.8 MPa, which was approximately 170% greater than those of UHPC matrix without any fiber. The flexural strengths of UHPC with 5% to

20% silica fume were approximately 13-18 MPa, which were 7%-37% greater than that of the reference mixture. UHPC mixture made with 10% of silica fumed achieved the greatest flexural strength. Similarly to fiber-matrix bond properties and flexural strength of the UHPC matrix, too much addition of silica fume started to decrease the flexural strength of UHPC. Therefore, higher content of silica fume resulted not only decreased flexural strength but also high cost of UHPC.

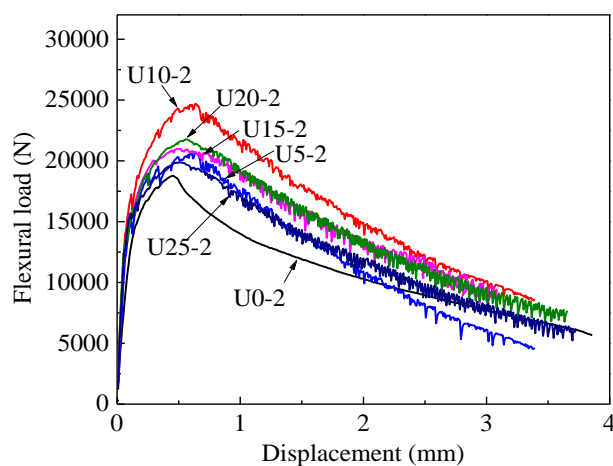


Figure 5.3. Flexural load-displacement relationship of UHPC made with 2% steel fibers at different silica fume contents

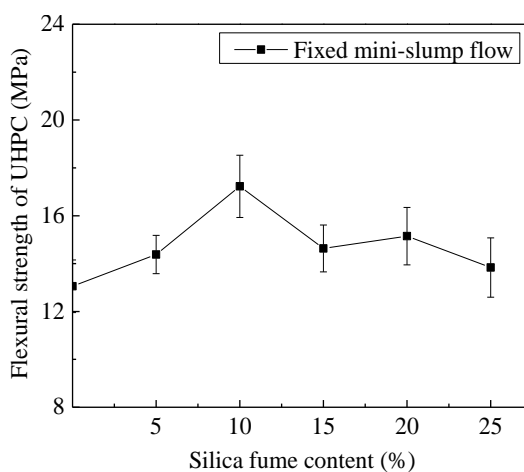


Figure 5.4. Flexural strength of UHPC made with 2% steel fibers at different silica fume contents

#### 5.4. TENSILE PROPERTIES OF UHPC MATRIX AND UHPC

The tensile properties of UHPC matrix and/or UHPC with different silica fume contents are illustrated in Figures 5.5 and 5.6.

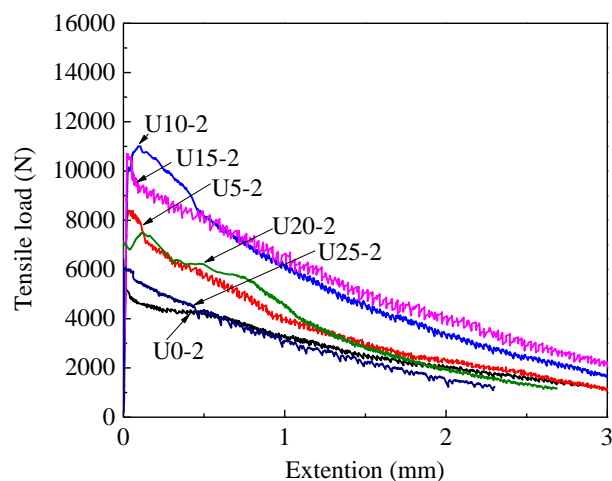


Figure 5.5. Tensile load-extension relationship of UHPC made with 2% steel fibers at different silica fume contents

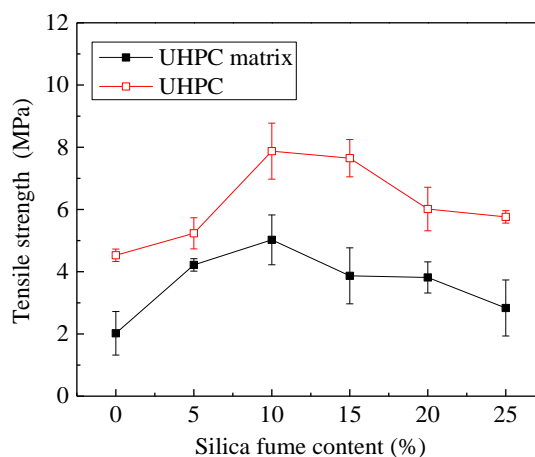


Figure 5.6. Tensile strengths of UHPC matrix and UHPC with different silica fume contents

With the increase of silica fume content, the tensile strength increased initially and then decreased when reaching a critical value of 10% and or 15%. The incorporation of 5%-20% silica fume enhanced the tensile strengths by 33%-70% when compared to

the reference mixture. Even though the tensile strength of UHPC made with 25% silica fume was still greater than that without any silica fume, but there is no need to add more silica fume from the cost-effective and strength aspects. This agrees well with the previous fiber-matrix bond, compressive, and flexural behavior results. Silica fume can densify and homogenize the microstructure of UHPC due to filling effect and highly pozzolanic reaction with calcium hydroxide to form C-S-H gel [132]. The increase in C-S-H gel and improvement in microstructure can significantly increase the fiber-matrix bond strength. Excessive silica fume up to 20% would increase the plastic viscosity and introduce air voids but has little effect on decreasing the calcium hydroxide content [126,132]. Moreover, the increase of plastic viscosity could increase the resistance for vertical orientation of fiber to the loading direction of samples, thus reducing the mechanical properties of UHPC. Therefore, 10%-20% silica fume is sufficient for desired mechanical properties and high cost-efficiency.

### **5.5. FLEXURAL AND TENSILE STRENGTHS RELATIONSHIP**

Through calculation, the flexural-to-tensile strength ratios of UHPC matrix and UHPC are plotted in Figure 5.7. The flexural-to-tensile strength ratio of UHPC matrix without fiber was in the range from 1.3 to 2.3. The addition of 2% steel fibers enhanced the corresponding value, which was 1.9 to 2.8. This agrees well with the flexural-to-tensile strength ratio of ordinary fiber-reinforced concrete, which is reported as varying between 1 and 3, depending on the geometry of reinforcement and specimens, and reinforcement volume [133].

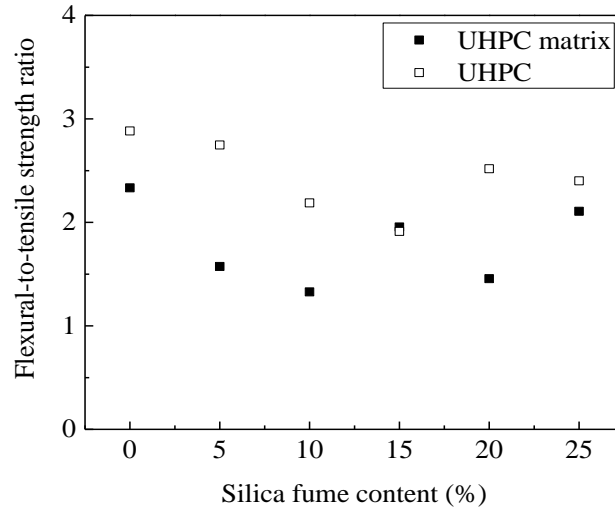


Figure 5.7. Flexural-to-tensile strength ratios of UHPC matrix and UHPC

## 5.6. PREDICTION OF TENSILE STRENGTH BASED ON FIBER-MATRIX BOND STRENGTH

In terms of the fiber-matrix bond and the tensile strengths of the non-fibrous UHPC matrix, the tensile strength of UHPC with certain fiber volume can be obtained. According to the composite theory, the tensile strength of fiber reinforced cement-based composites is the addition of tensile strengths of matrix and reinforcement. This can be determined according to the following equation (5.1):

$$\sigma_{tc} = \sigma_{tm}(1 - V_f) + \sigma_{tf}V_f \quad (5.1)$$

where  $\sigma_{tc}$  (MPa) is the tensile strength of fiber reinforced concrete composite;  $\sigma_{tm}$  (MPa) is the tensile strength of concrete matrix;  $V_f$  (unit-less) is the fiber content, by volume of concrete;  $\sigma_{tf}$  (MPa) is the average tensile strength of fiber.

The efficiency of steel fiber to sustain tensile stress is closely correlated with fiber length and fiber orientation. Therefore, coefficients of fiber length ( $\eta_l$ ) and orientation ( $\eta_\theta$ ) are considered in the calculation of tensile strength of fiber-reinforced concrete.

The tensile strength of UHPC with 2% steel fibers can be calculated in terms of Equation (5.2).

$$\sigma_{tc} = \sigma_{tm}(1 - V_f) + \eta_l \eta_\theta \sigma_{tf} V_f \quad (5.2)$$

where,  $\sigma_{tm}$  (MPa) is the tensile strength of UHPC matrix;  $\eta_\theta$  (unit-less) is the coefficient related to orientation of fiber in three dimensions, which was determined as 0.5;  $\sigma_{tf}$  (MPa) is the tensile strength of steel fiber;  $\eta_l$  (unit-less) is the length factor, which is closely related to the critical length and damage state of steel fiber.

According to previous research [134, 135], the critical length of fiber can be calculated from Equations. (5.3) and (5.4). If fiber pullout-length is greater than the critical length, pullout failure mode would be observed and Equation (5.3) will be used. Otherwise, Equation (5.4) will be used in the case of rupture failure of fiber.

$$\eta_l = \frac{l_f}{2l_f^{crit}} \quad \text{when } l_f \leq l_f^{crit} \quad (5.3)$$

$$\eta_l = 1 - \frac{l_f^{crit}}{2l_f} \quad \text{when } l_f > l_f^{crit} \quad (5.4)$$

The relationship between the tensile strength of fiber ( $\sigma_{tf}$ ) and fiber critical length ( $l_f^{crit}$ ) for failure is presented in Equation (5.5).

$$\sigma_{tf} = \frac{2l_f^{crit}}{d_f} \tau \quad (5.5)$$

Therefore, the following equation can be finally derived to calculate the tensile strength of the composite material:

$$\sigma_{tc} = \sigma_{tm}(1 - V_f) + \eta_\theta \frac{l_f}{d_f} \tau V_f \quad (5.6)$$

The predicted and experimental tensile strengths of UHPC made with 2% of steel fibers are plotted in Figure 5.8. The data is dispersed around the equality line with a relative coefficient of 0.64.

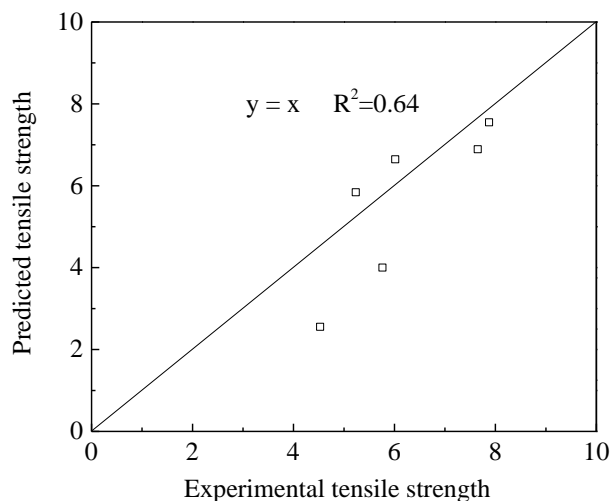


Figure 5.8. Predicted and experimental tensile strengths of UHPC with 2% steel fibers

## 5.7. SUMMARY

This study investigated the influence of silica fume content, varying from 5% to 25% with a basis of 5%, on pullout bond properties of embedded fibers and mechanical properties of UHPC matrix and UHPC made with 2% steel fibers at a fixed mini-slump flow of 280 mm. The involved mechanical properties include flexural and tensile strengths. The flexural-to-tensile strength ratio of both UHPC matrix and UHPC were established. The tensile strength of UHPC was predicted using the composite theory with consideration of the performance of UHPC matrix and material characteristics. Based on the results of this study, the following conclusions can be drawn:

(1) The incorporation of 5%-25% improved the fiber-matrix bond and mechanical properties of both UHPC matrix and UHPC made with 2% steel fibers. The optimal silica fume content for UHPC matrix and UHPC with 2% steel fibers were 10%-20%. Compared to the reference mixture, the fiber-matrix bond strength, flexural strength, and tensile strength of UHPC were enhanced by 440-540%, 7%-37%, and 33%-70%, respectively. With silica fume content further increased up to 25%, the corresponding values were significantly decreased.

(2) The flexural-to-tensile strength ratio of UHPC matrix without fiber was in the range from 1.3 to 2.3, it increased to 1.9 to 2.8 with the addition of 2% steel fibers.

(3) The tensile strength of UHPC made with 2% steel fibers can be efficiently predicted using the composite theory with considering the properties of UHPC matrix, consumed fiber orientation coefficient of 0.5, and fiber characteristics, including fiber geometry, volume, and diameter. The values were dispersed around the equality line with a relative coefficient of 0.64.



## 6. MULTI-SCALE INVESTIGATION OF MICROSTRUCTURE, FIBER BOND, AND MECHANICAL PROPERTIES OF UHPC WITH NANO-CaCO<sub>3</sub>

### 6.1. BACKGROUND

Nanotechnology has attracted much interest over the past decade. Since the introduction of nanomaterials, extensive research has been conducted to promote their use in cement-based materials. It is well known that nanomaterials can provide significant enhancement in performance of cement-based material given their physical effect (filling and nucleation effect) as well as the chemical reactivity [136]. Nano-silica (nano-SiO<sub>2</sub>) [137], nano-alumina (nano-Al<sub>2</sub>O<sub>3</sub>) [138], nano-titanium oxide (nano-TiO<sub>2</sub>) [139], nano-CaCO<sub>3</sub> [140], nano iron (Fe<sub>2</sub>O<sub>3</sub>), and nanotubes [141] have been studied for use in cement-based materials. Among those, nano-SiO<sub>2</sub> and nano-CaCO<sub>3</sub> are commonly used. This is because nano-CaCO<sub>3</sub> is relatively cheap due to abundant supplying of CaCO<sub>3</sub> in limestone, chalk, and marble, while nano-SiO<sub>2</sub> can present superior performance given its high specific area and pozzolanic activity [142]. Prototypes of limestone and silica fume have been employed in cement-based materials for many years [106143].

Limestone powder can be considered as a non-costly replacing material for cement because of its richness in natural resources, which is an ideal alternative material to replace cement [144, 145]. Although it was first considered as filler, some studies indicated that it shows accelerating effect from chemical reaction with tricalcium aluminate (C<sub>3</sub>A) to form carboaluminate compound, especially when the limestone powder is finely ground. Although limestone powder does not show pozzolanic effect to consume calcium hydroxide [146,147], its interaction with tricalcium silicate (C<sub>3</sub>S) can

accelerate the hydration of  $C_3S$  [147,148]. Nano/micro limestone has been incorporated in cement-based materials to investigate its effect on microstructure, heat of hydration, autogenous shrinkage, and mechanical properties of concrete [142,149]. The optimal nano- $CaCO_3$  (NC) content can vary with mixture composition, water-to-cementitious ratio, and flowability of mixture. Li et al. [149] studied the effect of NC on mechanical properties of UHPC matrix at a water-to-binder ratio of 0.16 and 0.17. They found that the incorporation of 3% NC, by mass of cement, improved compressive strength by about 11%-17% under 2 d of heat curing and then 26 d of standard curing compared to the control mixture. Wu et al. [146] reported that NC had limited effect on strength development of UHPC matrix from 3 to 7 d but significant influence from 7 to 28 d under standard curing. Xu et al. [150] indicated that the addition of 1%-2% NC could improve the compressive strength of the high-performance concrete by 13%-18% under standard curing temperature. Camiletti et al. [142] suggested that replacement of 2.5%-5% NC to cement showed about 32%-75% improvement in the 24 h compressive strength of UHPC matrix with respect to that of the control mixture. However, aforementioned studies focus mainly on the mechanical properties of matrix and/or UHPC. There is a perceived lack of information on the effect of NC on the microstructure, fiber-matrix bond properties, and mechanical properties of UHPC. Fiber, as an essential component of UHPC, plays a vital role in enhancing the strength and toughness of the composite material through the fiber-matrix interface. Therefore, optimizing the microstructure, fiber-matrix bond properties, and eventually the mechanical properties of UHPC is of great significance.

This paper presented a multi-scale investigation that focuses on evaluating the effect of nano- $CaCO_3$  on fiber-matrix bond properties, microstructure of UHPC matrix

(without fiber), as well as mechanical properties of UHPC reinforced with 2% steel fibers. It aims at providing new insights into enhancing mechanical properties of UHPC through optimization of fiber-matrix bond properties and microstructure, which finally targets at multi-scale enhancement of performance for UHPC.

## **6.2. EFFECT OF NANO-CaCO<sub>3</sub> ON INTERFACIAL FIBER-MATRIX BOND AND MECHANICAL PROPERTIES OF UHPC MATRIX**

Effect of nano-CaCO<sub>3</sub> on fiber pullout-slip curve and compressive strength of UHPC matrix made without any steel fibers were illustrated in the following part.

**6.2.1. Fiber Pullout-Slip Curves.** Figure 6.1 shows the effect of nano-CaCO<sub>3</sub> content on pullout load-slip curves of the UHPC matrix at 1, 3, 7, and 28 d. All curves showed increased pullout load with the increase in slip. The pullout load then remained almost unchanged for a certain slip after reaching the peak value. Afterward, the pullout load decreased until the fibers were completely pulled out from the matrix.

The embedded fibers in the UHPC matrix with nano-CaCO<sub>3</sub> experienced debonding at a greater pullout load capacity, especially at later ages, compared to the reference mixture without any nano-CaCO<sub>3</sub> (NC0). The peak loads for NC0 was 15, 17, 30, and 32 N at 1, 3, 7, and 28 d, respectively. It increased to 21, 30, 46, and 62 N, respectively, when 3.2% nano-CaCO<sub>3</sub> was added. Moreover, the area surrounded by the pullout load-slip curves of UHPC matrix with nano-CaCO<sub>3</sub> became significantly bigger, especially after 7 d, thus indicating a significant improvement in toughness.

**6.2.2. Experimental and Predicted Bond Strengths.** Figure 6.2 illustrates the effect of nano-CaCO<sub>3</sub> content on fiber-matrix bond strength and compressive strength of

the UHPC matrix. As observed from Figure 6.2(a), the incorporation of nano- $\text{CaCO}_3$  remarkably enhanced the bond strength. The bond strength of embedded fibers in the reference specimen (NC0) at 28 d was 3.3 MPa and increased to 5 MPa with the increase of nano- $\text{CaCO}_3$  content. However, the bond strength decreased when the nano- $\text{CaCO}_3$  exceeded a critical value of 3.2% or 4.8%.

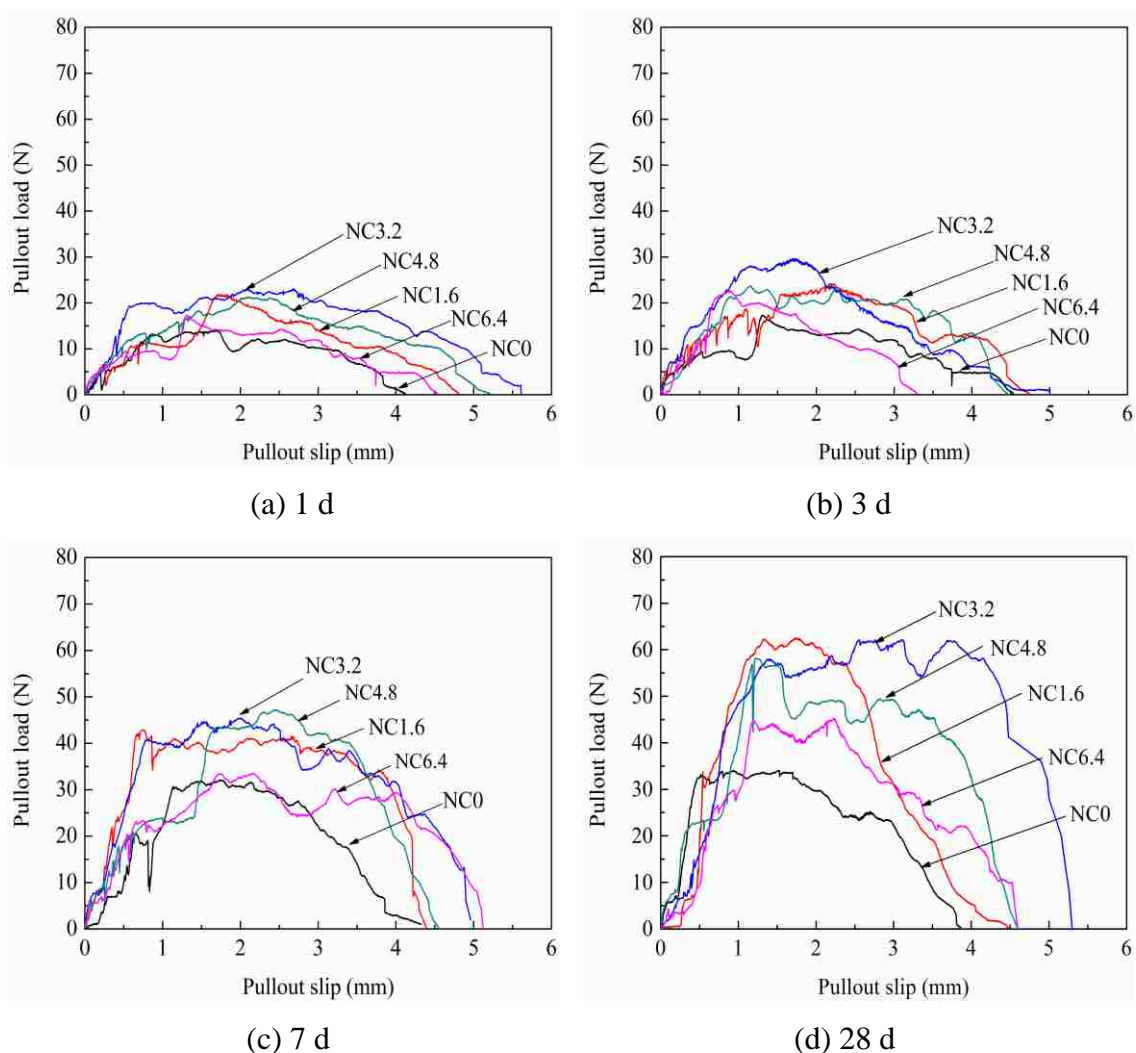


Figure 6.1. Fiber pullout load-slip curves of UHPC matrix with different nano- $\text{CaCO}_3$  contents

The bond strength of the embedded fibers in NC6.4 at 28 d was about 4 MPa. Therefore, the optimal dosage of nano-CaCO<sub>3</sub> in terms of the bond strength was in the range from 1.6% to 4.8%. Nano-CaCO<sub>3</sub> can improve the microstructure and increase the content of C-S-H because of its nucleation effect. Furthermore, it can chemically react with C<sub>3</sub>A and increases the roughness of fibers due to precipitation of reaction product onto the fiber surface [151]. This could improve the frictional bond and eventually the fiber-matrix bond strength. However, high nano-CaCO<sub>3</sub> content can lead to increase in viscosity, drop in flowability, and uninform dispersion, which can introduce cracks and pores, especially at the fiber-matrix interface. This will be discussed in Section 6.3.

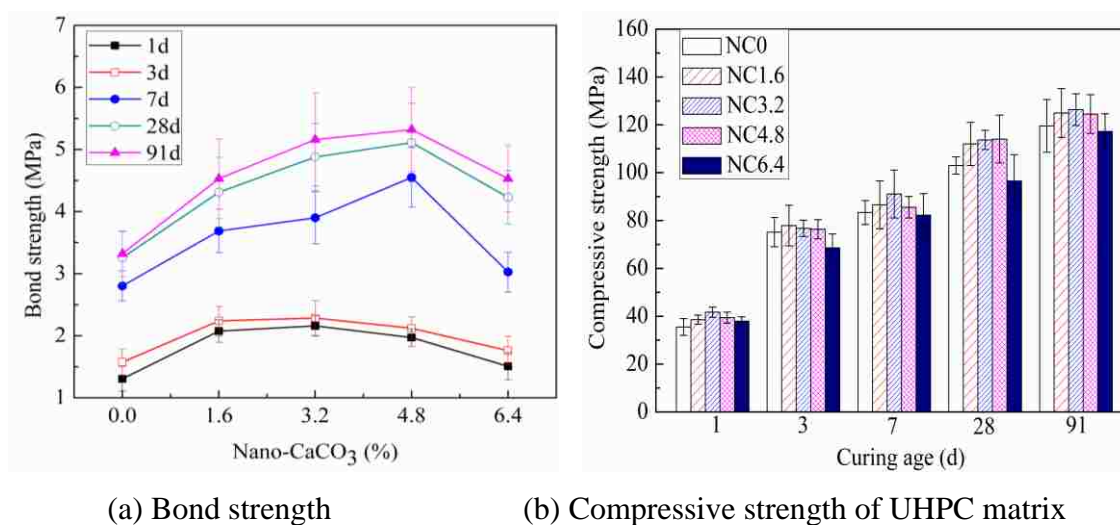


Figure 6.2. Effect of nano-CaCO<sub>3</sub> on fiber-matrix bond strength and compressive strength of UHPC matrix

As can be also seen from Figure 6.2(a), the bond strength increased considerably between the age of 1 and 7 d, but was almost stable after 28 d. For example, the bond strength of NC3.2 at 1 d was approximately 2 MPa, and increased to approximately 3.8

MPa at 7 d. At 91 d, the bond strength was 5.2 MPa, which was only 8% greater than that at 28 d. The change in bond strength was closely related to the compressive strength of the matrix.

As shown in Figure 6.2(b), the compressive strength of the UHPC matrix increased by approximately 175% from 1 to 7 d, but only by 28% from 7 to 91 d. The incorporation of 1.6%-4.8% nano-CaCO<sub>3</sub> increased the compressive strength by 3-15 MPa, which was 8%-18% greater than the reference specimen, depending on curing age. This is comparable to the results reported by Li et al. [149] that UHPC with 3% NC exhibited an increase in compressive strength of 11%-17% after 2 d of heat curing and then 26 d of standard curing compared to the control mixture. The incorporation of nano-CaCO<sub>3</sub> can obviously increase the heat of hydration due to high surface energy. Moreover, it enhances the packing density of the matrix and acts as nucleation seeds for the precipitation of C-S-H, thus improving the early-age mechanical properties of the UHPC matrix [146]. However, the enhancement in compressive strength associated with nano-CaCO<sub>3</sub> is relatively low, which might be due to standard curing and very dense structure of UHPC.

The response surface methodology was employed to estimate the bond strength at the fiber-matrix interface of UHPC matrix as a function of nano-CaCO<sub>3</sub> content and curing time. This can enable the interpretation of the significant effect of various parameters on expected outputs. A second order model was established to predict bond strength, which is expressed as follows [152]:

$$Y = b_0 + \sum_{i=1}^k b_i X_i + \sum_{i=1}^k b_i X_i^2 + \sum_{i < j} b_{ij} X_i X_j \quad (6.1)$$

where  $Y$  is the predicted response;  $X_i$  is the quantitative variables ( $i=1, 2, 3, \dots$ );  $b_0$ ,  $b_i$ , and  $b_{ij}$  are the least square estimates of regression coefficients.

Table 6.1 summarizes the estimates for bond strength. Performing the Student  $t$ -test with a significant level of 0.05, the model should allow those terms with a “Prob>|t|” value less than 0.05, which is considered to be statistically significant.

Table 6.1. Parameter estimates for fiber-matrix bond strength through statistical analysis

| Term  | Estimate  | Std Error | t Ratio | Prob> t |
|---|-----------|-----------|---------|---------|
| Intercept   | 2.87      | 0.244147  | 11.74   | <.0001* |
| Nano-CaCO <sub>3</sub> content                                    | 10.22     | 4.813085  | 2.12    | 0.0472* |
| Age   | 0.07      | 0.007838  | 8.67    | <.0001* |
| (Nano-CaCO <sub>3</sub> - 0.032)*(Nano-CaCO <sub>3</sub> - 0.032) | -1027.81  | 254.2355  | -4.04   | 0.0007* |
| (Age - 25.96)*(Age - 25.96)                                       | -0.001024 | 0.000172  | -5.97   | <.0001* |
| (Age-25.96)*(Nano-CaCO <sub>3</sub> content-0.032)                | 0.22      | 0.142663  | 1.52    | 0.1450  |

Note: \* denotes statistically significant term

The term (Age - 25.96) \* (Nano-CaCO<sub>3</sub> content - 0.032) was eliminated from the bond strength evaluation since it was greater than 0.05. The predicted bond strength ( $\tau_{\max}$ ) can be then expressed as follows:

$$\tau_{\max} = 1.16 + 0.118 X_1 - 0.001 X_1^2 + 75.996 X_2 - 1027.81 X_2^2 \quad (6.2)$$

where  $\tau_{\max}$  (MPa) is the predicted bond strength;  $X_1$  (d) is the curing age;  $X_2$  (unit-less) is the nano-CaCO<sub>3</sub> content.

The contour diagram and actual by predicted plot for bond strength are shown in Figure 6.3. As observed from Figure 6.3(a), good bond strength over 3 MPa was obtained for specimens with nano-CaCO<sub>3</sub> content in the range from 3.2% to 5% after

approximately 28 d standard curing. The actual bond strength was closely scattered around the line of equality with a correlation coefficient ( $R^2$ ) of 0.86, as can be seen from Figure 6.3(b). This suggests that the predicted bond strength from this model fitted well with the experimental bond strength.

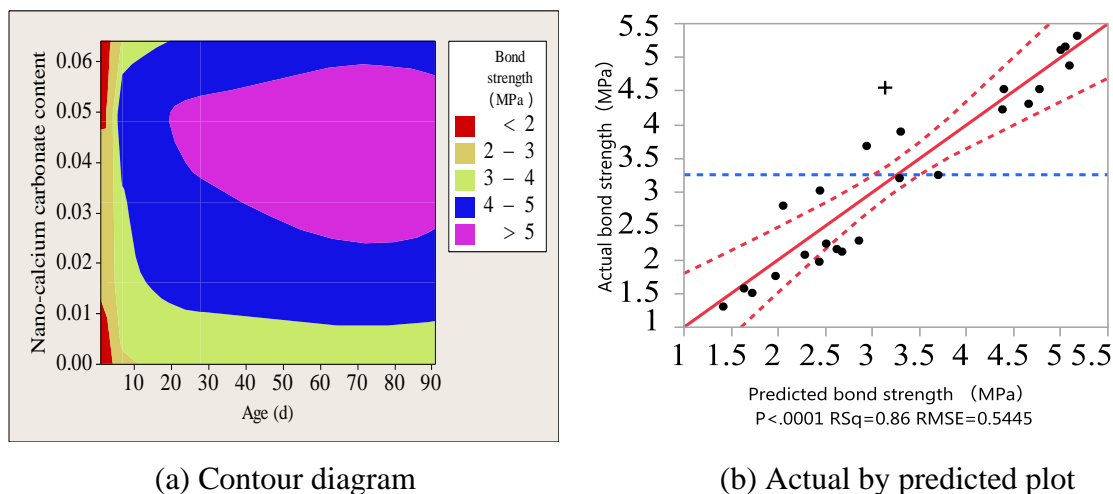


Figure 6.3. Predicted fiber-matrix bond strength with variation of nano- $\text{CaCO}_3$  content and curing age

**6.2.3. Experimental and Predicted Pullout Energies.** The effect of nano- $\text{CaCO}_3$  content on pullout energy between the embedded fibers and the UHPC matrix is depicted in Figure 6.4. The pullout energy is defined as the energy dissipation during pullout process through integrating the area under load-slip curves. Change in pullout energy with nano- $\text{CaCO}_3$  content and curing age was similar to that of bond strength. However, the enhancement of pullout energy was much more significant than that of bond strength, especially after 7 d. The pullout energy of the embedded fibers in the NC3.2 matrix with 3.2% nano- $\text{CaCO}_3$  at 3 d was 55  $\text{N}\cdot\text{mm}$  and increased to 160, 250, and 248  $\text{N}\cdot\text{mm}$  at 7, 28, and 91 d, respectively. This is consistent with the results reported



by Chan et al. [33]. The main reason for this improvement was due to the fact that nano-CaCO<sub>3</sub> can lead to interfacial toughening effect associated with the dense structure and/or improved hydration products, which will be discussed in Section 6.3 [153].

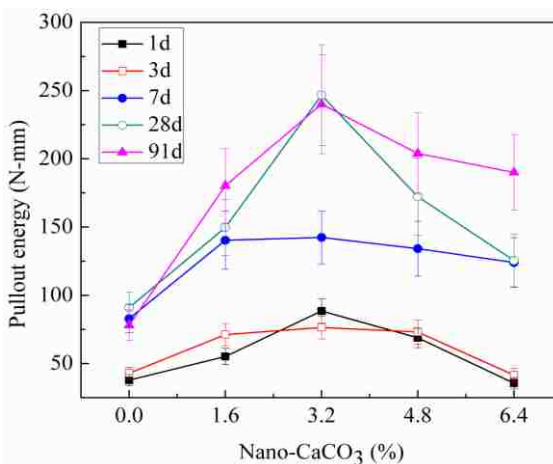


Figure 6.4. Effect of nano-CaCO<sub>3</sub> content on fiber-matrix pullout energy

Based on the parameter estimates as shown in Table 6.2, a statistical model that can be used to predict pullout energy is as follows:

$$P = 25.82 + 4.227 X_1 - 0.038X_1^2 + 4179.177 X_2 - 63499.89 X_2^2 + 15.916 X_1X_2 \quad (6.3)$$

where P (N·mm) is the predicted pullout energy; X<sub>1</sub> (d) is the curing age; X<sub>2</sub> (unit-less) is the nano-CaCO<sub>3</sub> content, by mass of cementitious materials.

Table 6.2. Parameter estimates for pullout energy through statistical analysis

| Term  | Estimate  | Std Error | t Ratio | Prob> t |
|---|-----------|-----------|---------|---------|
| Intercept   | 103.30    | 12.54393  | 8.23    | <.0001* |
| Nano-CaCO <sub>3</sub> content                                    | 529.00    | 247.2628  | 2.14    | 0.0456* |
| Age   | 2.76      | 0.402582  | 6.86    | <.0001* |
| (Nano-CaCO <sub>3</sub> - 0.032)*(Nano-CaCO <sub>3</sub> - 0.032) | -63499.89 | 13060.95  | -4.86   | 0.0001* |
| (Age - 26)*(Age - 26)   | -0.04     | 0.008789  | -4.33   | 0.0004* |
| (Nano-CaCO <sub>3</sub> - 0.032)*(Age - 26)                       | 15.92     | 7.295189  | 2.18    | 0.0419* |

Note: \* denotes statistically significant term

Figure 6.5 shows the contour diagram and actual by predicted plot for pullout energy. From Figure 6.5(a), it can be seen that specimens with nano-CaCO<sub>3</sub> content from 2% to 5% after 20 d had satisfied pullout energy. Its pullout energy after 20 d was higher than 200 N·mm. The actual pullout energy fitted well with the predicted values from this model with a correlation coefficient of 0.84, as shown in Figure 6.5(b). However, it should be noted that change in mixture design and other factors, such as embedded fiber length, curing regime, fiber shape, can affect the fiber-matrix bond properties.

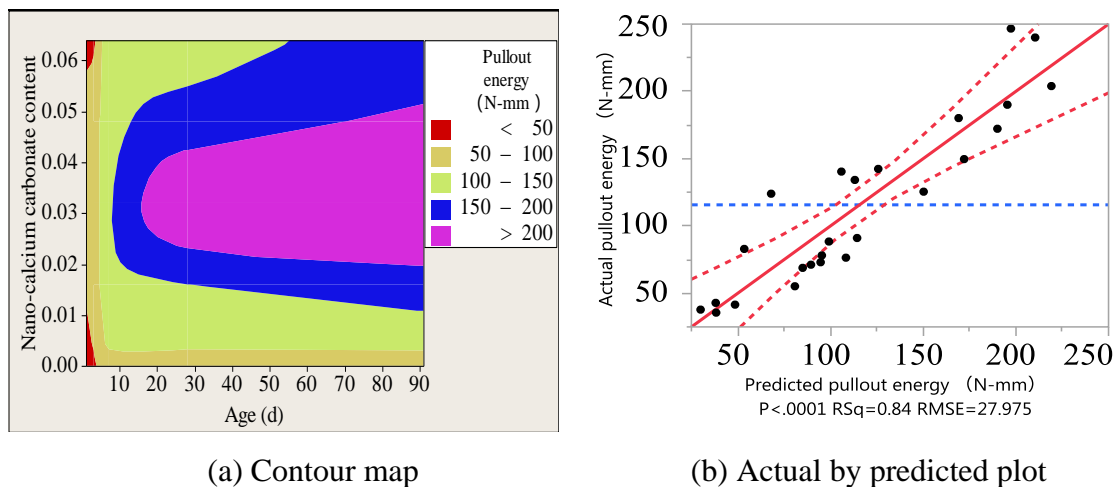


Figure 6.5. Predicted pullout energy with variation of nano-CaCO<sub>3</sub> content and curing age

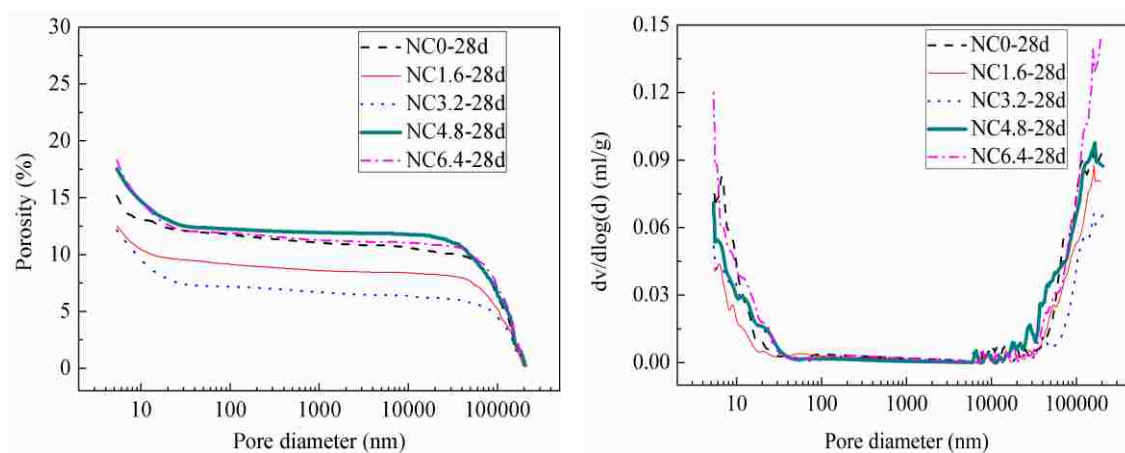
### 6.3. EFFECT OF NANO-CaCO<sub>3</sub> ON MICROSTRUCTURE OF UHPC MATRIX

The porosity and pore size distribution of different UHPC matrix made with different nano-CaCO<sub>3</sub> contents were investigated by using MIP analysis.

**6.3.1. MIP Results.** Figure 6.6 shows the porosity and pore size distribution of UHPC containing different nano-CaCO<sub>3</sub> contents at 28 d. It can be seen from Figure 6.6(a), within a specified dosage of 3.2%, the total porosity decreased with the increase of

nano-CaCO<sub>3</sub> content. With further increase in dosage, the porosity began to increase.

When the nano-CaCO<sub>3</sub> content increased from 0 to 3.2%, the porosity decreased from 15.2% to 12.5%.



(a) Porosity at 28 d

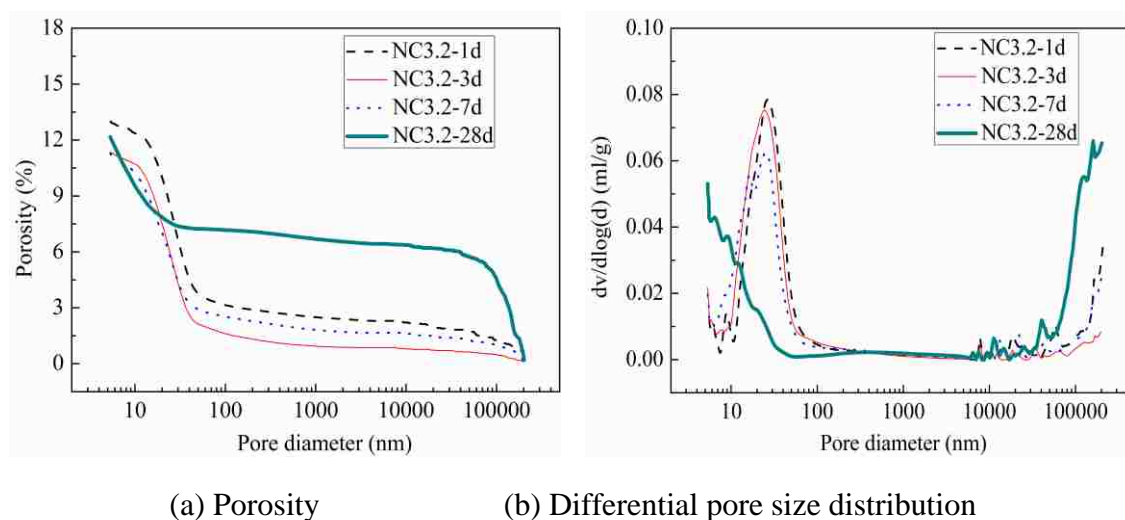
(b) Differential pore size distribution at 28 d

Figure 6.6. Effect of nano-CaCO<sub>3</sub> content on porosity and pore size distribution of UHPC matrix at 28 d

However, with the nano-CaCO<sub>3</sub> content increased further from 3.2% to 6.4%, the porosity increased from 12.5% to 17.5%. Although nano-CaCO<sub>3</sub> can efficiently fill internal pores of the hydrated cement paste, high content of such nanoparticles can lead to agglomeration and reduction in flowability and increase in viscosity. For the pore size distribution shown in Figure 6.6(b), the  $dv/d\log(d)$  curves of the five UHPC matrix were superposed covering pore size from 40 to 100,000 nm. For pore size smaller than 40 nm, the curves for UHPC matrix containing nano-CaCO<sub>3</sub> shifted to left indicating finer pores when compared to the NC0 reference sample without any nano-CaCO<sub>3</sub>. Furthermore, the peak value, i.e. inflection point on the  $dv/d\log(d)$  curve, corresponding to critical pore size decreased. This peak value corresponds to capillary pores, which has great influence

on the permeability of concrete [154]. It also reflects the connectivity of the pores and tortuosity of penetration path in concrete. The results indicated that the addition of appropriate nano- $\text{CaCO}_3$  content efficiently reduce the porosity, refine the pores, and thus making UHPC matrix denser and more homogeneous.

Figure 6.7 shows the effect of age on porosity and pore size distribution of UHPC matrix containing different nano- $\text{CaCO}_3$  contents.



(a) Porosity

(b) Differential pore size distribution

Figure 6.7. Effect of age on porosity and pore size distribution of NC series

It can be observed from Figure 6.7(a) that the total porosity decreased with age due to continued hydration. The NC3.2 at 28 d had a slightly larger total porosity than those at 3 and 7 d. This may be due to the increased volume of pores larger than  $5 \mu\text{m}$ , as presented in Figure 6.7(b). It can be also observed that the peak value on  $dv/d\log(d)$  curve reduced gradually with age. The value was 0.08 ml/g with a diameter of 30 nm at 1 d. At 7 d, it reduced to 0.06 ml/g. With age prolonged to 28 d, it reduced further and

shifted to finer pores with diameter of 10 nm only. This corresponds with the results of considerable increase in strength.

Figure 6.8 shows the pore volume distribution of UHPC matrix, which includes gel micro-pores (< 10 nm), meso-pores (10-50 nm), middle capillary pores (50-100 nm), large capillary pores (100-5000 nm), and macro-pores (>5000 nm) [118].

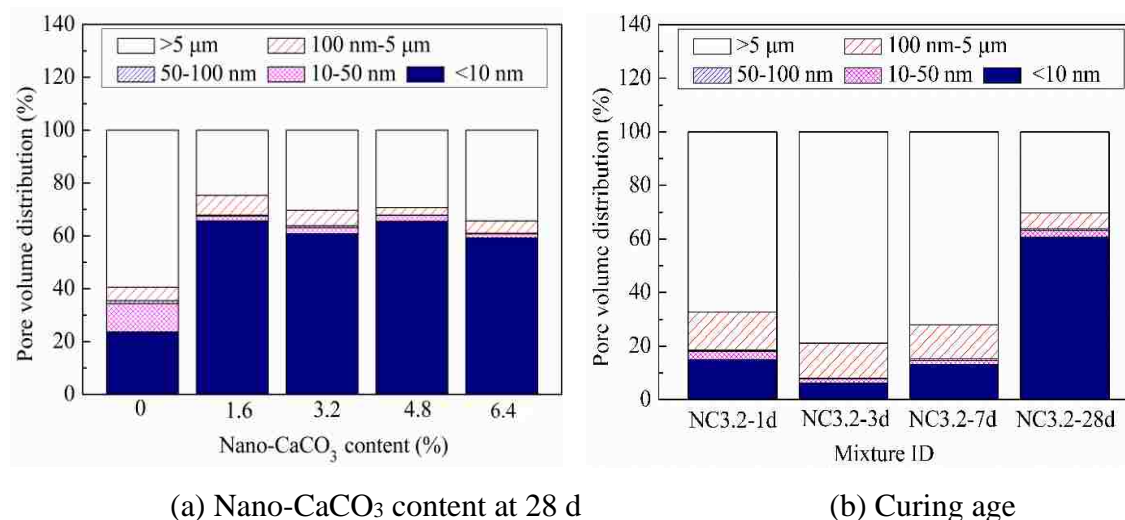


Figure 6.8. Effect of nano-CaCO<sub>3</sub> content and curing age on pore volume distribution of UHPC matrix

As shown in Figure 6.8(a), the reference sample (NC0) at 28 d exhibited micro-pores, meso-pores, middle and large capillary pores volume of 23.6%, 10.8%, 1.1%, and 5.1%, respectively. The incorporation of nano-CaCO<sub>3</sub> particles resulted in refinement of the microstructure with increased volume of meso-pores (10-50 nm) up to 60%. The volume of meso-pores was limited to 2%, whereas almost no 50-100 nm pores were observed.

From Figure 6.8(b), it can be seen that the volume of pores less than 10 nm increased with age, while the large capillary pores in the range of 100-5000 nm decreased. Therefore, the use of 3.2% nano-CaCO<sub>3</sub> led to a densification of the microstructure and enhancement of the homogeneity of the UHPC matrix.

**6.3.2. TG/DTG Analysis.** Figure 6.9 shows the TG and DTG curves of UHPC matrix with different nano-CaCO<sub>3</sub> contents at 28 d. The hydration products in the hardened concrete are C-S-H with endothermal peak at approximately 80 - 90 °C, ettringite with endothermal peak around 130°C, calcium hydroxide (CH) with an endothermal peak in the range of 450 - 550 °C, and calcium carbonate with endothermal peak in the range of 600 - 700 °C. The endothermal peaks at the four temperature ranges are due to the dehydration of C-S-H and ettringite, decomposition of CH and CaCO<sub>3</sub>, respectively.

It can be seen from Figure 6.9(b), at the first temperature range of 50 - 150 °C, not only the endothermal peak intensity but also the covered range increased with the increase of nano-CaCO<sub>3</sub> content. At 450 - 550 °C, there was no obvious change for the samples with and without nano-CaCO<sub>3</sub>. As the temperature increased to 600 - 700 °C, the decomposition of CaCO<sub>3</sub> increased with the increase of nano-CaCO<sub>3</sub> content, which suggested a larger amount of nano-CaCO<sub>3</sub> acted as filler in UHPC matrix. It should be noted the curve change for UHPC matrix with a high dosage of nano-CaCO<sub>3</sub> (4.8% to 6.4%) was smoother than with low dosage of nano-CaCO<sub>3</sub>. This might be attributed to the sufficient and/or well-crystallized CaCO<sub>3</sub> from incorporated nano-CaCO<sub>3</sub> particles.

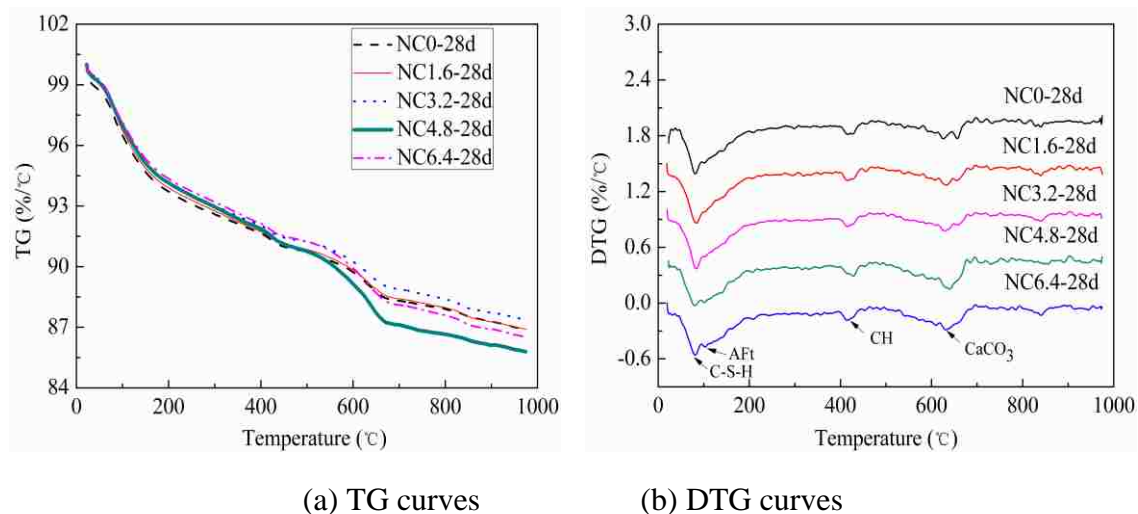


Figure 6.9. TG and DTG curves of UHPC matrix with different nano-CaCO<sub>3</sub> contents at 28 d

Figure 6.10 shows the TG and DTG curves of the NC3.2 at 1, 3, 7, and 28 d. No significant difference between the DTG curves for UHPC matrix can be found at 1, 3, and 7 d. All mixtures exhibited a strong AFt peak at 130 °C without obvious C-S-H peak. However, when the age reached 28 d, significant peak with a strong intensity corresponding to C-S-H appeared. Moreover, the intensity of the endothermal peak of CaCO<sub>3</sub> decreased. This suggests increased C-S-H content and decreased CaCO<sub>3</sub> content as curing age prolonged to 28 d. It indicated that in the presence of CaCO<sub>3</sub>, mono-carbonate and/or hemi-carbonate could be formed through reacting with C<sub>3</sub>A. Limestone could also interact with the AFm and AFt phases. Weerdt et al. [163] stated that when limestone was incorporated, a peak of mono-carbonate (MC) or hemi-carbonate (HC) would appear at around 175 °C. This agrees well with that significant strength increase from 7 to 28 d. The formation of C-S-H may be first due to the pozzolanic reaction between silica fume and CH. The incorporation of nano-CaCO<sub>3</sub> could combine with C-S-

H to form a new compound with space network structure, optimizing the internal structure and consequently improving the mechanical properties of cement-based materials.

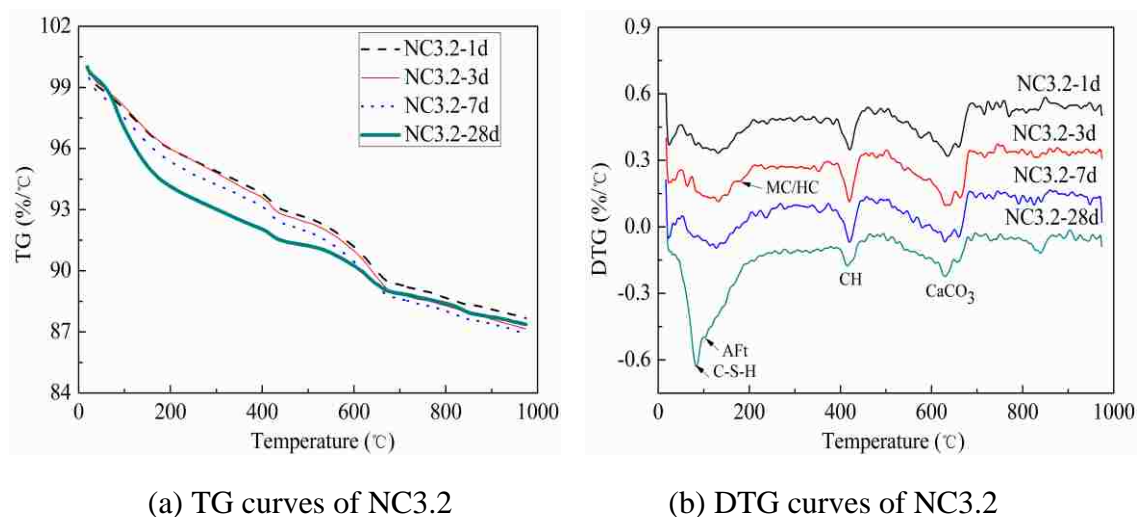


Figure 6.10. TG and DTG curves of NS3.2 at different ages

**6.3.3. CH Content.** The determination of the CH content in concrete samples is an effective method to follow the degree of hydration as a function of time. Figure 6.11 compares the relative amounts of CH formed in the NC with age. It can be seen that the CH content in NC series decreased with age. The CH content in UHPC matrix at 1, 3, and 7 d was hardly changed, however, it decreased significantly from 7 to 28 d.

In NC series, the 20% silica fume can help to consume CH to form C-S-H (Equation 6.4). Nano-CaCO<sub>3</sub> mainly reacts with C<sub>3</sub>A to form carboaluminates, as shown in Equations (6.5) and (6.6). Several researchers have demonstrated that limestone does not show pozzolanic properties to produce C-S-H gel [163]. This corresponds to the



limited change of CH content in UHPC matrix samples made with different nano-CaCO<sub>3</sub> contents. However, the incorporation of nano-CaCO<sub>3</sub> can change the C-S-H structure, such as the Ca/Si ratio, and thus affecting mechanical properties of UHPC matrix sample [155].

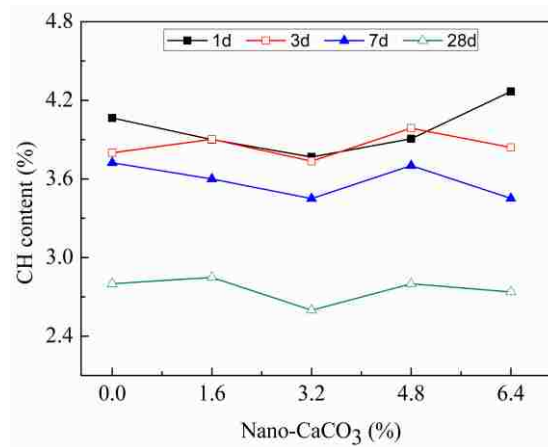
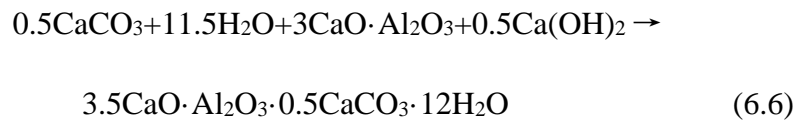
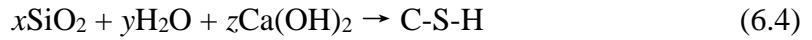


Figure 6.11. Amount of CH formed in UHPC matrix with different nano-CaCO<sub>3</sub> contents with age

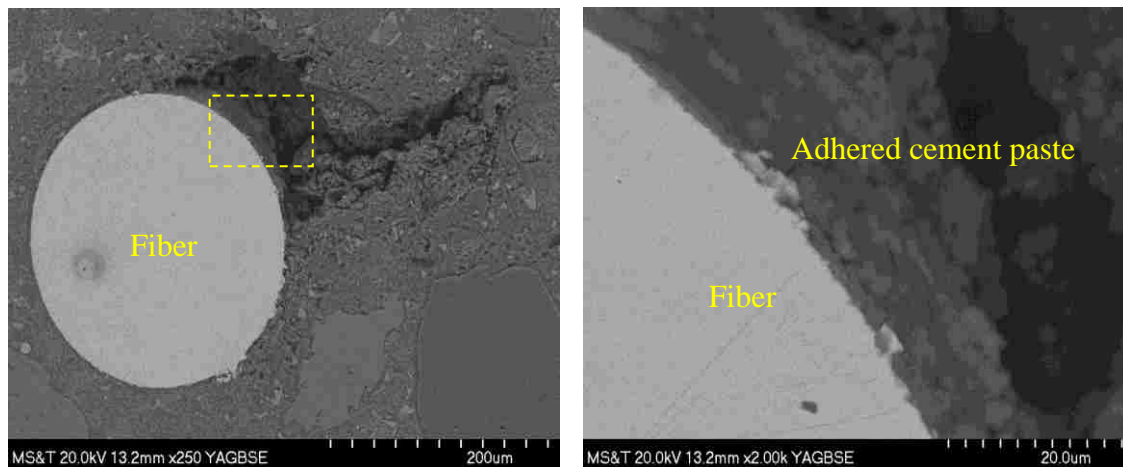
**6.3.4. BSEM Image Analysis.** The BSEM observation of an embedded fiber in the UHPC matrix is shown in Figure 6.12. Porous microstructure around the fiber in NC3.2 at 7 d was observed, which might be due to bleeding and/or wall effect [156]. Cement paste was adhered on the fiber surface, as observed from the right figure of Figure 6.12(a). Such porous zone can decrease the contact area between the matrix and

fiber and eventually the bond strength. At 28 d, fiber-matrix interface was well-bonded in NC3.2. Some disconnected pores with sizes in the range from 2 to 20  $\mu\text{m}$  were observed from the right image of Figure 6.12(b).

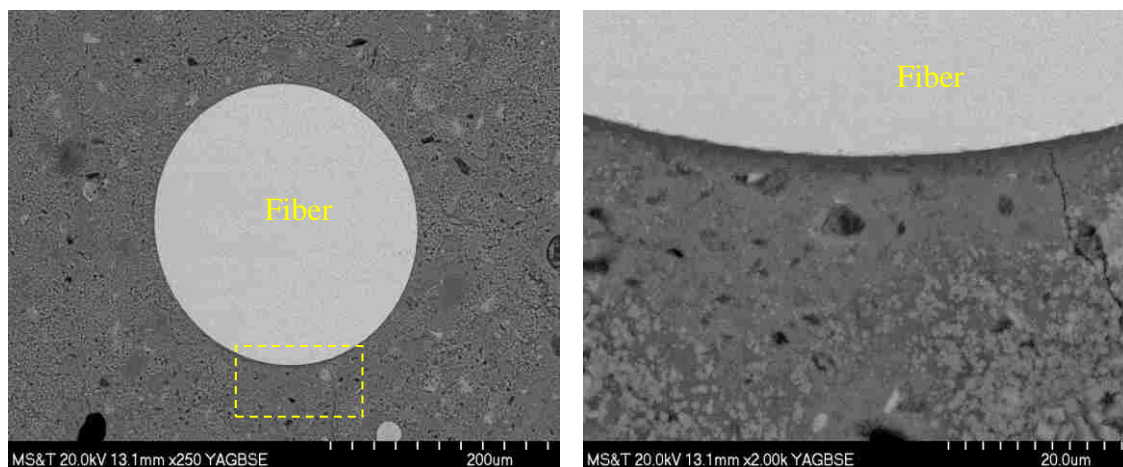
From the right image of Figure 6.12(c), an obvious crack was observed within a thickness of 4 to 5  $\mu\text{m}$  bulk paste adhering to the fiber in NC6.4. This was distinct from the results in the reference samples (NC0) made without any nano- $\text{CaCO}_3$ , in which cracking occurred very close to the steel fiber surface. It is reported that two types of bond failure occur during the fiber pullout from the matrix, which are adhesive and cohesive failures [100]. The cohesive failure is a failure occurred in the bulk layer of the adhesive and is usually the desired failure mode. The adhesive failure occurs at the interface between the adhesive and the adhered materials.

In Figure 6.12(d), adhesive failure was observed in NC0 with obvious cracking space between the actual fiber and the matrix interface. It should be noted that the deformation of steel fiber in Figure 6.12 (d) might be because of slightly fiber inclination from cutting. In Figure 6.12(c), NC6.4 indicated the cohesive failure mode, in which cracking occurred within the matrix with some cement pastes adhered to the steel fiber. This suggests higher strength of hydration products associated with the incorporation of nano- $\text{CaCO}_3$  to render greater bond strength. However, excessive nano- $\text{CaCO}_3$  can result in increase in viscosity and agglomeration issue, leading to more pores and lower bond strength.

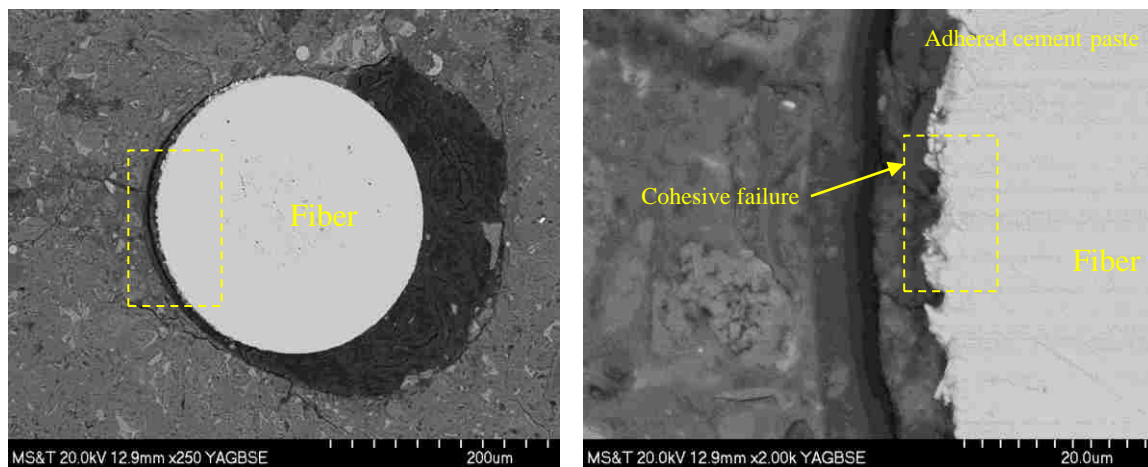
**6.3.5. Optical Microscopy Analysis.** Figure 6.13 shows optical microscopy images of NC6.4 at 28 d. Pores with diameter of 50-200  $\mu\text{m}$ , aggregate, cement paste, as well as agglomeration of nano- $\text{CaCO}_3$  can be identified in the matrix.



(a) NC3.2 at 7 d

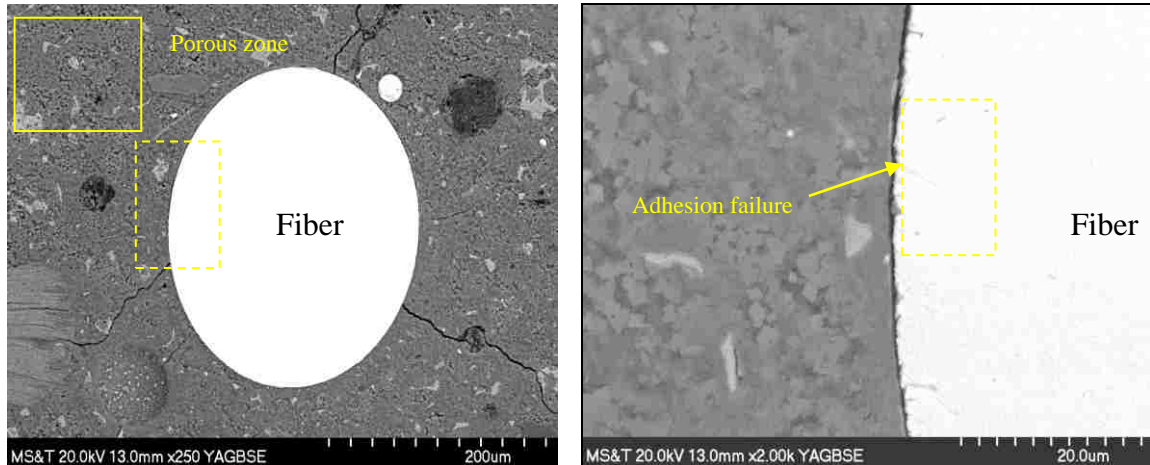


(b) NC3.2 at 28 d



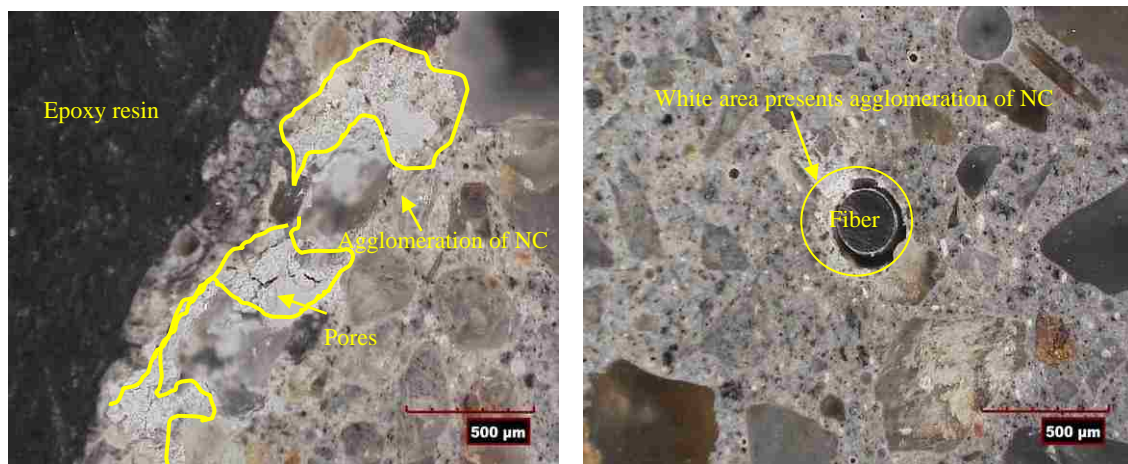
(c) NC6.4 at 28 d

Figure 6.12. BSEM images for UHPC matrix with an embedded fiber



(d) NC0 at 28 d

Figure 6.12. BSEM images for UHPC matrix with an embedded fiber (cont.)



(a) Agglomeration around aggregate

(b) Agglomeration around embedded fiber

Figure 6.13. Optical microscopy observation of UHPC matrix made with 6.4% nano- $\text{CaCO}_3$ 

In Figure 6.13(a), serious agglomeration with the irregular area around aggregates was observed. This introduced apparent pores and cracks between the matrix and aggregate to increase the porosity. As can be seen from Figure 6.13(b), agglomeration occurred near the embedded fiber with the obvious porous zone at the interface. This can

lead to a great reduction in fiber-matrix bond strength and eventually mechanical properties of UHPC.

**6.3.6. Micro-Hardness Characteristics.** Table 6.3 shows the micro-hardness of UHPC matrix with different distances to fiber edge. The micro-hardness of steel fiber was in the range of 760 to 800 HV. With the increase of distance to fiber edge, the micro-hardness increased. The micro-hardness was lowest within distances of 40 to 80  $\mu\text{m}$  from fiber edge, which was in the range of 60 to 100 HV, depending on matrix composition. However, the micro-hardness remained almost constant when distance reached 160  $\mu\text{m}$ . The lower micro-hardness within distance of 40 to 80  $\mu\text{m}$  was due to greater porosity associated with bleeding/wall effect, as was observed from BSEM images.

It can also be noted that the micro-hardness changed obviously with prolongation of age and mixture proportion. The micro-hardness of NC3.2 beyond 160  $\mu\text{m}$  to fiber edge was 89.9 HV at 1 d. It increased gradually to 103.9 and 143.9 HV, respectively, at 7 and 28 d. This corresponds well with the change in matrix strength and fiber bond strength. Besides, compared to NC0 and NC6.4 at 28 d, NC3.2 exhibited obvious higher micro-hardness. The micro-hardness of NC6.4 at 28 d was comparable to the reference sample NC0, but was slightly lower than that of NC3.2. The bond between straight fiber and matrix was mainly dominated by adhesion or chemical bond, which is governed by the main hydration product C-S-H with a diameter of 10 nm [182]. Nano- $\text{CaCO}_3$  can react with  $\text{C}_3\text{A}$  to form carboaluminates, but also act as nucleus to change the C-S-H structure, such as Ca/Si ratio, and thus affecting the bond properties [153].

Table 6.3. Variation of micro-hardness in UHPC matrix with and without nano-CaCO<sub>3</sub> at different ages

| Distance | Micro-hardness (HV) |          |           |           |         |
|----------|---------------------|----------|-----------|-----------|---------|
|          | NC3.2-1d            | NC3.2-7d | NC3.2-28d | NC6.4-28d | NC0-28d |
| Fiber    | 797.5               | 774.6    | 778.6     | 763.3     | 791.0   |
| 40 μm    | 63.2                | 76.6     | 96.6      | 73.5      | 79.3    |
| 80 μm    | 79.5                | 72.6     | 102.6     | 75.7      | 84.4    |
| 120 μm   | 86.6                | 93.8     | 103.8     | 90.4      | 95.2    |
| 160 μm   | 92.3                | 101.4    | 131.4     | 101.7     | 110.8   |
| 200 μm   | 89.9                | 103.9    | 143.9     | 102.5     | 105.4   |
| 240 μm   | 91.0                | 106.3    | 143.3     | 96.5      | 113.5   |

#### 6.4. EFFECT OF NANO-CaCO<sub>3</sub> ON MECHANICAL PROPERTIES OF UHPC

Effect of nano-CaCO<sub>3</sub> content on compressive and flexural strengths of UHPC made with 2% of steel fibers were evaluated.

**6.4.1. Compressive Strength.** Figure 6.14 compares the effect of nano-CaCO<sub>3</sub> content on 28 d compressive strength of UHPC reinforced with 2% steel fibers. The 28-d compressive strength of the UHPC reference specimen (NC0-2) was 142.2 MPa. It increased by 2% and 10% when 1.6% and 3.2% nano-CaCO<sub>3</sub> were incorporated, respectively. The improvement in compressive strength correlated with nano-CaCO<sub>3</sub> was limited because UHPC is extremely dense with a large amount of fine particles acting as filler and high rigidity associated with steel fibers.

With greater nano-CaCO<sub>3</sub> content, the compressive strength showed a decreased tendency. The compressive strengths of NC4.8-2 and NC6.4-2 specimens were 138.3 and 125.1 MPa, respectively, which were decreased by 3% and 12% in comparison with the reference samples. Therefore, UHPC with 3.2% NC obtained the highest compressive

strength, which is in good agreement with fiber-matrix bond properties and MIP results. Camilette et al. [142] indicated that UHPC samples replaced with 5% NC, by mass of cement, obtained the highest compressive strength. However, the compressive strength decreased when the NC content increased to 10%. The optimal NC content by the mass of cement in this study corresponded to 4%, which was very close to the content in Ref. [142]. Although similar flowability was kept for the five UHPC mixtures, the viscosity increased with the increase in nano-CaCO<sub>3</sub> content. This can introduce pores and cracks and increase the porosity of samples so as to decrease the compressive strength [146].

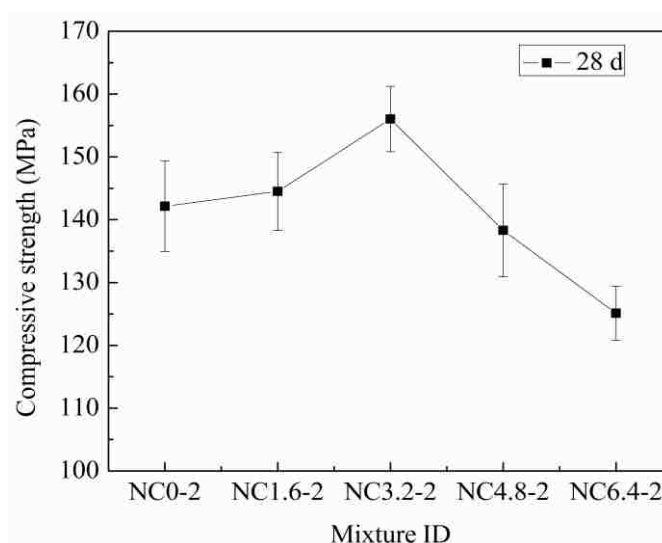


Figure 6.14. Compressive strength of UHPC with different nano-CaCO<sub>3</sub> contents

**6.4.2. Flexural Behavior.** The influence of nano-CaCO<sub>3</sub> content on the flexural behavior of UHPC is illustrated in Figure 6.15. Initially, the five UHPC mixtures showed a similar linear branch after applying the flexural load. Afterward, they displayed different peak load values. NC3.2-2 exhibited the highest peak load of 20,974 N,

followed by that of NC1.6-2 and then NC0-2. The incorporation of 4.8% and 6.4% nano- $\text{CaCO}_3$  led to a decrease in peak load, which were 14,639 and 15,198 N, respectively.

Beyond the peak load, the curves showed continuous zig-zag patterns, indicating enhanced toughness associated with the fibers. The decrease in load within a pattern was due to pullout of fibers in the specified section. With these fibers gradually being pulled out, the load was transferred to the fibers at the upper section along the cracking propagation path and then increased to a certain stage. A high deflection of 10 mm was reached to get a low constant load, which suggests good ductility.

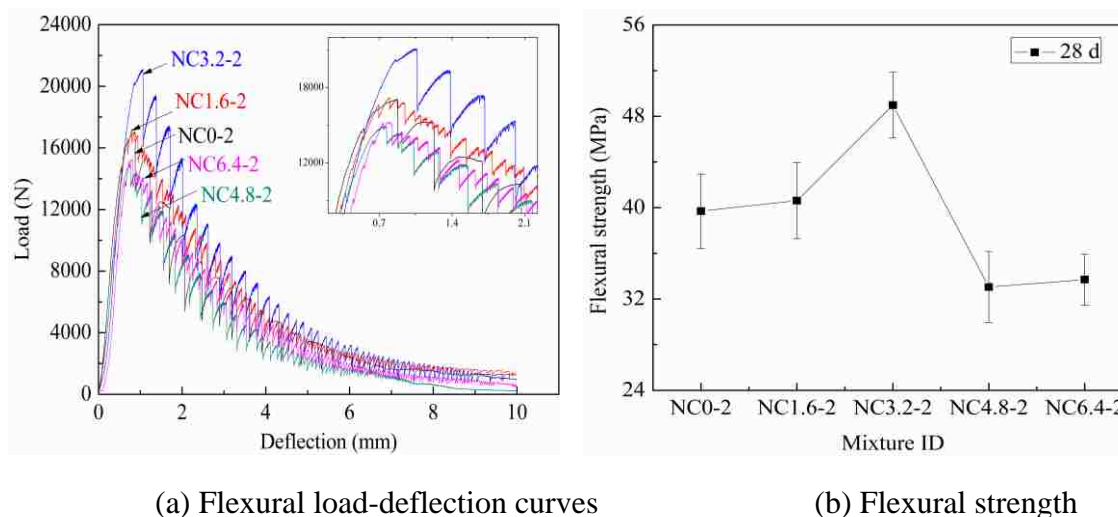


Figure 6.15. Flexural load-deflection curves of UHPC with different nano- $\text{CaCO}_3$  contents

From Figure 6.15(b), it can be seen that the flexural strength increased with nano- $\text{CaCO}_3$  content first but then decreased when the dosage exceeded 3.2%. The flexural strength of UHPC without nano- $\text{CaCO}_3$  at 28 d was 40.6 MPa and increased by 23% when 3.2% nano- $\text{CaCO}_3$  was used. The improvement in flexural behavior was much greater than the compressive strength. However, when the high nano- $\text{CaCO}_3$  content was



used, the flexural strength decreased to 33.0 MPa, which was 19% lower than that of the reference specimen. This was consistent with the fiber bond properties and compressive strength of UHPC.

## 6.5. DISCUSSION

The results presented in this study indicated that the fiber-pullout behavior, compressive strength of matrix (without fiber), and mechanical properties of UHPC increased initially with the increase of nano-CaCO<sub>3</sub> content. However, when the nano-CaCO<sub>3</sub> content exceeds a certain value (3.2%), all the aforementioned parameters showed a decreased tendency. Some mixtures even exhibited a lower strength than that of the reference specimen. The incorporation of nano-CaCO<sub>3</sub> can reduce the porosity and refine the pores due to physical effect through acting as filler and providing nucleation sites. As demonstrated by MIP results, the pore volume with an apparent diameter less than 50 nm was increased from 33% to 70%, while those pores larger than 5  $\mu$ m decreased from 60% to 30% with the addition of nano-CaCO<sub>3</sub>. Nano-CaCO<sub>3</sub> can be absorbed onto C-S-H and/or fiber to increase the content and optimize the microstructure of C-S-H, and enhance frictional bond to render greater fiber-matrix bond strength. As observed from BSEM images, cohesive failure occurred in the samples with nano-CaCO<sub>3</sub>, while adhesive failure presented in the reference sample. Meanwhile, nano-CaCO<sub>3</sub> can react with C<sub>3</sub>A to form hemi- and/or mono-carboaluminate and also stabilize ettringite, thus leading to an increased volume of hydrates and eventually greater strength [163].

However, when the nano-CaCO<sub>3</sub> content exceeds a certain value (3.2%), the agglomeration of nano-CaCO<sub>3</sub>, increased viscosity, and reduced flowability of the

mixture can result in more cracks and air voids near the embedded fibers and aggregates. Such cracks and air voids are triggers for the failure of concrete, which can lead to a reduction in fiber-matrix bond properties and eventually decrease in mechanical properties of UHPC. Therefore, appropriate nano-CaCO<sub>3</sub> content should be used to secure dense microstructure and desired strength and toughness of UHPC.

## 6.6. SUMMARY

This paper presented a multi-investigation on the effect of different nano-CaCO<sub>3</sub> contents on microstructure, fiber pullout behavior, and mechanical properties of UHPC reinforced with 2% steel fibers at curing age from 1 to 91 d. The nano-CaCO<sub>3</sub> contents varied from 0 to 6.4%, by the mass of cementitious materials. Based on the results from this study, the following conclusions can be drawn:

(1) The incorporation of suitable nano-CaCO<sub>3</sub> could significantly enhance the interfacial bond properties between embedded fibers and UHPC matrix. The interfacial bond strength and pullout energy increased first with the increase of nano-CaCO<sub>3</sub> content, then decreased when a critical value of 3.2% was exceeded. The bond strength and pullout energy were improved by 45% and 200%, respectively, in comparison with the reference specimen at 28 d standard curing.

(2) The bond strength was significantly improved from 1 to 7 d, but was almost mature after 28 d of standard curing. The bond strength and pullout energy can be efficiently predicted given the curing time and nano-CaCO<sub>3</sub> content using the response surface methodology.

(3) The compressive and flexural strengths of UHPC made with 2% steel fibers increased with the incorporation nano-CaCO<sub>3</sub> particles, but decreased when excessive nano-CaCO<sub>3</sub> was used. UHPC with 3.2% nano-CaCO<sub>3</sub> particles reached the highest compressive and flexural strengths, which were 10% and 23%, respectively, greater than those of the reference specimen under 28 d standard curing. This suggests nano-CaCO<sub>3</sub> was efficient in enhancing the efficiency of fiber-matrix stress transfer.

(4) Appropriate nano-CaCO<sub>3</sub> content decreased porosity and transformed adhesive failure into cohesive failure, as verified by MIP and BSEM observation. Besides, nano-CaCO<sub>3</sub> can react with C<sub>3</sub>A to form hemi- and/or mono-carboaluminate and also stabilize ettringite, thus leading to an increased volume of hydrates and eventually greater strength. However, excessive nano-CaCO<sub>3</sub> content increased the porosity of matrix and introduced weak interface due to agglomeration issues.

## 7. UNDERSTANDING MECHANISM UNDERLYING STRENGTH ENHANCEMENT OF UHPC MODIFIED WITH NANO-SiO<sub>2</sub>

### 7.1. BACKGROUND

As an intrinsically heterogeneous material, the structure of cement-based materials can be generally discretized into four multi-scale phases: nano, micro, meso, and macro [36]. The macro-properties of cement-based materials are dominated by the structure at the nano-scale level. The main hydration product, C-S-H, occupies at least 60%-70% by volume of the hardened cement paste. It is a nano-scale material with average diameter around 10 nm [157]. It is suggested that C-S-H has low, high, and ultra-high density forms with different hardness and elastic modulus values and volume fractions [158]. High-density C-S-H degrades much slower than low-density C-S-H under external environmental condition [158]. Furthermore, water loss from pores in the C-S-H gel can lead to considerable autogenous shrinkage, which can cause cracking and loss of strength and durability of UHPC matrix [159]. Therefore, it is vital to optimize the microstructure of cement-based materials from the nano-scale to ensure high performance.

The incorporation of nano-particles exhibited the following effect to densify the microstructure and improve the properties of cement-based materials. Firstly, the filler effect - filling pores due to very fine particle size to enhance packing density of the system [160]. Secondly, the seeding or nucleation effect - providing nucleation sites for the formation of C-S-H seeds. Additional chemical effect- forming certain new substances to increase the volume of hydration products. Rong et al. [160] found that nano-SiO<sub>2</sub> accelerated the hardening and enhanced mechanical properties of UHPC when

3% nano-SiO<sub>2</sub>, by mass of cementations materials, was incorporated. Ghafari et al. [161] reported that nano-SiO<sub>2</sub> reduced the workability of UHPC and increased compressive strength, especially at an early age. Although nano-SiO<sub>2</sub> could improve mechanical properties, their hydration mechanisms, hardening processes, and age dependencies are different depending on mixture proportion, use of SP type and dosage [162]. This could lead to different hydration products and thereby change in mechanical properties [147,163,164]. Based on literature review, no information focuses on the contribution of nano-SiO<sub>2</sub> on the interfacial bond properties between fibers and UHPC.

In order to understand the mechanisms behind strength enhancement of UHPC made with nano-SiO<sub>2</sub>, the compressive strength of UHPC matrix, fiber-matrix bond, and mechanical properties of UHPC with five different nano-SiO<sub>2</sub> contents were investigated. Pore structure and air void of the samples were investigated by mercury intrusion porosimetry (MIP) and 3D micro-tomography, respectively. Backscatter scanning electron microscopy (BSEM) and micro-hardness measurement were employed to evaluate the microstructural features associated with the matrix and/or interface. The study seeks to understand the mechanism underlying strength enhancement of UHPC improved with nano-SiO<sub>2</sub>.

## **7.2. EFFECT OF NANO-SiO<sub>2</sub> ON FIBER-MATRIX BOND PROPERTIES OF UHPC MATRIX**

Figure 7.1 shows the effect of nano-SiO<sub>2</sub> content on pullout load-slip curves of embedded fibers in UHPC matrix at 3 and 91 d. Generally, the pullout behavior can be divided into four distinct regions, including well bonded region (OP), partially debonded

region (PQ), fully debonded region (QR), and fiber pullout/slip region (RS), as illustrated in Figure 7.2 [165,166].

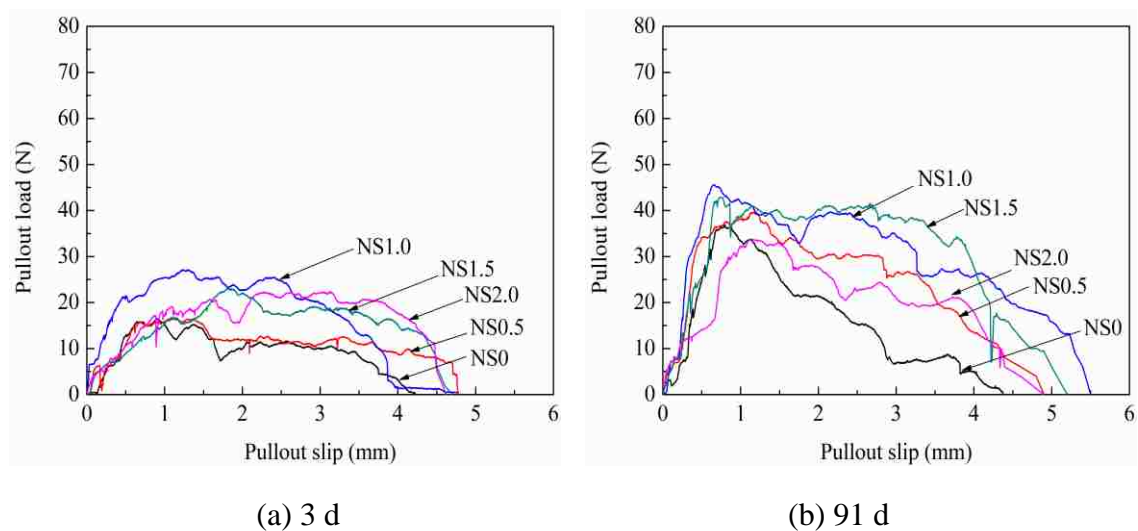


Figure 7.1. Pullout load-slip curves of embedded fibers in UHPC matrix with different nano-SiO<sub>2</sub> contents

At the well-bonded region, the pullout load increases linearly with slip at low slip values. The resistance in this stage is provided by adhesion or chemical bond with surrounding UHPC matrix [167]. When the peak load was achieved, the load began to decrease. However, the mixtures with nano-SiO<sub>2</sub> did not show suddenly and dramatically drop of the load with the increasing of slip from approximately 1 to 3 mm. This can be due to high frictional coefficient and fiber surface pressure associated with higher matrix packing density from the surrounding mortar [59, 168]. In this range, fibers were gradually debonded and pulled out from the UHPC matrix with the occurrence of micro-cracking at the ITZ. Once the fibers were fully debonded from the matrix (point R in Figure 7.2), the pullout behavior is mainly governed by friction stress, which is a

combined action of abrasion and compaction of cement and sand particles surrounding the fibers [168]. The friction shear stress decreased with the increase of slip due to the crumbling of cement matrix and a decrease of the roughness of the failure surface [168].

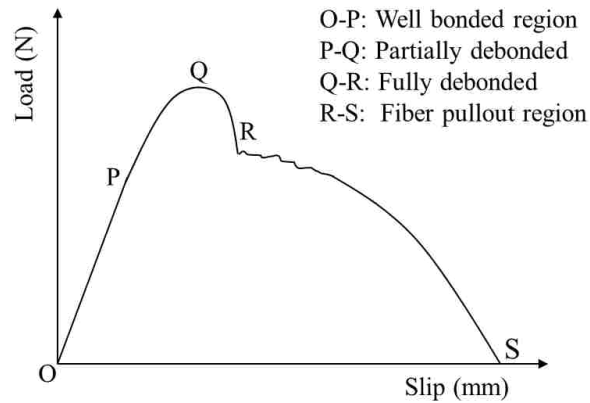


Figure 7.2. Typical pullout load versus slip relationship [182]

Figure 7.3 illustrates the effect of nano-SiO<sub>2</sub> content on bond strength of fiber-matrix interface and compressive strength of UHPC matrix. As can be seen from Figure 7.3(a), the bond strength increased with the increase of nano-SiO<sub>2</sub> content from 0 to approximately 1%, but then decreased at a higher content. For the NS2.0 matrix, the bond strengths were reduced to comparable values as that of the NS0.5 matrix. Therefore, the optimal nano-SiO<sub>2</sub> content for bond strength can be considered to be 1%. The mini-slump flow of UHPC matrix incorporated with 1% nano-SiO<sub>2</sub> was 190 mm. This value dropped to 150 mm at 2% nano-SiO<sub>2</sub>. Agglomeration issues associated with excessive nano-SiO<sub>2</sub> dosage can lead to some weak zones in the internal structure of concrete [169].

As can be also seen from Figure 7.3(a), bond strength increased considerably at an early age up to 7 d, and increased slightly afterward until the age of 91 d. The bond

strength of the NS1.0 mixture at 1 d was approximately 2 MPa, it increased to 3.5 MPa at 7 d and to approximately 4 MPa at 91 d. Chan and Chu [33] investigated the fiber-matrix bond strength of reactive powder concrete at a W/CM ratio of 0.21 to 0.23 under 3-d high-temperature curing. The bond strength for nine fibers with an embedded fiber length of 10 mm was 5.5 MPa. Greater bond strength in that research was because of the change in C-S-H structure associated with higher temperature curing [170,171]. The bond strength in this research agrees well with the change in the compressive strength of the UHPC matrix, as illustrated in Figure 7.3(b). Generally, the higher the compressive strength of the matrix is, the greater the bond strength would be [55]. Nano-SiO<sub>2</sub> particles can increase the heat of hydration due to filler effect and pozzolanic activity [146], and thus densifying the microstructure and improve early-age mechanical properties [160].

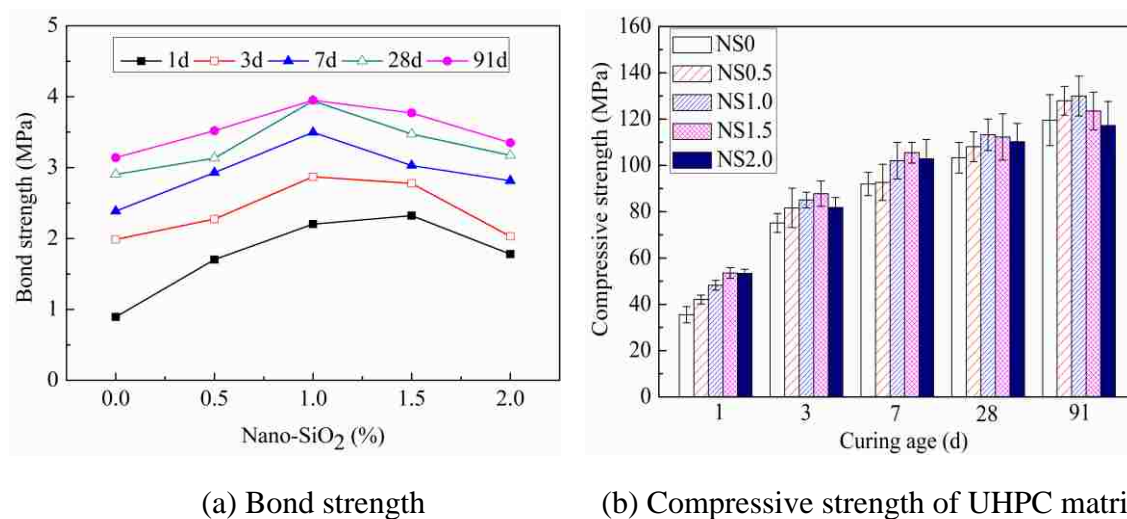


Figure 7.3. Effect of nano-SiO<sub>2</sub> content on bond strength of fiber-matrix interface and compressive strength of UHPC matrix



### 7.3. MECHANICAL PROPERTIES OF UHPC WITH 2% STEEL FIBERS

The effect of different and contents of nano-SiO<sub>2</sub> content on mechanical properties of UHPC made with 2% steel fibers is illustrated in Figure 7.4. The compressive and flexural strengths of UHPC were improved with the increase of nano-SiO<sub>2</sub> contents up to 1.0 %. The incorporation of 1% nano-SiO<sub>2</sub> was shown to improve the compressive and flexural strengths by 6% and 12%, respectively. The improvement in flexural strength was greater than that of the compressive strength because of optimization of the fiber-matrix interaction. However, the compressive and flexural strengths of UHPC made with the further content of nano-SiO<sub>2</sub> were reduced. At a higher content of nano-particles (NS2.0 mixture), the compressive and flexural strengths were even lower than those of the reference specimens.

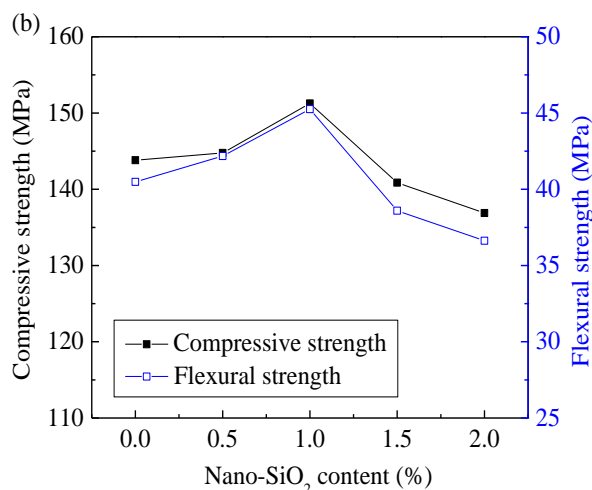


Figure 7.4. Effect of nano-SiO<sub>2</sub> content on compressive and flexural strengths of UHPC

Similar observation was reported by Ghafri et al. [172], who investigated the effect of nano-SiO<sub>2</sub> addition (0, 1%, 2%, 3%, and 4%) on strength of UHPC. The authors

found that the highest compressive strength was obtained at 3% nano-SiO<sub>2</sub>, by mass of cement. The optimal content of nano-particles depends on several factors, including W/CM, mixture proportion, type and content of superplasticizer, and nano-particle type and size.

#### 7.4. EFFECT OF NANO-SiO<sub>2</sub> ON MICROSTRUCTURE OF UHPC

MIP, 3D tomography, BSEM observation, and micro-hardness were used to characterize the microstructure of UHPC matrix.

**7.4.1. MIP Results.** Figure 7.5 illustrates the effect of nano-SiO<sub>2</sub> and curing age on total porosity of UHPC matrix. As can be seen from Figure 7.5(a), the porosity of matrix at 1 d decreased with the nano-SiO<sub>2</sub> content increasing to 1% but then increased when more nano-SiO<sub>2</sub> was used. This is in good agreement with the bond properties. Due to filling and nucleation effects of nano-SiO<sub>2</sub>, the pore structure of UHPC matrix can be refined.

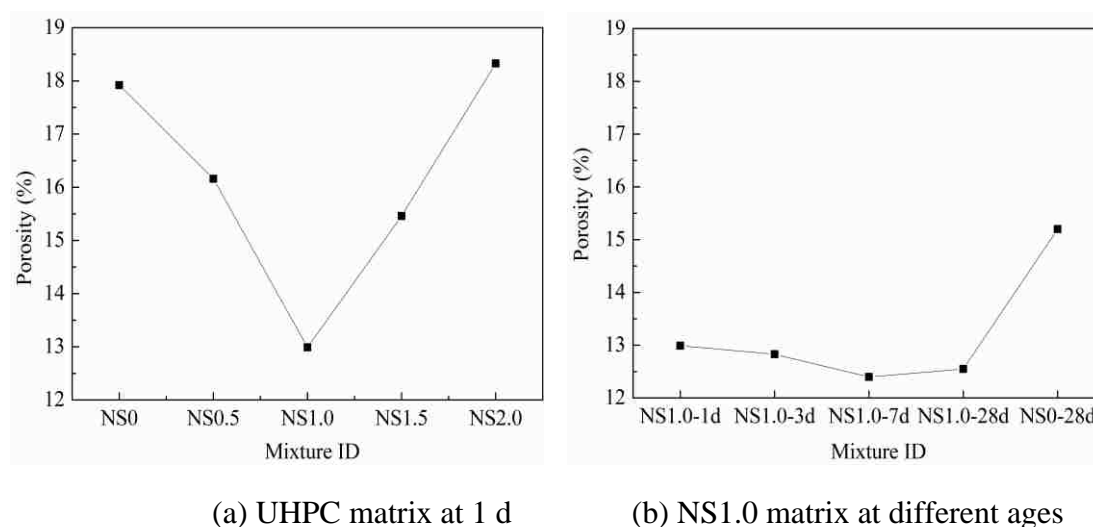


Figure 7.5. Effect of nano-SiO<sub>2</sub> content and curing age on total porosity of UHPC matrix

However, increased viscosity and agglomeration issues associated with more addition of nano-SiO<sub>2</sub> could introduce air bubbles, thus leading to increased porosity [160]. This is consistent with the findings reported by others [160]. The optimal nano-SiO<sub>2</sub> content can depend on many factors, such as W/CM, mixture proportion, chemical admixture, and nano-particle type [173]. Therefore, the optimal nano-SiO<sub>2</sub> content in this research was 1% by mass of cementitious materials.

Curing age exerted a limited effect on the porosity of NS1.0, as illustrated in Figure 7.5(b). The porosity of the NS1.0 matrix at 1 d was 13%, it slightly decreased to 12.5% at 7 and 28 d. Because of high surface energy originated from fine nano-SiO<sub>2</sub> particles, chemical effect can be rapidly released at very early age. The addition of 1% nano-SiO<sub>2</sub> could decrease the porosity by 29% and 19% compared to the reference sample at 1 and 28 d, respectively. Rong et al. [160] reported that the porosity of ultra-high performance cementitious composites with 3% nano-SiO<sub>2</sub> at 28 d was reduced by 25%.

Figure 7.6 shows the pore volume distribution of UHPC matrix, which includes gel micro-pores (< 10 nm), meso-pores (10-50 nm), middle capillary pores (50-100 nm), large capillary pores (100-5000 nm), and macro-pores (>5000 nm) [118]. As shown in Figure 7.6(a), there were equivalent pore volumes of 25% for meso-pore, middle capillary pore, large capillary pore, and macro-pore in the reference mixture (NC0) at 1 d. The incorporation of nano-SiO<sub>2</sub> particles resulted in refinement of the microstructure with increased volume of meso-pores (10-50 nm) by 70%. Besides, the nano-SiO<sub>2</sub> particles confined the volume of the 50-5000 nm pores to a limited value of 7% to 13%.

From Figure 7.6(b), it can be seen that the volume of 10-50 nm pores decreased with age due to further hydration, while the gel micro-pores with diameter less than 10 nm increased. The volume of meso-pores at 1 d was 65%, it decreased to 10% at 28 d. It was reported that the gel micro-pores correspond typically to gel pores in the C-S-H with water held by hydrogen bond [174]. This suggests that nano-SiO<sub>2</sub> can make the microstructure of UHPC denser and render it more homogeneous given the extremely fine particle size of the nano-SiO<sub>2</sub> and formation of C-S-H associated with pozzolanic effect. Moreover, the volume of 50-5000 nm pore was confined to a very small volume, which was 3% to 7% only.

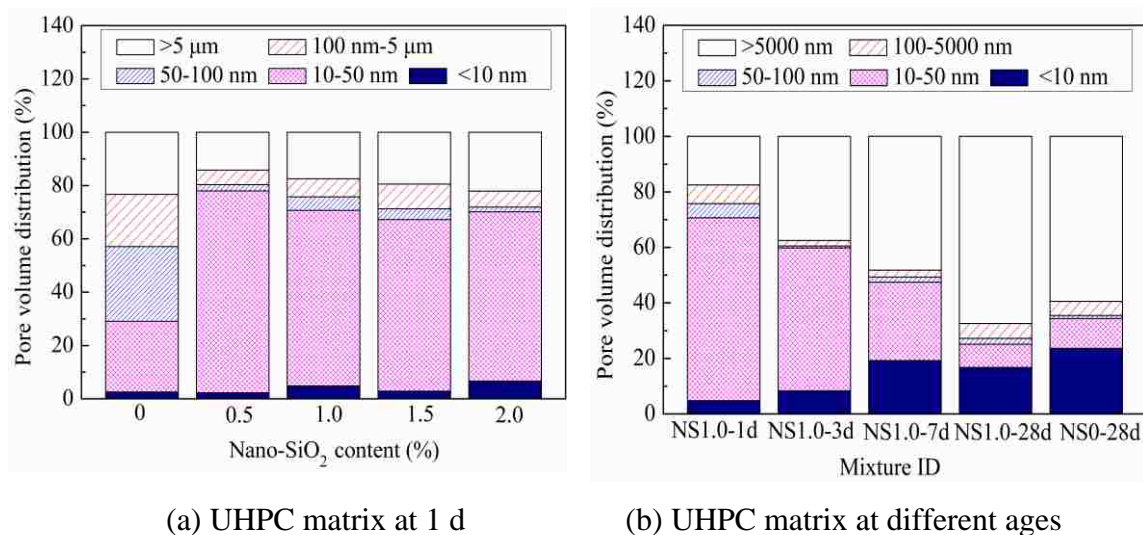


Figure 7.6. Pore volume distribution of UHPC matrix made with different nano-SiO<sub>2</sub> contents and at various ages

**7.4.2. 3D Micro-Tomography.** The distribution of steel fiber, aggregates, and air voids can be visualized and evaluated using 3D micro-tomography, which can be used to investigate the microstructure and property relationship. Figure 7.7 presents the typical

3D images of the NS0 sample, respectively, each containing an embedded fiber after pullout testing. The whole, top, right, and front views of each sample were presented. The density difference and defect volume of the mixtures were presented by the color difference. The cementitious matrix of the sample are displayed in grey, and the aggregates appear in black, while the defect areas are presented in blue, green, and orange, depending on defect volume. Through image analysis, the void distribution in samples was non-homogeneous with defects irregularly dispersed. Under loading, cracking would be initiated at such defects and propagates further along the weak lines [175].

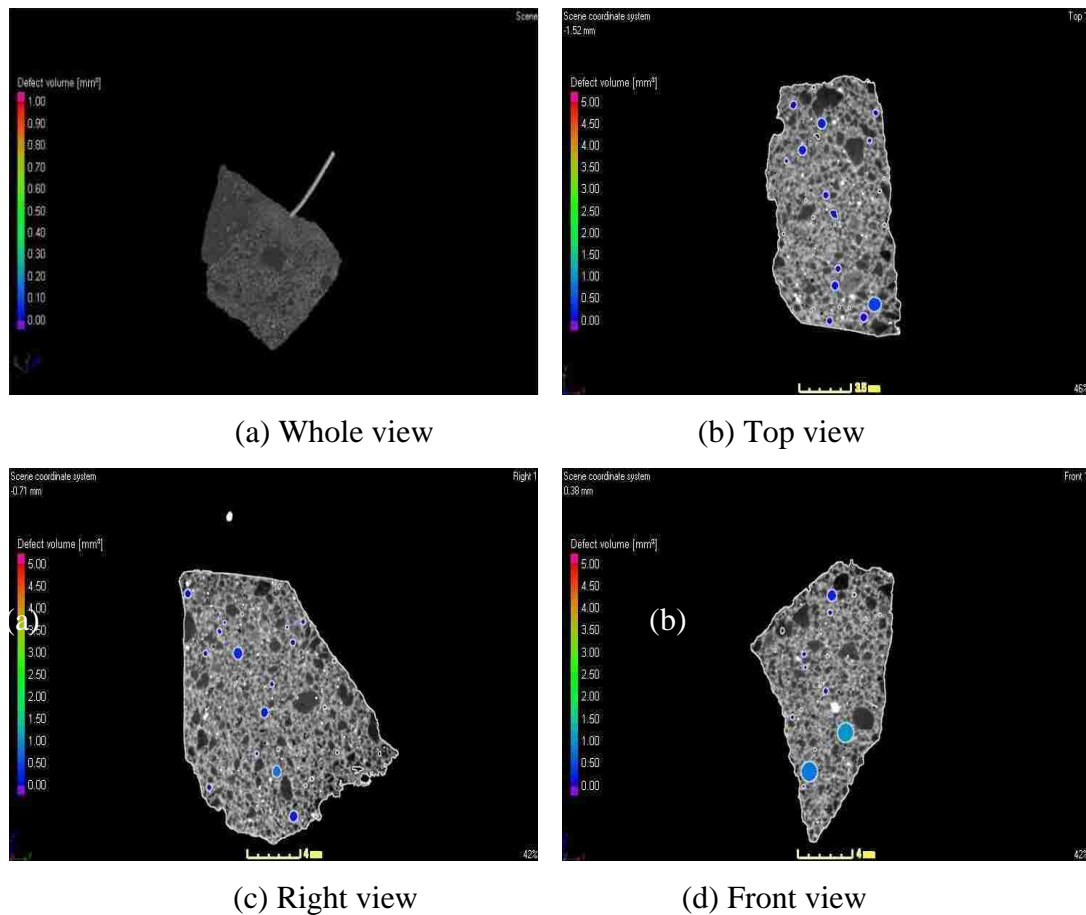


Figure 7.7. 3D micro-tomography of the reference sample (NS0) with an embedded fiber at 28 d after fiber pullout testing

The material volume, void volume, void surface, voids at X, Y, and Z plane, and calculated void content in typical samples with and without nano-particles are summarized in Table 7.1.

Table 7.1. Void distribution in UHPC matrix with and without nano-SiO<sub>2</sub> observed from 3D micro-tomography

| Mixture      | Material volume (mm <sup>3</sup> ) | Void volume (mm <sup>3</sup> ) | Void content (%) | Void surface (mm <sup>2</sup> ) | Void at X plane (mm <sup>2</sup> ) | Void at Y plane (mm <sup>2</sup> ) | Void at Z plane (mm <sup>2</sup> ) |
|--------------|------------------------------------|--------------------------------|------------------|---------------------------------|------------------------------------|------------------------------------|------------------------------------|
| NS0 - 28 d   | 1111.5                             | 16.9                           | 1.5              | 366.6                           | 60.7                               | 64.5                               | 62.3                               |
| NS1.0 - 28 d | 767.8                              | 9.9                            | 1.3              | 246.0                           | 42.8                               | 41.6                               | 42.0                               |
| NS2.0 - 28 d | 661.3                              | 13.6                           | 2.0              | 321.1                           | 54.6                               | 56.0                               | 54.0                               |

It can be seen that the incorporation of a suitable content of nano-particles reduced the volume of weak zones from 1.5% to 1.2%, but excessive nano-particle content reversely increased the air voids to 2%. Appropriate nano-particles can fill pores to reduce void proportion and to render more homogeneous internal structure and fiber-matrix interface [175]. However, too much nano-particles can introduce more defect zones and weaker interfacial zone due to agglomeration issues, which is more vulnerable to strength loss under loading. This explains why the compressive and flexural strengths of UHPC increased first but decreased with the increase of nano-particle content.

#### 7.4.3. BSEM Observation of UHPC Matrix with and without Nano-SiO<sub>2</sub>.

Figure 7.8 shows the SEM observation of UHPC matrix made with and without nano-particles. In the reference sample (NC0), a non-homogeneous cementitious matrix with

clusters of unshaped hydration products was observed. The nano-SiO<sub>2</sub> provides nucleation sites for the formation of fiber-like C-S-H, as observed in Figure 7.8(b), which can tightly bond with C-S-H gel particles. Abundant round nuclei were observed with particle size in the range from 1 to 6 μm, which were gradually grown into larger regular ones with the prolongation of hydration time.

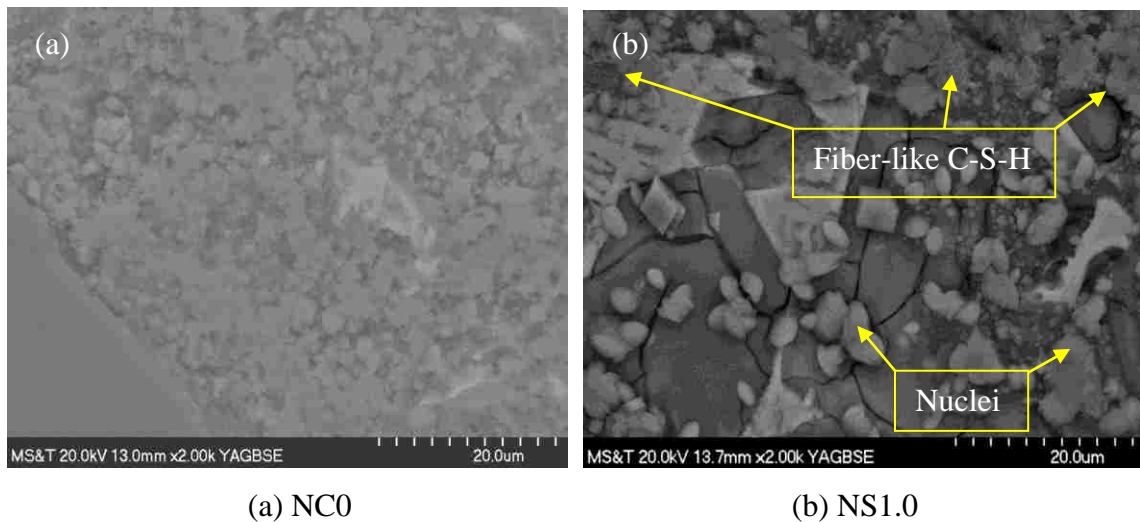


Figure 7.8. BSEM observation of UHPC matrix with and without nano-particles

**7.4.4. BSEM Observation of Fiber-Matrix Interface.** BSEM images of an embedded fiber in different UHPC matrices are shown in Figure 7.9. BSEM images can indicate different grey levels of unhydrated cement and hydration products, which vary with the atomic numbers. The unhydrated grains appear brighter than hydration products, and pores appear darker [176,177]. As observed from Figure 7.9, the unhydrated cement particles in the UHPC matrix decreased with curing time. There were a lot of unhydrated cement particles in the NS1.0 sample, especially at 1 d. The microstructure around the embedded fiber within the distance of 50 μm from the fiber surface was more porous than

that in the NS1.0 matrix at 7 d. The porous zone around the fiber at 7 d might due to bleeding and/or wall effect, which can reduce the contact area with the matrix, and thus the bond properties [178].

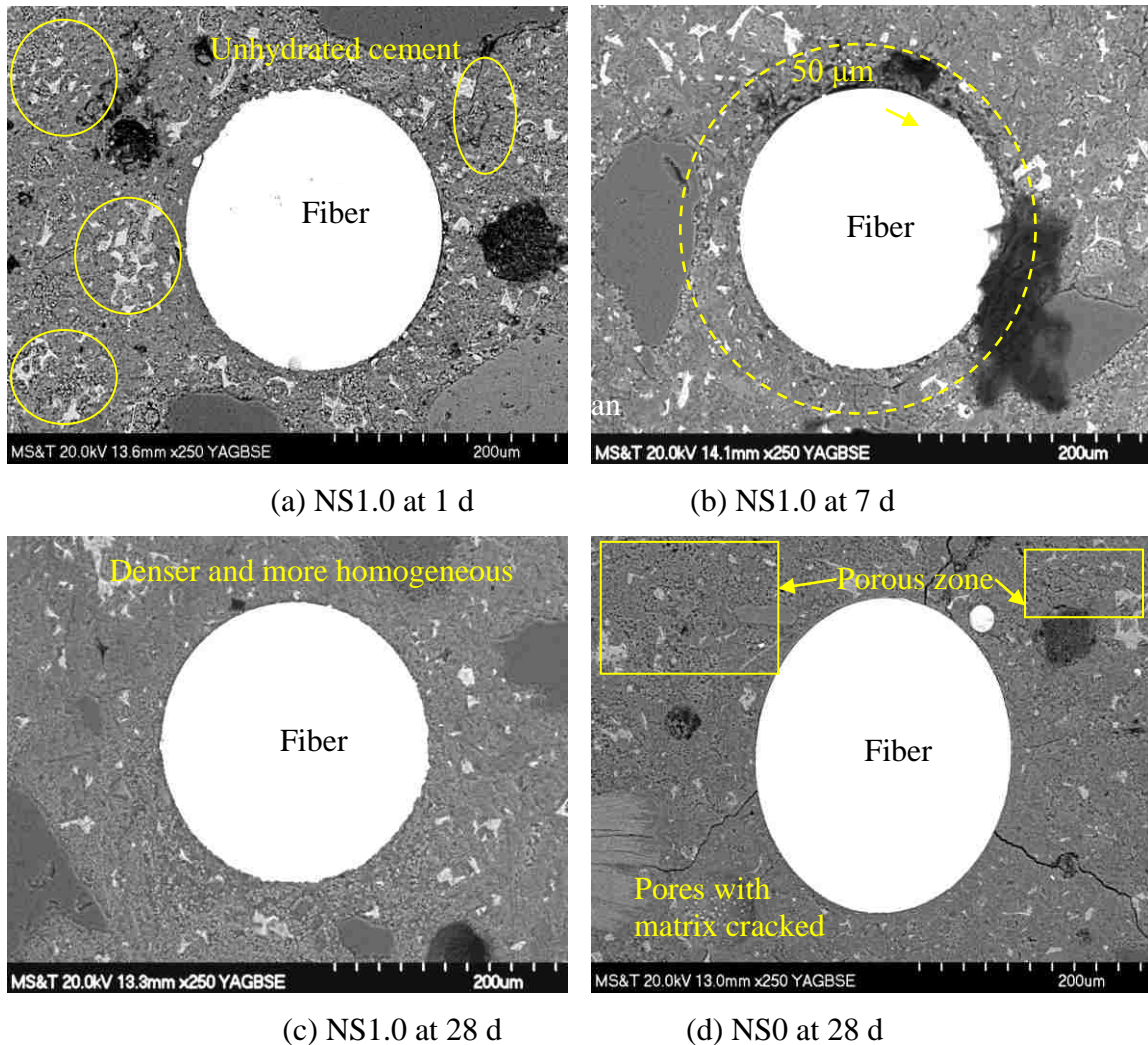


Figure 7.9. BSEM images of UHPC made with 0 and 1% nano-SiO<sub>2</sub> with an embedded fiber

No obvious ITZ was observed around the fiber in both the NS1.0 and the NS0 matrices at 28 d. However, more porous zone was observed in the NS0 sample (Figure 6.4 d), while denser and more homogeneous matrix exhibited in the NS1.0 sample. There



were micro-cracks propagating from the fiber edge into the NS0 matrix. This may be formed during sample preparation. Micro-hardness testing was conducted on the same sample in the vicinity of fiber (within 240  $\mu\text{m}$  to the edge of the fiber) to validate the homogeneity of the stiffness of hydration products. These results are discussed in Section 7.4.6.

Surface plots of BSEM images are illustrated in Figure 7.10. These plots reflect the roughness quality of the polished samples shown in Figure 7.10. The difference in roughness between fiber and UHPC matrix of approximately 200  $\mu\text{m}$  was observed due to the very high stiffness of the fiber compared to that of the matrix.

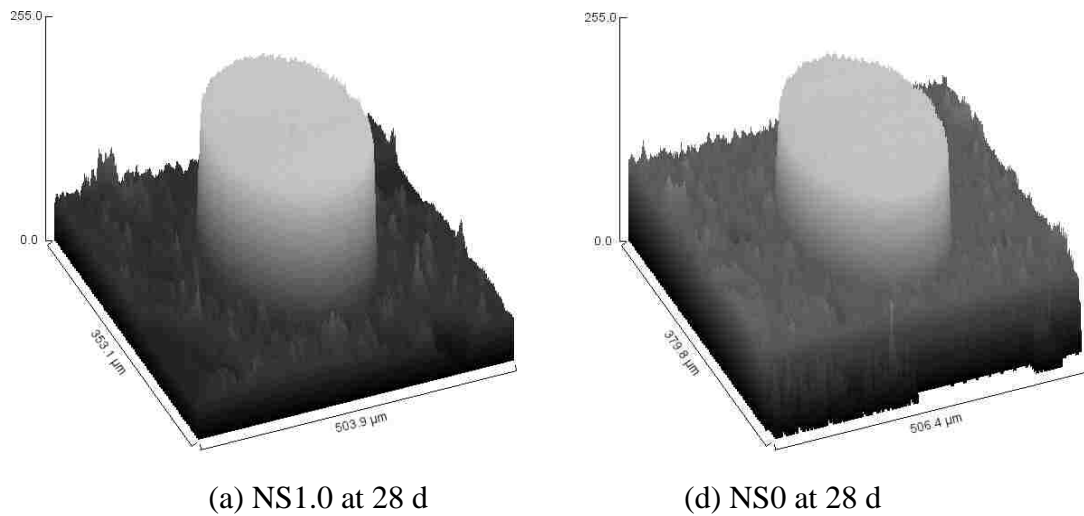


Figure 7.10. Surface plot of UHPC sample with an embedded fiber

**7.4.5. Element Mapping of Fiber-Matrix Interface.** Polished samples with embedded fibers obtained from various UHPC mixtures after the pullout testing were subjected to chemical element mapping. The results of the element mappings of the reference mixture NS0 are shown in Figure 7.11.

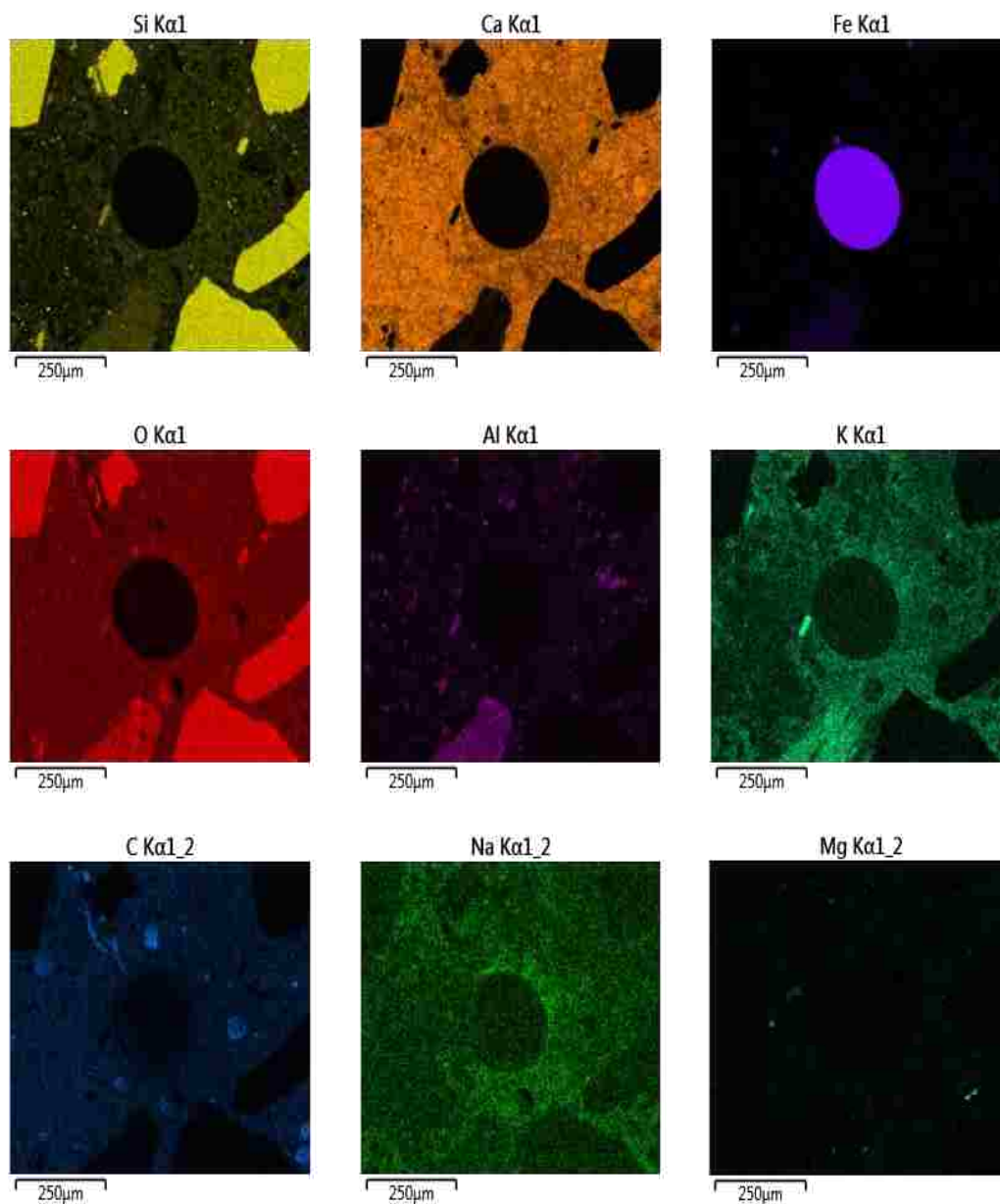


Figure 7.11. Element mappings of fiber-matrix interface in the reference mixture NS0

The distribution of various elements, including Fe, Al, Si, Ca, K, O, C, Na, and Mg, at the fiber-matrix interface, was determined. The primary elements around the steel fiber were Ca, Si, O, and K in addition to small amounts of Al, Mg, and Na. Through element identification, the irregular bright particles in the Si image (Figure 7.11) were

identified as sand, while the circular area in the middle of that image corresponds to steel fiber. The remaining part of the image was cementitious matrix.

Images of the main elements, including Ca, Si, and Fe, at the fiber-matrix interface in the NS1.0 mixture are presented in Figure 7.12. Generally, the brighter the area is, the greater content and purer element would be. The Si image in the NS1.0 mixture was brighter than that in the reference mixture. This indicated that the Si element in the NS1.0 mixture because of corresponding rich sources from nano-SiO<sub>2</sub>. These are good implications of changes in Ca/Si ratio of C-S-H, which can mainly affect the fiber-matrix bond and mechanical properties of UHPC [179].

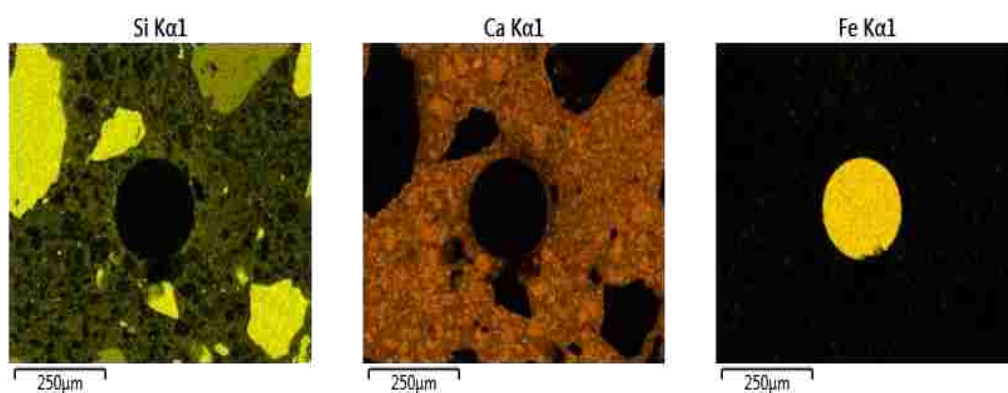


Figure 7.12. Element mappings of fiber-matrix interface in the NS1.0 mixture

Figures 7.13 and 7.14 present the morphology of fiber-matrix interface and element atomic distribution along the indicated scanning lines that started from the fiber surface into the matrix. The main elements along the scanning line are found to be Fe and O. Within a distance of 50  $\mu\text{m}$  to the left starting point (0  $\mu\text{m}$ ), Fe and C were the primary elements, indicating the steel fiber zone. Beyond this zone, the atomic percentage of Fe significantly decreased to nearly zero, whereas the O, Ca, and Si elements predominated,

suggesting a layer of cement paste. During the line scanning, the aggregate was avoided to prevent interference of the results because of its richness in Si. In the references mixture (NC0), the atomic percentage of Ca was greater than that of the atomic percentage of Si, indicating an increased Ca/Si ratio. The atomic percentage of Ca was found to occupy about 15% to 40% of the total atomic percentage along the scanning line, while the Si atomic takes up to 10%-20%.

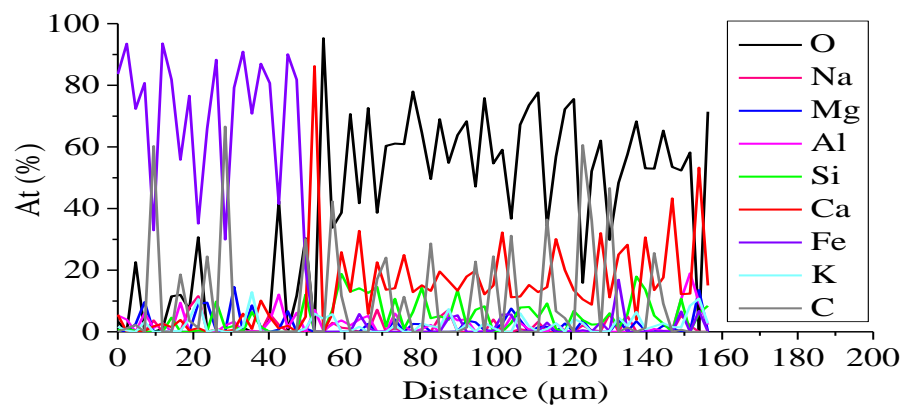
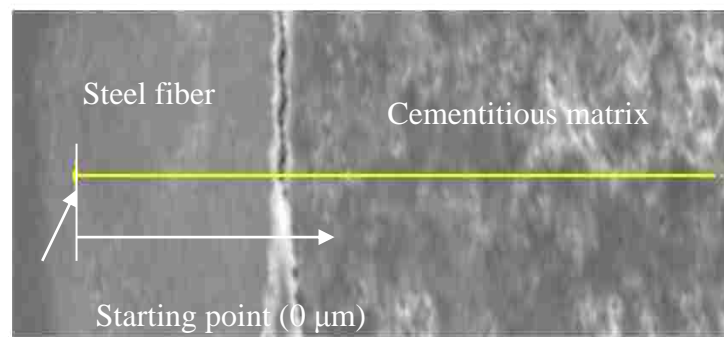


Figure 7.13. Morphology and element atomic number distribution along the scanning line in the NS0 mixture

In the NS1.0 mixture depicted in Figure 7.11, the atomic percentages of the Si were greater than that of the Ca, except the area beyond 130  $\mu\text{m}$  distance.

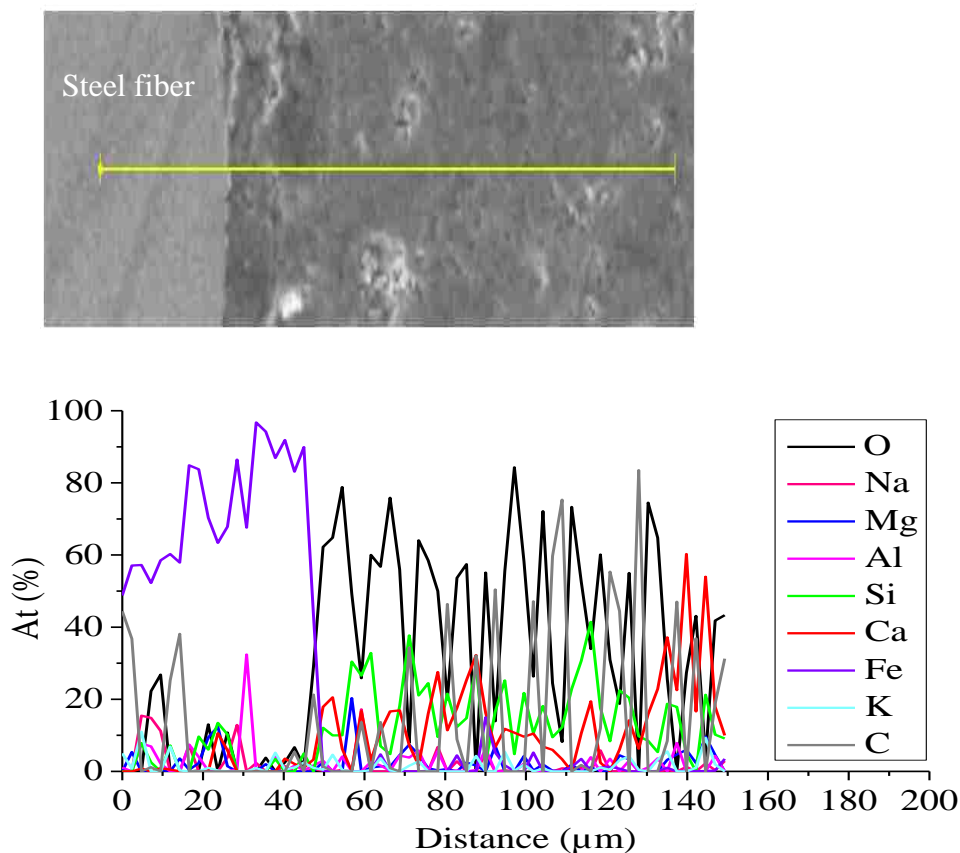


Figure 7.14. Morphology and element atomic number distribution along the scanning line in the NS1.0 mixture

The atomic percentages of Ca and Si took up to 5%-40% and 10%-50%, respectively. This suggests the decreased Ca/Si ratio of the hydration products associated with Si element from nano-SiO<sub>2</sub>. The decrease in Ca/Si ratio can lead to longer silica chain length, resulting in improved mechanical properties of the C-S-H, including elastic modulus and hardness [180]. Pelisser et al. [179] indicated that the elastic modulus and hardness of synthesized C-S-H increased with the decreased of Ca/Si ratio. The mean Ca/Si ratio of C-S-H gel in OPC paste was reported to vary from 1.2 to 2.1 and can decrease with the decrease in W/CM, use of supplementary cementitious materials, and increase in curing temperature [181].

**7.4.6. Micro-Hardness of Matrix around Fiber.** Table 7.2 summarizes the micro-hardness results of the UHPC matrix that were obtained at different distances from the fiber edge. The measurements were conducted on the same sample used for BSEM observation. The micro-hardness of fiber was 770-790 HV. With the increase of distance from the fiber edge, the micro-hardness value of the matrix increased. For example, in the NS1.0 sample at 28 d, the micro-hardness of the matrix at 40  $\mu\text{m}$  from the surface was 84.1 HV. It increased to 88.6 and 100.5 HV at 80 and 120  $\mu\text{m}$ , respectively. The micro-hardness did not significantly change beyond 120  $\mu\text{m}$ . For the NS1.0 samples at 1 and 7 d, the micro-hardness within a distance of 80  $\mu\text{m}$  from the fiber edge was obviously lower than that with far distance. This was attributed to the porous microstructure as observed in Figure 7.9 (a and b).

The micro-hardness increased with prolongation of hydration time. For the NS1.0 sample at 1, 7, and 28 d, the micro-hardness at 80  $\mu\text{m}$  from the fiber edge were 82.9, 85.4, and 96.6 HV, respectively. In addition, the NS1.0 at 28 d showed greater micro-hardness compared to the reference sample NS0. This indicated that the incorporation of 1% nano-SiO<sub>2</sub> can enhance the quality of the matrix. It was suggested that bond between fibers and matrix was mainly dominated by adhesion or chemical bond, which is governed by the main hydration product C-S-H with a diameter of 10 nm [182]. In addition to the pozzolanic reaction of nano-SiO<sub>2</sub> that resulted in a greater volume of C-S-H gel, the nano-SiO<sub>2</sub> acts as nucleus for the precipitation of C-S-H. These mechanisms can lead to the better bond of the C-S-H, and thus enhancing bond properties with steel fiber and matrix.

Table 7.2. Micro-hardness of UHPC matrix within 240  $\mu\text{m}$  from the fiber edge

| No.               | Micro-hardness (HV) |          |           |         |
|-------------------|---------------------|----------|-----------|---------|
|                   | NS1.0-1d            | NS1.0-7d | NS1.0-28d | NS0-28d |
| Fiber             | 785.5               | 774.6    | 774.6     | 791.0   |
| 40 $\mu\text{m}$  | 62.2                | 66.6     | 84.1      | 79.3    |
| 80 $\mu\text{m}$  | 82.9                | 85.4     | 96.6      | 84.4    |
| 120 $\mu\text{m}$ | 85.4                | 87.9     | 100.5     | 95.2    |
| 160 $\mu\text{m}$ | 91.7                | 97.5     | 121.3     | 110.8   |
| 200 $\mu\text{m}$ | 95.3                | 98.7     | 123.5     | 105.4   |
| 240 $\mu\text{m}$ | 92.0                | 101.0    | 117.2     | 113.5   |

## 7.5. SUMMARY

This paper presented a multi-scale investigation of the effect of different nano-SiO<sub>2</sub> contents on microstructure, fiber pullout behavior, and mechanical properties of UHPC reinforced with 2% steel fibers. Four concentrations of nano-SiO<sub>2</sub>, varying from 0 to 2.0%, were chosen to prepare UHPC. A reference mixture made of 20% silica fume but without any nano-particle was used. Advanced material characterization techniques, such as scanning electronic microscopy (SEM), X-ray diffraction, and 3D micro-tomography, were employed to elucidate the mechanisms underlying the enhancement of mechanical properties of UHPC made with nano-SiO<sub>2</sub>. Based on the results presented in this study, the following conclusions can be drawn:

(1) Nano-SiO<sub>2</sub> can significantly enhance the interfacial bond properties between fibers and UHPC matrix. The bond strength and pullout energy increased first with the increase of nano-SiO<sub>2</sub> content, but then decreased when a critical value of 1% was exceeded. Such change was consistent with the compressive strength development of

matrix. The bond strength and pullout energy of UHPC matrix with 1% nano-SiO<sub>2</sub> after 28-d standard curing were enhanced by approximately 35% and 70%, respectively, when compared to the reference sample.

(2) Mechanical properties of UHPC made with different nano-SiO<sub>2</sub> contents increased initially with the increase of nano-SiO<sub>2</sub> content, but decreased when exceeding a critical value of 1%. High content of nano-SiO<sub>2</sub> resulted in great loss of compressive and flexural strengths. The values could be even lower than those of the reference specimen.

(3) Nano-SiO<sub>2</sub> could serve as nuclei for the precipitation of C-S-H, hence leading to more C-S-H content and alteration of C-S-H structure. The Ca/Si ratio in the reference sample was greater than 1. The inclusion of Si element from nano-SiO<sub>2</sub> decreased the Ca/Si ratio to a lower value, leading to longer silica chain length and eventually improved mechanical properties of the C-S-H. The addition of 1% nano-SiO<sub>2</sub> resulted in the lowest porosity of matrix associated with denser and more homogeneous microstructure. ITZ with a thickness of 50 μm was observed due to the wall and bleeding effect in correlation with lower micro-harness compared to the bulk matrix.



## 8. HOW DOES FIBER SHAPE AFFECT FIBER PULLOUT BEHAVIOR AND MECHANICAL PROPERTIES OF UHPC?

### 8.1. BACKGROUND

Several strategies can be used to improve bond properties at interfacial transition zone (ITZ) between the matrix and embedded fibers, including: (1) densification of the cementitious matrix [101,171]; (2) use of deformed fibers [59]; (3) surface treatment of fibers, such as plasma treatment for polyethylene fibers [100]. The level of the bond increase resulting from the use of deformed fibers appears to offer the highest degree of bond improvement [100]. The bond mechanism between embedded fibers and the surrounding matrix typically includes three parts: (1) adhesion or chemical bond; (2) friction; and (3) mechanical anchorage and interlock of the fiber [183]. Adhesion is initially solicited during pullout testing and is closely correlated with the properties of the ITZ. After full debonding is attained, friction and/or mechanical anchorage between the fiber and matrix play a dominant role through the slippage of fibers [184]. The use of deformed fibers can efficiently enhance bond given additional mechanical interlocking provided by the fiber geometry [40]. Several geometries of deformed fibers exist, including hooked, corrugated, flattened-end, twisted, and irregular fibers.

Pullout behavior between fiber and matrix depends on several factors, including fiber type and geometry, loading rate, matrix strength, curing condition, use of supplementary cementitious materials, embedment length and the inclination angle of the fibers. Wu et al. [132] indicated that UHPC matrix incorporated with 15%-25% silica fume after 28 d standard curing resulted in stable bond properties. Wille et al. [101] reported that the equivalent bond strengths of hooked and twisted fibers were about four

to five times higher than that of straight fibers embedded in the same UHPC matrix. Abu-Lebdeh et al. [55] suggested that the peak load and pullout energy of hooked fibers can be approximately two and a half times greater than those of straight fibers. In that research, a very-high strength concrete (VHSC) matrix with ratio W/CM of 0.16 was used. The fiber pullout was determined using a single-side pullout test. Furthermore, Abu-Lebdeh et al. [55] suggested that both the maximum pullout load and total pullout energy increased with the increase of compressive strength of the matrix given the dense microstructure of the high strength concrete. Beglarigale and Yazici [185] investigated the fiber-matrix pullout behavior in UHPC. Smooth and hooked steel fibers were used at different embedment lengths. Pullout peak loads of hooked fibers were 390%, 65%, 51%, and 38% higher than those of straight fibers with embedment lengths of 10, 20, 30, and 40 mm, respectively. In the pullout process, the hooked and corrugated fibers were subjected to plastic deformation after pullout, leading to a substantial increase in pullout behavior [186, 187].

Fiber shape greatly affects the mechanical properties, especially tensile and flexural behavior, of ultra-high performance fiber reinforced concrete (UHPFRC) [40, 188]. Wu et al. [40] reported that fiber shape had little effect on first crack strength but a considerable effect on peak load of flexural load-displacement relationship. In addition, a constitutive model was adopted to generate the relationship through normalizing the flexural load-deflection curve and it agreed well with the experimental results. Park et al. [71] suggested that UHPFRC produced with twisted fiber demonstrated the best tensile properties, whereas those with smooth macro-fibers exhibited the worst performance. Quantitative research has been done by far about the effect of fiber shape on pullout

behavior of fiber and/or mechanical properties of UHPC. However, there is a perceived lack of information on the relationship between pullout behavior and mechanical properties of UHPC. How does fiber shape affect fiber pullout behavior and hence mechanical properties of mechanical properties of UHPC remains an interesting topic.

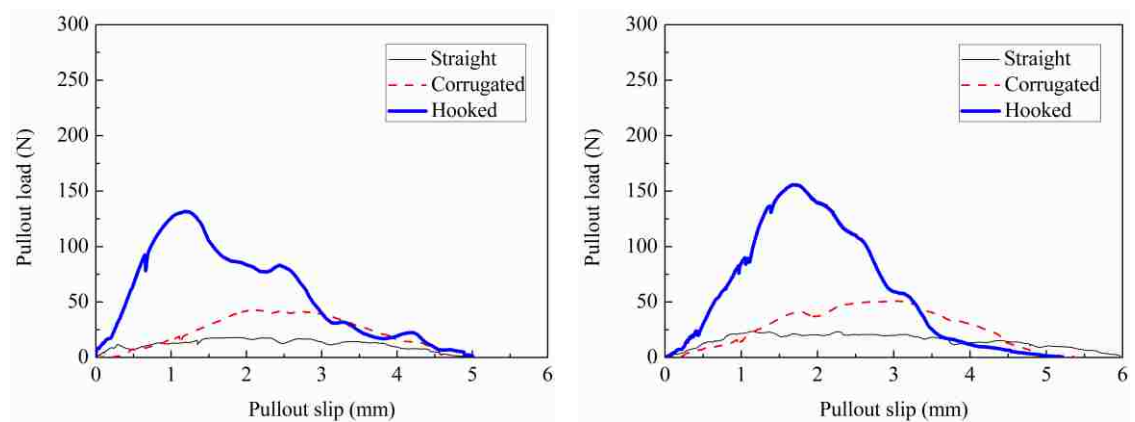
This study aims at evaluating the bond properties between different shaped fibers and UHPC matrix as well as its relationship with microstructure and mechanical properties of UHPC. The influences of straight, corrugated, and hooked fibers on bond properties and mechanical properties of UHPC with 2% of these fibers at different ages were experimentally evaluated. Advanced materials characterization techniques including mercury intrusion porosimetry (MIP), X-ray diffraction (XRD), and thermal gravimetric (TG) analyses were employed to characterize the microstructure of the matrix and/or fiber-matrix interface. The bond strength related to both microstructure and mechanical properties of UHPC was established. Flexural strengths of UHPC with different fiber geometries were predicted using pullout bond strength of embedded fiber and the flexural strength of the UHPC matrix based on composite theory. It is of the purpose to enhance the bond properties of fiber and eventually the overall mechanical properties of UHPC.

## **8.2. EFFECT OF STEEL FIBER SHAPE ON INTERFACIAL BOND PROPERTIES BETWEEN FIBER AND UHPC MATRIX**

Effect of straight, hooked, and corrugated fiber on fiber-matrix bond properties were investigated.

**8.2.1. Pullout Load-Slip Relationship.** The pullout load-slip curves of UHPC embedded with different shaped fibers that were determined at 1, 3, 7, 28, and 91 d are shown in Figure 8.1. The results indicated that samples with hooked fibers had the

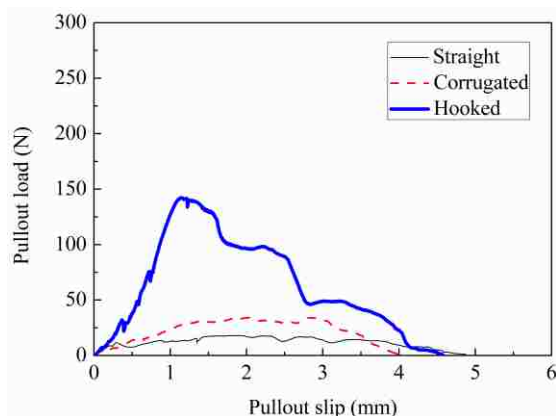
highest pullout peak load and pullout energy or pullout toughness (area under the curve), whereas those embedded with straight fibers showed the lowest corresponding values. The pre-peak branches, or the ascending branches, for the three fibers had both a linear and non-linear parts [165,166]. In the linear part, the fibers were well bonded to the matrix, which resulted in an elastic behavior. At this region, the hooked fibers had the steepest slope, followed by that of the corrugated fibers, and then that of the straight fibers. In the non-linear part of the ascending part of the pullout load-slip curves, it can be generally found that the slopes of the curves started to decrease with further increase in pullout load to peak values. The loss of stiffness was related to irrecoverable deformation at the fiber-matrix interface. In this region, the fiber can be partially debonded from the matrix [183]. With further increase in the slip, the pullout load gradually decreased to zero, suggesting fibers were completely pulled out from the pulled half of the dog-bone shaped specimen.



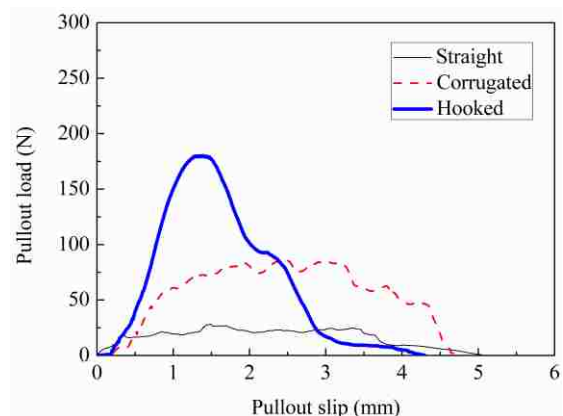
(a) U15 at 1d

(b) U20 at 1d

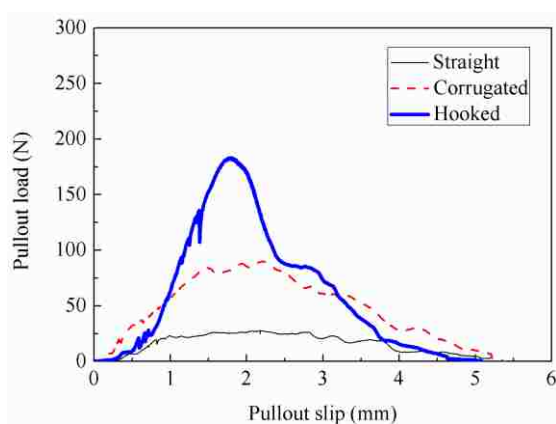
Figure 8.1. Pullout load-slip curves of the U15 and U20 matrix embedded with different fiber geometries



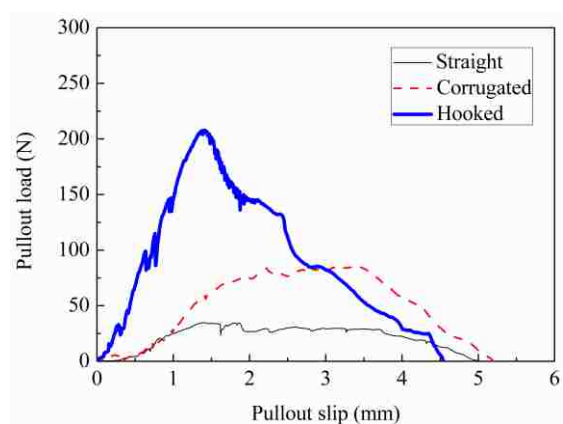
(c) U15 at 3 d



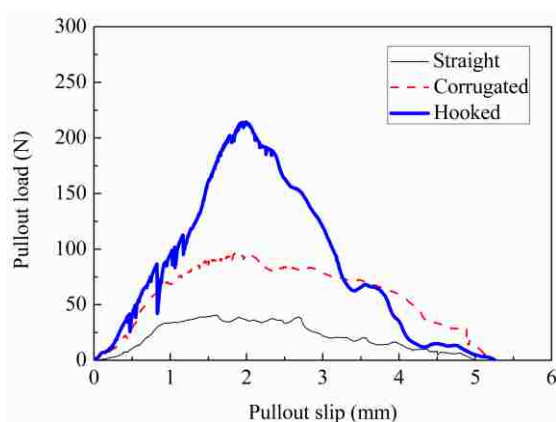
(d) U20 at 3 d



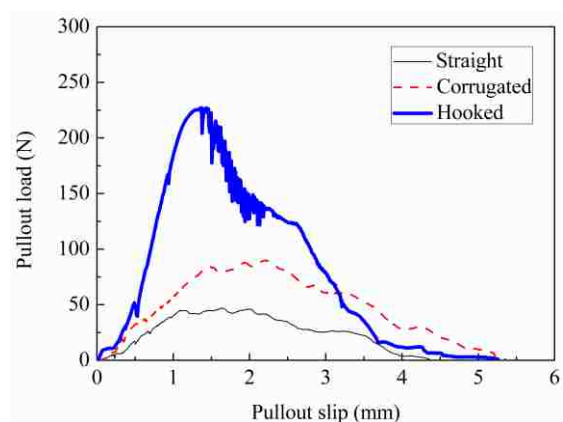
(e) U15 at 7 d



(f) U20 at 7 d



(g) U15 at 28 d



(h) U20 at 28 d

Figure 8.1. Pullout load-slip curves of the U15 and U20 matrix embedded with different fiber geometries (cont.)

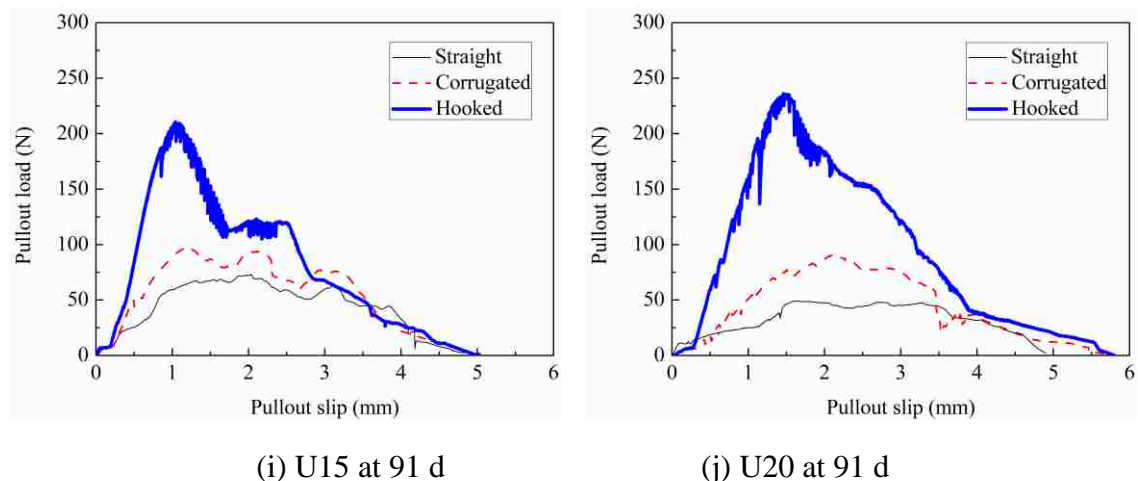


Figure 8.1. Pullout load-slip curves of the U15 and U20 matrix embedded with different fiber geometries (cont.)

As observed in Figure 8.1, peak load increased with curing time. For the hooked fibers in the U20 matrix at 1 d, the peak load was 150 N and increased to 175, 208, 225, and 235 N at 3, 7, 28, and 91 d, respectively. A similar trend of increase in peak load with curing time was found for the U15 matrix. The peak load for the three fibers in the U20 matrix was slightly greater than that in the U15 matrix due to the greater compressive strength of the matrix. Banthia [189] investigated the fiber-matrix bond of steel fiber reinforced concrete using a double-sided pullout testing. It was found that the peak load of straight and hooked fiber ( $l = 60$  mm,  $d = 0.6$  mm) in a matrix (W/CM of 0.35) after 28 d moist curing were 54 and 228 N, respectively. The results were comparable to 50 and 225 N in this study with the matrix at the same age. It should be noted that fiber-matrix bond varies with the type of fiber, embedded length of fiber, and properties of matrix.

**8.2.2. Bond Strength to Embedded Fibers.** Figure 8.2 shows the effect of fiber shape on bond strength for the U15 and U20 matrix at different ages. The two matrices exhibited similar gains in bond strength with age. They both increased rapidly during the first 7 d and gradually reached a constant value thereafter. The bond strength between the

straight fibers and the U15 matrix at 1 d was 2.0 MPa; it increased to 3.0 MPa at 28 d. At 91 d, only a slight increase in bond strength was observed.

The change in the bond strength of the embedded fibers in U20 mixture was similar to the U15 mixture, except for slightly higher strength. This might be due to higher packing density at the ITZ associated with the incorporation of 20% silica fume, which leads to higher compressive strength of the matrix [59]. On the other hand, higher autogenous shrinkage associated with the greater use of silica fume could take place, which can lead to clamping pressure and confinement of embedded fibers [190]. Chan and Chu [33] obtained a bond strength of 4.8-5.5 MPa with reactive powder concrete after heat curing using the same pullout testing. The lower bond strength obtained in this research was because of standard curing.

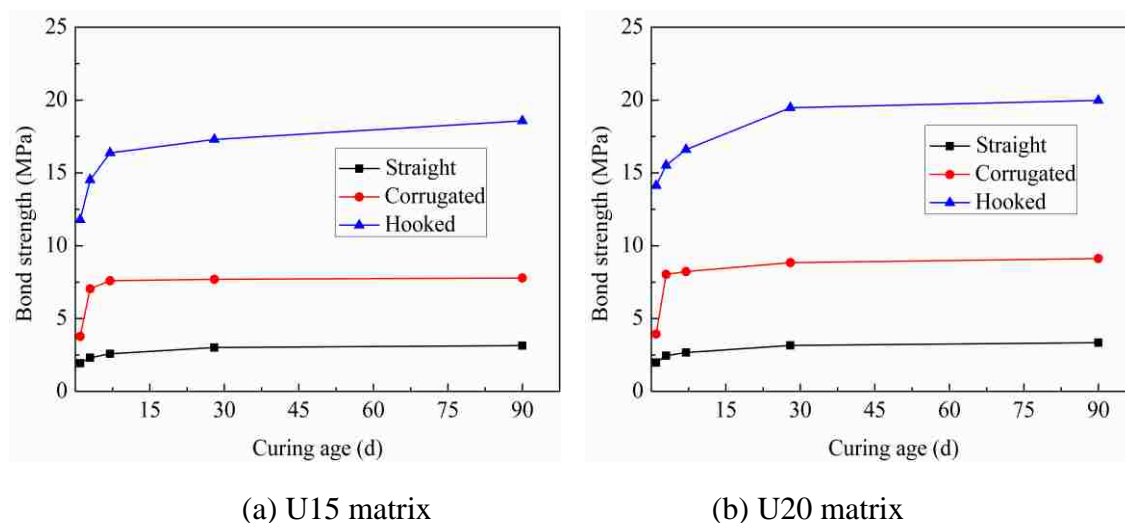


Figure 8.2. Effect of fiber shape on bond strength between fiber and U15 and U20 matrix

As also illustrated in Figure 8.2, fiber shape had a significant effect on the bond strength. The bond strengths of corrugated and hooked fiber with U20 matrix at 28 d

were 7.5 and 19.2 MPa, respectively. They were seven and three times higher than those with straight fibers. The results were in good agreement with the findings in Ref. [59, 189], in which the bond strength of UHPC with deformed fibers was five times more than that with straight fibers. Therefore, additional mechanical anchorage from the deformed fiber significantly improve the bond properties of fiber-matrix interface [183].

**8.2.3. Pullout Energy.** Pullout energy, or pullout toughness, is defined as the energy dissipated during fiber pullout process, which can be obtained by integrating the area under pullout load-slip curve. Figure 8.3 illustrates the effect of the fiber shape on pullout energy.

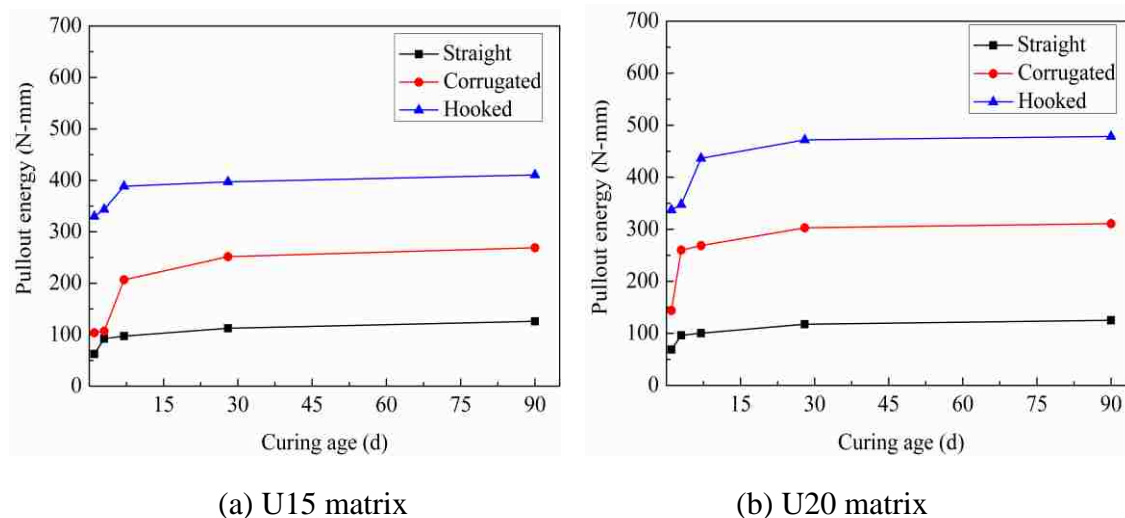


Figure 8.3. Effect of fiber shape on pullout energy between fiber and matrix for the U15 and U20 matrix

The three types of fiber exhibited similar trend for the variation of pullout energy with age as that of bond strength varied with time. Hooked fibers again achieved the highest pullout energy, whereas straight fibers showed the lowest value. The pullout energies of hooked and corrugated fibers were five and three times higher than those of

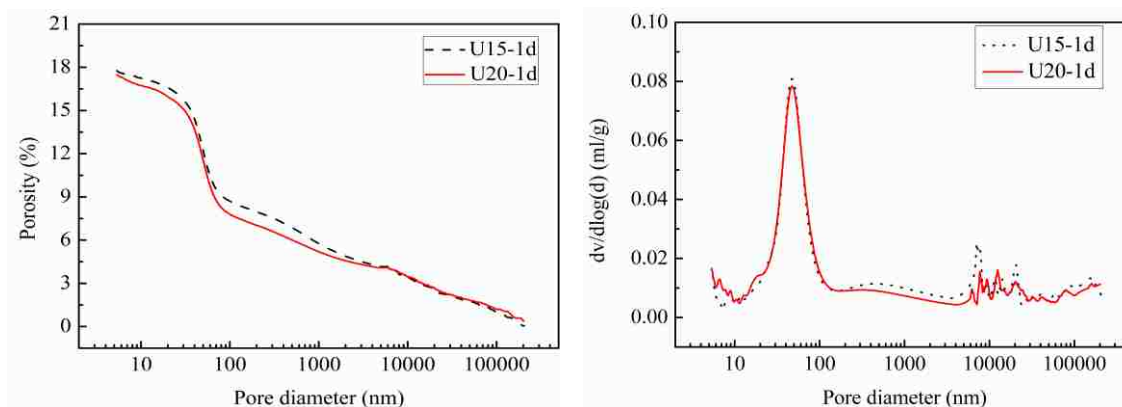


the straight fibers. Therefore, deformed fibers considerably enhanced the toughness of the composite material. The pullout energy for the U20 mixtures was higher, especially for those with corrugated and hook-end fibers, than that of the U15 mixtures. This was consistent with the results of bond strength.

### 8.3. MICROSTRUCTURAL EXAMINATION

To investigate the pore structure and porosity of the different mixtures of U15 and U20, MIP analysis was examined.

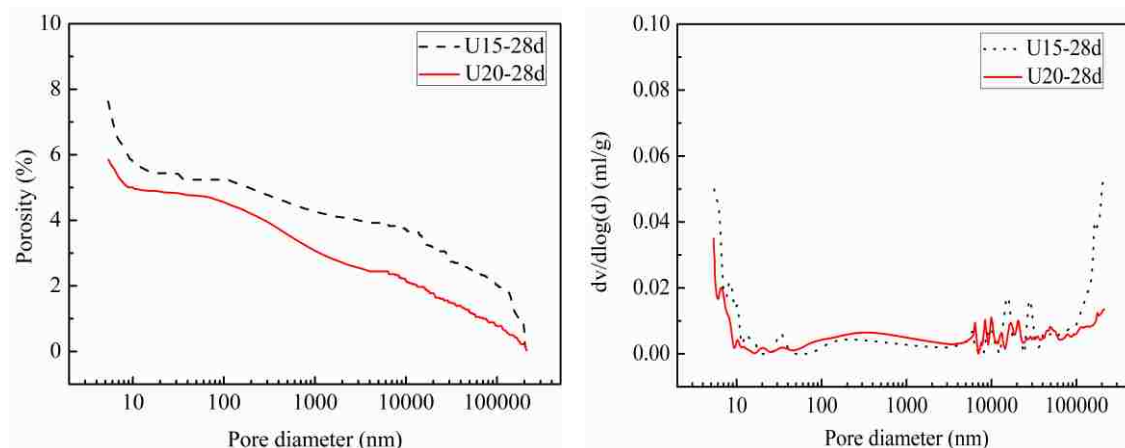
**8.3.1. MIP Measurement.** Figure 8.4 depicts the MIP results of the U15 and U20 matrix at 1 and 28 d. The change in pore size distribution of the U15 and U20 matrix showed a similar trend and did not change much. However, the U20 matrix had a slightly lower porosity of 17.5% and 5.9% at 1 and 28 d, respectively, compared to 17.8% and 7.6% of the U15 matrix. This corresponded well with the previous bond properties to fiber. Therefore, the U20 matrix with 5% more silica fume resulted in a denser microstructure and better bond properties.



(a) Porosity at 1 d

(b) Differential pore size distribution at 1 d

Figure 8.4. MIP results of the U15 and U20 matrix at 1 and 28 d



(c) Porosity at 28 d

(d) Differential pore size distribution at 28 d

Figure 8.4. MIP results of the U15 and U20 matrix at 1 and 28 d (cont.)

From Figure 8.4(b), it can be seen that the most probable pore size (critical pore size), corresponding to the inflection point on  $dv/d\log(d)$  curve, of the matrix at 1 d was 50 nm. It was refined to 5 nm at 28 d, as observed in Figure 8.4(d). The most probable pore size mainly reflects the connectivity and tortuosity of pores in concrete. Generally, the lower the most probable pore size and corresponded intruded volume, the poorer the connectivity and tortuosity of the pores. Therefore, the microstructure of UHPC was gradually refined with curing time.

**8.3.2. Optical Microscopy Observation.** Figure 8.5 shows the optical microscopy observation of fiber before and after pullout testing. Significant abrasion on the surface of pulled out steel fiber (top one in the figure) can be obviously observed when compared to the original fiber. The coating brass film on the surface of the pulled out fiber was abraded, with a lot of scratches on the fiber surface and a length of 5 mm part presented black. From Figure 8.5(b and c), it can be observed that the pullout half of hooked and corrugated fiber became relatively straight. Although they were not fully

straightened, their initial shape was lost. Therefore, deformed fiber can provide effectively mechanical anchorage associated with plastic deformation during pullout process, and thus enhancing the bond properties between fiber and matrix.

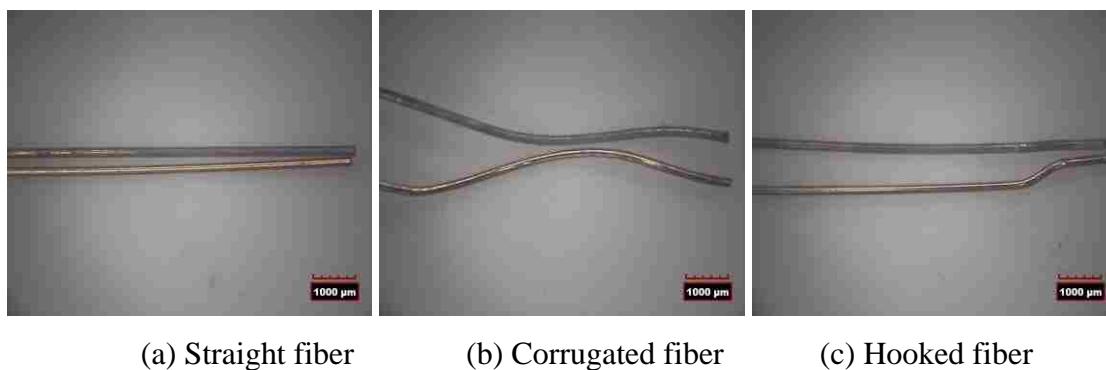


Figure 8.5. Optical microscopy observation of fiber before and after pullout from matrix

**8.3.3. XRD Analysis.** Figure 8.6 shows XRD patterns of the U20 mixture that were tested at age of 1, 7, and 28 d. The crystal phases of UHPC samples are shown to be composed of quartz ( $\text{SiO}_2$ ) from the sand with characteristic peaks at  $2\theta = 21.1^\circ$ ,  $26.8^\circ$ ,  $39.7^\circ$ ,  $50.4^\circ$ , and  $60.1^\circ$ . Small amounts of AFt (at  $9.7^\circ$ ),  $\text{Ca}(\text{OH})_2$  (at  $18.1^\circ$ ,  $34.0^\circ$ , and  $47.2^\circ$ ), and unhydrated cement clinker, such as  $\text{C}_3\text{S}$  and  $\text{C}_2\text{S}$  (at  $29.4^\circ$ ,  $30.1^\circ$ ,  $32.2^\circ$ ,  $32.8^\circ$ ,  $34.5^\circ$ , and  $39.0^\circ$ ) were also observed. The intensity of AFt was low given its limited content compared to other phases.

As illustrated in Figure 8.6, an obviously new peak at about  $28.2^\circ$  appeared at 7 and 28 d, except 1 d. Nonat [191] obtained C-S-H hydration by mixing fine  $\text{C}_3\text{S}$  and  $\text{SiO}_2$ . It was found that C-S-H showed a strong peak at this point. Wang et al. [192] also observed a tobermorite peak at this point. This peak might be due to poor-crystallized C-S-H associated with the hydration of  $\text{C}_3\text{S}$  and/or  $\text{C}_2\text{S}$ . Besides, the intensity of  $\text{Ca}(\text{OH})_2$

of U20 at 28 d was very weak compared to those at an early age, indicating effective pozzolanic reaction between silica fume and  $\text{Ca(OH)}_2$  with age.

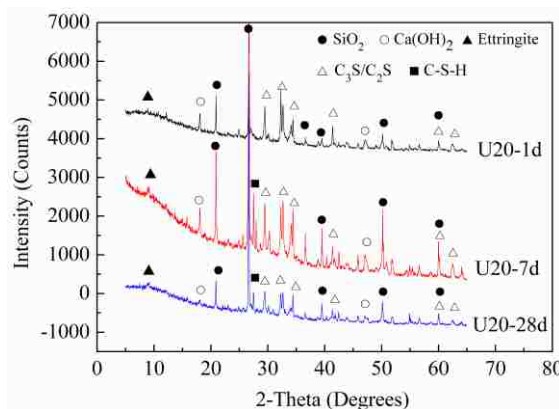


Figure 8.6. XRD patterns of U20 mixture at different ages

The semi-quantitative analysis of hydration products in the U20 mixture at different ages is summarized in Table 8.1. With the increase of curing time, the content of unhydrated cement  $\text{C}_3\text{S}$  and/or  $\text{C}_2\text{S}$  and CH decreased gradually. A reduction of calcium silicate ( $\text{C}_3\text{S}$  and/or  $\text{C}_2\text{S}$ ) of 24% was observed between 1 and 7 d, then 8% between 7 and 28 d. This corresponded well with the age-dependency of bond properties. The CH content at 28 d was 3% only, which decreased by 62% compared to that at 1 d. Therefore, good pozzolanic reaction between the silica fume and CH favors bond properties between the fiber and matrix.

Table 8.1. Semi-quantitative analysis of hydration products in the U20 mixture at different ages

| No.        | Unhydrated $\text{C}_3\text{S}$ and/or $\text{C}_2\text{S}$ (%) | CH (%) | Ettringite (%) |
|------------|---|--------|----------------|
| U20 - 1 d  | 29.7  | 7.9    | 5.8            |
| U20 - 7 d  | 22.0  | 7.0    | 6.0            |
| U20 - 28 d | 20.2  | 3.0    | 7.1            |

**8.3.4. Calcium Hydroxide Content.** Figure 8.7 compares the CH content in the U15 and U20 mortars at different ages determined by TG analysis. The CH content for U20 at 1, 7, and 28 d were 5.8%, 4.7%, and 2.2%, respectively, which were slightly lower than that from XRD analysis. This was because the proportion obtained from XRD only accounted for crystal composition.

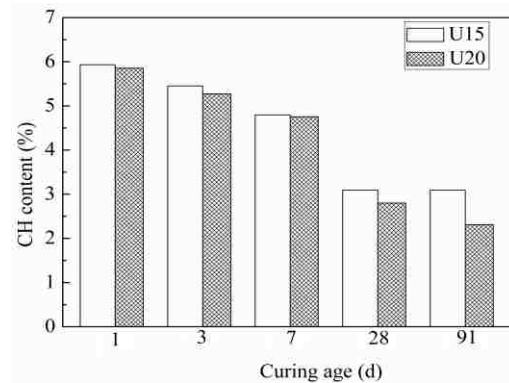


Figure 8.7. CH content in the U15 and U20 matrix at different ages

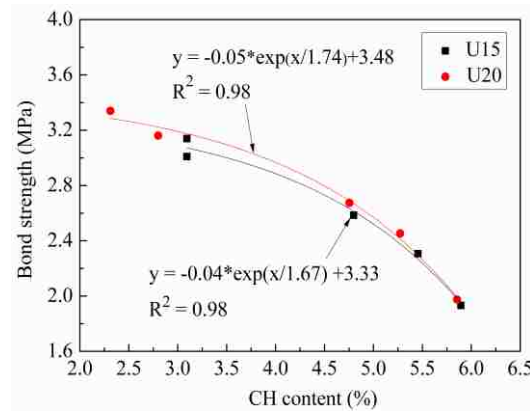


Figure 8.8. Relationship between bond strength of straight fiber and CH content

Besides, the CH content in the U20 matrix was slightly lower than that in the U15 matrix. This validated the previous bond properties and MIP results perfectly. The

addition of 20% silica fume in the U20 mixture led to further reduction in porosity and increased C-S-H content, which allowed better bond stress transfer at the fiber-matrix interface. The relationship between the bond strength of straight fiber and CH content can be observed from Figure 8.8. The interfacial bond strength decreased exponentially with the increase in CH content with correlation coefficients up to 0.98.

#### **8.4. EFFECT OF STEEL FIBER SHAPE ON MECHANICAL PROPERTIES OF UHPC WITH 2% STEEL FIBERS**

Based on the above results, the U20 matrix that exhibited better bond to fiber and denser microstructure was finally chosen to investigate the effect of fiber shape on mechanical properties of UHPC prepared with 2% steel fiber.

**8.4.1. Compressive Strength.** Figure 8.9 compares the compressive strength of UHPC with the incorporation of 2% straight, corrugated, and hooked fibers.

The 28-d compressive strength of the U20 matrix with no fiber was 115.3 MPa, and increased to 142.2, 151.6, and 153.6 MPa when 2% straight, corrugated, and hooked fibers were used, respectively. Therefore, the incorporation of 2% steel fiber can increase the compressive strength by 20 to 40 MPa, depending on the curing time and fiber shape. The improvement in compressive strength associated with the use of steel fiber is due to the intrinsic rigidity of the fiber. This was consistent with the results reported in the literature [22,63]. The magnitude of such increase depends on the fiber dosage, fiber geometry, and curing time. The highest compressive strength was obtained with the hooked fiber, followed by the corrugated fiber and finally the straight fiber. However, the effect of fiber shape on compressive strength of UHPC was limited to a certain value, which was only 1 to 7 MPa.

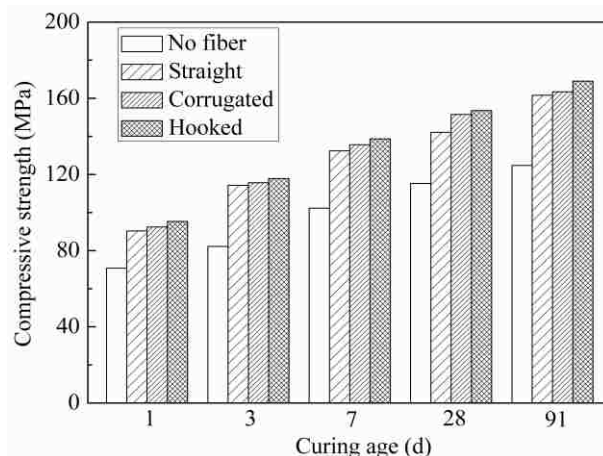
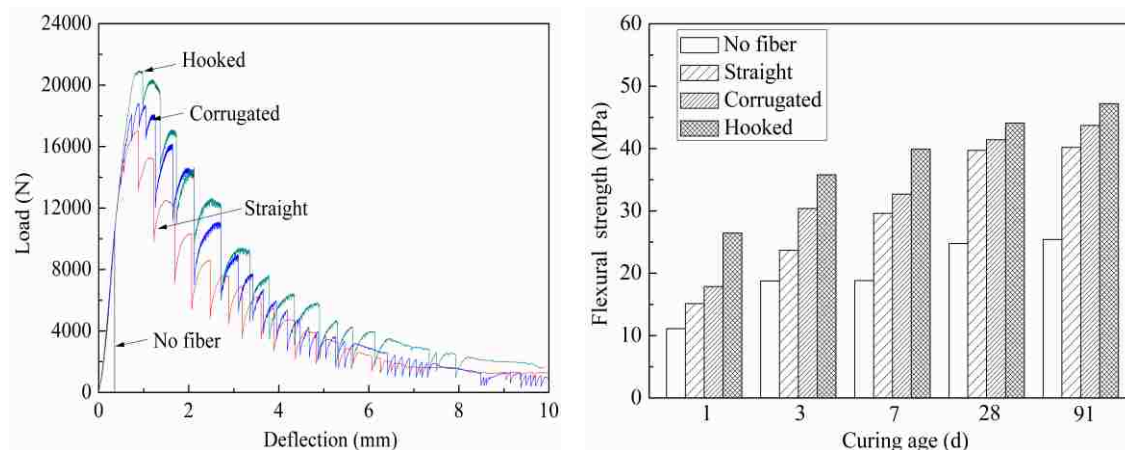


Figure 8.9. Compressive strength development of UHPC made with 2% straight, corrugated, and hooked steel fibers

**8.4.2. Flexural Behavior.** The incorporation of 2% steel fiber significantly improved the flexural behavior, as observed in Figure 8.10. The reference specimen with no fiber had a sudden drop after reaching the peak load of approximately 10,570 N, as can be seen from Figure 8.10(a). UHPC specimens with any of the three fiber types exhibited the same increase in load-deflection until the first cracking load of 14,200 N, which was 34% greater than that of the non-fibrous UHPC. The similar linear branches for the three fibers were attributed to the same UHPC matrix. This was due to the first cracking strength depends mainly on the matrix strength. This was consistent with the results reported in the literature [40]. After the linear branch, a nonlinear branch of the load-deflection curve was obtained to reach the peak load, carrying capacity of UHPC with hooked fiber exhibited the highest flexural strength. Beyond peak load, all UHPC exhibited progressive fiber pullout similar load-deflection behavior. All UHPC specimens had some residual flexural strength at very high deflection value of 10 mm, indicating good ductility with 2% steel fiber.



(a) Flexural load-deflection curves at 28 d      (b) Flexural strength

Figure 8.10. Flexural load-deflection curves of UHPC made with 2% straight, corrugated and hooked steel fibers

From Figure 8.10 (b), it can be seen that the flexural strength increased with curing time and incorporation of 2% steel fiber. The flexural strength of UHPC with no fiber at 28 d was 24.8 MPa and increased to 39.7 MPa with the incorporation of 2% straight fiber. When 2% corrugated and hooked fibers were used, the flexural strengths increased to 41.72 and 44.09 MPa, respectively. Therefore, UHPC with hooked fiber demonstrated the best mechanical properties, followed by corrugated fiber and straight fiber.

**8.4.3. Bond Strength vs. Flexural Strength of UHPC.** Figure 8.11 depicts the relationship between bond strength to embedded fiber and flexural strength of UHPC made with different fiber geometries. With the increase of bond strength, the flexural strength of UHPC gradually increased. For the straight fiber, when bond strength increased from 2 to 3.5 MPa, the flexural strength of UHPC increased from 15 to 40 MPa. On the other hand, different bond strengths were needed to obtain the same flexural



strength of UHPC made with different fiber shapes. For instance, when the bond strength to straight, hooked, and corrugated fibers were 3.3, 8.8, and 16.6 MPa, respectively, a flexural strength of 40 MPa can be achieved. The flexural strengths of UHPC made with corrugated and hooked fiber were enhanced by 8% to 28% and 17% to 50%, respectively when compared to straight fiber.

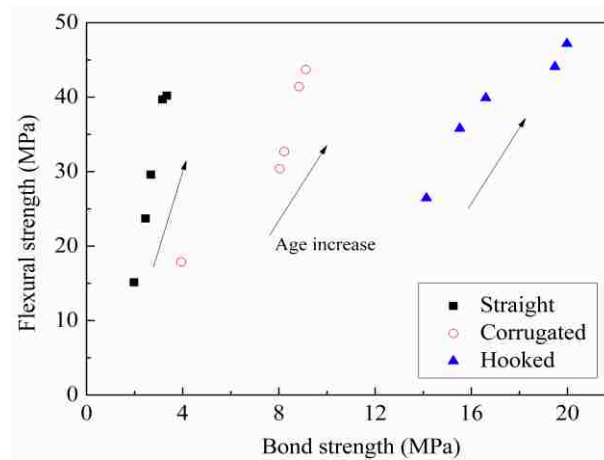


Figure 8.11. Bond strength vs. flexural strength of UHPC with 2% steel fibers of different shapes

## 8.5. PREDICTION OF FLEXURAL STRENGTH OF UHPC BASED ON COMPOSITE THEORY

According to the composite theory, the tensile strength of fiber reinforced cement-based composites can be calculated according to Equation (8.1):

$$\sigma_{tc} = \sigma_{tm}(1 - V_f) + \sigma_{tf}V_f \quad (8.1)$$

where  $\sigma_{tc}$  (MPa) is the tensile strength of fiber reinforced concrete composite;  $\sigma_{tm}$  (MPa) is the tensile strength of concrete matrix;  $V_f$  (unit-less) is the content of fiber, by volume of concrete;  $\sigma_{tf}$  (MPa) is the average tensile strength of fiber.

A Linear relationship exists between flexural strength ( $\sigma_{fc}$ ) and tensile strength ( $\sigma_{tc}$ ) of fiber reinforced cement-based composites, as shown in Equation (8.2).

$$\sigma_{fc} = \alpha \sigma_{tc} \quad (8.2)$$

Based on the composite mechanics theory, the flexural strength of UHPC with 2% steel fiber can be calculated in terms of Equation (8.3).

$$\sigma_{fc} = \alpha [\sigma_{fm}(1 - V_f) + \sigma_{tf} V_f] = \sigma_{fm}(1 - V_f) + \alpha \eta_l \eta_\theta \sigma_{tmax} V_f \quad (8.3)$$

where  $\alpha$  is the flexural-to-tensile strength ratio, which was determined of 2.0 according to previous research;  $\sigma_{fm}$  (MPa) is the flexural strength of UHPC matrix;  $\eta_\theta$  (unit-less) is the coefficient related to orientation of fiber in three-dimensional space, which was determined as 0.5 [193];  $\sigma_{tmax}$  (MPa) is the maximum tensile strength of steel fiber;  $\eta_l$  (unit-less) is the length factor, which is closely related to the critical length and damage state of steel fiber. The critical length can be expressed as follows:

$$l_f^{crit} = \frac{d_f \sigma_{tmax}}{2\tau} \quad (8.4)$$

where  $l_f^{crit}$  is the critical length of steel fiber (mm);  $d_f$  is the fiber diameter (mm);  $\tau$  is the bond strength between steel fiber and UHPC matrix (MPa).

Based on previous research [194], the corresponding  $\eta_l$  during flexural loading can be calculated from Equations (8.5) and (8.6), respectively.

$$\eta_l = 1 - \frac{l_f^{crit}}{2l_f} \quad \text{when } l_f > l_f^{crit} \quad (8.5)$$

$$\eta_l = \frac{l_f}{2l_f^{crit}} \quad \text{when } l_f \leq l_f^{crit} \quad (8.6)$$

It was observed from the pullout and flexural behavior testing that the steel fibers were pulled out from the UHPC matrix. Therefore, the Equation (8.6) can be used to calculate  $\eta_l$  and the flexural strength can be expressed as follows:

$$\sigma_{fc} = \sigma_{fm}(1 - V_f) + \alpha\eta_0 \frac{l_f}{d_f} V_f \tau \quad (8.7)$$

The predicted flexural strength ( $\sigma_{fc}$ ) of the UHPC can be calculated based on bond strength to fiber ( $\tau$ ) and flexural strength of matrix ( $\sigma_{fm}$ ), which were determined experimentally. The predicted vs. experimental values of flexural strengths of UHPC are summarized in Table 8.2.

Table 8.2. Predicted and experimental values of flexural strength of UHPC

| Time (d) | Flexural strength of matrix (MPa) | Experimental $\sigma_{fc}$ of UHPC (MPa) |      |      | Predicted $\sigma_{fc}$ of UHPC (MPa) |      |      | Predicted value /experimental value |      |      |
|----------|-----------------------------------|--|------|------|---------------------------------------|------|------|-------------------------------------|------|------|
|          |                                   | S  | C    | H    | S                                     | C    | H    | S                                   | C    | H    |
| 1        | 11.1                              | 15.1                                     | 17.9 | 26.5 | 13.5                                  | 16.0 | 29.3 | 0.89                                | 0.90 | 1.11 |
| 3        | 18.8                              | 23.7                                     | 30.4 | 35.8 | 21.6                                  | 28.9 | 38.6 | 0.91                                | 0.95 | 1.08 |
| 7        | 18.8                              | 29.6                                     | 32.7 | 39.9 | 22.0                                  | 29.2 | 40.1 | 0.74                                | 0.89 | 1.00 |
| 28       | 24.8                              | 39.7                                     | 41.4 | 44.1 | 28.4                                  | 35.8 | 49.6 | 0.71                                | 0.86 | 1.12 |
| 91       | 25.4                              | 40.2                                     | 43.7 | 47.2 | 29.3                                  | 36.8 | 50.9 | 0.73                                | 0.84 | 1.08 |

**Note:** S, C, and H denote straight, corrugated, and hooked fibers, respectively.

The ratios of predicted value to experimental value were in the range from 0.8 to 1.1, except three data for the straight fiber. The error was within 15%, indicating that the predicted flexural strengths agreed well with the experimental values. The larger difference between predicted and experimental flexural strengths of UHPC with straight

fiber might be due to high sensitivity to the orientation of fiber. Therefore, fiber shape had a remarkable strengthening effect on UHPC.

## 8.6. SUMMARY

This study investigated the influence of straight, corrugated, and hooked steel fibers on pullout bond properties between embedded fibers and mechanical properties of UHPC made with 2% steel fibers. Advanced materials characterization techniques including MIP, TG, and XRD analysis were employed to evaluate the matrix and/or the interface of the matrix with embedded fibers. The relationship between bond strength and mechanical properties was established. Based on the results of this study, the following conclusions can be drawn:

(1) The use of deformed fibers effectively enhanced the interfacial bond properties between fibers and UHPC matrix, as well as mechanical properties of UHPC. Pullout bond strength and toughness of embedded hooked fibers were approximately seven and five times greater, respectively, than those with straight fibers, and three and three times greater than those of corrugated fibers.

(2) Pullout bond strength did not significantly increase beyond 7 or 28 d, depending on the fiber type. Good exponential correlation was established between CH content and pullout bond strength of embedded fibers. The pullout behavior of the UHPC matrix prepared with 20% silica fume was greater than that with 15% silica fume. This was confirmed by lower porosity and less CH content in the matrix.

(3) Fiber shape had limited effect on compressive strength of UHPC but significant influence on flexural strength. Depending on the curing age, the flexural

strength of UHPC with 2% corrugated and hooked fibers were 8% to 28% and 17% to 50%, respectively, greater than that with straight fibers.

(4) Flexural strength of UHPC incorporating different shaped fibers can be predicted using pullout bond strength of embedded fibers and flexural strength of the non-fibrous UHPC matrix based on the composite theory. The prediction takes into consideration of fiber volume, fiber length, fiber diameter, coefficient related to the orientation of fibers in three dimensions. The ratios of predicted to measured value were between 0.8 and 1.1.

## 9. COMPARISON OF STATIC AND IMPACT FLEXURAL PROPERTIES OF OPTIMIZED UHPC WITH SCMS AND NANOPARTICLES

### 9.1. BACKGROUND

Ultra-high performance concrete (UHPC) is a new type of composite material that can develop high compressive strength over 150 MPa, high tensile strength ranging from 5 to 15 MPa given the low water-to-binder ratio use of steel fibers [15, 96]. The fracture energy of UHPC can vary from 8,560 to 40,000 J/m<sup>2</sup>, which is approximately 220 times greater than that of conventional mortar [195]. Because of these excellent mechanical properties and ductility, UHPC has a great potential application in structural elements that require high impact resistance, strength, and toughness [196]. Several studies have demonstrated the superior performance of UHPC under static loading conditions [197-198]. However, limited information is available on the dynamic behavior of UHPC, especially on mixture composition. The response of concrete structure subjected to impact loading differs greatly from that under static loading.

The dynamic mechanical properties of UHPC can be evaluated using the drop-weight impact and Split-Hopkinson-Pressure-Bar (SHPB) test methods [84, 199]. The drop weight impact testing is a low velocity testing, which can be conducted through releasing a drop weight from a known height to impact the specimen. Habel et al. [61] employed this method to investigate the dynamic bending properties of ultra-high performance fiber-reinforced concrete (UHPFRC) plate specimens. The dynamic bending strength of the UHPFRC specimens under dynamic loading were increased by 15%-60%, depending on the mass of drop weight, when compared to those under quasi-static loading. Rong et al. [85] found that the dynamic compression behavior of ultra-high

performance cement-based composites was improved with the increase of fiber volume from 0% to 4%. Zhang et al. [199] reported the dynamic tensile strength of UHPC made with 4% steel fibers measured using SHPB method was up to 15 MPa, which was 50% greater than the static tensile strength. Su et al. [200] used the SHPB test to study the effect of steel fibers of the same diameter but different lengths of 6 and 15 mm on dynamic compression properties of UHPC. The increase in fiber length from 6 to 15 mm improved the dynamic properties of UHPC by approximately 11%. At a total fiber volume of 2%, UHPC reinforced with 1.5% long steel fibers (13 mm) and 0.5% short steel fibers (6 mm) demonstrated the highest static and dynamic compressive behaviors. Such values were 19% and 14%-24%, respectively, greater than that with 2% short fibers. Fiber hybridization can improve mechanical properties due to combined benefits exerted from these fibers. For example, high modulus fibers play a significant role in enhancing the tensile strength, while low modulus fibers dominated the ductility [201]. Long steel fibers play a dominating role in improving the impact resistance capacity of UHPC [202]. At a total fiber volume of 2%, UHPC reinforced with 1.5% long fibers (13 mm) and 0.5% short fibers (6 mm) demonstrated the highest static and dynamic compressive behaviors, which were 19% and 14%-24%, respectively, greater than those with 2% short fibers [88].

UHPC is initially produced with high content of cement and silica fume, steel fiber, and special type of finely ground quartz sand. Recently, many attempts have been used to enhance the performance and cost-effectiveness of UHPC. This includes the use of hybrid fibers [203], replacement of quartz sand by natural and masonry sand [204,205], and use of supplementary cementitious materials (SCMs) [206-207]. SCMs,

such as fly ash and slag, can be used to substantially replace portland cement and/or silica fume and enhance the sustainability of UHPC. Due to their glassy structure and fine size, the flowability and strength of UHPC can be enhanced. Yazici et al. [206] prepared UHPC through various replacement ratios of slag (20%, 40%, and 60%) to cement and reported that the greatest compressive strength was found in the mixture made with 20% slag. In another study, UHPC mixtures made with 20% to 40% fly ash or slag obtained high compressive and flexural properties [207]. Furthermore, the performance of UHPC can be improved using a small amount of nano-particles. They can appropriately enhance the mechanical properties and durability of UHPC due to the pozzolanic, nucleation, and filler effects [208,211]. The use of 3.2% nano-CaCO<sub>3</sub> was reported to enhance the 28 d fiber-matrix bond strength and static flexural strength by 45% and 23%, respectively [209]. The fiber-matrix bond strength of UHPC incorporated with 1% nano-SiO<sub>2</sub> was increased by 35% compared to the control mixture [210]. Su et al. [216] investigated nano-CaCO<sub>3</sub>, nano-SiO<sub>2</sub>, nano-TiO<sub>2</sub>, and nano-Al<sub>2</sub>O<sub>3</sub> on dynamic compression and tensile properties of UHPC and reported that nano-CaCO<sub>3</sub> demonstrated the highest strength. According to the literature review, there is a perceived lack of comparative studies on fiber-matrix bond and dynamic mechanical properties of UHPC made with different types of SCM and nano-particles.

This study presented here was undertaken to investigate the fiber-matrix bond and static and dynamic mechanical properties of UHPC made with various types of SCMs and nano-particles. The investigation included non-fibrous UHPC matrix and UHPC mixtures prepared with 2% steel fibers. A reference UHPC mixture made with 20% silica fume replacement to binder was used. Five mixtures incorporated slag, fly ash, nano-



CaCO<sub>3</sub>, and nano-SiO<sub>2</sub> in addition to 20% silica fume in ternary or quaternary mixtures were also used. Drop weight impact three-point bending testing was conducted to investigate the impact flexural behavior of the specimens, while the static flexural behavior was evaluated using specimens with the same size.

## **9.2. STATIC AND IMPACT MECHANICAL PROPERTIES OF UHPC MATRIX**

Static and impact mechanical properties of the six non-fibrous mixtures made with different components were compared.

**9.2.1. Static Compressive and Flexural Strengths of UHPC Matrix.** Figure 9.1 compares the static compressive and flexural strengths of the UHPC matrix that determined at 7 and 28 d. The 7 d compressive strength of the reference mixture (U20) was 89.6 MPa. The incorporation of 20% SL or 20% FA decreased the 7 d compressive strength by approximately 10%, while nano-particles increased it by approximately 15% compared to the reference specimens.

With prolongation of curing time to 28 d, the SL20 and FA20 mixtures exhibited slightly greater compressive strengths (5 MPa) than that of the reference specimens. The decrease in compressive strength associated with SL and/or FA at early age might be due to delayed reactivity of cement and relatively weak chemical bond of the hydration products [211]. The addition of nano-particles rendered the highest compressive strength at 7 and 28 d, which was 10% greater than that of the reference specimen.

The static flexural load-deflection curves of the UHPC matrix are presented in Figure 9.2. The load changed linearly with the increase of deflection. Once reaching the

ultimate strength, the UHPC matrix exhibited a sudden drop at a deflection of approximate 0.4 mm, reflexing a brittle failure.

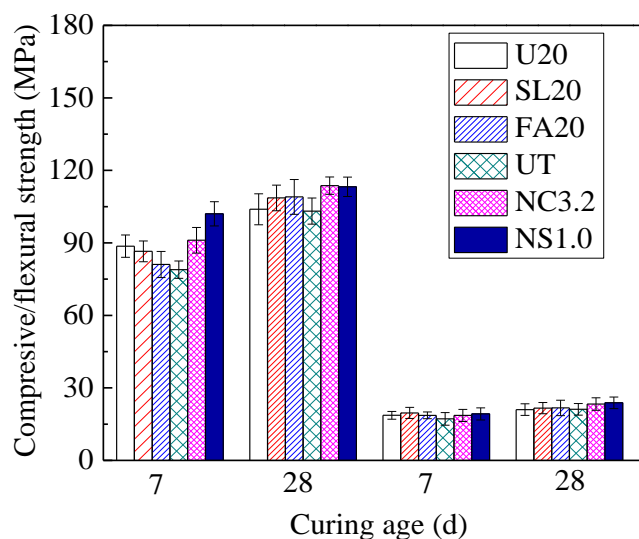


Figure 9.1. Static compressive and flexural strengths of UHPC matrix at 7 and 28 d

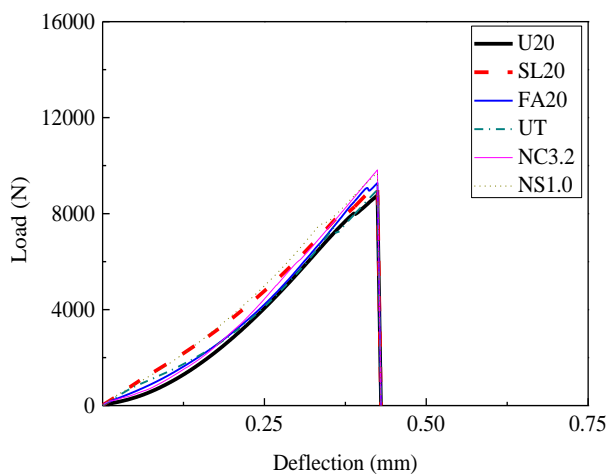


Figure 9.2. Static flexural strengths of investigated UHPC matrix at 28 d

As can be also seen from Figure 9.2, the flexural strengths of the investigated UHPC matrix were approximately 19 MPa at 7 d. With curing age prolonged to 28 d, the two mixtures with nano-particles demonstrated a greater improvement, which was approximately 10% when compared to the reference specimens. This agrees well with the compressive strength results.

**9.2.2. Impact Flexural Behavior of UHPC Matrix.** The impact flexural load-deflection curves of the UHPC matrix under impact loading are shown in Figure 9.3. Parabola flexural load-deflection curves were observed, in which an increasing branch of the load with the increase of deflection to approximately 0.7 mm initially occurred. After reaching the peak load, it gradually dropped to zero at a deflection of 1.1 mm. Compared to the U20 mixture, the incorporation of either SCM or nano-particles enhanced the peak load value. The NC3.2 mixture exhibited the highest peak load of 14,500 N, which was 20% greater than that of the reference mixture.

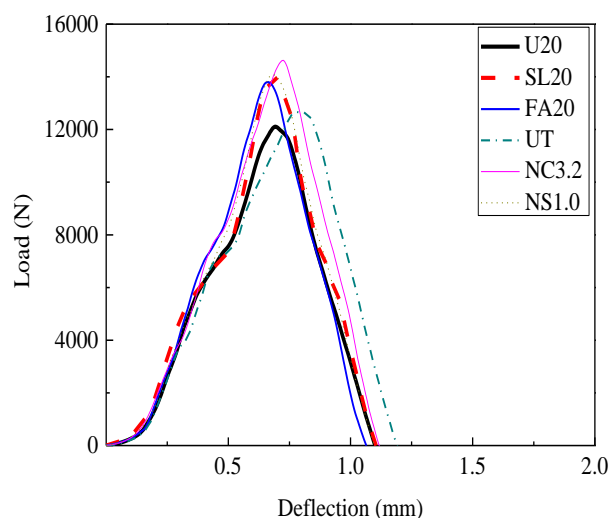


Figure 9.3. Impact flexural load-deflection curves of UHPC matrix at 28 d

Table 9.1 summarizes the static and impact flexural properties of the UHPC matrix at 28 d. The static flexural strength of the specimens ranged from 21 to 24 MPa; it was enhanced by 30%-38% under impact loading. This can be due to the exertion of additional inertia effects under high loading rate, leading to much-localized damage and hence increased impact flexural strength [212]. Dynamic increase factor (DIF), which is the ratio of impact flexural strength to static flexural strength of specimens at the same curing age, was used to compare the improving efficiency of the flexural properties related to SCMs or nano-particles. As observed from Table 9.2, the SL20 mixture showed the highest DIF value, followed by that of the NC3.2 mixture. This demonstrates that the incorporation of 20% SL or 3.2% NC showed better improvement in flexural strength.

Moreover, the use of SCM and nano-particles in ternary or quaternary mixtures increased the total impact energy during impact loading. The total energy of the reference specimen was 6.11 J and increased by 20% and 10% for the NC3.2 and SL20 mixtures, respectively. Compared to the total static energy, the total impact energy was six times greater.

Table 9.1. Summary of static and dynamic flexural properties of UHPC matrix at 28 d

| Mixture | Velocity (m/s) | Impact flexural strength (MPa) | Static flexural strength (MPa) | DIF  | Total impact energy (J) | Total static energy (J) |
|---------|----------------|--------------------------------|--------------------------------|------|-------------------------|-------------------------|
| U20     | 0.27           | 28.6                           | 21.0                           | 1.36 | 6.1                     | 0.9                     |
| SL20    | 0.31           | 32.8                           | 21.6                           | 1.52 | 6.7                     | 1.2                     |
| FA20    | 0.30           | 28.4                           | 21.7                           | 1.31 | 6.5                     | 1.0                     |
| UT      | 0.28           | 29.4                           | 21.1                           | 1.39 | 6.8                     | 0.9                     |
| NC3.2   | 0.26           | 34.3                           | 23.3                           | 1.47 | 7.3                     | 1.4                     |
| NS1.0   | 0.33           | 33.0                           | 23.8                           | 1.38 | 6.8                     | 1.1                     |

### 9.3. BOND PROPERTIES BETWEEN EMBEDDED FIBERS AND UHPC MATRIX

Figure 9.4 illustrates the bond strength and pullout energy between the embedded fibers and the UHPC matrix. The fiber-matrix interfacial bond properties play a dominated role in determining the stress transfer efficiency from the matrix to the fiber as well as strain-hardening behavior. Generally, the higher the fiber-bond properties are, the greater the strength and toughness of the UHPC would be. The addition of SCM and nano-particles improved both the bond strength and the pullout energy. The NC3.2 mixture exhibited the greatest bond strength and pullout energy, followed by those of the SL20 mixture. The bond strength of the reference mixture (U20) at 28 d was 3.3 MPa. It increased by 30% and 48% for SL20 and NC3.2, respectively. The use of SL, FA, and NS can contribute to the interfacial bond properties mainly through the pozzolanic, filling and/or nucleation effects [211]. For nano- $\text{CaCO}_3$ , except the nucleation effect to be absorbed onto the main binding phase C-S-H, to change its structure, it also possesses the ability to react with  $\text{C}_3\text{A}$  to form mono- and/or hemi-carboaluminate [213]. This would generate more hydration products and benefit the fiber-matrix bond properties. In addition, the UT mixture showed the lowest bond strength and toughness, in exception of the reference mixture. This might be attributed to dilution effect to cement because of greater use of SCM content. Wong et al. [211] studied the influence of FA content, varying from 15% to 55%, on the bond strength and fracture properties of mortar-aggregate interface at a water-to-binder ratio of 0.3. The interfacial bond strength and fracture toughness at 28 d increased when 15% FA was incorporated but decreased with further content up to 45% and 55%.

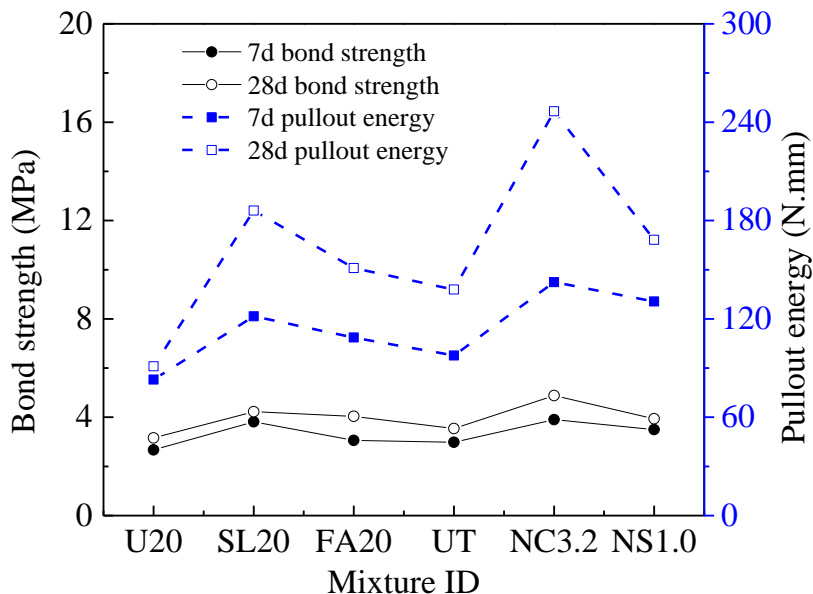


Figure 9.4. Fiber-matrix bond properties at 7 and 28 d

#### 9.4. STATIC AND IMPACT MECHANICAL PROPERTIES OF UHPC

Static and impact mechanical properties of the six UHPC made with 2% steel fibers were investigated.

**9.4.1. Static Compressive and Flexural Strengths of UHPC.** Figure 9.5 illustrates the static compressive and flexural strengths of the UHPC mixtures containing 2% steel fibers after 7 and 28 d of age. The compressive strengths of the UHPC specimens with various SCM or nano-particle types were similar, which were approximately 120 and 155 MPa at 7 and 28 d, respectively. Such values were approximately 9%-14% greater than that of the reference specimens. However, their static flexural strengths showed an apparent difference. UHPC mixture with 3.2% nano- $\text{CaCO}_3$  (NC3.2-2) or 20% slag (SL20-2) exhibited the highest flexural strength, depending on curing time. Their flexural strengths were increased by 15%-22% in

comparison to the reference specimen. In addition, the UT-2 mixture demonstrated a relatively low flexural strength, but was still slightly greater than that of the reference specimen. This is in good agreement with the fiber-matrix bond properties.

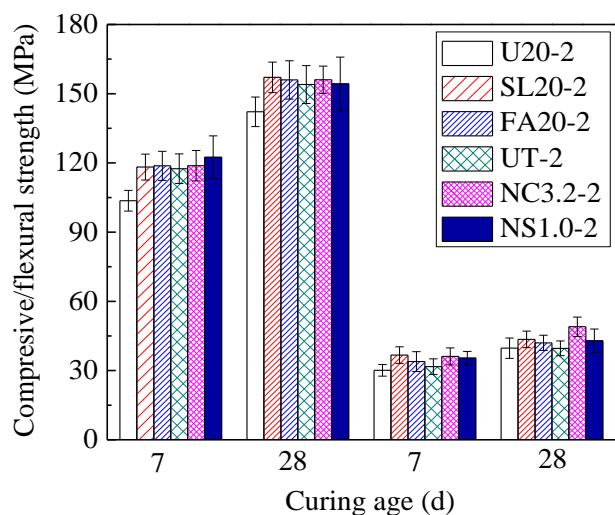


Figure 9.5. Static compressive and flexural strengths of UHPC at 7 and 28 d

The static flexural load-deflection curve of UHPC is illustrated in Figure 9.6. It can be divided into three regions: (1) a linear elastic region; (2) a non-linear region until peak load; and (3) a deflection softening region with curved patterns [214]. In the linear elastic zone, the load increased linearly with the increment of deflection. When the cracking was initiated, the load increased nonlinearly with the deflection at a lower slope to reach the peak load. In this region, the occurrence of cracks was accompanied by fibers gradually be pulled out from the matrix. In the deflection softening region, zig-zag patterns associated with fiber bridging and then fiber pullout processes in the

corresponding crack sections were observed. The size of the patterns decreased with the increase of deflection, indicating decreased capacity in sustaining further loads.

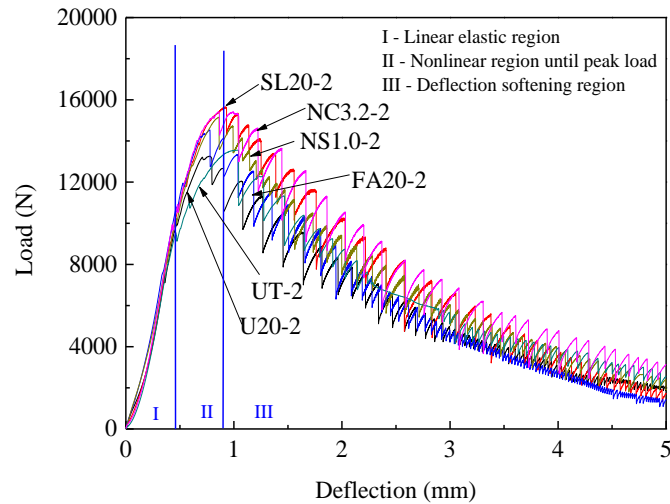


Figure 9.6. Static flexural load-deflection curves of UHPC at 7 d

**9.4.2. Impact Flexural Properties of UHPC.** Figure 9.7 depicts the impact flexural load-deflection curves of UHPC specimens made with 2% steel fibers. The flexural load-deflection relationship can be divided into five regions. Onset of region I, a small initiated load was acted with setting of the loading system. The load then increased linearly with the mid-span deflection at a greater slope until cracking occurred (Region I). In this region, the slope was closely correlated to the flexural strength of the matrix. The NC3.2-2 mixture showed the highest slope, followed by those of SL20-2, NS1.0-2, and FA20-2. A non-linear ascending part (Region II) was followed by the appearance of the peak load at a deflection of approximately 1 mm. The peak flexural strength was strongly linked to the matrix strength and fiber-matrix bond strength. After a sudden drop in the



load (Region III), the load reincreased (Region IV) and eventually reached zero load (V). The reincreased load might be due to the downward acceleration of the drop hammer and/or occurrence of multiple flexural cracks [215]. The first and second peak values varied significantly with the mixture composition. The ternary UHPC mixtures with the incorporation of 20% SL or 3.2% NC had the highest peak load values, which were 20%-30% higher than that of the reference UHPC (U20-2).

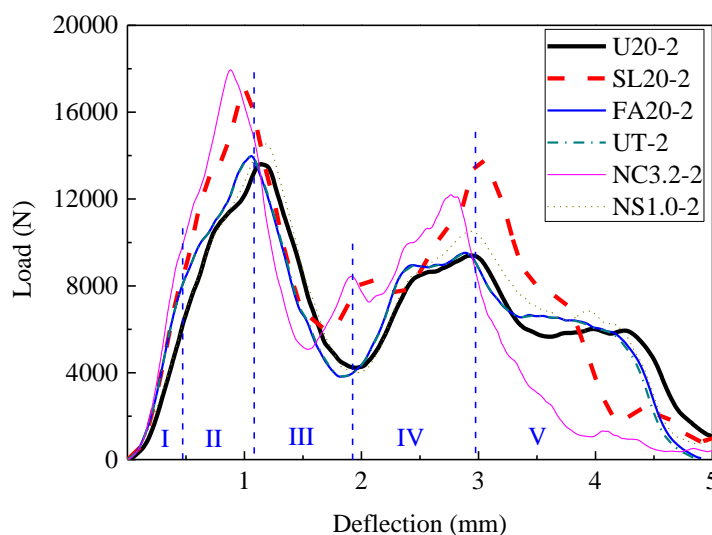


Figure 9.7. Impact flexural load-deflection curves of UHPC at 7 d

Other researchers investigated the effect of nano-particles, including NC, NS, nano-TiO<sub>2</sub>, and nano-Al<sub>2</sub>O<sub>3</sub>, on dynamic compression and tensile properties of UHPC [216]. The authors reported that the UHPC made with 3% nano-CaCO<sub>3</sub> exhibited better crack confinement and the highest compression strength increment. Similarly, Wu et al. [207] compare the static flexural properties of UHPC made with either slag or fly ash replacements of 0, 20%, 40%, and 60% and found that the specimens with the same

content of SL demonstrated better flexural strength and toughness, regardless of curing regime. This contribution associated with SL mixture can be attributed to high pozzolanic effect and nearly the same hydraulic activity as portland cement, which can result in better efficiency in improving interfacial bond properties [217].

Table 9.2 shows the static and dynamic flexural strengths of UHPC at 7 d. The ratios of impact flexural strengths to static flexural strengths (i.e. DIF) varied between 1.02 and 1.16. Generally, the DIF increases with the increase in strain rate and impact velocity [215]. Their total impact energies ranged from 32 to 40 J, which were six times greater than those of the UHPC matrix without any fiber. It should be noted that the total static energy was greater than the total impact energy for some mixtures, which might be due to slower energy dissipation in longer loading time. The loading time for conducting static flexural strength was 5 min, compared to few seconds for the impact flexural strength loading.

Table 9.2. Summary of static and dynamic flexural strengths of UHPC at 7 d

| Mixture | Velocity<br>(m/s) | Impact<br>flexural<br>strength<br>(MPa) | Static<br>flexural<br>strength<br>(MPa) | DIF  | Total<br>impact<br>energy<br>(J) | Total<br>static<br>energy (J) |
|---------|-------------------|---|---|------|----------------------------------|-------------------------------|
| U20-2   | 1.53              | 33.9                                    | 30.1                                    | 1.13 | 36.6                             | 34.9                          |
| SL20-2  | 1.55              | 39.9                                    | 36.7                                    | 1.09 | 38.6                             | 39.1                          |
| FA20-2  | 1.53              | 36.8                                    | 33.9                                    | 1.09 | 32.9                             | 38.5                          |
| UT-2    | 1.54              | 34.5                                    | 31.7                                    | 1.09 | 32.7                             | 33.0                          |
| NC3.2-2 | 1.36              | 42.1                                    | 36.2                                    | 1.16 | 37.8                             | 44.6                          |
| NS1.0-2 | 1.38              | 36.1                                    | 35.4                                    | 1.02 | 36.1                             | 39.4                          |

## 9.5. RADAR CHART ANALYSIS FOR FIBER-MATRIX BOND AND FLEXURAL PROPERTIES

Figure 9.8 compares the fiber-matrix bond and flexural properties of the six UHPC mixtures using radar analysis with considering eight related outputs. The outputs were normalized to compare the contribution of each mixture to the mechanical properties of UHPC. The surrounding areas connected by the eight normalized outputs of the investigated mixtures were integrated. Generally, the greater the area is, the better the flexural properties of UHPC would be. Given the same type and geometry of steel fibers, the flexural strength and toughness of UHPC are governed by the quality of matrix, fiber-matrix interfacial bond, and orientation of fibers. Both SL, FA, NC, and NS can be used to replace cement and improve the flexural properties. The NC3.2-2 and SL20-2 mixtures showed better flexural properties, as can be seen from Fig. 9.8(b).

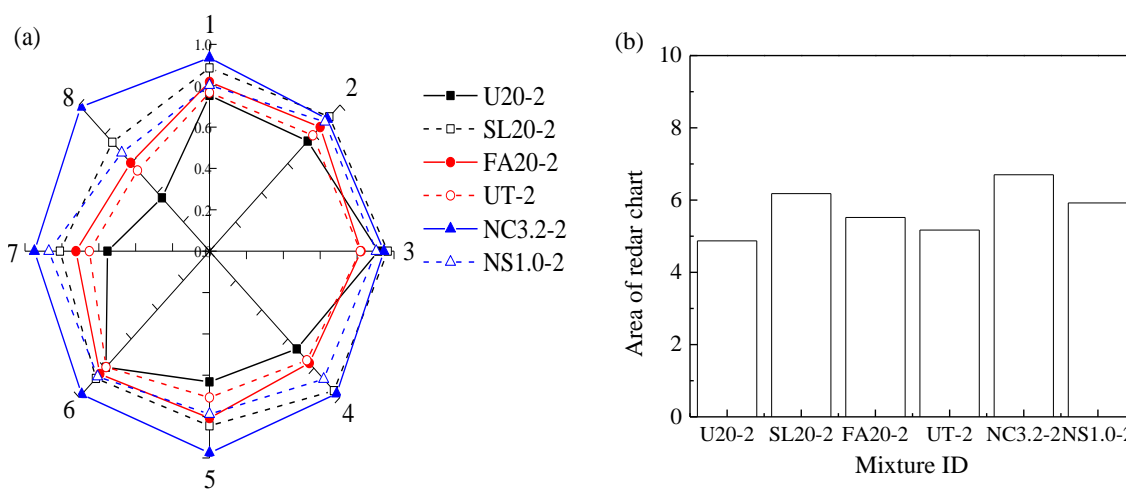


Figure 9.8. Radar chart analysis (a) Radar chart; and (b) Surrounding area (Note: outputs from 1 to 7 denote 7-d impact flexural strength, 7-d static flexural strength, 7-d impact total energy, 7-d bond strength, 28-d bond strength, 28-d static flexural strength, 7-d pullout energy, and 28-d pullout energy, respectively)

## 9.6. SUMMARY

This study investigated the mechanical properties of UHPC made with various types and combinations of SCM and nano-particles. The binary mixture with 20% SF, ternary mixtures with 20% SF + 20% FA, 20% SF + 20% SL, 20% SF + 3.2% NC, and 20% SF + 1.0% NS, and quaternary mixture with 20% SF + 20% FA + 20% SL were used. Fiber-matrix bond properties, compressive strength, and static and impact flexural properties of both UHPC matrix and UHPC incorporating 2% steel fibers were evaluated. Based on the results presented in this study, the following conclusions can be drawn:

(1) The incorporation of 20% SL, 20% FA, 3.2% NC, and 1.0% NS in ternary mixtures increased the 28 d compressive and flexural strength of UHPC matrix (without fiber) by 9%-14% compared to the reference mixture.

(2) Under static flexural loading, the UHPC matrix exhibited a sudden drop at a deflection of approximate 0.4 mm once reaching the peak load. Parabolic flexural load-deflection curves were observed to render greater flexural strength and toughness under impact loading. The impact flexural strength of the UHPC matrix was increased by 30% to 38% compared to the static flexural strength. The total impact energy was six times greater than the total static energy.

(3) The incorporation of 20% SL, 20% FA, 3.2%NC, and 1% NS in ternary UHPC mixtures exerted a comparable effect on compressive strength of UHPC with 2% steel fibers. However, a distinct difference in fiber-bond and flexural strengths of UHPC was observed. Ternary UHPC mixtures with 20% SL or 3.2% NC exhibited better fiber-matrix bonds, which were 30%-48% greater than the reference mixture.

(4) The change in flexural properties of investigated UHPC mixtures made with 2% steel fibers agreed well with the fiber-matrix bond properties. Ternary UHPC mixtures with 20% SL or 3.2% NC had better flexural properties. The 28 d static flexural strengths were improved by 15%-22%, in comparison to the reference specimen. The 7 d impact flexural strengths were enhanced by 20%-30%. The incorporation of 20% FA and 20% SL in quaternary mixture reduced the strength gain due to dilution effect to cement. Therefore, slag and nano-CaCO<sub>3</sub> are recommended for enhancing the flexural properties of UHPC.

## 10. CONCLUSIONS AND FUTURE WORK

### 10.1. CONCLUSIONS

This study focuses on the multi-scale investigation of UHPC in terms of fiber-matrix interfacial properties, microstructure, mechanical properties, and their interrelationships. It aims at preparing cost-effective UHPC with dense structure and superior strength and toughness. The following four parts were undertaken to achieve this goal: 1) influence of different types and contents of SCMs, including silica fume, slag, fly ash, nano-particles, on properties of non-fibrous UHPC matrix. Such properties include flowability, heat of hydration, matrix strength, and fiber-matrix bond properties; 2) investigation on microstructure of matrix and fiber-matrix interface using advanced techniques, such as TG, MIP, XRD, SEM, and micro-hardness; 3) improvement on fiber-matrix bond properties using deformed fibers, including corrugated and hooked fibers, and clarification of bond strengthening and toughening mechanisms associated with fiber geometry; and 4) study on effect of SCM, nano-particles, and fiber geometry on mechanical properties of UHPC made with 2% steel fibers. Based on the corresponding experimental results, the relationship between fiber-matrix bond strength and flexural strength of UHPC was established based on the composite theory. In terms of the corresponding investigation, the following results can be drawn:

**10.1.1. Silica Fume Series.** These include two silica fume series of UHPC matrix made with fixed SP dosage and fixed flowability.

**10.1.1.1. UHPC matrix with fixed SP dosage.** (1) Due to the accelerated hydration of cement by silica fume, the compressive and flexural strengths of UHPC

matrix containing 15%-25% silica fume were enhanced by 10-25 MPa after 28 d standard curing when compared to that of the reference sample.

(2) The CH content and porosity of samples with 15%-25% silica fume were only 3% and 5%-8% after 28 d, respectively. However, when 25% silica fume was replaced, strengths began to decrease due to reduced flowability and slightly increased porosity.

**10.1.1.2. UHPC matrix and UHPC with fixed flowability.** (1) The incorporation of 5%-25% improved the mechanical properties of UHPC with fixed mini-slump flow. The optimal silica fume content for UHPC matrix and UHPC with 2% steel fibers were 10%-20%. Compared to the reference mixture, the flexural and tensile strengths of UHPC made with 10%-20% silica fume were enhanced by 7%-37% and 33%-70%, respectively. With silica fume content further increased up to 25%, the corresponding values were significantly decreased.

(2) The flexural-to-tensile strength ratio of UHPC matrix without fiber was in the range from 1.3 to 2.3, while increased to 1.9 to 2.8 with the addition of 2% steel fibers.

(3) The tensile strength of UHPC made with 2% steel fibers can be efficiently predicted using the composite theory with considering the properties of UHPC matrix, consumed fiber orientation coefficient of 0.5, and fiber characteristics, including fiber geometry, fiber volume, and fiber diameter. The values were dispersed around the equality line with a relative coefficient of 0.64.

**10.1.2. Nano-CaCO<sub>3</sub> Series.** (1) The incorporation of suitable nano-CaCO<sub>3</sub> significantly enhanced the interfacial bond properties between embedded fibers and UHPC matrix. The interfacial bond strength and pullout energy increased first with the increase of nano-CaCO<sub>3</sub> content, then decreased when a critical value of 3.2% was

exceeded. The bond strength and pullout energy were improved by 45% and 200%, respectively, in comparison with the reference specimen after 28 d standard curing.

(2) The bond strength was significantly improved from 1 to 7 d, but was almost mature after 28 d of standard curing. The bond strength and pullout energy can be efficiently predicted given the curing time and nano-CaCO<sub>3</sub> content using the response surface methodology.

(3) The compressive and flexural strengths of UHPC made with 2% steel fibers increased with the incorporation nano-CaCO<sub>3</sub> particles, but decreased when excessive nano-CaCO<sub>3</sub> was used. UHPC with 3.2% nano-CaCO<sub>3</sub> particles reached the highest compressive and flexural strengths, which were 10% and 23%, respectively, greater than those of the reference specimen under 28 d standard curing. This suggests nano-CaCO<sub>3</sub> was efficient in enhancing the efficiency of fiber-matrix stress transfer. Appropriate nano-CaCO<sub>3</sub> content decreased porosity and transformed adhesive failure into cohesive failure, as verified by MIP and BSEM observation. However, excessive nano-CaCO<sub>3</sub> content increased the porosity due to agglomeration issues.

**10.1.3. Nano-SiO<sub>2</sub> Series.** (1) Nano-SiO<sub>2</sub> significantly enhanced the interfacial bond properties between fibers and UHPC matrix. The bond strength and pullout energy increased first with the increase of nano-SiO<sub>2</sub> content, but then decreased when a critical value of 1% was exceeded. Such change was consistent with the compressive strength development of matrix. The bond strength and pullout energy of UHPC matrix with 1% nano-SiO<sub>2</sub> after 28-d standard curing were enhanced by approximately 35% and 70%, respectively, when compared to the reference specimen.



(2) Mechanical properties of UHPC made with different nano-SiO<sub>2</sub> contents increased initially with the increase of nano-SiO<sub>2</sub> content, but decreased when exceeding a critical value of 1%. High content of nano-SiO<sub>2</sub> resulted in great loss of compressive and flexural strengths. The values could be even lower than those of the reference specimen.

(3) Nano-SiO<sub>2</sub> could serve as nuclei for the precipitation of C-S-H, hence leading to more C-S-H content and alteration of C-S-H structure. The Ca/Si ratio in the reference sample was greater than 1. The inclusion of Si element from nano-SiO<sub>2</sub> decreased the Ca/Si ratio to lower value, leading to longer silica chain length and eventually improved mechanical properties of the C-S-H. The addition of 1% nano-SiO<sub>2</sub> resulted in the lowest porosity of matrix associated with denser and more homogeneous microstructure. ITZ with a thickness of 50 μm was observed due to the wall and bleeding effect in correlation with lower micro-harness compared to the bulk matrix.

**10.1.4. UHPC Reinforced with Different Fiber Geometries.** (1) The use of deformed fibers effectively enhanced the interfacial bond properties between fibers and UHPC matrix, as well as mechanical properties of UHPC. Pullout bond strength and toughness of embedded hooked fibers were approximately seven and five times greater, respectively, than those with straight fibers, and three times greater than those of corrugated fibers.

(2) Pullout bond strength did not significantly increase beyond 7 or 28 d, depending on the fiber type. Good exponential correlation was established between CH content and pullout bond strength of embedded fibers. The pullout behavior of the UHPC

matrix prepared with 20% silica fume was greater than that with 15% silica fume. This was confirmed by lower porosity and less CH content in the matrix.

(3) Fiber shape had limited effect on compressive strength of UHPC but significant influence on flexural strength. Depending on the curing age, the flexural strength of UHPC with 2% corrugated and hooked fibers were 8% to 28% and 17% to 50%, respectively, greater than that with straight fibers.

(4) Flexural strength of UHPC incorporating different shaped fibers can be predicted using pullout bond strength of embedded fibers and flexural strength of the non-fibrous UHPC matrix based on the composite theory. The prediction takes into consideration of fiber volume, fiber length, fiber diameter, coefficient related to the fiber orientation in three dimensions. The ratios of predicted to measured value were between 0.8 and 1.1.

**10.1.5. UHPC with Optimized Composition.** (1) The incorporation of 20% SL, 20% FA, 3.2% NC, and 1.0% NS in ternary mixtures increased the 28 -d compressive and flexural strength of UHPC matrix (without fiber) by 9%-14% compared to the reference mixture.

(2) Under static flexural loading, the UHPC matrix exhibited a sudden drop at a deflection of approximate 0.4 mm once reaching the peak load. Parabolic flexural load-deflection curves were observed to render greater flexural strength and toughness under impact loading. The impact flexural strength of the UHPC matrix was increased by 30% to 38% compared to the static flexural strength. The total impact energy was six times greater than the total static energy.

(3) The incorporation of 20% SL, 20% FA, 3.2% NC, and 1.0% NS in the ternary UHPC mixtures exerted a comparable effect on compressive strength of UHPC with 2% steel fibers. However, a distinct difference in fiber-bond and flexural strengths of UHPC was observed. Ternary UHPC mixtures with 20% SL or 3.2% NC exhibited better fiber-matrix bond, which was 30%-48% greater than that of the reference mixture.

(4) The change in flexural properties of investigated UHPC mixtures made with 2% steel fibers agreed well with the fiber-matrix bond properties. Ternary UHPC mixtures with 20% SL or 3.2% NC obtained better flexural properties. The 28 d static flexural strengths were improved by 15%-22%, in comparison to the reference specimen. The 7 d impact flexural strengths were enhanced by 20%-30%. The incorporation of 20% FA and 20% SL in quaternary mixture reduced the strength gain due to dilution effect to cement. Therefore, slag and nano-CaCO<sub>3</sub> are recommended in enhancing the flexural properties of UHPC.

## 10.2. FUTURE RESEARCH

Based on the findings from this study, the following research perspectives are recommended:

(1) The rheological properties of UHPC made with different types and contents of nano-particles and fiber geometries and their effect on flexural and tensile strength of UHPC should be investigated.

(2) The nano-mechanical properties, including indentation modulus and hardness, of hydration products in UHPC optimized with different types and contents of SCMs and nano-particles should be investigated.

(3) Modelling of deformed fiber pullout behavior and flexural/tensile strength of UHPC made with different fiber geometries should be carried out with the consideration of mixture composition, fiber-matrix bond strength, and fiber orientation.

(4) Multi-scale modelling of mechanical properties of UHPC that takes into consideration the fiber-matrix bond strength characteristics and the nano-mechanical properties of the hydration products should be developed.

## APPENDIX

### PEER-REVIEWED JOURNAL ARTICLES

#### Published

- [1] Wu, Z., Khayat, K.H., Shi, C. (2018). How do fiber shape and matrix composition affect fiber pullout behavior and flexural properties of UHPC? *Cement and Concrete Composites*. 2018, 90, 193-201.
- [2] Wu, Z., Shi, C., Khayat, K.H. (2018). Multi-scale investigation of microstructure, fiber pullout behavior, and mechanical properties of ultra-high performance concrete with nano-CaCO<sub>3</sub> particles. *Cement and Concrete Composites*, 86, 255-265.
- [3] Wu, Z., Khayat, K.H., Shi, C. (2017). Effect of nano-SiO<sub>2</sub> particles and curing time on development of fiber-matrix bond properties and microstructure of ultra-high strength concrete. *Cement and Concrete Research*, 95, 247-256.
- [4] Wu, Z., Shi, C., Khayat, K.H. (2016). Influence of silica fume content on microstructure development and bond to steel fiber in ultra-high strength cement-based materials (UHSC). *Cement and Concrete Composites*, 71, 97-109.
- [5] Wu, Z., Shi, C., Khayat, K.H., Wan, S. (2016). Effects of different nanomaterials on hardening and performance of ultra high strength cement-based materials. *Cement and Concrete Composites*, 70: 24-32.
- [6] Shi, C., Wu, Z., Xiao, J., Wang, D., Huang, Z., Fang, Z. (2015). A review on ultra high performance concrete Part I: raw materials and mixture design. *Construction and Building Materials*, 101: 741-751.

#### Submitted

- [7] Wu, Z., Shi, C., Khayat, K.H. (2018). Effect of Effect of SCM and nano-particles on static and dynamic flexural properties of UHPC. Accepted by *Construction and Building Materials*.
- [8] Wu, Z., Khayat, K.H., Shi, C., Tutikian, B.F. (2018). Study of mechanisms underlying strength enhancement of UHPC modified with nano-SiO<sub>2</sub> and nano-CaCO<sub>3</sub>. Submitted to *Cement and Concrete Research*.

#### In progress

- [9] Control of rheology, strength, and fiber bond of UHPC using silica fume

## PEER-REVIEWED CONFERENCE PAPERS

- [10] Wu, Z., Shi, C., Khayat, K.H. (2015). Optimization of microstructure and pullout behavior of fibers in ultra-high performance concrete with the help of nano-particles and heat curing. Proceedings of the 1st International Conference on UHPC Materials and Structures, Oct., 27-30, Changsha, China. pp: 7-22.
- [11] Wu, Z., Shi, C., Khayat, K.H. (2016). Reinforcement mechanisms of fibers in UHPC composites, Proceedings of the 15th International Inorganic-Bonded Fiber Composites Conference, Nov., 7-11, 2016, Fuzhou, China. pp: 8-23.

The following pages provides the first page of the above published work.



Contents lists available at ScienceDirect

Cement and Concrete Composites

journal homepage: [www.elsevier.com/locate/cemconcomp](http://www.elsevier.com/locate/cemconcomp)

## How do fiber shape and matrix composition affect fiber pullout behavior and flexural properties of UHPC?

Zemei Wu<sup>a,b,\*</sup>, Kamal Henri Khayat<sup>a,b,\*\*</sup>, Caijun Shi<sup>a,\*\*\*</sup><sup>a</sup> College of Civil Engineering, Hunan University, Changsha 410082, PR China<sup>b</sup> Department of Civil, Architectural and Environmental Engineering, Missouri University of Science and Technology, Rolla, MO, 65401, USA

### ARTICLE INFO

**Keywords:**  
Fiber shape  
Flexural properties  
Microstructure  
Pullout behavior  
UHPC

### ABSTRACT

The use of steel fiber is essential to secure high strength and ductility in producing ultra-high performance concrete (UHPC). In this study, the interfacial bond properties between embedded steel fibers with different shapes (straight, hooked, and corrugated fibers) and UHPC matrices proportioned with either 15% or 20% silica fume, by mass of binder, under different curing times were investigated. Flexural properties of UHPC reinforced with 2% different shaped fibers were also evaluated. Test results showed that corrugated and hooked fibers significantly improved the bond properties by three to seven times when compared to those with straight fibers. The flexural strength of UHPC with corrugated and hooked fibers were enhanced by 8%–28% and 17%–50%, respectively. Microstructural results from MIP, BSEM, and TG confirmed the change in bond properties. The bond strength of straight fibers exponentially increased with the decrease of calcium hydroxide content. Based on the composite theory, the flexural strengths of UHPC made with different shaped fibers can be efficiently predicted using the fiber-matrix bond strength, the flexural strength of the UHPC matrix (non-fibrous matrix), and the parameters of fibers. The ratios of predicted to measured flexural strengths ranged between 0.8 and 1.1, in which straight fibers showed a larger discreteness due to higher sensitivity of flexural strength associated with the orientation of fibers.

### 1. Introduction

Non-fiber-reinforced concrete is a quasi-brittle material that can undergo brittle failure under tensile load. The brittleness of concrete increases with the increase of concrete strength. In order to use it in structural elements subjected to tensile, fatigue, and impact loads, the design of this composite material should be optimized to ensure adequate strength, ductility, and energy absorbing capacity [1,2]. Ultra-high performance concrete (UHPC) is a new class of materials typically characterized by high content of cementitious materials (800–1200 kg/m<sup>3</sup>), water-to-cementitious material (W/CM) ratio of  $0.20 \pm 0.02$ , use of 1%–4% steel fibers by volume of concrete [3]. The inclusion of short and randomly distributed fibers can significantly improve its strength and toughness [4,5].

The bond at the interface between the fiber and the matrix can greatly affect mechanical properties of the composite material, including that of UHPC. When a composite material is subjected to external loads, the matrix would initially sustain the load and then the fiber through stress transferring at the fiber-matrix interface [6]. When

a fiber is pulled out from the matrix, two failure modes would occur: a debonding or a fracture of the fiber [12]. Fiber rupture will be observed if the pullout load that corresponding to the tensile strength of the fiber is lower than that of the shear strength of the matrix. This failure mode is not ideal from the point of view of reinforcement because of limited energy dissipation and underutilization of the potential mechanical property of the fiber [7,13]. Besides, the energy is released abruptly, which can dramatically decrease the toughness of the composite material. However, if appropriate high tensile strength approaching to the ultimate tensile strength of fiber is exerted, higher energy dissipated associated with the fiber-matrix interface could be obtained.

Several strategies can be used to improve bond properties at interfacial transition zone (ITZ) between the embedded fibers and the matrix, including: (1) densification of the cementitious matrix [8–10]; (2) use of deformed fibers [11]; (3) surface treatment of fibers, such as plasma treatment for polyethylene fibers [12]. The increase level of bond resulting from the use of deformed fibers appears to offer the highest degree of bond improvement [12,13]. The bond mechanism between embedded fibers and surrounding matrix typically includes

\* Corresponding author. College of Civil Engineering, Hunan University, Changsha 410082, PR China.

\*\* Corresponding author. College of Civil Engineering, Hunan University, Changsha 410082, PR China.

\*\*\* Corresponding author.

E-mail addresses: [zemeianmian@gmail.com](mailto:zemeianmian@gmail.com) (Z. Wu), [khayat@mst.edu](mailto:khayat@mst.edu) (K.H. Khayat), [cshi@hnu.edu.cn](mailto:cshi@hnu.edu.cn) (C. Shi).<https://doi.org/10.1016/j.cemconcomp.2018.03.021>

Received 4 October 2016; Received in revised form 12 April 2017; Accepted 22 March 2018

Available online 27 March 2018

0958-9465/© 2018 Published by Elsevier Ltd.



Contents lists available at ScienceDirect

## Cement and Concrete Composites

journal homepage: [www.elsevier.com/locate/cemconcomp](http://www.elsevier.com/locate/cemconcomp)

## Multi-scale investigation of microstructure, fiber pullout behavior, and mechanical properties of ultra-high performance concrete with nano-CaCO<sub>3</sub> particles

Zemei Wu<sup>a, b</sup>, Caijun Shi<sup>a, \*</sup>, Kamal Henri Khayat<sup>a, b, \*\*</sup><sup>a</sup> Key Laboratory for Green & Advanced Civil Engineering Materials and Application Technology of Hunan Province, College of Civil Engineering, Hunan University, Changsha 410082, PR China<sup>b</sup> Department of Civil, Architectural and Environmental Engineering, Missouri University of Science and Technology, Rolla 65401, MO, USA

## ARTICLE INFO

## Article history:

Received 20 May 2017

Received in revised form

12 October 2017

Accepted 14 November 2017

Available online 21 November 2017

## Keywords:

Fiber-matrix bond properties

Mechanical properties

Microstructure

Nano-CaCO<sub>3</sub>

UHPC

Statistical model

## ABSTRACT

The mechanical properties of a fiber-reinforced concrete are closely related to the properties of the matrix, fiber, and fiber-matrix interface. The fiber-matrix bond property is mainly governed by the adhesion between the fiber and surrounding cement materials, as well as the strength of materials at the interfacial transition zone. In this paper, the effect of nano-CaCO<sub>3</sub> content, varying between 0 and 6.4%, by mass of cementitious materials, on microstructure development, fiber-matrix interfacial bond properties, and mechanical properties of ultra-high performance concrete (UHPC) reinforced with 2% steel fibers were investigated. The bond properties, including bond strength and pullout energy, were evaluated. Mercury intrusion porosimetry (MIP), backscattered electron microscopy (BSEM), optical microscopy, and micro-hardness testing were used to characterize the microstructure of matrix and/or interfacial transition zone (ITZ) around an embedded steel fiber. Test results indicated that the incorporation of 3.2% nano-CaCO<sub>3</sub> significantly improved the fiber-matrix bond properties and the flexural properties of UHPC. This was attributed to densification and strength enhancement of ITZ as observed from micro-structural analyses. Beyond the nano-CaCO<sub>3</sub> content of 3.2%, the fiber bond and mechanical properties of UHPC decreased due to increased porosity associated with agglomeration of the nano-CaCO<sub>3</sub>.

© 2017 Elsevier Ltd. All rights reserved.

### 1. Introduction

Ultra-high performance concrete (UHPC) is produced with high content of binder, low water-to-binder ratio, use of small fibers, and/or absence of coarse aggregate [1,2]. The design of UHPC involves in reduction in porosity, improvement in microstructure, enhancement in homogeneity, and increase in strength and toughness [2–4]. The superior strength and ductility can enable the production of lightweight and flexible UHPC structure, whereas dense structure, excellent durability, and stability can endow the structure with long service life and low maintenance [5,6]. Although UHPC is less porous compared to conventional concrete, a

relatively weak interfacial transition zone (ITZ) still exists. The strength and ductility of fiber-reinforced concrete mainly depend on the quality of the micro- and nano-scale structure, especially at the fiber-matrix interface. Therefore, it is essential to engineer the microstructure of the ITZ in order to enhance fiber-matrix bond in UHPC. Such properties have marked influence on macro-properties. There are three main ways to improve the bond at the fiber-matrix interface: 1) densification of the cementitious matrix using supplementary of cementitious materials (SCMs), nano-particles, and high temperature curing [7]; 2) enhancement of mechanical anchorage through the use of deformed fibers [8]; and 3) improvement of fiber-matrix friction by surface treatment [9].

Densification of the cementitious matrix is the most fundamental method, which targets at densifying the microstructure and enhancing the strength of the matrix. A high amount of SCMs, such as silica fume, slag, fly ash, and a small amount of nano-materials have been used for this purpose [10,11]. It was reported that incorporation of 15% to 25% silica fume, by mass of cementitious

\* Corresponding author.

\*\* Corresponding author. Key Laboratory for Green &amp; Advanced Civil Engineering Materials and Application Technology of Hunan Province, College of Civil Engineering, Hunan University, Changsha 410082, PR China.

E-mail addresses: [cshi@hnu.edu.cn](mailto:cshi@hnu.edu.cn) (C. Shi), [khayat@mst.edu](mailto:khayat@mst.edu) (K.H. Khayat).





## Effect of nano-SiO<sub>2</sub> particles and curing time on development of fiber-matrix bond properties and microstructure of ultra-high strength concrete

Zemei Wu<sup>a,b</sup>, Kamal Henri Khayat<sup>a,b,\*</sup>, Caijun Shi<sup>a,\*\*</sup>

<sup>a</sup> College of Civil Engineering, Hunan University, Changsha 410082, Hunan, PR China

<sup>b</sup> Department of Civil, Architectural and Environmental Engineering, Missouri University of Science and Technology, Rolla 65409, MO, USA

### ARTICLE INFO

#### Article history:

Received 4 December 2016

Received in revised form 23 February 2017

Accepted 28 February 2017

Available online xxxxx

#### Keywords:

Bond strength

Microstructural analysis

Nano-SiO<sub>2</sub>

Pullout energy

Statistical model

Steel fiber

UHSC

### ABSTRACT

Bond properties between fibers and cementitious matrix have significant effect on the mechanical behavior of composite materials. In this study, the development of steel fiber-matrix interfacial bond properties in ultra-high strength concrete (UHSC) proportioned with nano-SiO<sub>2</sub> varying between 0 and 2%, by mass of cementitious materials, was investigated. A statistical model relating either bond strength or pullout energy to curing time and nano-SiO<sub>2</sub> content was proposed by using the response surface methodology. Mercury intrusion porosimetry (MIP) and backscatter scanning electron microscopy (BSEM) were used to characterize the microstructure of the matrix and the fiber-matrix interface, respectively. Micro-hardness around the embedded fiber and hydration products of the matrix were evaluated as well. Test results indicated that the optimal nano-SiO<sub>2</sub> dosage was 1% in terms of the bond properties and the microstructure. The proposed quadratic model efficiently predicted the bond strength and pullout energy with consideration of curing time and nano-SiO<sub>2</sub> content. The improvement in bond properties associated with nano-silica was correlated with denser matrix and/or interface and stronger bond and greater strength of hydration products based on microstructural analysis.

Published by Elsevier Ltd.

### 1. Introduction

Ultra-high performance concrete (UHPC) is an advanced composite material typically made with very low water-to-binder ratio of  $0.20 \pm 0.02$  and contains high content of binder, high efficiency superplasticizer, and high strength fibers [1]. As an intrinsically heterogeneous material, its mechanical properties are governed by the quality of the matrix, the characteristic of the fiber, and the quality of the interfacial transition zone (ITZ) between the fiber or aggregate and the matrix [2–4]. The bond properties of fiber-matrix interface play a predominant role in the mechanical properties of composite materials because of stress transferring at this interface, which can make an intrinsically brittle material into a ductile one [5,6]. The microstructure of UHPC is denser and more homogenous than that of ordinary concrete [7,8]. However, as the fiber-matrix interface bridging different phases with various stiffnesses, it is a special component and still the most important yet least understood part in UHPC. Therefore, optimization of

the properties at the fiber-matrix interface is necessary for improving the overall mechanical behavior of composite materials.

With the advance and development of nanotechnology, the efficiency of using nano-SiO<sub>2</sub> in cement-based materials has been investigated. These include the effect on microstructure [9,10], heat of hydration [10, 11], workability and rheological properties [12–15], mechanical properties [9,16], dimensional stability [17], and durability [18,19]. Because of its extremely small size and highly pozzolanic activity, it can act as nuclei or filler in cement paste to accelerate the heat of hydration [11], densify the microstructure [9,10], and hence enhance the homogeneity and improve the early-age mechanical properties and durability [16,17]. So far, no information focuses on the contribution of nano-particles on the interfacial bond properties between fibers and ultra-high strength concrete (UHSC).

This study aims at investigating the influence of different nano-SiO<sub>2</sub> contents, varying from 0 to 2%, by mass of cementitious material, on the fiber-matrix bond and microstructure of UHSC. A simple and effective doubled-sided pullout testing was conducted to evaluate the interfacial bond properties, which include pullout load-slip relationship, bond strength, and pullout energy. Mercury intrusion porosimetry (MIP), backscatter scanning electron microscopy (BSEM), micro-hardness measurement, and X-ray diffraction (XRD) analysis were employed to evaluate the microstructural features associated with the matrix and/

\* Corresponding author at: College of Civil Engineering, Hunan University, Changsha 410082, Hunan, PR China.

\*\* Corresponding author.

E-mail addresses: [khayat@mst.edu](mailto:khayat@mst.edu) (K.H. Khayat), [cshi@hnu.edu.cn](mailto:cshi@hnu.edu.cn) (C. Shi).



## Influence of silica fume content on microstructure development and bond to steel fiber in ultra-high strength cement-based materials (UHSC)



Zemei Wu<sup>a,b</sup>, Caijun Shi<sup>a,\*</sup>, K.H. Khayat<sup>b</sup>

<sup>a</sup> College of Civil Engineering, Hunan University, Changsha 410082, PR China

<sup>b</sup> Department of Civil, Architectural and Environmental Engineering, Missouri University of Science and Technology, Rolla, MO 65401, USA

### ARTICLE INFO

#### Article history:

Received 26 July 2015

Received in revised form

20 December 2015

Accepted 7 May 2016

Available online 9 May 2016

#### Keywords:

UHSC

Silica fume

Steel fiber

Compressive and flexural strengths

Microstructure

Fiber pullout behavior

### ABSTRACT

The use of silica fume can significantly enhance mechanical properties of concrete given its beneficial filling and pozzolanic effects. In this study, a simple and effective double-side pullout testing method was adopted to characterize the interfacial bond properties, which include pullout load-slip relationship, bond strength, and pullout energy, of steel fiber-matrix in ultra-high strength cement-based material (UHSC) with 0–25% silica fume by the mass of binder. The effects of silica fume content on flowability, heat of hydration, compressive and flexural strengths, hydration products, and pore structure of matrix at different curing time were evaluated as well. Backscatter scanning electron microscopy (BSEM) and micro-hardness measurement were used to examine the quality of interfacial transition zone (ITZ) around the fiber. In terms of the results, the optimal silica fume content could be in the range of 15%–25%. UHSC mixtures with these dosages of silica fume showed significant improvement in pullout behavior. Its bond strength and pullout energy at 28 d could increase by 170% and 250% compared to the reference samples without any silica fume. The microstructural observation verified the findings on the macro-properties development. Formation of more and higher strength of hydration products and refinement of ITZ around the fiber ensured higher micro-hardness, and thus improved the bond to fiber.

© 2016 Elsevier Ltd. All rights reserved.

### 1. Introduction

Ultra-high strength cement-based material (UHSC) is an advanced material characterized by use of high content of cementitious materials, sand, superplasticizer and/or fibers, and absence of coarse aggregate [1]. The very low water-to-binder ratio ( $w/b$ ) and dense microstructure allow its high strength generally over 120 MPa and superior durability. However, the higher the compressive strength is, the more brittle the matrix becomes. Fiber has been proven as an essential part for UHSC [2,3]. With the incorporation of proper fibers, the initiation, propagation or coalescence of cracks can be efficiently controlled. Many types of fiber, such as carbon, steel, and polypropylene fibers have been used in UHSC. Steel fiber is the most commonly used one because of its superior tensile strength over 2000 MPa. The incorporation of such steel fiber ensures satisfactory mechanical properties, such as

tensile, bending, and shear strengths of UHSC [4,5]. However, bond failure associated with fiber-matrix interface is the primary reason leading to the failure of the whole structure [6]. It was reported that there exists two different interfacial failure modes when steel fibers are pulled out from matrix [7]. One is adhesive failure often occurring at actual fiber-matrix interface, while the other one is adherent failure taking place in matrix. Both failure modes would directly lead to underutilization of fiber or matrix without fully exerting their own mechanical capacity, and eventually result in cracking of composites. Therefore, improvement in the bond properties between fiber and matrix is of great significance.

The performance of fiber reinforced composites is governed by the quality of matrix, geometry and type of fiber, and quality of interfacial transition zone (ITZ) between the fiber or aggregate and matrix [7–9]. Several strategies can be used to improve the bond properties at fiber-matrix interface, including: (1) densification of the cementitious matrix and ITZ [8,9]; (2) use of deformed fibers [4,10]; (3) surface treatment of fibers, such as plasma treatment for polyethylene fibers [7]. Because ITZ has a thickness varying between 10 and 100  $\mu\text{m}$ , and contains large preferentially calcium

\* Corresponding author.

E-mail address: [cshi@hnu.edu.cn](mailto:cshi@hnu.edu.cn) (C. Shi).



## Effects of different nanomaterials on hardening and performance of ultra-high strength concrete (UHSC)



Zemei Wu<sup>a, b</sup>, Caijun Shi<sup>a, \*</sup>, K.H. Khayat<sup>b</sup>, Shu Wan<sup>a</sup>

<sup>a</sup> College of Civil Engineering, Hunan University, Changsha 410082, PR China

<sup>b</sup> Department of Civil, Architectural and Environmental Engineering, Missouri University of Science and Technology, Rolla, MO, USA

### ARTICLE INFO

#### Article history:

Received 19 July 2015

Received in revised form

9 January 2016

Accepted 26 March 2016

Available online 29 March 2016

#### Keywords:

UHSC

Nano-CaCO<sub>3</sub>

Nano-SiO<sub>2</sub>

Hydration

Strength

Calcium hydroxide

Pore structure

### ABSTRACT

Nanomaterials have attracted much interest in cement-based materials during the past decade. In this study, the effects of different nano-CaCO<sub>3</sub> and nano-SiO<sub>2</sub> contents on flowability, heat of hydration, mechanical properties, phase change, and pore structure of ultra-high strength concrete (UHSC) were investigated. The dosages of nano-CaCO<sub>3</sub> were 0, 1.6%, 3.2%, 4.8%, and 6.4%, by the mass of cementitious materials, while the dosages of nano-SiO<sub>2</sub> were 0, 0.5%, 1.0%, 1.5%, and 2%. The results indicated that both nano-CaCO<sub>3</sub> and nano-SiO<sub>2</sub> decreased the flowability and increased the heat of hydration with the increase of their contents. The optimal dosages to enhance compressive and flexural strengths were 1.6%–4.8% for the nano-CaCO<sub>3</sub> and 0.5%–1.5% for the nano-SiO<sub>2</sub>. Although compressive and flexural strengths were comparable for the two nanomaterials after 28 d, their strength development tendencies with age were different. UHSC mixtures with nano-SiO<sub>2</sub> showed continuous and sharp increase in strength with age up to 7 d, while those with nano-CaCO<sub>3</sub> showed almost constant strength between 3 and 7 d, but sharp increase thereafter. Thermal gravimetry (TG) analysis demonstrated that the calcium hydroxide (CH) content in UHSC samples decreased significantly with the increase of nano-SiO<sub>2</sub> content, but remained almost constant for those with nano-CaCO<sub>3</sub>. Mercury intrusion porosimetry (MIP) results showed that both porosity and critical pore size decreased with the increase of hydration time as well as the increase of nanoparticles content to an optimal threshold, beyond which porosity decreased. The difference between them was that nano-CaCO<sub>3</sub> mainly reacted with C<sub>3</sub>A to form carboaluminates, while nano-SiO<sub>2</sub> reacted with Ca(OH)<sub>2</sub> to form C–S–H. Both nano-CaCO<sub>3</sub> and nano-SiO<sub>2</sub> demonstrated nucleation and filling effects and resulted in less porous and more homogeneous structure.

© 2016 Elsevier Ltd. All rights reserved.

### 1. Introduction

Ultra-high strength cement based-material (UHSC) is a novel type of composite materials with superior static and dynamic mechanical properties, and excellent durability. Such material can be used in marine structures, defense and military engineering applications, and high building construction [1–3]. However, as an intrinsically heterogeneous material, the structure of cement-based materials can be generally discretized into four multi-scale phases: nano, micro, meso, and macro [4]. The macro-properties of cement-based materials are dominated by the structure at the nano-scale level. The main hydration product, C–S–H, occupies at least 60–70% by volume of the hardened cement paste. It is a nano-scale

material with average diameter around 10 nm [5]. It is suggested that C–S–H has low, high, and ultra-high density forms with different hardness and elastic modulus values and volume fractions [4,6]. High density C–S–H degrades much slower than low density C–S–H under external environmental condition [6]. Furthermore, water loss from pores in the C–S–H gel can lead to considerable autogeneous shrinkage, which can cause cracking and loss in strength and durability of UHSC [7]. Therefore, it is vital to optimize the microstructure of cement-based materials from the nano-scale to ensure high performance.

Nanotechnology has attracted much interest over the past decade. Since the introduction of nanomaterials, extensive research has been conducted to promote their use in cement-based material. It is well known that nanomaterials can provide significant enhancement in performance of cement-based material given their physical effect (filling and nucleation effects) as well as the chemical reactivity [8]. Nano-silica (nano-SiO<sub>2</sub>) [9], nano-alumina (nano-

\* Corresponding author.

E-mail address: [cshi@hnu.edu.cn](mailto:cshi@hnu.edu.cn) (C. Shi).



Contents lists available at ScienceDirect

## Construction and Building Materials

journal homepage: [www.elsevier.com/locate/conbuildmat](http://www.elsevier.com/locate/conbuildmat)

## Review

## A review on ultra high performance concrete: Part I. Raw materials and mixture design



Caijun Shi\*, Zemei Wu, Jianfan Xiao, Dehui Wang, Zhengyu Huang, Zhi Fang

College of Civil Engineering, Hunan University, Changsha 410082, PR China

## HIGHLIGHTS

- Four theoretical principles for production of UHPC, including reduction in porosity, improvement in microstructure, enhancement in homogeneity, and increase in toughness, are reviewed.
- Effects of different raw materials on performance of UHPC are summarized.
- Mixture design, sample preparation, and curing regimes are discussed.
- Use of conventional materials and common technology are trends for production of UHPC.

## ARTICLE INFO

## Article history:

Received 17 September 2014  
 Received in revised form 28 August 2015  
 Accepted 15 October 2015

## Keywords:

Ultra high performance concrete  
 Theoretical principles  
 Raw materials  
 Mixture design  
 Curing regime

## ABSTRACT

Ultra high performance concrete (UHPC) refers to cement-based materials exhibiting compressive strength higher than 150 MPa, high ductility, and excellent durability. This paper reviews the theoretical principles, raw materials, mixture design methods, and preparation techniques for UHPC. Reduction in porosity, improvement in microstructure, enhancement in homogeneity, and increase in toughness are four basic principles for UHPC design. Raw materials, preparation technique, and curing regimes have significant influence on properties of UHPC. The use of widely available supplementary cementitious materials, such as fly ash and slag for partial/complete replacement of cement and silica fume, could significantly reduce the materials cost without sacrifice of strength. The use of high temperature curing results in denser microstructure and better performance than room temperature curing does, but obviously limits its applications of UHPC. Thus, preparation of UHPC using widely available raw materials, common technology, such as conventional casting and room temperature curing, are trends for production of UHPC.

© 2015 Elsevier Ltd. All rights reserved.

## Contents

|  |     |
|--|-----|
| 1. Introduction .....  | 742 |
| 2. Theoretical principles for production of UHPC .....               | 742 |
| 2.1. Reduction in porosity .....                                     | 742 |
| 2.1.1. Close packing of raw materials .....                          | 742 |
| 2.1.2. Water reduction using high performance superplasticizer ..... | 743 |
| 2.2. Improvement in microstructure .....                             | 743 |
| 2.3. Enhancement in homogeneity .....                                | 743 |
| 2.4. Increase in toughness .....                                     | 743 |
| 3. Raw materials .....   | 744 |
| 3.1. Cementitious components .....                                   | 744 |
| 3.1.1. Portland cement .....   | 744 |
| 3.1.2. Silica fume (SF) .....  | 744 |
| 3.1.3. Granulated blast furnace slag (GGBFS) .....                   | 744 |

\* Corresponding author.  
 E-mail address: [cshi@hnu.edu.cn](mailto:cshi@hnu.edu.cn) (C. Shi).

## BIBLIOGRAPHY

- [1] Shah, S.P., Swartz, S.E., Ouyang, C. (1995). Fracture mechanics of concrete, John Wiley & Sons, Inc., New York.
- [2] ACI Committee 544. (2014). Fiber Reinforced Concrete. Main Committee Meeting Minutes. ACI Spring Convention. Reno, Nevada.
- [3] Roumaldi J.P., Batson G. B. Mechanics of crack arrest in concrete, 1963.
- [4] Romualdi, J.P., Mandel, J.A. (1964). Tensile strength of concrete affected by uniformly distributed and closely spaced short lengths of wire reinforcement. In *Journal Proceedings*, 61(6), 657-672.
- [5] Yao, W., Li, J., Wu, K. (2003). Mechanical properties of hybrid fiber-reinforced concrete at low fiber volume fraction. *Cement and concrete research*, 33(1), 27-30.
- [6] Khayat, K.H., & Roussel, Y. (2000). Testing and performance of fiber-reinforced, self-consolidating concrete. *Materials and Structures*, 33(6), 391-397.
- [7] Haynes, H.H. (1968). *Investigation of fiber reinforcement methods for thin shell concrete* (No. NCEL-TN-979). Naval Civil Engineering Laboratory, Port Hueneme, CA, N-979, 1-26.
- [8] Lankard, D.R., & Newell, J.K. (1984). Preparation of highly reinforced steel fiber reinforced concrete composites. *Special Publication*, 81, 287-306.
- [9] Hackman, L.E., Farrell, M.B., & Dunham, O.O. (1992). Slurry infiltrated mat concrete (SIMCON). *Concrete International*, 14(12), 53-56.
- [10] Li, H., Xu, S., & Leung, C.K. (2009). Tensile and flexural properties of ultra high toughness cementitious composite. *Journal of Wuhan University of Technology-Mater. Sci. Ed.*, 24(4), 677-683.
- [11] Li, V.C., & Leung, C.K. (1992). Steady-state and multiple cracking of short random fiber composites. *Journal of Engineering Mechanics*, 118(11), 2246-2264.
- [12] Li, V.C., Mishra, D.K., & Wu, H.C. (1995). Matrix design for pseudo-strain-hardening fibre reinforced cementitious composites. *Materials and Structures*, 28(10), 586-595.
- [13] Li, V.C., Wang, S., & Wu, C. (2001). Tensile strain-hardening behavior of polyvinyl alcohol engineered cementitious composite (PVA-ECC). *ACI Materials Journal-American Concrete Institute*, 98(6), 483-492.
- [14] Richard, P., & Cheyrezy, M.H. (1994). Reactive powder concretes with high ductility and 200-800 MPa compressive strength. *Special Publication*, 144, 507-518.

- [15] Richard, P., & Cheyrezy, M. (1995). Composition of reactive powder concretes. *Cement and concrete research*, 25(7), 1501-1511.
- [16] ACI 239 (2012), Committee in Ultra-High Performance Concrete, Minutes of Committee Meeting October 2012, ACI Annual Conference 2012, Toronto, ON, Canada.
- [17] Schmidt, M., & Fehling, E. (2005). Ultra-high-performance concrete: research, development and application in Europe. *ACI Special publication*, 228, 51-78.
- [18] Meng, W., Valipour, M. and Khayat, K.H. (2017). Optimization and performance of cost-effective ultra-high performance concrete. *Materials and structures*, 50(1), 9.
- [19] Meng, W. & Khayat, K.H. (2017). Effects of saturated lightweight sand content on key characteristics of ultra-high-performance concrete. *Cement and Concrete Research*, 101, 46-54.
- [20] C1856/C1856M – 17 (2017). Standard practice for fabricating and testing specimens of ultra-high performance concrete.
- [21] Habel, K. (2004). Structural behaviour of elements combining ultra-high performance fibre reinforced concretes (UHPFRC) and reinforced concrete. 2004, Ph.D. dissertation, Lausanne, École Polytechnique Fédérale De Lausanne, Switzerland.
- [22] Wu, Z., Shi, C., He, W., & Wang, D. (2016). Uniaxial compression behavior of ultra-high performance concrete with hybrid steel fiber. *Journal of Materials in Civil Engineering*, 28(12), 06016017.
- [23] Röbler, M., Odler, I. (1985). Investigations on the relationship between porosity, structure and strength of hydrated portland cement pastes I. Effect of porosity. *Cement and Concrete Research*, 15(2): 320-330.
- [24] Odler, I., Röbler, M. (2005). Investigations on the relationship between porosity, structure and strength of hydrated Portland cement pastes. II. Effect of pore structure and of degree of hydration. *Cement and Concrete Research*, 15(3), 401-410.
- [25] Lian, C., Zhuge, Y., & Beecham, S. (2011). The relationship between porosity and strength for porous concrete. *Construction and Building Materials*, 25(11), 4294-4298.
- [26] Yajun, J., & Cahyadi, J. H. (2003). Effects of densified silica fume on microstructure and compressive strength of blended cement pastes. *Cement and Concrete Research*, 33(10), 1543-1548.
- [27] Park, C.K., Noh, M.H., Park, T.H. (2005). Rheological properties of cementitious materials containing mineral admixtures. *Cement and Concrete Research*, 35(5): 842-849.

- [28] Saric-Coric, M., Khayat, K.H., & Tagnit-Hamou, A. (2003). Performance characteristics of cement grouts made with various combinations of high-range water reducer and cellulose-based viscosity modifier. *Cement and Concrete Research*, 33(12), 1999-2008.
- [29] Khayat, K.H., Lessard, M., (1995). Influence of Early Heat Curing on Properties of 100-MPa Air-Entrained Concrete, *Transportation Research Record*, 1458, Concrete Research, 91-98
- [30] Wu, Z., Shi, C., Khayat, K.H. (2015). Optimization of microstructure and pullout behavior of fibers in ultra-high performance concrete with the help of nano-particles and heat curing. Proceedings of the 1st International Conference on UHPC Materials and Structures, pp.7-22, Oct27-30, Changsha, China.
- [31] Reda, M. M., Shrive, N. G., & Gillott, J. E. (1999). Microstructural investigation of innovative UHPC. *Cement and Concrete Research*, 29(3), 323-329.
- [32] Shmidt, M, Fehling, E, Grundlagen der Betontechnologie von Hochund Ultra Hochleistungsbeton und Anwendung von UHPC im Bruckenbau. In: Ultra high performance concrete - 10 years of research and development at the University of Kassel. Kassel, Germany. 2007, 70-81.
- [33] Chan, Y. W., Chu, S.H. (2004). Effect of silica fume on steel fiber bond characteristics in reactive powder concrete. *Cement and Concrete Research*, 34(7), 1167-1172.
- [34] Sellevold, E.J., & Bjøntegaard, Ø. (2006). Coefficient of thermal expansion of cement paste and concrete: Mechanisms of moisture interaction. *Materials and Structures*, 39(9), 809-815.
- [35] Elsharief, A., Cohen, M.D., & Olek, J. (2003). Influence of aggregate size, water cement ratio and age on the microstructure of the interfacial transition zone. *Cement and Concrete Research*, 33(11), 1837-1849.
- [36] Sorelli, L., Constantinides, G., Ulm, F.J., & Toutlemonde, F. (2008). The nano-mechanical signature of ultra high performance concrete by statistical nanoindentation techniques. *Cement and Concrete Research*, 38(12), 1447-1456.
- [37] Zhao, S., & Sun, W. (2014). Nano-mechanical behavior of a green ultra-high performance concrete. *Construction and Building Materials*, 63, 150-160.
- [38] Prabha, S.L., Dattatreya, J. K., Neelamegam, M., & Seshagirirao, M. V. (2010). Study on stress-strain properties of reactive powder concrete under uniaxial compression. *International Journal of Engineering Science and Technology*, 2(11), 6408-6416.
- [39] Zollo, R.F. (1997). Fiber-reinforced concrete: an overview after 30 years of development. *Cement and Concrete Composites*, 19(2), 107-122.

- [40] Wu, Z., Shi, C., He, W., & Wu, L. (2016). Effects of steel fiber content and shape on mechanical properties of ultra high performance concrete. *Construction and Building Materials*, 103, 8-14.
- [41] Wuest, J., EPF, C.E., Brühwiler, E., & ETH, D.C.E. (2008). Model for predicting the UHPFRC tensile hardening. In *Ultra High Performance Concrete (UHPC): Proceedings of the Second International Symposium on Ultra High Performance Concrete*, Kassel, Germany, March 05-07, 2008 (No. 10, p. 153). Kassel university press GmbH.
- [42] Yoo, D.Y., Kang, S.T., & Yoon, Y.S. (2016). Enhancing the flexural performance of ultra-high-performance concrete using long steel fibers. *Composite Structures*, 147, 220-230.
- [43] Maso, J.C. (1980). The bond between aggregates and hydrated cement pastes. *7th Int. Cong. on the Chem. of Cement, Paris, France*, 3, VII-1.
- [44] Hadley, D. W. (1972). Nature of the paste-aggregate interface. Ph.D thesis, Purdue University.
- [45] Horne, A.T., Richardson, I.G., & Brydson, R.M.D. (2007). Quantitative analysis of the microstructure of interfaces in steel reinforced concrete. *Cement and Concrete Research*, 37(12), 1613-1623.
- [46] Mondal, P., Shah, S.P., & Marks, L. (2007). A reliable technique to determine the local mechanical properties at the nanoscale for cementitious materials. *Cement and Concrete Research*, 37(10), 1440-1444.
- [47] Lyubimova, T.Y., & Pinus, E.R. (1962). Crystallization structure in the contact zone between aggregate and cement in concrete. *Colloid J. USSR*, 24(5), 491-498.
- [48] Zimbelmann, R. (1985). A contribution to the problem of cement-aggregate bond. *Cement and Concrete Research*, 15(5), 801-808.
- [49] Bentur, A., Mindess, S. *Fibre reinforced cementitious composites*. CRC Press, 2006.
- [50] Sun Wei, J.A. Mandel and Said Samir. *J. Amer. Concrete Inst. Proc.* 1986, 597-600.
- [51] Akçaoğlu, T., Tokyay, M., & Çelik, T. (2005). Assessing the ITZ microcracking via scanning electron microscope and its effect on the failure behavior of concrete. *Cement and Concrete Research*, 35(2), 358-363.
- [52] Igarashi, S., Bentur, A., & Mindess, S. (1996). The effect of processing on the bond and interfaces in steel fiber reinforced cement composites. *Cement and Concrete Composites*, 18(5), 313-322.
- [53] Igarashi, S., Bentur, A., & Mindess, S. (1996). Microhardness testing of cementitious materials. *Advanced Cement Based Materials*, 4(2), 48-57.



- [54] Zhu, W., & Bartos, P.J.M. (1997). Assessment of interfacial microstructure and bond properties in aged GRC using a novel microindentation method. *Cement and Concrete Research*, 27(11), 1701-1711.
- [55] Abu-Lebdeh, T., Hamoush, S., Heard, W., & Zornig, B. (2011). Effect of matrix strength on pullout behavior of steel fiber reinforced very-high strength concrete composites. *Construction and Building Materials*, 25(1), 39-46.
- [56] Chan, Y.W., & Li, V.C. (1997). Effects of transition zone densification on fiber/cement paste bond strength improvement. *Advanced cement based materials*, 5(1), 8-17.
- [57] Banthia, N., & Trottier, J.F. (1995). Concrete Reinforced with Deformed Steel Fibers-Part II: Toughness Characterization. *ACI Materials Journal-American Concrete Institute*, 92(2), 146-154.
- [58] Banthia, N., & Trottier, J.F. (1994). Concrete reinforced with deformed steel fibers, part I: bond-slip mechanisms. *Materials Journal*, 91(5), 435-446.
- [59] Wille, K., & Naaman, A.E. (2013). Effect of Ultra-High-Performance Concrete on Pullout Behavior of High-Strength Brass-Coated Straight Steel Fibers. *ACI Materials Journal*, 110(4).
- [60] Park, S.H., Kim, D.J., Ryu, G.S., & Koh, K.T. (2012). Effect of adding micro fibers on the pullout behavior of high strength steel fibers in UHPC matrix. *Proceedings of Hipermat*, 541-548.
- [61] Habel, K., Viviani, M., Denarié, E., & Brühwiler, E. (2006). Development of the mechanical properties of an ultra-high performance fiber reinforced concrete (UHPRFC). *Cement and Concrete Research*, 36(7), 1362-1370.
- [62] Toledo, Filho, R.D., Koenders, E. A.B., Formagini, S., & Fairbairn, E. M. R. (2012). Performance assessment of ultra high performance fiber reinforced cementitious composites in view of sustainability. *Materials & Design*, 36, 880-888.
- [63] Zhang, Y., Sun W., Liu S.F., Jiao C.J., Liu J.Z. (2008). Preparation of C200 green reactive powder concrete and its static–dynamic behaviors. *Cement and Concrete Composites*, 30(9), 831-838.
- [64] Yang, S.L., Millard, S.G., Soutsos, M.N., Barnett, S.J., & Le, T.T. (2009). Influence of aggregate and curing regime on the mechanical properties of ultra-high performance fibre reinforced concrete (UHPRFC). *Construction and Building Materials*, 23(6), 2291-2298.
- [65] Yang, S., & Diao, B. (2009). Influence of curing regime on the ductility of ultra-high performance fiber reinforced concrete (UHPRFC). In *ICCTP 2009: Critical Issues In Transportation Systems Planning, Development, and Management* (pp. 1-7).

- [66] Hannawi, K., Bian, H., Prince-Agbodjan, W., & Raghavan, B. (2016). Effect of different types of fibers on the microstructure and the mechanical behavior of ultra-high performance fiber-reinforced concretes. *Composites Part B: Engineering*, 86, 214-220.
- [67] Hassan, A.M.T., Jones, S. W., & Mahmud, G.H. (2012). Experimental test methods to determine the uniaxial tensile and compressive behaviour of ultra high performance fibre reinforced concrete (UHPFRC). *Construction and building materials*, 37, 874-882.
- [68] Charron, J.P., Denarié, E., & Brühwiler, E. (2008). Transport properties of water and glycol in an ultra high performance fiber reinforced concrete (UHPFRC) under high tensile deformation. *Cement and Concrete Research*, 38(5), 689-698.
- [69] Kang, S.T., Lee, Y., Park, Y.D., & Kim, J.K. (2010). Tensile fracture properties of an ultra high performance fiber reinforced concrete (UHPFRC) with steel fiber. *Composite Structures*, 92(1), 61-71.
- [70] Wille, K., Kim, D.J., & Naaman, A.E. (2011). Strain-hardening UHP-FRC with low fiber contents. *Materials and Structures*, 44(3), 583-598.
- [71] Park, S.H., Kim, D.J., Ryu, G.S., & Koh, K.T. (2012). Tensile behavior of ultra high performance hybrid fiber reinforced concrete. *Cement and Concrete Composites*, 34(2), 172-184.
- [72] Huang, Z., Li, C., Liu, Y. (2014). The effect of polyethylene fiber on the properties of UHPC. *Material Review*. 28(20): 111-115.
- [73] Birol, T., Hasgul, U., Terzi, M., Yavas, A., Turker, K., & Yazici, H. (2016). Effect of Different Steel Fiber Type and Content in Flexural Behavior of Ultra High Performance Fiber Reinforced Concrete.
- [74] Sivakumar, A., & Santhanam, M. (2007). Mechanical properties of high strength concrete reinforced with metallic and non-metallic fibres. *Cement and Concrete Composites*, 29(8), 603-608.
- [75] Qian, C.X., & Stroeven, P. (2000). Development of hybrid polypropylene-steel fibre-reinforced concrete. *Cement and Concrete Research*, 30(1), 63-69.
- [76] Kim, D.J., Park, S.H., Ryu, G.S., & Koh, K.T. (2011). Comparative flexural behavior of hybrid ultra high performance fiber reinforced concrete with different macro fibers. *Construction and Building Materials*, 25(11), 4144-4155.
- [77] Hai, R., Liu, J., Zhang, M., Zhang, L. (2016). Performance of hybrid steel - polyvinyl alcohol fiber reinforced ultra high performance concrete. *Concrete*. 5: 95-97.

- [78] Toutanji, H., & Bayasi, Z. (1998). Effects of manufacturing techniques on the flexural behavior of steel fiber-reinforced concrete. *Cement and Concrete Research*, 28(1), 115-124.
- [79] Barnett, S.J., Lataste, J.F., Parry, T., Millard, S.G., & Soutsos, M.N. (2010). Assessment of fibre orientation in ultra high performance fibre reinforced concrete and its effect on flexural strength. *Materials and Structures*, 43(7), 1009-1023.
- [80] Kang, S.T., Lee, B.Y., Kim, J.K., & Kim, Y.Y. (2011). The effect of fibre distribution characteristics on the flexural strength of steel fibre-reinforced ultra high strength concrete. *Construction and Building Materials*, 25(5), 2450-2457.
- [81] Nguyen, D.L., Kim, D.J., Ryu, G.S., & Koh, K.T. (2013). Size effect on flexural behavior of ultra-high-performance hybrid fiber-reinforced concrete. *Composites Part B: Engineering*, 45(1), 1104-1116.
- [82] Lee, M.G., Wang, Y.C., & Chiu, C.T. (2007). A preliminary study of reactive powder concrete as a new repair material. *Construction and building materials*, 21(1), 182-189.
- [83] Ku, H., Cheng, Y.M., Snook, C., & Baddeley, D. (2005). Drop weight impact test fracture of vinyl ester composites: micrographs of pilot study. *Journal of composite materials*, 39(18), 1607-1620.
- [84] Habel, K., & Gauvreau, P. (2008). Response of ultra-high performance fiber reinforced concrete (UHPFRC) to impact and static loading. *Cement and Concrete Composites*, 30(10), 938-946.
- [85] Rong, Z., Sun, W., & Zhang, Y. (2010). Dynamic compression behavior of ultra-high performance cement based composites. *International Journal of Impact Engineering*, 37(5), 515-520.
- [86] Xu, G., Magnani, S., & Hannant, D.J. (1998). Durability of hybrid polypropylene-glass fibre cement corrugated sheets. *Cement and Concrete Composites*, 20(1), 79-84.
- [87] Yu, R., Spiesz, P., & Brouwers, H.J.H. (2014). Static properties and impact resistance of a green Ultra-High Performance Hybrid Fibre Reinforced Concrete (UHPHFRC): experiments and modeling. *Construction and Building Materials*, 68, 158-171.
- [88] Wu, Z., Shi, C., He, W., & Wang, D. (2017). Static and dynamic compressive properties of ultra-high performance concrete (UHPC) with hybrid steel fiber reinforcements. *Cement and Concrete Composites*, 79, 148-157.
- [89] Naaman, A. E., Najm, H. (1991). Bond-slip mechanisms of steel fibers in concrete. *Materials Journal*, 88(2), 135-145.

- [90] Romualdi, J.P., & Mandel, J.A. (1964). Tensile strength of concrete affected by uniformly distributed and closely spaced short lengths of wire reinforcement. In *Journal Proceedings*, 61(6): 657-672.
- [91] Roumaldi, J.P., & Batson, G.B. (2008). *Mechanics of crack arrest in concrete* (No. SP-249-12).
- [92] Chinese National Standard (2005). Test methods for flowability of cement paste, GB2419-2005, Beijing, China.
- [93] Chinese National Standard (2009). The test method for property of bond between steel fiber and mortar. CECS13-2009. 64-68, Beijing, China.
- [94] China National Standards (1999). Method of testing cements - determination of strength, GB/T 17671-1999, Beijing, China (in Chinese).
- [95] Pacheco, F., Christ, R., GIL, A., Tutikian, B. (2016). SEM and 3D microtomography application to investigate the distribution of fibers in advanced cementitious composites. *Revista IBRACON de Estruturas e Materiais*, 9(6) 824-841.
- [96] Shi, C., Wu, Z., Xiao, J., Wang, D., Huang, Z., & Fang, Z. (2015). A review on ultra high performance concrete: Part I. Raw materials and mixture design. *Construction and Building Materials*, 101, 741-751.
- [97] Wang, D., Shi, C., Wu, Z., Xiao, J., Huang, Z., & Fang, Z. (2015). A review on ultra high performance concrete: Part II. Hydration, microstructure and properties. *Construction and Building Materials*, 96, 368-377.
- [98] Yoo, D.Y., Shin, H.O., Yang, J.M., & Yoon, Y.S. (2014). Material and bond properties of ultra high performance fiber reinforced concrete with micro steel fibers. *Composites Part B: Engineering*, 58, 122-133.
- [99] Lee, S.F., & Jacobsen, S. (2011). Study of interfacial microstructure, fracture energy, compressive energy and debonding load of steel fiber-reinforced mortar. *Materials and structures*, 44(8), 1451-1465.
- [100] Li, V.C., Wu, H.C., & Chan, Y.W. (1996). Effect of plasma treatment of polyethylene fibers on interface and cementitious composite properties. *Journal of the American Ceramic Society*, 79(3), 700-704.
- [101] Wille, K., & Naaman, A.E. (2012). Pullout behavior of high-strength steel fibers embedded in ultra-high-performance concrete. *ACI Materials Journal*, 109(4).
- [102] Scrivener, K.L., & Nematy, K.M. (1996). The percolation of pore space in the cement paste/aggregate interfacial zone of concrete. *Cement and Concrete Research*, 26(1), 35-40.

- [103] Wang, X.H., Jacobsen, S., He, J.Y., Zhang, Z.L., Lee, S.F., & Lein, H.L. (2009). Application of nanoindentation testing to study of the interfacial transition zone in steel fiber reinforced mortar. *Cement and Concrete Research*, 39(8), 701-715.
- [104] Rangaraju, P.R., Olek, J., & Diamond, S. (2010). An investigation into the influence of inter-aggregate spacing and the extent of the ITZ on properties of Portland cement concretes. *Cement and Concrete Research*, 40(11), 1601-1608.
- [105] Wang, X.H., Jacobsen, S., Lee, S.F., He, J.Y., & Zhang, Z.L. (2010). Effect of silica fume, steel fiber and ITZ on the strength and fracture behavior of mortar. *Materials and structures*, 43(1-2), 125.
- [106] Wu, Z., Shi, C., Gao, P., Wang, D., & Cao, Z. (2014). Effects of deicing salts on the scaling resistance of concrete. *Journal of Materials in Civil Engineering*, 27(5), 04014160.
- [107] Kadri, E.H., & Duval, R. (2009). Hydration heat kinetics of concrete with silica fume. *Construction and Building Materials*, 23(11), 3388-3392.
- [108] Vikan, H., & Justnes, H. (2007). Rheology of cementitious paste with silica fume or limestone. *Cement and Concrete Research*, 37(11), 1512-1517.
- [109] Lura, P., Jensen, O.M., & van Breugel, K. (2003). Autogenous shrinkage in high-performance cement paste: An evaluation of basic mechanisms. *Cement and Concrete Research*, 33(2), 223-232.
- [110] Zhang, W., Zhang, Y., Liu, L., Zhang, G., & Liu, Z. (2012). Investigation of the influence of curing temperature and silica fume content on setting and hardening process of the blended cement paste by an improved ultrasonic apparatus. *Construction and Building Materials*, 33, 32-40.
- [111] Esteves, L.P. (2011). On the hydration of water-entrained cement-silica systems: combined SEM, XRD and thermal analysis in cement pastes. *Thermochimica Acta*, 518(1), 27-35.
- [112] Ye, G., Liu, X., De Schutter, G., Poppe, A.M., & Taerwe, L. (2007). Influence of limestone powder used as filler in SCC on hydration and microstructure of cement pastes. *Cement and Concrete Composites*, 29(2), 94-102.
- [113] Pane, I., & Hansen, W. (2005). Investigation of blended cement hydration by isothermal calorimetry and thermal analysis. *Cement and concrete research*, 35(6), 1155-1164.
- [114] Zhang, T., Yu, Q., Wei, J., Gao, P., Chen, P., & Hu, J. (2012). Micro-structural development of gap-graded blended cement pastes containing a high amount of supplementary cementitious materials. *Cement and Concrete Composites*, 34(9), 1024-1032.

- [115] Halamickova, P., Detwiler, R.J., Bentz, D.P., & Garboczi, E.J. (1995). Water permeability and chloride ion diffusion in Portland cement mortars: relationship to sand content and critical pore diameter. *Cement and concrete research*, 25(4), 790-802.
- [116] Ghafari, E., Costa, H., Júlio, E., Portugal, A., & Durães, L. (2014). The effect of nanosilica addition on flowability, strength and transport properties of ultra high performance concrete. *Materials & Design*, 59, 1-9.
- [117] Metha, P.K., Monterio, P.J.M. (2006). *Concrete, Microstructure, Properties and Materials*. McGraw-Hill, London.
- [118] Zeng, Q., Li, K., Fen-Chong, T., & Dangla, P. (2012). Pore structure characterization of cement pastes blended with high-volume fly-ash. *Cement and Concrete Research*, 42(1), 194-204.
- [119] Jennings, H. M. (2000). A model for the microstructure of calcium silicate hydrate in cement paste. *Cement and concrete research*, 30(1), 101-116.
- [120] Setter, N., & Roy, D.M. (1978). Mechanical features of chemical shrinkage of cement paste. *Cement and Concrete Research*, 8(5), 623-634.
- [121] Jensen, O.M., Hansen P.F. (1996). Autogenous deformation and change of the relative humidity in silica fume-modified cement paste. *ACI Materials Journal*, 93(6), 539-543.
- [122] Russell, H.G. and Graybeal, B.A., (2013). Ultra-high performance concrete: A state-of-the-art report for the bridge community (No. FHWA-HRT-13-060).
- [123] Wille, K., Naaman, A.E., and El-Tawil, S., (2011). Optimizing Ultra-High-Performance Fiber- Reinforced Concrete, *Concrete International*, 33(9), September
- [124] Teichmann, T. and Schmidt, M., (2002) Mix Design and Durability of Ultra High Performance Concrete (UHPC), *Proceedings of the 4th International Ph.D. Symposium in Civil Engineering*, Munich, pp. 341–347.
- [125] Williams, E. Graham, S.S., Reed, P.A., & Rushing, T.S. (2009). Laboratory characterization of cor-tuf concrete with and without steel fibers, Technical Report No. ERDC/GSL TR-02-22, U.S. Army Corps of Engineers, Engineer Research and Development Center, Washington, D.C.
- [126] Wallevik, O.H., (1983). Description of fresh concrete properties by use of two-point workability test instrument. the Norwegian Institute of Technology, M.Sc. thesis, Trondheim, Norway.
- [127] Kim, D.J., El-Tawil, S., & Naaman, A. E. (2010). Effect of matrix strength on pullout behavior of high-strength deformed steel fibers. *Special Publication*, 272, 135-150.

- [128] Park, S.H., Ryu, G.S., Koh, K.T., & Kim, D.J. (2014). Effect of shrinkage reducing agent on pullout resistance of high-strength steel fibers embedded in ultra-high-performance concrete. *Cement and Concrete Composites*, 49, 59-69.
- [129] Kang, S.H., Kim, J.J., Kim, D.J., & Chung, Y.S. (2013). Effect of sand grain size and sand-to-cement ratio on the interfacial bond strength of steel fibers embedded in mortars. *Construction and Building materials*, 47, 1421-1430.
- [130] Gray, R.J. (1983). Experimental techniques for measuring fibre/matrix interfacial bond shear strength. *International journal of adhesion and adhesives*, 3(4), 197-202.
- [131] Lee, Y., Kang, S.T., & Kim, J.K. (2010). Pullout behavior of inclined steel fiber in an ultra-high strength cementitious matrix. *Construction and Building Materials*, 24(10), 2030-2041.
- [132] Wu, Z., Shi, C., & Khayat, K.H. (2016). Influence of silica fume content on microstructure development and bond to steel fiber in ultra-high strength cement-based materials (UHSC). *Cement and Concrete Composites*, 71, 97-109.
- [133] Maalej, M. and Li, V.C., 1994. Flexural/tensile-strength ratio in engineered cementitious composites. *Journal of Materials in Civil Engineering*, 6(4), pp.513-528.
- [134] Krenchel, H. Fibre Reinforcement, Akademisk Forlag, Copenhagen, 1964.
- [135] Han, B., Dong, S., Ou, J., Zhang, C., Wang, Y., Yu, X., Ding, S. (2016). Microstructure related mechanical behaviors of short-cut super-fine stainless wire reinforced reactive powder concrete. *Materials & Design*, 2016, 96: 16-26.
- [136] Sanchez, F., & Sobolev, K. (2010). Nanotechnology in concrete—a review. *Construction and building materials*, 24(11), 2060-2071.
- [137] Ji, T. (2005). Preliminary study on the water permeability and microstructure of concrete incorporating nano-SiO<sub>2</sub>. *Cement and Concrete Research*, 35(10), 1943-1947.
- [138] Li, Z., Wang, H., He, S., Lu, Y., & Wang, M. (2006). Investigations on the preparation and mechanical properties of the nano-alumina reinforced cement composite. *Materials Letters*, 60(3), 356-359.
- [139] Li, H., Zhang, M. H., & Ou, J. P. (2007). Flexural fatigue performance of concrete containing nano-particles for pavement. *International Journal of fatigue*, 29(7), 1292-1301.
- [140] Shaikh, F.U., & Supit, S.W. (2014). Mechanical and durability properties of high volume fly ash (HVFA) concrete containing calcium carbonate (CaCO<sub>3</sub>) nanoparticles. *Construction and building materials*, 70, 309-321.

- [141] Metaxa, Z.S., Konsta-Gdoutos, M.S., & Shah, S.P. (2009). Carbon nanotubes reinforced concrete. *Special Publication*, 267, 11-20.
- [142] Camiletti, J., Soliman, A.M., & Nehdi, M.L. (2013). Effects of nano-and micro-limestone addition on early-age properties of ultra-high-performance concrete. *Materials and structures*, 46(6), 881-898.
- [143] Bensted, J. (1983). Further hydration investigations involving Portland cement and the substitution of limestone for gypsum. *World cement*, 14(10), 383-392.
- [144] Ramezani-pour, A.A., Ghiasvand, E., Nickseresht, I., Mahdikhani, M., & Moodi, F. (2009). Influence of various amounts of limestone powder on performance of Portland limestone cement concretes. *Cement and Concrete Composites*, 31(10), 715-720.
- [145] Tsivilis, S., Batis, G., Chaniotakis, E., Grigoriadis, G., & Theodossis, D. (2000). Properties and behavior of limestone cement concrete and mortar. *Cement and Concrete Research*, 30(10), 1679-1683.
- [146] Wu, Z., Shi, C., Khayat, K.H., & Wan, S. (2016). Effects of different nanomaterials on hardening and performance of ultra-high strength concrete (UHSC). *Cement and Concrete Composites*, 70, 24-34.
- [147] Péra, J., Husson, S., & Guilhot, B. (1999). Influence of finely ground limestone on cement hydration. *Cement and Concrete Composites*, 21(2), 99-105.
- [148] Ramezani-pour, A.A., Ghiasvand, E., Nickseresht, I., Mahdikhani, M., & Moodi, F. (2009). Influence of various amounts of limestone powder on performance of Portland limestone cement concretes. *Cement and Concrete Composites*, 31(10), 715-720.
- [149] Li, W., Huang, Z., Cao, F., Sun, Z., & Shah, S. P. (2015). Effects of nano-silica and nano-limestone on flowability and mechanical properties of ultra-high-performance concrete matrix. *Construction and Building Materials*, 95, 366-374.
- [150] Xu, Q. L., Meng, T., & Huang, M.Z. (2012). Effects of nano-CaCO<sub>3</sub> on the compressive strength and microstructure of high strength concrete in different curing temperature. In *Applied Mechanics and Materials* Trans Tech Publications, 121, 126-131).
- [151] Moon, J., Oh, J.E., Balonis, M., Glasser, F.P., Clark, S.M., Monteiro, P.J. (2012). High pressure study of low compressibility tetracalcium aluminum carbonate hydrates 3CaO·Al<sub>2</sub>O<sub>3</sub>·CaCO<sub>3</sub>·11H<sub>2</sub>O. *Cement and Concrete Composites*, 42(1), 105-110.
- [152] Nambiar, E. K., & Ramamurthy, K. (2006). Models relating mixture composition to the density and strength of foam concrete using response surface methodology. *Cement and Concrete Composites*, 28(9), 752-760.



- [153] Ramezaniapour, A.A., Ghiasvand, E., Nickseresht, I., Mahdikhani, M., & Moodi, F. (2009). Influence of various amounts of limestone powder on performance of Portland limestone cement concretes. *Cement and Concrete Composites*, 31(10), 715-720.
- [154] Ye, G (2003). Experimental study and numerical simulation of the development of the microstructure and permeability of cementitious materials. TU Delft, Delft University of Technology.
- [155] Ramezaniapour, A.A., Ghiasvand, E., Nickseresht, I., Mahdikhani, M., and Moodi, F. (2009). Influence of various amounts of limestone powder on performance of Portland limestone cement concretes. *Cement Concrete Composite*, 31(10), 715-720.
- [156] Scrivener, K.L., Crumbie, A.K., & Laugesen, P. (2004). The interfacial transition zone (ITZ) between cement paste and aggregate in concrete. *Interface Science*, 12(4), 411-421.
- [157] Richardson, I.G. (1999). The nature of CSH in hardened cements. *Cement and Concrete Research*, 29(8), 1131-1147.
- [158] Mondal, P., Shah, S.P., & Marks, L.D. (2008). Nanoscale characterization of cementitious materials. *ACI Materials Journal*, 105(2), 174-179.
- [159] Soliman, A.M., & Nehdi, M.L. (2011). Effect of drying conditions on autogenous shrinkage in ultra-high performance concrete at early-age. *Materials and Structures*, 44(5), 879-899.
- [160] Rong, Z., Sun, W., Xiao, H., & Jiang, G. (2015). Effects of nano-SiO<sub>2</sub> particles on the mechanical and microstructural properties of ultra-high performance cementitious composites. *Cement and Concrete Composites*, 56, 25-31.
- [161] Ghafari, E., Costa, H., Júlio, E., Portugal, A., & Durães, L. (2014). The effect of nanosilica addition on flowability, strength and transport properties of ultra high performance concrete. *Materials & Design*, 59, 1-9.
- [162] Sato, T., & Beaudoin, J.J. (2011). Effect of nano-CaCO<sub>3</sub> on hydration of cement containing supplementary cementitious materials. *Advances in Cement Research*, 23(1), 33-43.
- [163] De Weerdt, K., Justnes, H., Kjellsen, K.O., & Sellevold, E.J. (2010). Fly ash-limestone ternary composite cements: synergetic effect at 28 days. *Nordic Concrete Research*, 42(2), 51-70.
- [164] Hooton, R.D., Nokken, M., & Thomas, M.D.A. (2007). Portland-limestone cement: state-of-the-art report and gap analysis for CSA A 3000. *Report prepared for St. Lawrence Cement*.

- [165] Naaman, A.E., Namur, G.G., Alwan, J.M., & Najm, H.S. (1991). Fiber pullout and bond slip. I: Analytical study. *Journal of Structural Engineering*, 117(9), 2769-2790.
- [166] Naaman, A.E., Namur, G.G., Alwan, J.M., & Najm, H.S. (1991). Fiber pullout and bond slip. II: Experimental validation. *Journal of Structural Engineering*, 117(9), 2791-2800.
- [167] Cunha, V.M., Barros, J.A., & Sena-Cruz, J. (2007). *Pullout behaviour of hooked-end steel fibres in self-compacting concrete*. Universidade do Minho. Escola de Engenharia. Departamento de Engenharia Civil.
- [168] Alwan, J.M., Naaman, A.E., & Hansen, W. (1991). Pull-out work of steel fibers from cementitious composites: analytical investigation. *Cement and Concrete Composites*, 13(4), 247-255.
- [169] Kawashima, S., Hou, P., Corr, D.J., & Shah, S.P. (2013). Modification of cement-based materials with nanoparticles. *Cement and Concrete Composites*, 36, 8-15.
- [170] Masse, S., Zanni, H., Lecourtier, J., Roussel, J.C., & Rivereau, A. (1993). <sup>29</sup>Si solid state NMR study of tricalcium silicate and cement hydration at high temperature. *Cement and concrete research*, 23(5), 1169-1177.
- [171] Wu, Z., Shi, C., Khayat, K.H., Zhu, D. (2016). Optimization of microstructure and pullout behavior of fibers in ultra-high strength concrete with the help of nanoparticles and heat curing. In proceeding 1st International Conference on UHPC Materials and Structures 27 - 30 Oct, Changsha, China.
- [172] Ghafari, E., Costa H., Júlio, E., Portugal, A., Durães, L. (2014). The effect of nanosilica addition on flowability, strength and transport properties of ultra high performance concrete. *Materials & Design*, 59, 1-9.
- [173] Sanchez, F., & Sobolev, K. (2010). Nanotechnology in concrete—a review. *Construction and building materials*, 24(11), 2060-2071.
- [174] Jennings, H.M. (2000). A model for the microstructure of calcium silicate hydrates in cement paste. *Cement and Concrete Research*, 30, 101-116.
- [175] Erdem, S., Dawson, A. R., & Thom, N.H. (2012). Influence of the micro-and nanoscale local mechanical properties of the interfacial transition zone on impact behavior of concrete made with different aggregates. *Cement and Concrete Research*, 42(2), 447-458.
- [176] Scrivener, K.L. (2004). Backscattered electron imaging of cementitious microstructures: understanding and quantification. *Cement and Concrete Composites*, 26(8), 935-945.

- [177] Ash, J.E., Hall, M.G., Langford, J.I., & Mellas, M. (1993). Estimations of degree of hydration of Portland cement pastes. *Cement and Concrete Research*, 23(2), 399-406.
- [178] Scrivener, K.L., Crumie, A.K., & Laugesen, P. (2004). The interfacial transition zone (ITZ) between cement paste and aggregate in concrete. *Interface Science*, 12(4), 411-421.
- [179] Pelisser, F., Gleize, P.J.P., & Mikowski, A. (2012). Effect of the Ca/Si molar ratio on the micro/nanomechanical properties of synthetic CSH measured by nanoindentation. *The Journal of Physical Chemistry C*, 116(32), 17219-17227.
- [180] Chen, J.J., Thomas, J.J., Taylor, H.F., Jennings, H.M. (2004) Solubility and structure of calcium silicate hydrate. *Cement and Concrete Research*, 34(9), 1499-1519.
- [181] Richardson, I.G. (1999) The nature of CSH in hardened cements. *Cement and Concrete Research*, 29(8), 1131-1147.
- [182] Pompo, A., Stupak, P.R., Nicolais, L., & Marchese, B. (1996). Analysis of steel fibre pull-out from a cement matrix using video photography. *Cement and Concrete Composites*, 18(1), 3-8.
- [183] Robins, P., Austin, S., & Jones, P. (2002). Pull-out behaviour of hooked steel fibres. *Materials and Structures*, 35(7), 434-442.
- [184] Lee, Y., Kang, S.T., & Kim, J.K. (2010). Pullout behavior of inclined steel fiber in an ultra-high strength cementitious matrix. *Construction and Building Materials*, 24(10), 2030-2041.
- [185] Beglarigale, A., & Yazıcı, H. (2015). Pull-out behavior of steel fiber embedded in flowable RPC and ordinary mortar. *Construction and Building Materials*, 75, 255-265.
- [186] Chanvillard, G., & Aïtcin, P.C. (1996). Pull-out behavior of corrugated steel fibers: Qualitative and statistical analysis. *Advanced Cement Based Materials*, 4(1), 28-41.
- [187] Zile, E., & Zile, O. (2013). Effect of the fiber geometry on the pullout response of mechanically deformed steel fibers. *Cement and concrete research*, 44, 18-24.
- [188] Kim, D.J., Park, S.H., Ryu, G.S., & Koh, K.T. (2011). Comparative flexural behavior of hybrid ultra high performance fiber reinforced concrete with different macro fibers. *Construction and Building Materials*, 25(11), 4144-4155.
- [189] Banthia, N. (1990). A study of some factors affecting the fiber–matrix bond in steel fiber reinforced concrete. *Canadian Journal of Civil Engineering*, 17(4), 610-620.

- [190] Zhang, M.H., Tam, C.T., & Leow, M.P. (2003). Effect of water-to-cementitious materials ratio and silica fume on the autogenous shrinkage of concrete. *Cement and Concrete Research*, 33(10), 1687-1694.
- [191] Nonat, A. (2004). The structure and stoichiometry of C-S-H. *Cement and Concrete Research*, 34(9), 1521-1528.
- [192] Wang, S., Peng, X., Tang, L., Zeng, L., & Lan, C. (2014). Influence of inorganic admixtures on the 11Å-tobermorite formation prepared from steel slags: XRD and FTIR analysis. *Construction and Building Materials*, 60, 42-47.
- [193] Gao, X. (2010). Research on the performance of UHPC with steel fiber (Master thesis). Hunan University, China.
- [194] Han, B., Dong, S., Ou, J., Zhang, C., Wang, Y., Yu, X., & Ding, S. (2016). Microstructure related mechanical behaviors of short-cut super-fine stainless wire reinforced reactive powder concrete. *Materials & Design*, 96, 16-26.
- [195] Guvensoy, G., Bayramov, F., Ilki, A., Sengul, C., Tasdemir, A., Kocaturk, N., & Yerlikaya, M. (2004, September). Mechanical behavior of high performance steel fiber reinforced cementitious composites under cyclic loading condition, ultra high performance concrete (UHPC). In Proceedings of the International Symposium on UHPC, Kassel, Germany (pp. 649-660).
- [196] Ross, C.A., Tedesco, J.W., & Kuennen, S.T. (1995). Effects of strain rate on concrete strength. *Materials Journal*, 92(1), 37-47.
- [197] Wille, K., Naaman, A.E., Parra-Montesinos, G.J. (2011). Ultra-high performance concrete with compressive strength exceeding 150 mpa (22 ksi): a simpler way, *ACI Material Journal*, 108(1), 34-46.
- [198] Hannawi, K., Bian, H., Prince-Agbodjan, W., Raghavan, B. (2016). Effect of different types of fibers on the microstructure and the mechanical behavior of Ultra-High Performance Fiber-Reinforced Concretes. *Composites Part B: Engineering*, 86, 214-220.
- [199] Zhang, Y., Sun, W, Liu, S, Jiao, C, Liu, J. (2008). Preparation of C200 green reactive powder concrete and its static–dynamic behaviors. *Cement and Concrete Composites*, 30(9), 831-838.
- [200] Su, Y., Li, J., Wu, C., Wu, P., & Li, Z.X. (2016). Effects of steel fibres on dynamic strength of UHPC. *Construction and Building Materials*, 114, 708-718.
- [201] Xu, G., Magnani, S., & Hannant, D. J. (1998). Durability of hybrid polypropylene-glass fibre cement corrugated sheets. *Cement and Concrete Composites*, 20(1), 79-84.

- [202] Yu, R., Spiesz, P., & Brouwers, H.J.H. (2014). Static properties and impact resistance of a green Ultra-High Performance Hybrid Fibre Reinforced Concrete (UHPHFRC): experiments and modeling. *Construction and Building Materials*, 68, 158-171.
- [203] Wu, Z. Shi, C., He, W., Wang, D. (2016). Uniaxial compression behavior of ultra-high performance concrete (UHPC) with hybrid steel fiber. *Journal of Materials in Civil Engineering*, 06016017-1-7.
- [204] Zhang, W.H., Zhang, Y.S. (2015). Research on the static and dynamic compressive properties of high performance cementitious composite (HPCC) containing coarse aggregate. *Archives of Civil and Mechanical Engineering*, 15(3), 711-720.
- [205] Collepardi, S., Coppola, L., Troli, R., Collepardi, M., (1997). Mechanical properties of modified reactive powder concrete, *ACI Special Publication*, 173, 1-22.
- [206] Yardımcı, M.Y., Yiğiter, H., Aydın, S. and Türkel, S., (2010). Mechanical properties of reactive powder concrete containing high volumes of ground granulated blast furnace slag. *Cement and Concrete Composites*, 32(8), 639-648.
- [207] Wu, Z., Shi, C., & He, W. (2017). Comparative study on flexural properties of ultra-high performance concrete with supplementary cementitious materials under different curing regimes. *Construction and Building Materials*, 136, 307-313.
- [208] Zhang, Y., Sun, W., Chen, Q., Chen, L. (2007). Synthesis and heavy metal immobilization behaviors of slag based geopolymer. *Journal of hazardous materials*, 143(1-2), 206-213.
- [209] Wu, Z., Shi, C., Khayat, K.H. (2018). Multi-scale investigation of microstructure, fiber pullout behavior, and mechanical properties of ultra-high performance concrete with nano-CaCO<sub>3</sub> particles. *Cement Concrete Composites*, 86, 255-265.
- [210] Wu, Z., Khayat, K.H., Shi, C. (2017). Effect of nano-SiO<sub>2</sub> particles and curing time on development of fiber-matrix bond properties and microstructure of ultra-high strength concrete. *Cement and Concrete Composites*, 95, 247-256.
- [211] Wong, Y.L., Lam, L., Poon, C.S., & Zhou, F.P. (1999). Properties of fly ash-modified cement mortar-aggregate interfaces. *Cement and Concrete Research*, 29(12), 1905-1913.
- [212] Bischoff, P.H., & Perry, S.H. (1991). Compressive behaviour of concrete at high strain rates. *Materials and structures*, 24(6), 425-450.
- [213] De Weerd, K., Haha, M.B., Le Saout, G., Kjellsen, K.O., Justnes, H., & Lothenbach, B. (2011). Hydration mechanisms of ternary Portland cements containing limestone powder and fly ash. *Cement and Concrete Research*, 41(3), 279-291.

- [214] Kim, D.J., Park, S.H., Ryu, G.S., & Koh, K.T. (2011). Comparative flexural behavior of hybrid ultra high performance fiber reinforced concrete with different macro fibers. *Construction and Building Materials*, 25(11), 4144-4155.
- [215] Yoo, D.Y., Banthia, N., & Yoon, Y.S. (2016). Impact resistance of ultra-high-performance fiber-reinforced concrete with different steel fibers. In *9th RILEM International Symposium on Fiber Reinforced Concrete (BEFIB 2016)*, Pacific Gateway Hotel, Vancouver, BC, Canada.
- [216] Su, Y., Li, J., Wu, C., Wu, P., & Li, Z.X. (2016). Influences of nano-particles on dynamic strength of ultra-high performance concrete. *Composites Part B: Engineering*, 91, 595-609.
- [217] Pal, S.C., Mukherjee, A., & Pathak, S.R. (2003). Investigation of hydraulic activity of ground granulated blast furnace slag in concrete. *Cement and Concrete Research*, 33(9), 1481-1486.

## VITA

Zemei Wu received her Masters degree in April 2012 in Road and Railway Engineering from Nanjing University of Aeronautics and Astronautics. She was granted the *Distinguished Masters Thesis Award*, which is one out of 10 in the department. She started her Ph.D. program in September 2012 at Hunan University under the supervision of Professor Caijun Shi and completed her Ph.D. in Civil Engineering in June 2017. In January 2015, Zemei started her dual Ph.D. program at Missouri S&T under the supervision of Professor Kamal H. Khayat. Professor Shi continued to supervisor her work. During her study at Hunan University, she was granted several awards and scholarships, including the *National Scholarship for Graduate Student*, the *Excellent Graduate Student Award*, and the *Outstanding Ph.D. Candidate Scholarship*. After graduation from Hunan University, Zemei received the *Outstanding Ph.D. dissertation Award* granted from The Chinese Ceramic Society, which is considered to be the greatest honor for Ph.D. students in relevant area of China. In April 2018, she was awarded the *Academic Excellence – Outstanding Ph.D. Student* by the Academy of Civil Engineers in the Department of Civil, Architectural and Environmental Engineering at Missouri S&T. In July 2018, she received her Ph.D. in Civil Engineering from Missouri S&T.

In total, Zemei has published 22 journal papers and 5 conference papers, of which she is the first author of 10. She served as an Associate Member of the American Concrete Institute (ACI) 234 on Silica Fume and ACI 239 on Ultra-High Performance Concrete. In 2017, she was awarded the *Outstanding Reviewer* for Cement and Concrete Composites, Construction and Building Materials, and Journal of Cleaner Production.